UNIVERSITÀ
DEGLI STUDI
DI PADOVA

DIPARTIMENTO DI FISICA e ASTRONOMIA "GALILEO GALILEI"

Scuola di Dottorato di Ricerca in Fisica
XXVI ciclo

Ph.D. Thesis

ANISOTROPIC PROPAGATION OF SURFACE PLASMON POLARITONS: STUDY AND EXPLOITATIONS.

Direttore della Scuola: Ch.mo Prof. Andrea Vitturi

Supervisore: Ch.mo Prof. Filippo Romanato

Dottorando: Enrico Gazzola

Abstract

Sinusoidally patterned metallic surfaces, known as plasmonic gratings, constitute one of the principal structures which allow to achieve the coupling between an incident light beam and a Surface Plasmon Polariton mode. A variety of phenomena are available when the grating is rotated of an azimuthal angle with respect to the incidence plane.

Aim of this work is a comprehensive investigation of the propagation properties of the surface mode under this configuration, correlating the role of the anisotropy introduced by the grating to the position and shape of the plasmonic resonance dip in the reflectance spectra. Analytical models and physical interpretations are provided; both experimental and computational means are exploited in order to validate the models, including the observation of innovative effects. Thin-film coupled modes, the Long Range and Short Range Surface Plasmon Polaritons, are studied and experimentally observed in the azimuthally rotated configuration.

Special attention is paid to the role of the plasmon radiative losses, due to the scattering by the grating. Their dependence on the grating amplitude and the plasmon propagation direction is unraveled, and correlated to the width of the observed plasmonic resonances.

The outcomes of these analyses lead to the evaluation of the sensitivity and Figure of Merit achievable when the considered configurations are exploited in the framework of Surface Plasmon Resonance sensing.

The developed concepts and methods are proved to be valuable tools to predict and understand the response of actual plasmonic structures applied as sensing devices against gaseous analytes. Experimental tests of the plasmonic platforms as TNT, hydrogen and aromatic compounds sensors are reported, giving promising results. A particularly remarkable experiment is the combined exploitation of Long Range modes and azimuthally rotated configuration to sensibly enhance the performance of a xylene sensor.

Sommario

Superfici metalliche con modulazione sinusoidale, note come grating plasmonici, costituiscono una delle principali strutture che permettono di ottenere l'accoppiamento tra un fascio di luce incidente e un Plasmone Polaritone di Superficie. Una varietà di fenomeni sono accessibili quando il grating viene ruotato di un angolo azimutale rispetto al piano di incidenza.

Scopo di questo lavoro è uno studio approfondito delle proprietà di propagazione del modo di superficie in questa configurazione, correlando il ruolo dell'anisotropia introdotta dal grating con la posizione e forma del dip di risonanza plasmonica negli spettri in riflettanza.

Vengono presentati modelli analitici e interpretazioni fisiche; metodi sia sperimentali che computazionali vengono impiegati per validare i modelli, includendo l'osservazione di nuovi effetti. I modi accoppiati di film sottile, ovvero i Plasmoni Long Range e Short Range, vengono studiati e osservati sperimentalmente nella configurazione ad azimuth ruotato.

Una particolare attenzione è dedicata al ruolo delle perdite radiative del plasmone, dovute allo scattering da parte del grating. La loro dipendenza dall'ampiezza del grating e dalla direzione di propagazione del plasmone è spiegata, e correlata con la larghezza delle risonanze plasmoniche osservabili.

I risultati di queste analisi conducono alla valutazione delle sensibilità e Figura di Merito che si possono ottenere quando le configurazioni considerate sono sfruttate nell'ambito della sensoristica a Risonanza Plasmonica di Superficie.

I concetti e metodi sviluppati si dimostrano strumenti di valore per predire e interpretare la risposta di strutture plasmoniche reali, applicate come dispositivi di sensing verso analiti allo stato gassoso. Le piattaforme plasmoniche vengono testate come sensori per TNT, idrogeno e composti aromatici, con risultati promettenti. Un esperimento particolarmente interessante è l'uso combinato dei modi Long Range e della configurazione ad azimuth ruotato per incrementare notevolmente le performance di un sensore di xylene.

Table of Contents

Preface ..... **- 7 -**

1. Fundamentals of Plasmonics ..... **- 13 -**

1.1. Surface Plasmon Polaritons ..... - 13 -

1.2. Surface Plasmon Polaritons on thin films ..... - 16 -

1.3. Excitation of Surface Plasmon Polaritons ..... - 20 -

1.4. SPPs on realistic multilayer structures ..... - 28 -

1.5. Optics of solids ..... - 32 -

2. Surface Plasmon Resonance sensing ..... **- 37 -**

2.1. Basic principles ..... - 37 -

2.2. Sensitivity enhancement strategies ..... - 40 -

3. Computational Methods ..... **- 45 -**

3.1. Chandezon's method ..... - 45 -

3.2. Modal Analysis ..... - 46 -

4. Experimental ..... **- 49 -**

4.1. Materials ..... - 49 -

4.2. Fabrication ..... - 52 -

4.3. Morphological Characterization ..... - 55 -

4.4. Optical Characterization ..... - 58 -

5. Advancements in Plasmonics ..... **- 61 -**

5.1. Two-dimensional SPP coupling and propagation ..... - 61 -

5.2. Resonance shape and SPP propagation ..... - 71 -

5.3. Coupled modes in conical mounting ..... - 81 -

5.4. SPR sensitivity calculations ..... - 87 -

6. Sensing applications ..... **- 97 -**

6.1. TNT sensing ..... - 98 -

6.2. H_2 and VOCs sensing with a nanocomposite matrix ..... - 104 -

6.3. Xylene sensing with coupled modes in conical mounting ..... - 109 -

7. Conclusions ..... **- 119 -**

8. APPENDICES ..... **- 121 -**

8.1. Fundamentals of plasmonics ..... - 121 -

8.2. SPP/radiation coupling ..... - 125 -

Ringraziamenti ..... **- 129 -**

References ..... **- 131 -**

Preface

Plasmonics is the branch of Nanophotonics that studies the interaction of optical-frequency electromagnetic waves with collective electronic excitations in metal films or nanoparticles, called Surface Plasmons.

Strong enhancement of the electromagnetic field and 1D or 2D confinement at sub-wavelength scales, sensitivity to changes in the environment and optical non-linearity are among the remarkable effects related to Surface Plasmons, that make them a valuable resource for application in fields like biosensing, nanoelectronics, energy harvesting, optical communications.

If the first observations of effects ascribable to the existence of Surface Plasmons date back to one century ago, only the last decades showed a breakout of this field, leading to cross-disciplinary researches worldwide.

The main reason is related to the advancements in nanofabrication and characterization technologies, which provided the possibility to realize and study suitable structures for the excitation and manipulation of Surface Plasmons; in fact, features at the nanometer scale are needed to this aim.

In parallel, improved computational power allows today full modelling and design of the structures before actual fabrication.

This thesis is devoted to the study of propagating plasmonic modes, known as Surface Plasmon Polaritons, on nanostructured metallic surfaces, and to their application to gas sensing devices.

Surface Plasmon Polaritons (SPP) are surface waves, localized at an interface between a metal and a dielectric, or in a thin metal film immersed in a dielectric environment, and propagating along it. Since their momentum is higher than the one of free radiation at the same frequency, they cannot be directly excited by light in normal conditions.

In the present work, the chosen strategy to provide extra momentum is diffraction, obtained by modelling the metal surface with a sinusoidal pattern of period of some hundreds of nm, comparable to the visible light wavelength. With this approach, a Surface Plasmon Polariton can be excited by illuminating the surface under the conditions that provides momentum-matching, called Surface Plasmon Resonance conditions, which appear as a dip in the reflectance spectrum.

When the surface mode is excited, the electromagnetic energy comes to be strongly confined in the proximity of the surface, with the fields evanescently probing the surrounding environment. Any change in the refractive index of the medium have the effect to alter the propagation constant of SPPs; then it comes natural to exploit them as probes for surface analysis and sensing devices.

A gas sensor is a device capable to recognize the presence of a specific analyte in the environment and traduce it into an electrical or optical signal. The principle of Surface Plasmon Resonance sensing is to bind the analyte molecules close to the metal surface, thus causing a change in refractive index of the dielectric medium probed by the evanescent fields of a propagating surface mode; the consequent alteration of the propagation constant of the mode affects the reflectance spectrum, appearing as a shift of the dip.

In this framework, a sensitive layer capable to selectively and efficiently capture the analyte molecules has to be deposited over the metallic grating; thus the same plasmonic platforms can then be exploited towards different analytes, possibly chemical or biological in nature, in liquid or gaseous environment, finding applications in different fields including medical diagnostics, environmental monitoring, food safe and security.

This is the reason why the research for plasmonic sensing devices involve many different specialists, from chemists to biologists for the sensitive layer optimization, together with physicists, material scientists and engineers for the investigation and characterization of the SPPs properties and for design, nanofabrication and characterization of the structures.

Of particular interest are the modes supported by metallic films of sub-wavelength thickness immersed in a symmetrical dielectric environment. Under these conditions, an hybridization of the surface modes of the two interfaces of the film occurs, resulting in two hybrid modes with different momentum for each frequency: a Long Range SPP and a Short Range SPP.

The first aim of this thesis was to provide an extensive investigation of the excitation of SPPs by a grating coupler and their propagation along an arbitrary direction with respect to the grating grooves, i.e. their propagation on an anisotropic surface. The results, in addition to their intrinsic interest, can also be seen as useful tools to understand and optimize the optical response of plasmonic structures to the aim of gas sensing.
The analysis includes issues related both to anisotropic coupling configuration, known as "conical mounting", and anisotropic propagation on the surface, with particular attention to the imaginary part of the SPP momentum and its physical meanings.

More specifically, a generalized analytical model, supported by geometrical schemes, have been provided to treat the excitation of SPPs under conical mounting configuration, allowing to calculate the position of the resonance dips in the reflectance spectra of a given structure and the corresponding propagation direction of the excited modes.

The imaginary part of the SPP propagation constant have been correlated to the width of the resonance dip, the losses suffered by the surface mode and consequently its propagation distance, with particular attention to radiative losses due to the scattering by the grating. Effects related to the polarization of the incident light, the grating amplitude and the conical mounting have been investigated and physical interpretations provided.

Any means on disposal was exploited to the aim of the analysis, in a synergy between analytical, numerical and experimental approaches. This included modal analysis of the plasmonic structures by Finite Element Method simulations, computation of the optical response of the structures by Chandezon's algorithm, and optical characterization of actual samples.

The models have been exploited to perform the first analysis and experimental observation of the coupling and propagation of Long Range and Short Range modes in conical mounting. Finally, estimations of the performances of SPPs as probes for SPR sensors have been provided, in term of sensitivity and Figure Of Merit, both under angular and spectral interrogation and with particular attention to the conical mounting configuration.

The second aim of this thesis was to collaborate to projects aimed to the development of actual sensing devices, to be tested against different kinds of analytes in gaseous state. In this framework, concepts and methods previously introduced proved to be valuable tools to predict and understand the response of complex structures.

The tested analytes included trinitrotoluene (TNT), hydrogen and aromatic Volatile Organic Compounds (VOCs), in particular xylene. Each analyte required the use of a specific sensitive layer, that could be a thick porous matrix or a molecular monolayer; the nature of the supported surface modes, i.e. single-interface or Long/Short Range modes, strongly depended on this choice.

In the TNT case, a monolayer, self-assembled over a gold surface, was exploited as a sensitive layer. The corresponding mode was a single-interface SPP, excited in conical mounting.

Preliminary tests of the sensor response in time to a certain analyte concentration have been performed, to put the basis for further developments.

Two kinds of nanocomposite, nanoporous matrices were tested against both hydrogen and aromatic VOCs, with promising results, that could give an insight into the interaction mechanisms between the sensitive layer and the analytes.

A symmetrical environment was produced, exploiting a material suitable both as a patternable substrate and as a thick sensitive layer, in order to provide a sensor based on Long and Short range SPPs. This device was tested against xylene, demonstrating the improved sensitivity of the Long Range mode in conical mounting.

These last two applications were developed in the framework of the PLATFORMS - "PLAsmonic nano-Textured materials and architectures FOR enhanced Molecular Sensing" strategic project of the University of Padova, STPD089KSC.

In summary, this thesis work is organized as follows:

Section 1: Fundamentals of Plasmonics

A concise but comprehensive treatment of the essential basis is provided. Derivation of the dispersion relation of the basic Surface Plasmon Polariton, propagating along a flat interface between a metallic and a dielectric medium, is outlined. Basic properties of confinement and propagation are introduced.

For the thin film case, the implicit dispersion relation of the supported modes is given, with particular attention to the symmetrical case. Approximated explicit dispersion relations are derived for the Long Range and Short Range SPPs.

In the Chapter "*Excitation of Surface Plasmon Polaritons*", the problem of SPP coupling to incident light is then addressed, presenting the two basic coupling strategies: the prism and the grating. Conical mounting configuration for gratings is introduced, with a geometrical representation of the momentum matching conditions, and the role of the incident light polarization in the coupling efficiency is explained.

The Lorentzian shape of the plasmonic resonance is given, pointing out the relation between the resonance width, the mode dissipation and the imaginary part of the momentum, and their role in the coupling efficiency.

The Chapter "*SPPs on realistic multilayer structures*" is devoted to some complications related to SPP excitation and propagation on realistic samples; in particular, Effective Medium Approximation is introduced in order to keep the multilayer into account. Some remarks are made about the SPP coupling by conformal gratings and in symmetrical environment. Finally, it is pointed out that some guided modes into dielectric layers may be encountered.

In the last Chapter, the basic theory of the optical properties of dielectric and metallic media is presented. In particular, relations are given between the complex refractive index and the complex dielectric function, and, in the case of metals, the density and collision frequency of free electrons, according to Drude model.

Section 2: Surface Plasmon Resonance sensing

Basic principles of SPR sensing are introduced, with a concise review of their performances and advantages. The principal parameters to characterize a sensor performance are defined.

In the second Chapter, a priori estimates of sensitivity and Figure of Merit of SPP modes are introduced, followed by an analysis of basic sensitivity enhancement strategies: the exploitation of Long Range modes and the conical mounting.

Section 3: Computational methods

Two useful computational tools are here described.

First, Chandezon's method, to rigorously solve the problem of a plane wave incident on a diffraction grating. This method, implemented on MATLAB, will be used to generate reflectance spectra similar to the experimental ones.

Second, Modal Analysis through Finite Element Method, to calculate the plasmonic eigenmodes of a given structure. This method was implemented on the COMSOL Multiphysics software, and can provide complementary information, including an analysis of the loss channels for an SPP propagating on a grating.

Section 4: Experimental

This Section is devoted to materials, fabrication techniques and characterization instruments.

Choice and synthesis of the materials to realize the actual plasmonic structures are presented in the first Chapter. This includes metals, functional materials for the fabrication steps and functional materials to be used as sensitive layers.

Fabrication techniques are briefly described in the second Chapter: thin film deposition procedures, Interferential Lithography and Nano-Imprinting.

Morphological characterization of the samples have been performed by Scanning Electron Microscope and Atomic Force Microscope, as described in the third Chapter.

Finally, the principal instrument for optical characterization, the Variable Angle Spectroscopic Ellipsometer, is introduced. Some of its functions, relevant for the present work, are briefly described: reflectance measurements to collect experimental spectra, spectroscopic ellipsometry to determine the dielectric function of thin films, and scatterometry to estimate the grating period.

Section 5: Advancements in Plasmonics

This Section represents the core of the thesis, providing an extensive investigation of SPPs propagation on the anisotropic surface defined by the grating.

The first Chapter, "*Two-dimensional SPP coupling and propagation*", is devoted to the real part of the SPP momentum. The concept of momentum-matching scheme is generalized to previously not considered conditions, achieving a general treatment of the grating coupling in conical mounting. The position of the resonance dips in the reflectance spectra can be analytically predicted; as an handy method to do this, maps can be generated with minimum computational effort.

In the last paragraph, the viewpoint is shifted from the coupling setup to the grating surface, calculating the propagation direction of the SPPs with respect to the grating grooves. Maps of the angle of propagation achievable through the grating coupling are generated and commented. A remarkable configuration is identified, in which it is achieved the simultaneous excitation of two identical SPP modes, by the same light beam, propagating along different directions.

The second Chapter, "*Resonance shape and SPP propagation*", is devoted to the study of the imaginary part of the SPP momentum, in relation to the intrinsic and radiative losses and the width of the SPR dip.

It is shown and explained that the incident light polarization does not affect the resonance width, since it only determine what fraction of incident light intensity does couple to the grating.

Then, a deep investigation of the dependence of radiative losses on the grating amplitude is performed, by means of both Modal Analysis and Chandezon's methods, verifying consistency between the results.

The main result is the demonstration that radiative losses are proportional to the square of the total amplitude; a physical interpretation of this fact is suggested, based on the interpretation of the resonant coupling as a quantum interference phenomenon.

In the "*Anisotropy*" Paragraph, the dependence of the radiative losses on the propagation direction with respect to the grating grooves is derived, by building an index ellipse for the SPP complex effective refractive indexes.
Some remarks follow, about the translation of these results to the reference system related to the coupling setup, through the coupling relations.
Finally, the model is validated by comparison to experimental data.

The developed models and methods find a first application in the Chapter "*Coupled modes in conical mounting*", where they are exploited to find a suitable configuration in which to satisfy the second resonant coupling conditions for Long Range and Short Range SPPs, and identify the corresponding dips in experimental spectra. As a complementary analysis, the propagation direction and length of the observed modes are also investigated, suggesting in particular that the Long Range SPP propagation length can be sensibly enhanced in conical mounting with respect to the null-azimuth case.

The last Chapter addresses the problem of theoretically calculate the sensitivity of an SPR sensor.
An analysis is exposed of the various terms that contribute to the overall sensitivity, starting with some remarks about the role of the sensitive layer.
A first attempt to evaluate the intrinsic sensitivity of the Long Range and Short Range modes is proposed; even if it comes to be a rough approximation, it preserves some qualitative results.
The factor related to the conical mounting is generalized to all the available coupling configurations, and the meaning of divergences is clarified.
The calculation of the sensitivity of an SPP mode excited in conical mounting is calculated for the spectral interrogation case, for the first time.
Finally, it is shown that the Figure of Merit is the same for the angular and spectral interrogation cases, and that its enhancement under conical mounting is essentially due to the reduction of radiative losses.

Section 6: Sensing applications
In this Section, actual sensing experiments are reported, in which SPR sensors are tested against analytes of strategic interest for security and health safety.

The first Chapter describes a sensing test of a basic gold plasmonic platform in conical mounting against TNT, with a molecular monolayer as a sensitive layer. Both the implemented SPR setup and the sensitive layer were well-established, but never combined together. The sensor response in time until saturation was investigated, and detection of explosive traces down to some tens of ppb was achieved.

In the second Chapter, two kinds of functional materials were exploited as sensitive layer against both hydrogen and aromatic VOCs. Reflectance spectra presented a number of dips; the corresponding modes were identified by comparison with theoretical expectations. Both sensitive materials showed satisfactory optical response, with reversible dynamics, against both analytes; the detection of hydrogen or VOCs can be discriminated through the direction of the dip shift.

The final Chapter presents the result of 30 ppm xylene detection by means of symmetrical thin-film plasmonic structure. This represents the first example of a sensing device that combines the two strategy, namely the Long Range SPP and the conical mounting, to achieve a great improvement in sensitivity.

29 January 2014, Padova

Enrico Gazzola

1. Fundamentals of Plasmonics

This Section provides a background on the essential notions of Plasmonics on which the present work is based.

It starts with the introduction of the most common Surface Plasmon Polariton modes on single interfaces and thin films, including the definitions of their basic properties. An approximate analytical treatment of the dispersion relation of thin-film modes is also derived.

The common strategies to provide coupling between free radiation and Surface Plasmon Polaritons are introduced; the grating coupling strategy is developed including a treatment of conical mounting configuration and coupling efficiency. Some remarks about the shape of the resonance curve and its relation to losses are made.

One Chapter addresses some issues related to realistic multilayer structures; in particular, an effective refractive index approach is introduced, together with some considerations about coupling configurations. The possible existence of waveguide modes into dielectric layers is also addressed.

The last Chapter is devoted to materials and includes an insight into the meaning of the optical constants from a Solid State Physics point of view.

1.1. Surface Plasmon Polaritons

Conductor-dielectric interfaces are known to support nonradiative propagating waves. They have long been known as Zenneck waves [1], Sommerfeld waves [2] or Fano modes [3], and in modern Optics are called Surface Plasmon Polaritons (SPPs) [4]. From the point of view of Solid State Physics, they can be described as quasi-particles originated by the coupling of surface plasma charge oscillations and the electromagnetic fields [5] (see also Appendix 8.1[a]).

a. SPP dispersion relation

Their dispersion relation can be derived through by classical Electrodynamics [6]; only the main results will be reported here.

Referring to Fig. 1, we look for a solution of the wave equation in the form of a wave propagating along the $\hat{x}$ direction along the metallic surface and evanescent along the $\hat{z}$ direction. Two independent solutions of this kind can be given that satisfy the boundary conditions for the continuity of the fields at the interface [7; 8], corresponding to transverse magnetic (TM) and transverse electric (TE) waves, respectively.

The equations for TE modes only admit the trivial solution of all fields to be equal to 0, meaning that no surface mode exist for this polarization. An intuitive explanation is that electron plasma oscillations would not occur, since they require a component of the electric field normal to the surface, while in TE modes the only non-zero component would be E_y.

The TM solutions for the magnetic and electric fields can be expressed by the following set of equations:

$$H_y(z) = \begin{cases} H_0 e^{iK_{spp}x} e^{-k_d z} & z > 0 \\ H_0 e^{iK_{spp}x} e^{k_m z} & z < 0 \end{cases}$$

$$E_x(z) = \begin{cases} iH_0 \dfrac{k_d}{\omega \varepsilon_0 \varepsilon_d} e^{iK_{spp}x} e^{-k_d z} & z > 0 \\ -iH_0 \dfrac{k_m}{\omega \varepsilon_0 \varepsilon_m} e^{iK_{spp}x} e^{k_m z} & z < 0 \end{cases}$$

$$E_z(z) = \begin{cases} -H_0 \dfrac{K_{spp}}{\omega \varepsilon_0 \varepsilon_d} e^{iK_{spp}x} e^{-k_d z} & z > 0 \\ -H_0 \dfrac{K_{spp}}{\omega \varepsilon_0 \varepsilon_m} e^{iK_{spp}x} e^{k_m z} & z < 0 \end{cases}$$

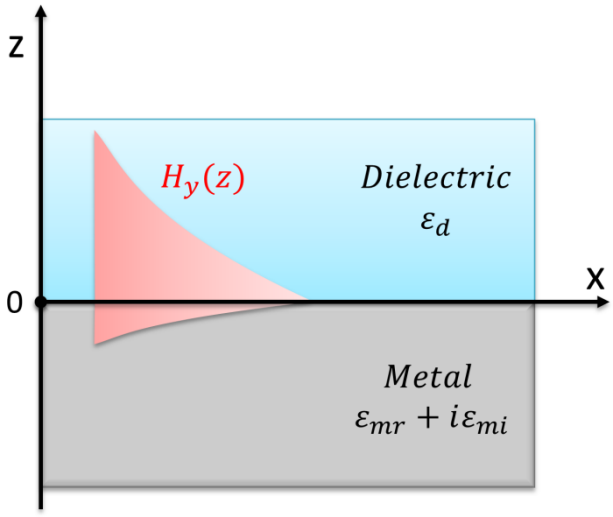

Fig. 1: Magnetic field profile of a single-interface surface plasmon polariton, propagating along the interface between a dielectric, of real relative permittivity ε_d, and a metal, of complex permittivity $\varepsilon_m = \varepsilon_{mr} + \varepsilon_{mi}$. The field presents an exponential decay into both the materials. The $\hat{x}$ direction is defined as an arbitrary direction along the surface, while the $\hat{z}$ direction is perpendicular to the surface.

With standard notation, ω is the wave frequency and ε_0 the vacuum permittivity. H_0 is related to the wave intensity and will not be a relevant parameter in the following treatment. K_{spp} is the propagation constant of the travelling wave, corresponding to the component of the wave vector in the direction of propagation, while k_m and k_d represent the perpendicular components in the two media, namely the metal and the dielectric, respectively.

The requirement to fulfill the wave equation in the two half-spaces yields the following expressions for k_m and k_d (being c the light speed in vacuum):

$$k_m^2 = K_{spp}^2 - \left(\frac{\omega}{c}\right)^2 \varepsilon_m$$

$$k_d^2 = K_{spp}^2 - \left(\frac{\omega}{c}\right)^2 \varepsilon_d$$

And also the SPP dispersion relation:

$$K_{spp} = \frac{\omega}{c} \sqrt{\frac{\varepsilon_m \varepsilon_d}{\varepsilon_m + \varepsilon_d}}$$

Fig. 2 reports a plot of this relation for the case of silver/air interface, in a frequency range including visible light and infrared radiation. It can be observed that K_{spp} is higher than the momentum of a free wave with the same frequency.

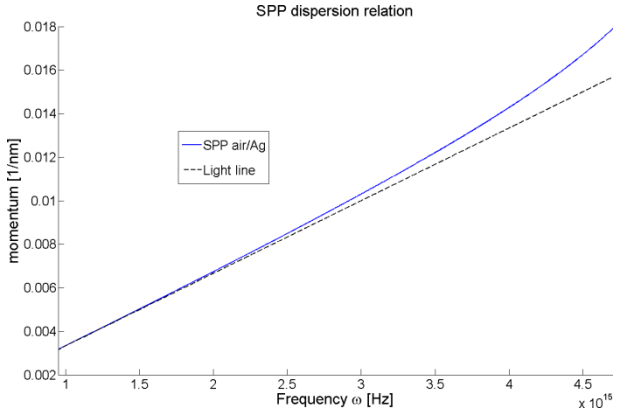

Fig. 2: Plot of the dispersion relation for an air/silver interface SPP in the infrared and visible spectrum, compared to the dispersion relation for a light wave in vacuum. It is apparent that, given the frequency, the SPP wavenumber, i.e. its momentum, is higher than the free wave one.

b. SPP confinement and propagation

The SPP is localized close to the surface, since it exponentially decays along $\pm\hat{z}$ as $e^{-k_{d,m}|z|}$.

The penetration depth into a material is defined as the distance at which the field falls of a $\frac{1}{e}$ factor. Thus the *penetration depths* into the dielectric and metal respectively are obtained as follows [9]:

$$\delta_d = \frac{1}{k_d} = \frac{c}{\omega}\sqrt{\frac{\varepsilon_m + \varepsilon_d}{-\varepsilon_d^2}}$$

$$\delta_m = \frac{1}{k_m} = \frac{c}{\omega}\sqrt{\frac{\varepsilon_m + \varepsilon_d}{-\varepsilon_m^2}}$$

Typical values are of few thousands of nm into the dielectric and few tens into the metal.

Since the metal permittivity is complex, also the SPP momentum is in general complex, with the imaginary part representing energy dissipation [4; 9]:

$$\varepsilon_m = \varepsilon_{mr} + i\varepsilon_{mi} \quad \Longrightarrow \quad K_{spp} = \beta + i\Gamma$$

This implies that the SPP has a finite propagation distance before being completely dissipated, due to the $e^{-\Gamma x}$ factor. An attenuation length can be defined as the distance at which the SPP intensity falls of a $\frac{1}{e}$ factor. Since the intensity $I \propto E^2 \sim e^{-2\Gamma x}$, the *attenuation length* is given as follows:

$$L = \frac{1}{2\Gamma}$$

And it assumes values ranging from few μm to hundreds of μm, depending on the SPP frequency and on the materials.

Under the reasonable approximation $|\varepsilon_{mi}| \ll |\varepsilon_{mr}|$, the following approximated equations are obtained (see Appendix 8.1[b]) for the real and imaginary parts of K_{spp}:

$$\beta = \frac{\omega}{c}\sqrt{\frac{\varepsilon_{mr}\varepsilon_d}{\varepsilon_{mr}+\varepsilon_d}}$$

$$\Gamma = \frac{\omega}{c}\left(\frac{\varepsilon_{mr}\varepsilon_d}{\varepsilon_{mr}+\varepsilon_d}\right)^{\frac{3}{2}}\frac{\varepsilon_{mi}}{2\varepsilon_{mr}^2}$$

The second formula shows that losses have a strong dependence on ε_d and ε_{mr}, besides the obvious one on ε_{mi}. In fact, if the dielectric refractive index is high, the field is forced to "spend more time" into the metal, thus increasing the dissipation [7; 8].

1.2. Surface Plasmon Polaritons on thin films

In principle a metal slab immersed in a dielectric environment, like the one depicted in Fig. 3, could support two SPPs, one on each interface. When the slab thickness is of the order of the SPP penetration depth, the interaction between the two modes can produce new phenomena [10-13].

a. Implicit dispersion relation

In the same way as for the single interface, one can look for TM modes propagating along $\hat{x}$, evanescent along $\hat{z}$ and independent on $\hat{y}$.

Applying the Superposition Principle to the two single interface SPPs, the generic solution can be expressed as follows [6]:

$$H_y(z) = \begin{cases} Ae^{iK_{spp}x}e^{-k_{d1}z} & z > a \\ Ce^{iK_{spp}x}e^{k_m z} + De^{iK_{spp}x}e^{-k_m z} & -a < z < a \\ Be^{iK_{spp}x}e^{k_{d2}z} & z < -a \end{cases}$$

$$E_x(z) = \begin{cases} iA\dfrac{k_{d1}}{\omega\varepsilon_0\varepsilon_{d1}}e^{iK_{spp}x}e^{-k_{d1}z} & z > a \\ -i\dfrac{e^{iK_{spp}x}}{\omega\varepsilon_0\varepsilon_m}(Ck_m e^{k_m z} - Dk_m e^{-k_m z}) & -a < z < a \\ -iB\dfrac{k_{d2}}{\omega\varepsilon_0\varepsilon_{d2}}e^{iK_{spp}x}e^{k_{d2}z} & z < -a \end{cases}$$

$$E_z(z) = \begin{cases} -A\dfrac{K_{spp}}{\omega\varepsilon_0\varepsilon_{d1}}e^{iK_{spp}x}e^{-k_{d1}z} & z > a \\ \dfrac{-K_{spp}e^{iK_{spp}x}}{\omega\varepsilon_0\varepsilon_m}(Ce^{k_m z} + De^{-k_m z}) & -a < z < a \\ -B\dfrac{K_{spp}}{\omega\varepsilon_0\varepsilon_{d2}}e^{iK_{spp}x}e^{k_{d2}z} & z < -a \end{cases}$$

The wave equation requires for the three layers that $k_j^2 = K_{spp}^2 - \left(\frac{\omega}{c}\right)^2\varepsilon_j$, for j = m, d_1 and d_2. A, B, C and D are free parameters corresponding to H_0 in the single-interface case.

Imposing the boundary conditions, an implicit expression for the SPPs dispersion relation is obtained as follows:

$$e^{4k_m a} = \frac{\rho_m - \rho_{d1}}{\rho_m + \rho_{d1}}\frac{\rho_m - \rho_{d2}}{\rho_m + \rho_{d2}}$$

Having define $\rho_j \equiv \frac{k_j}{\varepsilon_j}$. This expression could be reformulated using the properties of the hyperbolic tangent as follows:

$$\tanh(k_m a) = \frac{\sqrt{\rho_m - \rho_{d1}}\sqrt{\rho_m - \rho_{d2}} \mp \sqrt{\rho_m + \rho_{d1}}\sqrt{\rho_m + \rho_{d2}}}{\sqrt{\rho_m - \rho_{d1}}\sqrt{\rho_m - \rho_{d2}} \pm \sqrt{\rho_m + \rho_{d1}}\sqrt{\rho_m + \rho_{d2}}}$$

Where two branches are separated. This equation has in general four solutions, two of which correspond to bounded modes, while the other two are leaky waves [12].

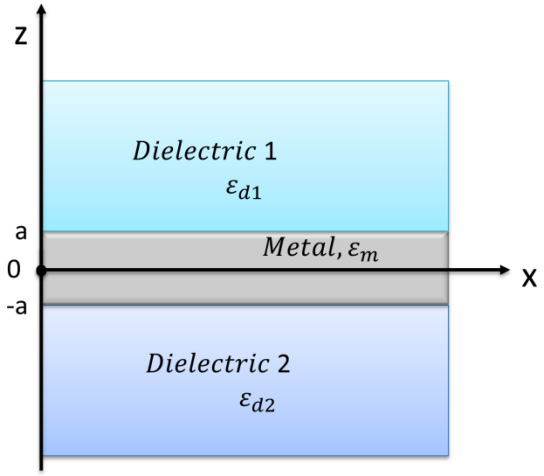

Fig. 3: A metal slab of thickness 2a, between two dielectric semi-spaces.

b. Symmetrical case and coupled modes

Most interesting is the case when the two dielectrics are the same, i.e. the metal slab is immersed in a symmetrical environment. Since $\varepsilon_{d1} = \varepsilon_{d2} \equiv \varepsilon_d \Rightarrow k_{d1} = k_{d2} \equiv k_d \Rightarrow \rho_{d1} = \rho_{d2} \equiv \rho_d$, the implicit dispersion relation becomes:

$$\tanh(k_m a) = \frac{(\rho_m - \rho_d) \mp (\rho_m + \rho_d)}{(\rho_m - \rho_d) \pm (\rho_m + \rho_d)} = \frac{-\rho_d/\rho_m}{-\rho_m/\rho_d}$$

The two bounded solutions represents two Fano modes resulting from the coupling between the two single-interface SPPs [11; 12]; for this reason they are addressed as "coupled modes". Their peculiar properties will now be analyzed in detail.

The first one is called *Long-Range SPP* (LR SPP) and its implicit dispersion relation is:

$$\tanh(k_m a) = -\frac{k_d \varepsilon_m}{k_m \varepsilon_d}$$

With $k_m^2 = K_{Long}^2 - \left(\frac{\omega}{c}\right)^2 \varepsilon_m$; $k_d^2 = K_{Long}^2 - \left(\frac{\omega}{c}\right)^2 \varepsilon_d$.

Using this relation into the general form of the fields, it follows that A = B and C = D, and consequently:

$$\begin{cases} H_y(z) = H_y(-z) \\ E_z(z) = E_z(-z) \\ E_x(z) = -E_x(-z) \end{cases}$$

The mode is then even in H_y and E_z and odd in E_x, as graphically shown in Fig. 4. This symmetry lowers the penetration of the evanescent fields into the metal layer, resulting in a weakened

confinement and low dissipation; this is the reason for its longer propagation, from which the label "Long Range" [11; 13]. An estimation of the LR SPP propagation distance is reported in Appendix 8.1[c], showing a strong dependence on ε_{mr} and, inversely, ε_d. Again, this is understood considering that under these conditions the field spends less time into the metal layer, thus reducing dissipation.

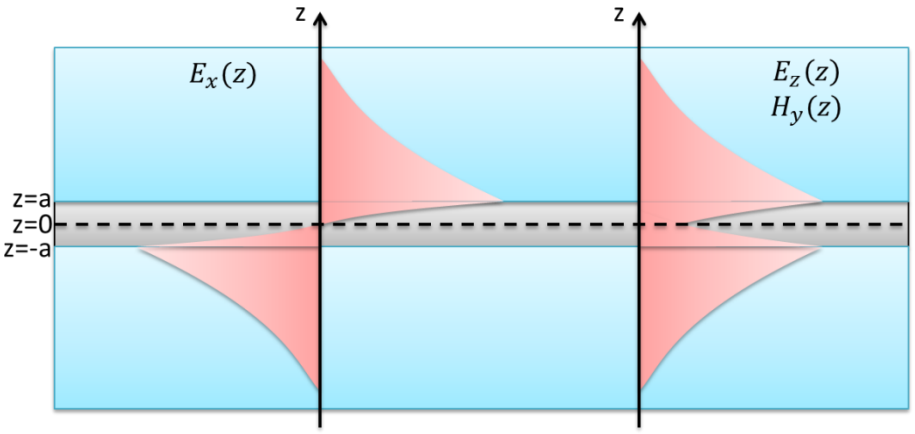

Fig. 4: Fields profile for the Long Range mode

Its more interesting property is that when the metal film thickness tends to 0, the mode tends to become a free plane wave propagating along $\hat{z}$ in the dielectric.
In fact, $a \to 0$ implies that $\tanh(k_m a) \to k_m a$, $k_d \to 0$ and $K_{Long} \to \frac{\omega}{c}\sqrt{\varepsilon_d}$.

From a momentum viewpoint, the following consideration can be made about $\beta_L = Re(K_{Long})$, neglecting the imaginary part of ε_m.
The hyperbolic tangent needs the geometrical constraint $\tanh(k_m a) \in (-1, 1)$, corresponding to the requirement $\left(\frac{k_d \varepsilon_m}{k_m \varepsilon_d}\right)^2 = \left(\frac{\beta_L^2 - \left(\frac{\omega}{c}\right)^2 \varepsilon_d}{\beta_L^2 - \left(\frac{\omega}{c}\right)^2 \varepsilon_m}\right)\left(\frac{\varepsilon_m}{\varepsilon_d}\right)^2 < 1$. Keeping into account that $|\varepsilon_m| > \varepsilon_d$, this easily leads to the following condition:

$$\beta_L < \frac{\omega}{c}\sqrt{\frac{\varepsilon_m \varepsilon_d}{\varepsilon_m + \varepsilon_d}} \equiv \beta_0$$

It means that, on equal frequency, the LR SPP momentum is smaller than the momentum of a single-interface SPP between the same materials.

The other solution, described by the implicit dispersion relation

$$\tanh(k_m a) = -\frac{k_d \varepsilon_m}{k_m \varepsilon_d}$$

is called *Short Range SPP* (SR SPP). Contrary to the LR mode, it is even in the E_x and odd in the E_z and H_y field profiles, as shown in Fig. 5:

$$\begin{cases} H_y(z) = -H_y(-z) \\ E_z(z) = -E_z(-z) \\ E_x(z) = E_x(-z) \end{cases}$$

This mode is strongly confined and strongly dissipated into the metal layer, resulting in short propagation. When the metal film thickness tends to 0, more and more energy is concentrated and

dissipated into the metal film, and β_S has to diverge in order to increase enough the decay constant k_m [12].

If $\beta_S \equiv Re(K_{short})$, the condition on the hyperbolic tangent gives: $\beta_S > \beta_0$.

The generation of these hybrid modes when the layer is thin enough can be seen as a strong-coupling condition between the two single-interface modes, that is generally known to produce modes hybridization and frequency splitting [14].

If the symmetry is broken, the electromagnetic energy of the LR SPP tends to concentrate in the medium with lower refractive index and the SR SPP energy in the other. With increasing refractive index asymmetry, their dispersion relations will accordingly tend to the ones of the two single-interface modes on the two interfaces [12].

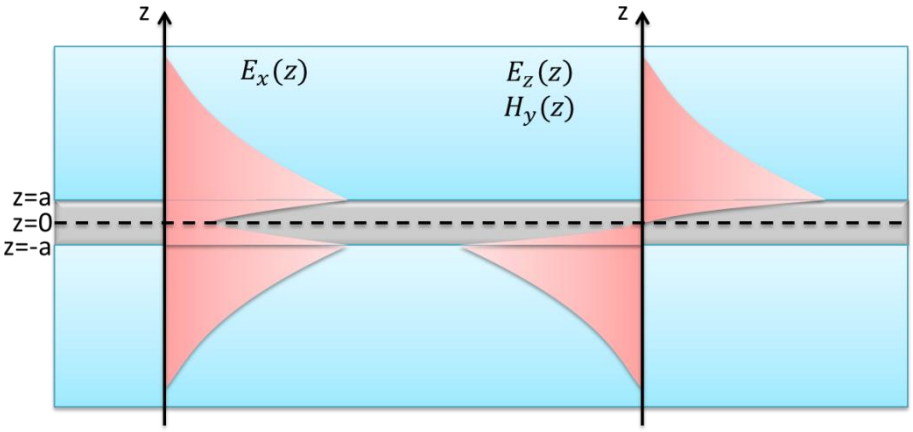

Fig. 5: Fields profile for the Short Range mode

c. Approximated dispersion relations

Explicit dispersion relations for the coupled modes cannot be analytically obtained, but it is useful for practical purpose to give approximated expressions [15].

The approximation consists in $\frac{k_d^2}{\left(\frac{\omega}{c}\right)^2 \varepsilon_d} \ll 1$, that is immediately verified for the LR SPP on a sufficiently thin film, since $k_d^{LR} \to 0$ when $a \to 0$ as seen before.

Thus we can take $k_m^{LR} = \sqrt{K_{Long}^2 - \left(\frac{\omega}{c}\right)^2 \varepsilon_m} \approx \frac{\omega}{c}\sqrt{\varepsilon_d - \varepsilon_m}$ and put it into the implicit LR SPP dispersion relation, that becomes:

$$\tanh\left(\frac{\omega}{c} a\sqrt{\varepsilon_d - \varepsilon_m}\right) \approx -\frac{\varepsilon_m \sqrt{K_{Long}^2 - \left(\frac{\omega}{c}\right)^2 \varepsilon_d}}{\frac{\omega}{c}\varepsilon_d \sqrt{\varepsilon_d - \varepsilon_m}}$$

This expression can be inverted to extract the LR SPP momentum:

$$K_{Long} \approx \frac{\omega}{c}\sqrt{\varepsilon_d + (\varepsilon_d - \varepsilon_m)\left(\frac{\varepsilon_d}{\varepsilon_m}\right)^2 \left[\tanh\left(\frac{\omega}{c} a\sqrt{\varepsilon_d - \varepsilon_m}\right)\right]^2}$$

It is less immediate to justify the approximation for the SR SPP case. The assumption is equivalent to:

$$\left(\frac{\omega}{c}a\right)^{-2}\frac{\varepsilon_d}{(\varepsilon_{mr}^2+\varepsilon_{mi}^2)^2}(\varepsilon_{mr}^2-\varepsilon_{mi}^2-2i\varepsilon_{mr}\varepsilon_{mi})\ll 1$$

Usually the condition is quite well satisfied for thin films (a ≈ few tens of nanometers) thanks to the hierarchy $\varepsilon_{mr} \gg \varepsilon_d \gg \varepsilon_{mi}$.

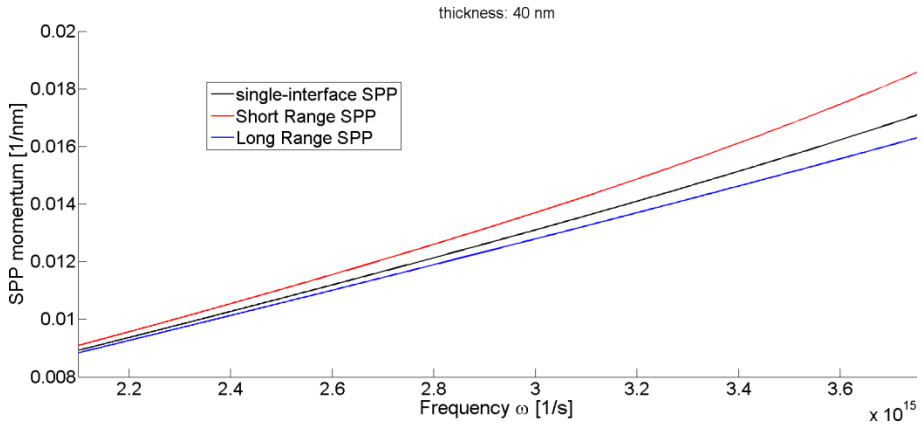

Fig. 6: Dispersion relations for the coupled modes supported by a 40-nm thick silver film in air, compared to the dispersion relation of a single-interface silver/air SPP.

The approximation then gives, for the SR SPP momentum:

$$K_{Short} \approx \frac{\omega}{c}\sqrt{\varepsilon_d + \frac{(\varepsilon_d-\varepsilon_m)\left(\frac{\varepsilon_d}{\varepsilon_m}\right)^2}{\left[\tanh\left(\frac{\omega}{c}a\sqrt{\varepsilon_d-\varepsilon_m}\right)\right]^2}}$$

In Fig. 6 the real part of these formulas is taken, in order to plot the dispersion relations for the coupled modes, in comparison to the one of a correspondent single-interface modes. The hierarchy $\beta_S > \beta_0 > \beta_L$ at equal frequency is verified.

A useful approximated expression for the real part of the coupled modes momenta is provided in Appendix 8.1[d].

1.3. Excitation of Surface Plasmon Polaritons

a. Basic coupling strategies

SPPs are nonradiative modes, which remain confined to the surface because their momentum β is greater than the momentum $k_i = \frac{\omega}{c}\sqrt{\varepsilon_d}$ of a free light wave propagating through the dielectric [6]. This implies that they cannot be excited by a light beam simply impinging on the metal surface. Two main strategies are widely used in order to couple the incident beam with an SPP mode: a prism coupler and a diffraction grating.

The first strategy is based on the *attenuated total reflection* (ATR) method and exploit a prism with refractive index n_p greater than the dielectric refractive index $\sqrt{\varepsilon_d}$. Two configurations exist, namely the Otto's and the Kretschmann-Raether's [16; 17].
In the Kretschmann-Raether's configuration, shown in Fig. 7(a), the metallic film is placed between the dielectric media and the prism. The incident light wave goes through the prism,

increasing its momentum of a factor n_p, and hits the metal film at an incidence angle θ greater than the critical angle of total internal reflection [18]. An evanescent wave penetrates the metal film and, if the film is sufficiently thin, it can couple with an SPP on the opposite surface when a resonance condition $\beta = n_p \frac{\omega}{c} \sin\theta$ is matched.

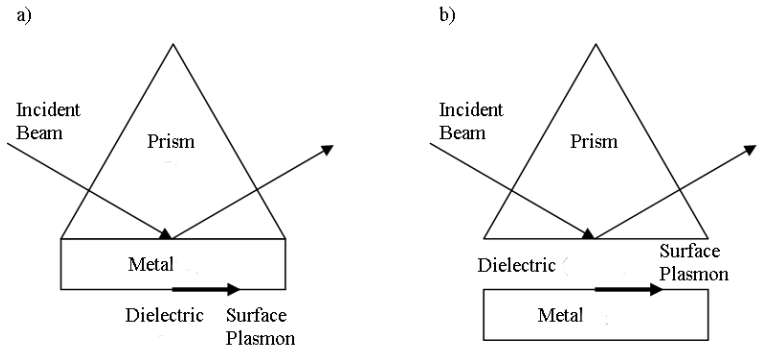

Fig. 7: Scheme of the two prism-coupling configurations. (a) Kretschmann-Raether's configuration and (b) Otto's configuration.

In the Otto's configuration, shown in Fig. 7(b), it is the dielectric layer to be placed between the prism and the metal. In the total internal reflection regime, the evanescent wave penetrates the dielectric layer and can couple with the SPP when the resonance condition is satisfied.
The main drawback of this coupling strategy is that the use of a prism constitutes a limit to the possibility of miniaturization of SPP based devices.

The alternative method to provide additional momentum is the diffraction of light incident on a metallic grating [18]. This requires to fabricate a periodic pattern at the metal/dielectric interface, with periodicity Λ of the same order of magnitude of the incident wavelength [3; 19; 20].
The basic configuration is as in Fig. 8, with a light beam of momentum $\vec{k}_i$ impinging the surface with an incident angle θ. The component of its momentum projected to the surface constitutes the transferred momentum $\vec{k}_T \equiv \vec{k}_i \sin\theta$ from the light to the surface plasmon. The $\hat{x}$ direction is conventionally taken as antiparallel to $\vec{k}_T$.

It is well known from Solid State Physics that for a periodic structure of period Λ the Bragg vector of modulus $G \equiv \frac{2\pi}{\Lambda}$ and direction along the grating grooves represents the grating momentum [21; 22]. When the incident light is diffracted by the periodic structure, additional momentum is provided by the grating as an integer multiple of G.
If j is the diffraction order, the momentum of the diffracted beam is given by $\vec{k}_j = \vec{k}_i + j\vec{G}$. Usually for plasmonic gratings at optical frequencies only the first diffraction order is relevant. The coupling between the incident light and the SPP is then realized when the momenta match the following resonance condition: $\vec{\beta} = \vec{k}_T \pm \vec{G}$.

In the basic configuration shown in Fig. 8, all these vectors are parallel, so the condition can be projected along $\hat{x}$ as follows:

$$\beta = k_i \sin\theta \pm G$$

When the metallic surface is illuminated by a light beam, as sketched in Fig. 9(a), with a scan in incidence angle, the plasmonic resonance manifests itself as a dip in the reflectance spectrum, that

appears as in Fig. 9(b). In fact, when the resonance condition is fulfilled, the energy of the light beam is transferred to the SPP mode.

While the resonance condition only provides momentum matching, the depth and shape of the resonance curve depend on other parameters, as it will be shown in the following chapters.

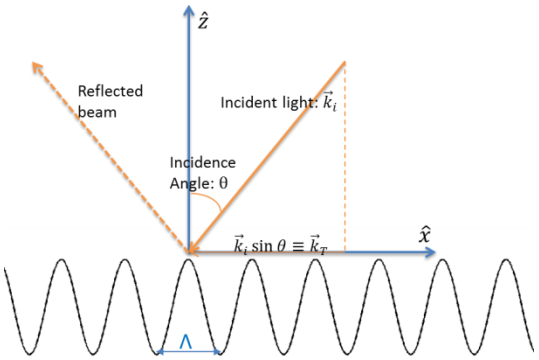

Fig. 8: Scheme of the basic grating coupling configuration. The incident light transfers the component of its momentum parallel to the surface.

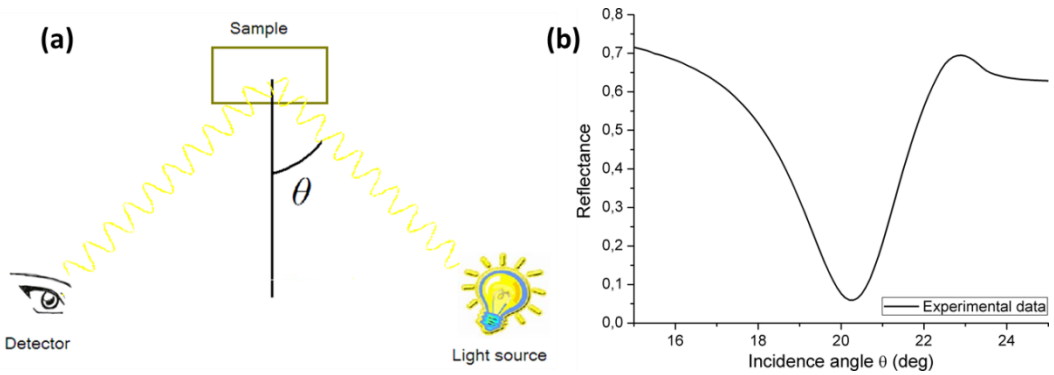

Fig. 9: (a) Concept of the reflectance measurement. (b) Plasmonic resonance dip seen in an angular scan, corresponding to the excitation of gold/air single-interface SPP with light of wavelenght 650 nm impinging on a 470-nm grating.

b. Conical mounting

In the last paragraph only the basic $\vec{G} \parallel \hat{x}$ case has been considered. New features of the plasmonic response arise when the plane of incidence is rotated with respect to the grating grooves, a configuration known as *conical mounting* [23-25].

The 3D configuration is represented in Fig. 10; the sample surface lies on the $(\hat{x}, \hat{y})$ plane, while the scattering plane is defined as the $(\hat{x}, \hat{z})$ plane, with the x-component of the incident light momentum directed along $-\hat{x}$. The angle between $\hat{x}$ and $\vec{G}$ is called the *azimuth* and conventionally labeled φ.

At non-zero azimuth the transferred momentum $\vec{k}_T$ is not parallel to the grating vector, thus the symmetry of the incidence configuration is broken and the resonance condition becomes two-dimensional. The component of the grating vector normal to the scattering plane is transferred to the SPP, which as a consequence propagates along a direction non parallel to the scattering plane. In particular, it has been shown that two SPPs can be excited by the same incident wavelength,

propagating on the surface in different directions [26]. The demonstration is straightforward with the advantage of a geometrical representation in the reciprocal space of the sample plane, as shown in Fig. 11(a). The scheme assumes G>β, that is usually true for SPPs at optical frequencies at an air/metal interface; for this reason only the j = -1 diffraction order can possibly satisfy the momentum matching condition $\vec{\beta} = \vec{k}_T + \vec{G}$.

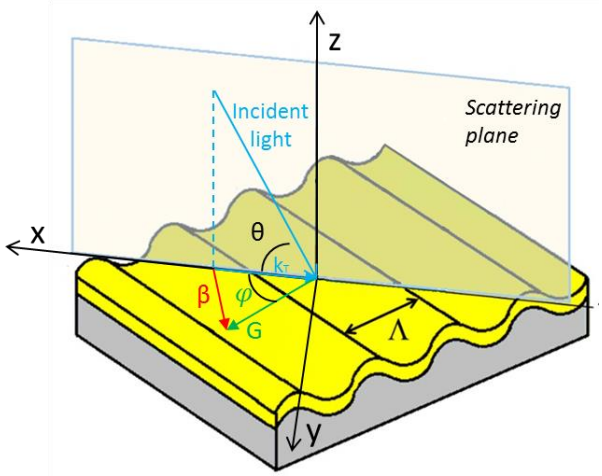

Fig. 10: Scheme of the vector conventions for a 1D grating of Λ period in conical mounting. The on-plane component $\vec{k}_T$ of the incident radiation is oriented along $-\hat{x}$. $\vec{G}$ is the grating Bragg vector and it is rotated of an azimuthal angle φ with respect to the x axis. The SPP momentum $\vec{\beta}$ is the result of the vector sum of $\vec{G}$ and $\vec{k}_T$.

Since the incident light will usually come from air, it will be assumed $k_i = \frac{2\pi}{\lambda}$ hereafter.

The vector condition can then be projected on the x and y axis as follows:

$$\begin{cases} \vec{\beta} \cdot \hat{x} = G\cos\varphi - \dfrac{2\pi}{\lambda}\sin\theta \\ \vec{\beta} \cdot \hat{y} = G\sin\varphi \end{cases}$$

For a given azimuthal angle φ and wavelength λ, two incidence angles θ can possibly satisfy the condition, corresponding to the excitation of two SPPs of $\vec{\beta}_+$ and $\vec{\beta}_-$ momenta equal in modulus but propagating along different directions; green arrows in Fig. 11(a). Correspondingly, two dips for each single wavelength are observed in the experimental reflectance spectra of Fig. 11(b). This cannot be observed for too low values of φ since the second excitation would require too high values for $\vec{k}_T$.

For increasing wavelength, $\beta(\lambda)$ decreases until the condition represented by the dashed line in the coupling scheme is reached, when the transferred momentum vector is tangential to the β circle. At this critical wavelength λ_c , only one mode can be excited, which propagates along the direction orthogonal to the incidence plane: a condition known as "merging condition" [26]. In the corresponding spectrum in fact, like the one in Fig. 11(b), for increasing wavelengths the dips are seen to get closer and merge as λ approaches the critical value. For $\lambda > \lambda_c$ the coupling becomes impossible. On the other hand the "merging condition" can also be explored by keeping the wavelength fixed and increasing φ.

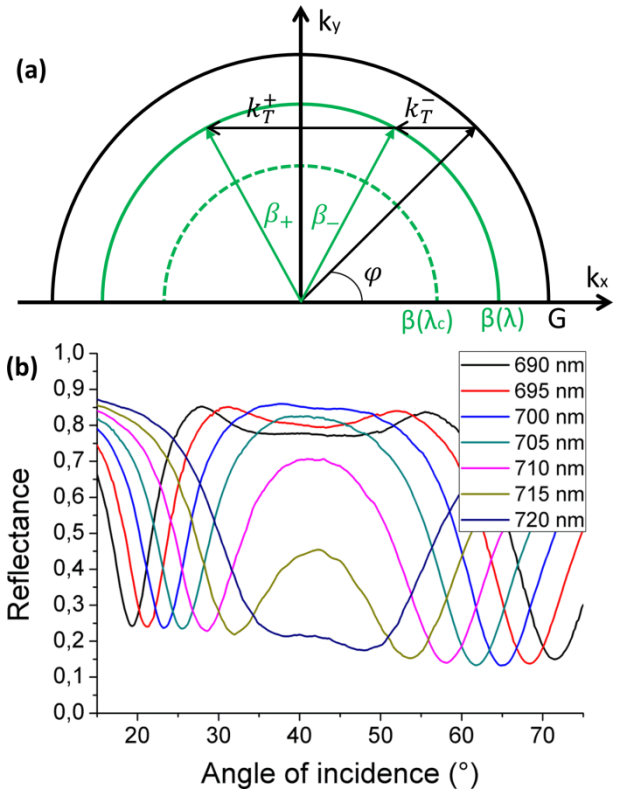

Fig. 11 (a): Sketch of coupling scheme in the G > β regime for a generic azimuth φ. It represents the reciprocal space of the sample plane, with the on-plane component of the incident light directed along $-\hat{x}$. It shows that for each wavelength λ two SPPs, $\vec{\beta}_+$ and $\vec{\beta}_-$, are excited, presenting the same modulus β(λ) and propagating along different directions, through the transfer of the $\vec{k}_T^+$ and $\vec{k}_T^-$ momenta respectively. The "merging condition" is satisfied when, for a certain wavelength λ_C, the two SPPs degenerate into a single SPP propagating along the y-axis. (b) Typical high-azimuth reflectance spectra associated to the coupling scheme shown in (a) for grating period Λ = 590 nm and azimuth φ = 56°. The existence of two resonances for a single wavelength, and of a single resonance at the merging condition, is shown.

It can be useful to solve in θ the resonance conditions (see Appendix 8.2.[a] for the derivation), for a fixed azimuthal angle, to extract the following two solutions, corresponding to the $\vec{\beta}_-$ and $\vec{\beta}_+$ SPPs [27]:

$$\sin\theta_{\mp} = \frac{\lambda}{\Lambda}\cos\varphi \mp \sqrt{N^2(\lambda) - \left(\frac{\lambda}{\Lambda}\sin\varphi\right)^2}$$

Where N(λ) is defined as the effective refractive index $N \equiv \beta\frac{c}{\omega}$, that is $N = \sqrt{\frac{\varepsilon_{mr}\varepsilon_d}{\varepsilon_{mr}+\varepsilon_d}}$ in the single-interface case. The request of reality of the square root term fixes the maximum azimuth that allows a plasmonic resonance to exist, namely:

$$\varphi^* = \sin^{-1}\left(\frac{\beta}{G}\right)$$

c. Coupling efficiency

The momentum matching conditions determine the position of the plasmonic dip in the angular scan, but they do give no information about the dip depth, that is correlated to the coupling efficiency.

It is known that the coupling efficiency strongly depends on the grating amplitude, defined as the vertical peak-to-valley distance. This dependence has been treated only through computer simulations by now, aimed to identify the amplitude that optimize the coupling efficiency for every specific structure and configuration [27].

The other crucial parameter is the incident light polarization [23]. It is known that a metallic grating only diffracts light with the electric field oriented along the grating vector, and completely reflects the other components [28]. This condition can be expressed by saying that only incident light with the electric field lying on the *grating symmetry plane* $(\hat{G}, \hat{z})$ can couple to the grating. In the φ = 0 configuration, the plane of incidence $(\hat{x}, \hat{z})$ coincides with the grating symmetry plane, thus the condition is fulfilled by p-polarized light.

In conical mounting the two planes no longer coincide, and $\vec{G}$ has an out-of-plane component $G_y = G \sin\varphi$; for this reason the right polarization to optimize the coupling is not the p-polarization any more. Defining the polarization as the α angle rotating counterclockwise from the plane of incidence to the electric field vector, as in Fig. 12, the optimal polarization α_{opt} is a periodic function of θ and φ, that can be easily derived as follows [29].

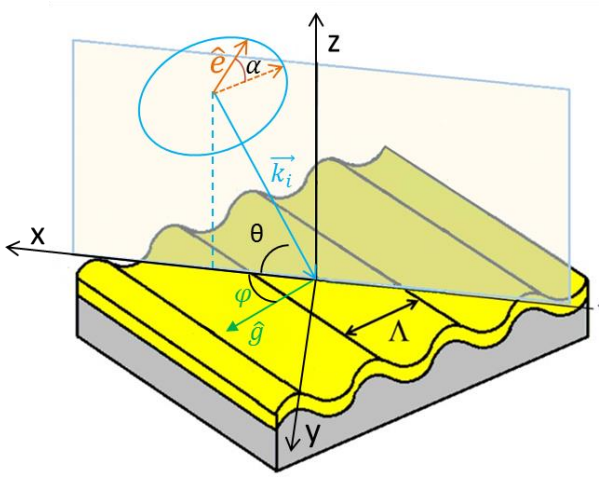

Fig. 12: Scheme of the vector conventions for a 1D grating of Λ period in conical mounting, with the definition of the incident light polarization. The electric field lies along the ê direction. The polarization angle, α, is defined as the counterclockwise rotation with respect to the plane of incidence, i.e. the $(\hat{x}, \hat{z})$ plane.

Assuming that all the diffracted power goes into the SPP excitation, the reflectance R is proportional to the electric field fraction perpendicular to the grating symmetry plane, that depends on both the azimuthal rotation and the incidence angle as follows:

$$R \propto |\hat{e} \cdot (\hat{g} \times \hat{z})|^2$$

Where $\hat{e}$ and $\hat{g}$ are the versors of the electric field and grating vector respectively, defined as follows:

$$\hat{e} = \frac{\vec{E}}{E} = (-\cos\alpha\cos\theta\,, \sin\alpha\,, -\cos\alpha\sin\theta)$$

$$\hat{g} = \frac{\vec{G}}{G} = (\cos\varphi\,, \sin\varphi\,, 0)$$

Using these definitions, R becomes:

$$R \propto |\cos\alpha\cos\theta\sin\varphi + \sin\alpha\cos\varphi|^2$$

That is 0 under the following condition, which defines the optimal polarization α_{opt}: $\tan\alpha_{opt} = -\tan\varphi\cos\theta$

Due to the π periodicity of the polarization, α_{opt} can be extracted as:

$$\alpha_{opt} = -\tan^{-1}(\tan\varphi\cos\theta) = \pi - \tan^{-1}(\tan\varphi\cos\theta)$$

Since this formula only depends on the φ and θ angles, curves of constant α_{opt} can be plotted on the (φ, θ) plane, obtaining the map in Fig. 13 valid for any value of the other parameters.

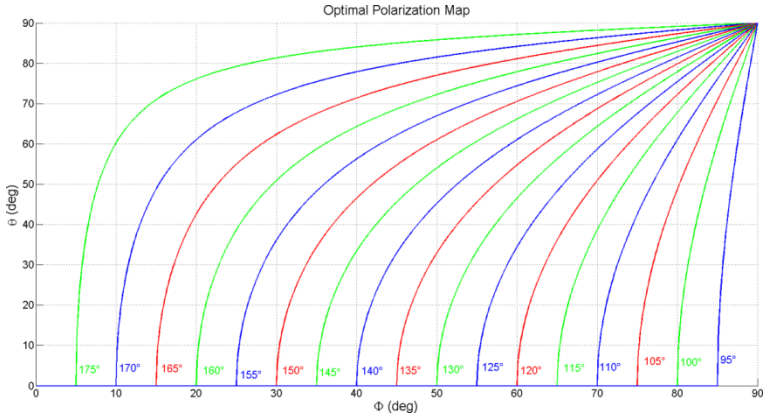

Fig. 13: Solutions of the optimal polarization formula are plotted on the (φ, θ) plane. Along each coloured curve, the optimal polarization has the value indicated in the corresponding label.

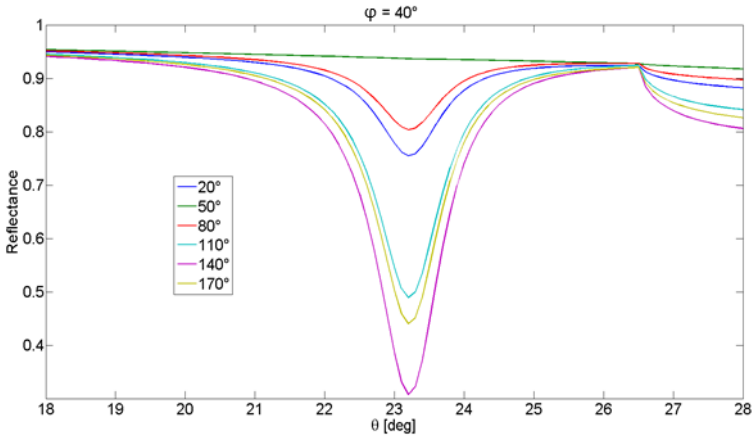

Fig. 14: Angular scan of the plasmonic resonance on a 500-nm grating, for 650-nm incident wavelength. The azimuthal angle is set to 40° and the spectrum is collected for various polarizations. It is in good agreement with the theoretical formula, which predicts the optimal polarization around 140°, and the worst polarization at about 50°.

When the polarization is optimized for the resonant θ and φ, the reflectance is minimum, while if the polarization is set to $\alpha_{opt} \pm \frac{\pi}{2}$ the dip disappears. The obvious reason is that at the orthogonal polarization no component of the field can couple to the grating. When the incident light is orthogonal to the grating vector (φ = 90°), p-polarized light is completely reflected but s-polarized is diffracted.

The complete dependence of R on the polarization can be derived as in Appendix 8.2.[b] and is given by [29]:

$$R \propto \frac{\cos^2\theta \sin^2\varphi + \cos^2\varphi}{2}[1 + \cos(2\alpha + \alpha_0)]$$

With $\alpha_0 = \sin^{-1}\left[\frac{-\sin 2\varphi \cos\theta}{\cos^2\theta \sin^2\varphi + \cos^2\varphi}\right]$. This formula is in good agreement with the observed trends, like the one reported in Fig. 14.

d. Losses and linewidth

The excitation of an SPP mode by ATR is equivalent to the prism coupling with a dielectric waveguide [30]; in particular the coupling is reciprocal and the energy propagating along the surface, or into the guide, tends to radiate back ("*leak*"). The main difference is that in the plasmonic case there are strong losses, due to the metal; losses are described by the imaginary part, Γ, of the SPP momentum, that can be decomposed into a term related to the intrinsic losses and a term related to leakage [31; 32]: $\Gamma = \Gamma_i + \Gamma_r$.

Since the dispersion of Chapter 1.1 has been derived for a flat surface, it represents a bound mode, thus it only gives the intrinsic term and not the radiative one, which depends on the coupler:

$$K_{spp} = \beta + i\Gamma_i = \frac{\omega}{c}\sqrt{\frac{\varepsilon_m \varepsilon_d}{\varepsilon_m + \varepsilon_d}}$$

Introducing the coupler (prism or grating), K_{spp} is perturbed in this general way:

$$K_{spp}^{(c)} = \beta + \delta\beta + i(\Gamma_i + \Gamma_r)$$

In the prism case, it is know that the reflectance in the proximity of the resonance can be approximated by the Lorentzian profile [4; 31; 33]:

$$R = 1 - \frac{4\Gamma_i\Gamma_r}{\left(n_p k_i \sin\theta - \beta - \delta\beta\right)^2 + (\Gamma_i + \Gamma_r)^2}$$

From which it is apparent that the width of the dip is strictly related to the total losses. In particular, the less loss, the sharper the resonance, since the lorentzian Full Width at Half Maximum is equal to $2(\Gamma_i + \Gamma_r)$.

In addition, it can be seen that R = 0 at the resonance only if $\Gamma_i = \Gamma_r$: thus this is the conditions that provides the optimal coupling between radiation and the SPP. This phenomenon can also be seen as an example of impedance matching: the SPP can be thought as a damped oscillator driven by a transmission line (the probe beam); only when the characteristic impedances of the oscillator and the beam (given by the coupling strength) are equal the back-reflection towards the source is cancelled [8; 31].

A deeper picture of what the dip in reflectance actually represents can be provided, using the concept of destructive interference between reflected and reradiated beam, or more precisely of a quantum interference between two indistinguishable paths [34]. The two paths are represented in Fig. 15: the incident photon either is reflected or it is converted into a surface mode, and then reradiated with a π phase shift. The paths destructively interfere, leaving as a result the excitation of the surface mode with the cancellation of the outgoing radiation.

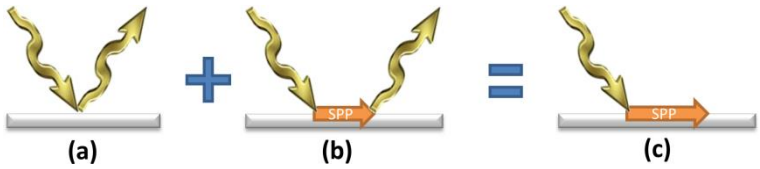

Fig. 15: Pictorial representation of the destructive interference between the two paths for the incoming photon. (a) reflection. (b) excitation of a surface mode and further re-emission. (c) eventually, the result is the cancellation of the outgoing beam for destructive interference.

The $\Gamma_i = \Gamma_r$ condition is found to be a universal condition for the coupling between a radiation field and a local oscillator [34], and it generally corresponds to a critical coupling regime, when the electromagnetic energy stored in the mode is maximal, since the re-radiated wave is suppressed [35].

Although this model has been developed for prism-coupled SPR sensors, it is also a good approximation for gratings [36]; in fact, since the grating acts as a coupler, an SPP propagating on a patterned metal surface will leak [23]. The $n_p k_i \sin\theta$ factor in the Lorentzian resonance is replaced, in this case, by $\left|\vec{k}_T + \vec{G}\right|$.

The field profiles symmetry of the thin-film coupled modes determine an enhancement of intrinsic losses for the SR SPP and a reduction for the LR SPP; the reason can be found in a deep analysis of the physical origin of this loss term. From a multipole Lorentz model approach, a relation can be derived between the SPP mode loss rate and the fraction of its energy stored as kinetic energy of the metals electrons, and an inverse relation between such kinetic energy and the magnetic energy [37].

Due to the inverse relation between propagation and losses, LR SPPs present a much sharper resonance, whose FWHM decrease with the film thickness [38; 39]. Obviously, the SR SPP shows the opposite behavior.

1.4. SPPs on realistic multilayer structures

Actual plasmonic structures are multilayer, due to the fabrication techniques, as it will be explained in Chapter 4.2.

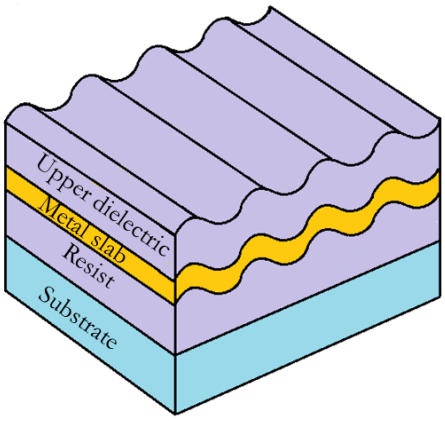

Fig. 16: Scheme of a realistic plasmonic grating; the structure is fabricated layer by layer. The resist is needed to realize the sinusoidal pattern. An upper dielectric layer can be deposited over the metal slab. Typical thicknesses are 100-200 nm for the dielectric layers and some tens of nm for the metal layer. Substrate is a quartz or silicon slide.

A typical stack is shown in Fig. 16: a patternable material called "resist" is deposited over a substrate and the metal layers are evaporated over it, following its sinusoidal shape. The metal layer can be exposed to air or a second dielectric layer can be deposited on it. The metal is usually a thin slab of some tens of nanometer, rather than a bulk, even when designed to support single-interface SPPs.

Such kind of structures is the same described in Chapter 1.2 and can in principle support two SPP modes, one at each metal/dielectric interface. If the upper dielectric is air or another medium with permittivity quite different from the resist permittivity, the two modes are decoupled.

Some remarks about the modes that can be supported by these structures and their excitations will now be made.

a. Effective Medium Approximation

Being the metal film thickness of the same order of the SPP penetration depth, a precise treatment of a single-interface SPP propagating on one of the surfaces should keep into account the interaction of its evanescent fields with the dielectric on the opposite side.

An approximation is introduced that provides an effective permittivity which includes this effect, treating the underlying layers as an effective medium. In the *Effective Medium Approximation* (EMA) the contribution of every underlying layer to the effective permittivity ε_{EMA} is weighed by its distance from the surface, using the exponential decay of the field [40].

Thus for a structure made of N layers, being d_j the thickness of the j-th layer of permittivity ε_j, and δ_m the SPP propagation depth (as defined in Paragraph 1.1.[b]), the general expression for the effective permittivity is as follows:

$$\varepsilon_{EMA} = \frac{2}{\delta_m} \sum_{j=1}^{N} \int_{d_{j-1}}^{d_{j-1}+d_j} \varepsilon_j e^{-2\frac{z}{\delta_m}} dz$$

Since δ_m depends on ε_{EMA} itself, according to $\delta_m = \frac{c}{\omega}\sqrt{\frac{\varepsilon_{EMA}+\varepsilon_d}{-\varepsilon_{EMA}^2}}$, a recursive calculation will be carried out until convergence.

For example, the upper layer could be a thin protective gold film of thickness d_{Au}, deposited over a thicker silver layer (of thickness d_{Ag}) and then the resist, as in the inset of Fig. 17. The zeroth order step would be to take $\delta_0 = \frac{c}{\omega}\sqrt{\frac{\varepsilon_{Au}+\varepsilon_d}{-\varepsilon_{Au}^2}}$ and calculate:

$$\varepsilon_{EMA}^{(0)} = \frac{2}{\delta_0}\left[\int_0^{d_{Au}} \varepsilon_{Au} e^{-2\frac{z}{\delta_0}} dz + \int_{d_{Au}}^{d_{Au}+d_{Ag}} \varepsilon_{Ag} e^{-2\frac{z}{\delta_0}} dz + \int_{d_{Au}+d_{Ag}}^{\infty} \varepsilon_{resist} e^{-2\frac{z}{\delta_0}} dz\right]$$

The penetration depth is then recalculated inserted $\varepsilon_{EMA}^{(0)}$ instead of ε_{Au} and used to calculate a more realistic $\varepsilon_{EMA}^{(1)}$. The iterations quickly converges and the last ε_{EMA} can be used into:

$$K_{spp} = \frac{\omega}{c}\sqrt{\frac{\varepsilon_{EMA}\varepsilon_d}{\varepsilon_{EMA}+\varepsilon_d}}$$

The result for the typical exemplifying case is represented by the red curve in Fig. 17, compared to the dispersion relation of a single-interface air/gold SPP (blue curve).

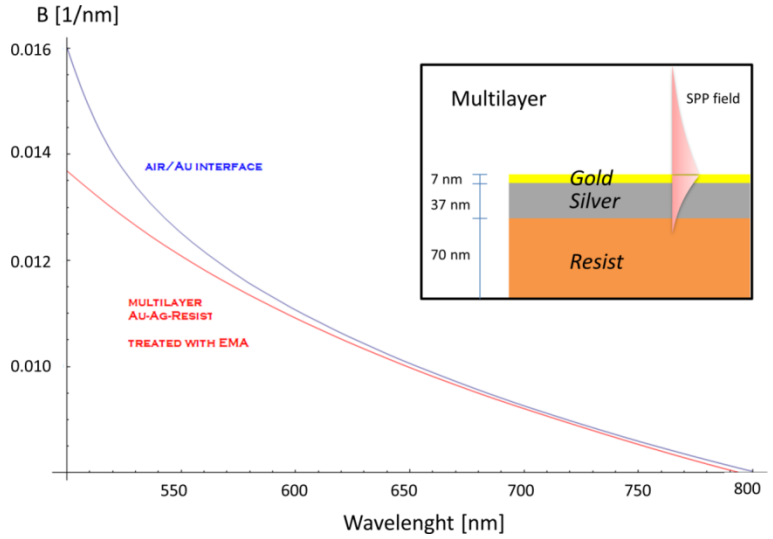

Fig. 17: (Inset) Profile of a typical multilayer structure; the thin gold layer protects the silver layer from oxidation. (Main figure) Dispersion relation of a air/gold single-interface SPP compared to the one of the actual multilayer structure, calculated through EMA.

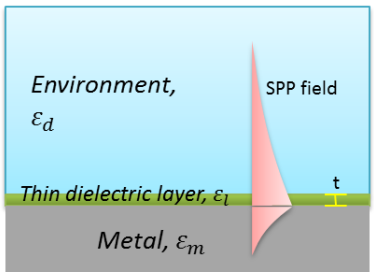

Fig. 18: A thin dielectric layer of permittivity ε_l is placed over the metal surface.

The same approximation can be used for the dielectric semi-space, when a thin dielectric layer is deposited over the metal surface for functional reasons (see Chapters 4.1 and 4.2). In particular, when the layer is much thinner than the SPP penetration depth, a straightforward analytical approximation can be provided as follows.
If t is the layer thickness, t << δ, and ε_l its permittivity, as in Fig. 18, and with the usual approximation $\varepsilon_{mi} \ll |\varepsilon_{mr}|, \varepsilon_d, \varepsilon_l$, the SPP dispersion relation will become [41]:

$$\beta \approx \frac{\omega}{c}\sqrt{\frac{\varepsilon_{mr}\varepsilon_d}{\varepsilon_{mr}+\varepsilon_d}} + t\left(\frac{\omega}{c}\right)^2 \frac{(\varepsilon_{mr}\varepsilon_d)^{\frac{3}{2}} \cdot (\varepsilon_{mr}\varepsilon_d - \varepsilon_l\varepsilon_d - \varepsilon_{mr}\varepsilon_l + \varepsilon_l^2)}{\varepsilon_l(\varepsilon_{mr}^2 - \varepsilon_d^2)(\varepsilon_{mr}+\varepsilon_d)}$$

If ε_l or t is individually modified, the change in β is unique and predictable.

b. Coupling issues

Since the structure examined in the last paragraph can support two SPP modes, it is reasonable to expect to observe two dips in the spectra; actually only the resonance corresponding to the mode propagating on the directly illuminated surface is observed.

The explanation of this phenomenon requires a deeper insight into the coupling process [42]. Since the momentum enhancement is provided by diffraction, it is the evanescent diffracted orders which excite the SPPs. To treat the coupling of the incident light to the SPP on the opposite

surface, all the transmitted fields through the metal slab have to be considered. They include the zeroth transmitted order and the evanescent diffracted orders; all these fields can pass through the second interface or be diffracted by it. The total transmitted field that can provide the SPP excitation is calculated with good approximation, showing that it is very weak, due to the reciprocal cancellation of the various contributions when both surfaces are conformally patterned, as in our case, depicted in Fig. 16. In fact, if only one surface is patterned, or if the two sinusoidal patterns are out of phase, both SPPs could be excited.

When a symmetrical environment is produced, the metal film supports the two coupled modes, that can be observed together in a single spectrum, as in Fig. 19. In fact, in this case each of the two modes involves both the interfaces and the previous reasoning does not apply. Moreover, due to the symmetry of the structure spectra acquired by illuminating the upper or lower surface of the sample are indistinguishable.

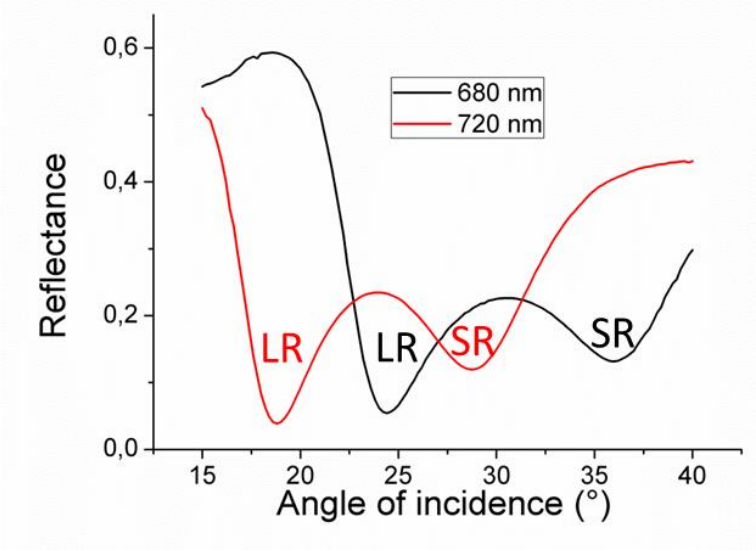

Fig. 19: Experimental spectra showing the dips corresponding to the coupled modes on a thin film, excited through a 590-nm grating.

c. Guided modes in a dielectric layer

In the multilayer structure, guided modes into a dielectric layer may exist and be excited by the grating coupler. In particular, a thick sensitive layer of thickness t of the order of some hundreds of nanometers, embedded between a lower index environment and the metal, constitutes in fact a dielectric/dielectric/metal waveguide (see Fig. 20).

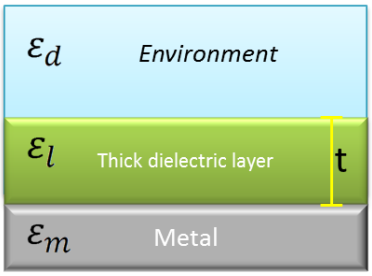

Fig. 20: A thick sensitive layer of thickness t seen as a dielectric/dielectric/metal waveguide.

Such a waveguide can support both TE and TM modes; with the quantities defined as in figure and being K_{wg} the (complex) momentum of the mode along the propagation direction, an implicit dispersion relation can be given, including the two cases [30]:

$$t * \sqrt{\varepsilon_l \left(\frac{\omega}{c}\right)^2 - K_{wg}^2} - N\pi = \tan^{-1}\left(R_D \sqrt{\frac{K_{wg}^2 - \varepsilon_d \left(\frac{\omega}{c}\right)^2}{\varepsilon_l \left(\frac{\omega}{c}\right)^2 - K_{wg}^2}}\right) + \tan^{-1}\left(R_M \sqrt{\frac{K_{wg}^2 - \varepsilon_m \left(\frac{\omega}{c}\right)^2}{\varepsilon_l \left(\frac{\omega}{c}\right)^2 - K_{wg}^2}}\right)$$

Where N = 0, 1, 2 … and the R_D and R_M factors are given by:

$$\begin{cases} R_D = \frac{\varepsilon_l}{\varepsilon_d} \\ R_M = \frac{\varepsilon_l}{\varepsilon_m} \end{cases} \quad \text{for TM modes}$$

$$R_D = 1 = R_M \quad \text{for TE modes}$$

Bragg diffraction can provide coupling of the incident light with a waveguide mode in the same way described in Chapter 1.3, observed as a dip in the reflectance spectrum. An example is reported in Fig. 21.

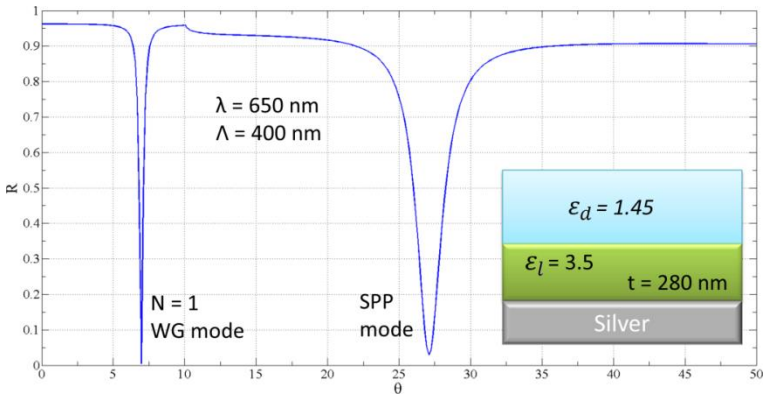

Fig. 21: Reflectance spectrum for the structure represented in the inset. The first dip corresponds to a guided TM mode of order 1, while the second dip to the SPP on the silver surface. Simulation based on Chandezon's method (see Chapter 3.1)

1.5. Optics of solids

The basic theory of optical functions of non-absorbing and absorbing media is here introduced, illustrating their meanings and pointing out the relations between the complex refractive index, the complex dielectric function and the electrons response to oscillating electromagnetic fields, according to Drude model.

a. Real and complex refractive index

The propagation of a monochromatic plane wave of wavelength λ and period τ is described by the oscillating factor: $e^{i(kx-\omega t)}$, with $k = \frac{2\pi}{\lambda}$ the wavenumber and $\omega = \frac{2\pi}{\tau}$ the wave frequency.
According to basic Electrodynamics [7; 18; 43], the refractive index for transparent (non-absorbing) homogeneous media is defined as the ratio of the phase velocity of the wave in vacuum to that of the wave in the medium: $n = \frac{c}{v}$.

The velocities can be expressed in relation to the magnetic permeabilities, μ_0 and μ for the vacuum and the medium respectively, and dielectric permittivities, ε_0 and ε, as follows: $c = \frac{1}{\sqrt{\mu_0 \varepsilon_0}}$; $v = \frac{1}{\sqrt{\mu\, \varepsilon}}$.
The relative dielectric permittivity ε_d is introduced such as $\varepsilon = \varepsilon_0 \varepsilon_d$, while for most materials $\mu \approx \mu_0$; thus the refractive index can be rewritten as: $n = \frac{\sqrt{\mu\, \varepsilon}}{\sqrt{\mu_0 \varepsilon_0}} \approx \sqrt{\varepsilon_d}$.
The wavenumber and the wavelength in the medium differ from the vacuum ones (k_0, λ_0) according to $\frac{\lambda_0}{\lambda} = \frac{k}{k_0} = n$, while the wave frequency ω is the same: $\omega = kv = k_0 c$.

In the more general case of an absorbing medium, a damping term has to be introduced [44 - 47]. A complex wavenumber $k = Re(k) + iIm(k)$ is defined through a complex "refractive index" $n + i\kappa$ such as $k = (n + i\kappa)k_0$. This gives an exponential decay of the electromagnetic wave driven by the factor: $e^{-Im(k)\cdot x} = e^{-\kappa k_0 x}$.
The physical interpretation of the so-called "complex refractive index" is subtle, since its real part does not in general satisfy the Snell's law for refraction as the real refractive index for transparent media does [48]. Concerning the imaginary part, the extinction of the wave will in general include not only the absorption but also the scattering [46]. Moreover, the damping of the wave does not even necessarily imply energy dissipation; in fact, such a dissipation is due to complex ε or μ, while κ may be non-zero also if ε and μ are real but negative [47].

The n and κ parameters are related to the real and imaginary part of the relative permittivity according to: $(n + i\kappa)^2 = \varepsilon_r + i\varepsilon_i$, that gives:

$$\begin{cases} \varepsilon_r = n^2 - \kappa^2 \\ \varepsilon_i = 2n\kappa \end{cases}$$

And the inverse system:

$$\begin{cases} n = \frac{1}{\sqrt{2}} \sqrt{\varepsilon_r + \sqrt{\varepsilon_r^2 + \varepsilon_i^2}} \\ \kappa = \frac{1}{\sqrt{2}} \sqrt{-\varepsilon_r + \sqrt{\varepsilon_r^2 + \varepsilon_i^2}} \end{cases}$$

For a weakly absorptive dielectric, with real ε_r and $\varepsilon_i << \varepsilon_r$, the condition $\kappa << n$ also holds, and the relations can be simplified as:

$$n = \sqrt{\varepsilon_r}$$
$$\kappa = \frac{\varepsilon_i}{2\sqrt{\varepsilon_r}}$$

This however is not valid for metals, due to the fact that ε_r is usually negative, thus the condition $\varepsilon_i << |\varepsilon_r|$ does not imply $\kappa << n$, but the contrary.

b. Drude-Lorentz model for metals

From a microscopic point of view, the meaning of the permittivity can be explained in terms of the electrons response to oscillating electromagnetic fields [43 - 46; 49]. Since the conduction electrons in metal are almost free to move, metals (and doped semiconductors) can be treated with good approximation as electrons/ions plasmas, when interband transitions can be neglected: this is the basis for Drude-Lorentz model.

Defining the constant factor $f_e \equiv \frac{q_e^2}{\varepsilon_0 m_e}$ (with q_e = electron charge, m_e = electron mass and ε_0 = vacuum permittivity) the frequency-dependent complex (relative) permittivity takes the form:

$$\varepsilon(\omega) = 1 - \frac{N_e q_e^2}{\varepsilon_0 m_e} \frac{1}{\omega^2 + i\omega\gamma}$$

Where N_e is the free electrons number density and γ represents a damping term. The value of N_e for common metals is in the range 10^{28} – 10^{29} m^{-3}, meaning that a metal is a very dense plasma [50]. In principle the damping parameter γ is due to different contributions, that includes the damping of atomic oscillators (bound electrons) and, in the case of metals, collisions of the free conduction electrons, and in general it could be frequency-dependent [43]. Since in metals the free-electrons contribution is dominant, damping is mainly due to the momentum losses by the electrons through collisions, thus γ can be identified with good approximation with the collision frequency ν [45; 49].

Separating the real and imaginary parts of the complex permittivity, the following relations are finally obtained, linking the three sets of parameters (n, κ), $(\varepsilon_r, \varepsilon_i)$ and (N_e, ν):

$$\begin{cases} \varepsilon_r = 1 - \dfrac{N_e f_e}{\omega^2 + \nu^2} = n^2 - \kappa^2 \\ \varepsilon_i = \dfrac{\nu}{\omega} \cdot \dfrac{N_e f_e}{\omega^2 + \nu^2} = 2n\kappa \end{cases}$$

The electronic density and the collision frequency can be a fortiori extracted through the inverted formulas:

$$\begin{cases} \nu = \omega \cdot \dfrac{2n\kappa}{1 - n^2 + \kappa^2} = \dfrac{\varepsilon_i \omega}{1 - \varepsilon_r} \\ N_e = \dfrac{\omega^2}{f_e}\left[\dfrac{(1 - n^2 + \kappa^2)^2 + 4(n\kappa)^2}{1 - n^2 + \kappa^2}\right] = \dfrac{\omega^2}{f_e} \cdot \dfrac{(1 - \varepsilon_r)^2 + \varepsilon_i^2}{1 - \varepsilon_r} \end{cases}$$

Since usual values of ν for metals and doped semiconductors range between 10^{13} and 10^{14} Hz [45], for optical frequencies the approximation $\omega >> \nu$ holds, thus the equations could be simplified as follows:

$$\begin{cases} \varepsilon_r = 1 - \dfrac{N_e f_e}{\omega^2} = n^2 - \kappa^2 \\ \varepsilon_i = \dfrac{\nu}{\omega} \cdot \dfrac{N_e f_e}{\omega^2} = 2n\kappa \end{cases}$$

This also implies that the weak absorption approximation $\varepsilon_i << |\varepsilon_r|$ is good at optical frequencies. As said before, for materials of negative ε_r this means that $\kappa >> n$, and in particular it gives the approximated relations: $n \approx \frac{\varepsilon_i}{2\sqrt{-\varepsilon_r}}$; $k \approx \sqrt{-\varepsilon_r}$.

The electronic density and the collision frequency can be a fortiori extracted through the inverted formulas:

$$\begin{cases} \nu = \omega \cdot \dfrac{2n\kappa}{1 - n^2 + \kappa^2} = \dfrac{\varepsilon_i}{1 - \varepsilon_r}\omega \\ N_e = \dfrac{\omega^2}{f_e}\left[\dfrac{(1 - n^2 + \kappa^2)^2 + 4(n\kappa)^2}{1 - n^2 + \kappa^2}\right] = \dfrac{\omega^2}{f_e} \cdot \dfrac{(1 - \varepsilon_r)^2 + \varepsilon_i^2}{1 - \varepsilon_r} \end{cases}$$

That under the weak absorption condition become:

$$\begin{cases} \nu = \dfrac{\varepsilon_i}{1-\varepsilon_r}\omega \approx \omega \cdot \dfrac{2n\kappa}{1+\kappa^2} \\ N_e \approx \dfrac{\omega^2}{f_e} \cdot (1-\varepsilon_r) \approx \dfrac{\omega^2}{f_e}(1+\kappa^2) \end{cases}$$

While the meaning of N_e is clear, a complete calculation of the contributions to ν would require a quantum-mechanical approach. Anyway, since the collisions involving appreciable momentum transfer occur between the electrons and phonons or defects [7], the collision frequency does not depend on the electron density, thus (N_e, ν) can be treated as a set of independent variables.

2. Surface Plasmon Resonance sensing

One of the main applications of Surface Plasmon Polaritons is as probes for sensing devices.

Basic principles of Surface Plasmon Resonance sensing are introduced in the first Chapter of this Section, also defining the main parameters to be considered to characterize their performances.

In the second Chapter, the problem of theoretical estimations of SPR sensitivity is addressed, and common strategy to enhance the sensitivity are presented, including the exploitation of thin-film coupled modes and the conical mounting configuration.

2.1. Basic principles

Optical sensing technology is knowing a great growth during the last decades. General advantages of sensors of this king are the wide available range of operative parameters and the stability of the device. In fact, variations in frequency, intensity, polarization, phase of the reflected or transmitted light can be analysed [51]; the devices are resistant to heat, corrosion, fire and electrical interferences, and they are suitable for in-situ operation [52].

a. SPR sensing strategies

Since SPPs are highly sensitive to changes of the refractive index in the vicinity of the surface, they are widely recognized as suitable probes for sensing devices [53-57]. The Surface Plasmon Resonance (SPR) sensors exploits the SPP properties to detect by optical means chemical or biological species, with aim of medical diagnostics, environmental monitoring and food safety. Among optical sensors, they are appreciated for the possibilities of extreme miniaturization and integration and for being a label-free technology.

The concept of SPR sensing is illustrated in Fig. 22. An SPP is excited on a metallic surface by an incident light beam; the excitation manifests itself as a fall of intensity of the reflected beam, as shown in Fig. 9. The SPP evanescent field probes the surrounding environment; if the refracting index of the surrounding medium changes, the propagation constant of the SPP changes too, affecting the reflectance spectrum through the coupling conditions.

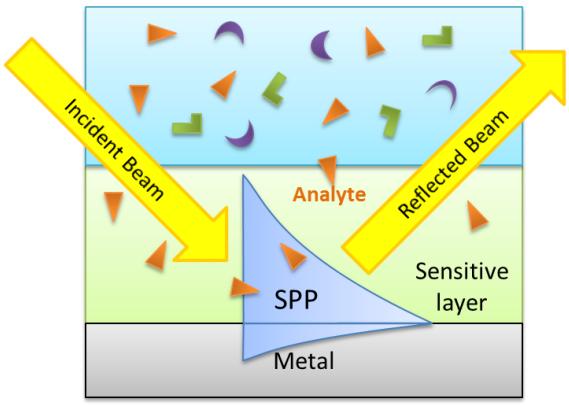

Fig. 22: Concept of SPR sensing. A functional sensitive layer, deposited over a metal surface, is optimized to capture a specific analyte present in the environment. The fields of an SPP propagating along the metal surface probe the sensitive layer. The SPP properties are investigated through reflectance measurements.

The principle can be exploited for a variety of different applications, both for detection of chemical [58; 59] and biological [60-62] analytes, both in gaseous [63-66] or liquid [67-69] environment.

In order to have an optical response only to the presence of a specific substance in the environment, a functional layer is needed, capable to capture the desired analyte and bound it close to the surface. In some cases, especially for biosensors, the sensitive layer can be made of a specific biorecognition element immobilized on the metal surface, such as antibodies [70; 71] or DNA sequences [72; 73]. For gas sensing applications other strategies are usually exploited, as it will be described in detail in Section 6.

Since the first reported SPR sensor [74], most SPR sensors employ the prism as a coupling strategy [75; 76], because they are of simple and cheap fabrication and demonstrate higher performances [77]. Their main drawbacks are the cumbersome optical alignment and the impossibility of miniaturization and integration, since they employ a refractive optical element. This is the reason for a growing interest in grating-coupled devices [78]; their potential for miniaturization provides the possibility to fabricate arrays of multiple gratings on a chip [79].

SPR sensors can be classified as sensors with angular, wavelength, intensity or phase interrogation, depending on which parameter of the reflected light is measured.
In sensors with *angular interrogation*, the incident light is monochromatic while the incident angle is scanned. The SPP resonance is observed as a dip in the angular reflectance spectrum [76; 80].
On the contrary, in the *wavelength interrogation* case the incidence angle is fixed and the incident wavelength is varied, performing a spectral scan. The resonance appears as a dip in the spectrum [58; 81; 82].
Within the *intensity interrogation* and the *phase interrogation* strategies, both the incidence angle and the light wavelength are fixed, and the variation of the intensity of the reflected beam [74], or its shift in phase respectively [83], is taken as sensor output.

b. Performance parameters

The main parameters that characterize a generic SPR sensor performances are: sensitivity, linearity, resolution, accuracy, range, limit of detection [84, 85].

Sensitivity is the ratio of change of the sensor output signal, Y, to the change in measurand, that is the analyte concentration: $\Sigma = \frac{\partial Y}{\partial c}$. It can be decomposed in two factors: the sensitivity of the sensor output to a change of the dielectric refractive index, also called *refractometric sensitivity*, Σ_n, and the conversion efficiency of the capture of the analyte into a change in refractive index:

$$\Sigma = \frac{\partial Y}{\partial n}\frac{\partial n}{\partial c} \equiv \Sigma_n \frac{\partial n}{\partial c}$$

In real cases, in the presence of a functional sensitive layer, it is useful to further decompose the sensitivity as follows:

$$\Sigma = \frac{\partial Y}{\partial n_{\mathrm{eff}}}\frac{\partial n_{\mathrm{eff}}}{\partial n_l}\frac{\partial n_{\mathrm{l}}}{\partial c}$$

where n_l is the refractive index of the sensitive layer and n_{eff} the effective refractive index felt by the SPP mode. Thus $\frac{\partial n_{\mathrm{l}}}{\partial c}$ represents the response of the sensitive layer to the analyte concentration and it depends on the adopted materials and binding techniques; $\frac{\partial n_{\mathrm{eff}}}{\partial n_l}$ represents the consequent effective modification of the whole structure from the SPP point of view. This last term is

particularly relevant in the case of thin sensitive layers, when the SPP fields penetrate deeply into the dielectric, as in Fig. 23, and it can be treated with the approximations provided in Paragraph 1.4.[a], but requires the knowledge of both the SPP mode and the supporting structure.
Considerations about the refractometric sensitivity of SPR sensors will be developed in the next Chapter.

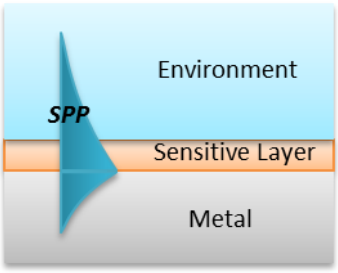

Fig. 23: When the sensitive layer is thinner than the SPP penetration depth into the dielectric region, an Effective Medium Approximation can be used for the effective dielectric permittivity felt by the SPP.

For practical purposes it usually is more significant to define a *Figure of Merit* (FOM) of the resonance, which keeps into account the difficulty to resolve the variation of the dip spectral position. Since this depends on the resonance width, FOM is commonly defined as $\frac{\Sigma}{FWHM}$, where FWHM = Full Width at Half Maximum of the resonance dip [86].

Linearity quantify the extent to which the sensor output response to the measurand is linear. It is usually defined as the maximum deviation from a linear function over the working range. SPR sensors response is usually a non-linear function of the analyte concentration; as a consequence, a careful calibration is essential to interpret their output.

Resolution is defined as the smallest change in the bulk refractive index that produces a detectable change in the SPR sensor output, and it is related to the noise of the system. The dominant sources of noise are the intensity fluctuations of the light source, the *shot noise* associated with photon statistics and the conversion of the light signal into an electric signal [85]. The standard deviations associated with these noise sources present different dependence on the light intensity, I, as follows:

- The noise in the intensity of the emitted light is proportional to the intensity itself: $\sigma_L(I) = \sigma_L^r I$, having define σ_L^r as a relative standard deviation, independent on I.
- The shot noise is related to the random arrival of photons to a photodetector. Since the photon flux from conventional light sources usually obeys Poisson statistics, the shot noise is proportional to the square-root of the light intensity [87]: $\sigma_S(I) = \sigma_S^r \sqrt{I}$
- The detector noise includes several contributions, mostly related to the temperature fluctuations, and it is independent on the light intensity: σ_D

The total noise on the measured light intensity is given by a statistical superposition of the three components, as follows: $\sigma_I(I) = \sqrt{(I\sigma_L^r)^2 + \left(\sigma_S^r \sqrt{I}\right)^2 + \sigma_D^2}$.
It can be reduced with a time averaging over N repeated measures, according to: $\sigma_I^N = \frac{\sigma_I}{\sqrt{N}}$
In order to translate the noise in the light intensity into a sensor output noise, the data processing algorithm has to be considered. Various algorithm have been developed: the centroid method [88], the polynomial fitting [89] and the optimal linear analysis [90] among them; since there is no relevant difference in the way they transform the noise from an angular of wavelength spectrum [91], the

simplest one will be considered. The centroid method calculates the geometric centre of the SPR dip below a set threshold I_T, using the following weighted centroid algorithm [92]:

$$x_c = \frac{\sum_i x_i (I_T - I_i)^2}{\sum_i (I_T - I_i)^2}$$

Where x_i is the spectral position of the intensity contribution I_i. If the noise σ_i associated to each I_i can be treated as independent, the resulting standard deviation on the dip position will be given by the usual propagation formula: $\sigma_c^2 = \sum_i \left(\frac{\partial x_c}{\partial I_i}\right)^2 \sigma_i^2$.

Finally, if the portion of the SPR dip used for the centroid calculation can be approximated by a lorentzian profile, the following expression can be derived for the resolution [93]:

$$\sigma_n = \frac{K}{\sqrt{N_c}} \frac{\sigma_T}{d_I} \frac{w}{\Sigma_n}$$

Where N_c is the number of points used for the centroid estimation, σ_T is the total intensity noise at the threshold, d_I the difference of intensity between I_T and the SPR minimum, w the width of the lorentzian resonance, Σ_n the refractive index sensitivity and K a factor that keeps into account the relative contribution of the different noise sources.
This formula shows that the ways to lower the resolution are: reduce the noise and the resonance width, increase the resonance depth and the sensitivity.

Accuracy quantifies the agreement between the measured value and the true value of the measurand, while *reproducibility* is the ability of the sensor to provide the same output when measuring the same value of the measurand.
The *range* is the span of the values of the measurand that can be measured by the sensor.

Limit of Detection (LOD) is the analyte concentration c_L that produces the smallest detectable output Y_L.
Y_L is usually taken as 3 standard deviations from the blank sample output Y_B (the signal in the absence of analyte), thus, if σ_B is the standard deviation of the blank measure, it is given by [94]: $Y_L = Y_B + 3\sigma_B$.
If the blank concentration $c_B = 0$, the LOD concentration c_L is:

$$c_L = \frac{3 \cdot \sigma_B}{\Sigma}$$

2.2. Sensitivity enhancement strategies

a. Basic performance estimates

Several authors reviewed and compared the sensitivity performances of the various kind of SPR sensors, providing some general results [31; 32; 36; 77; 95-98].

The expression for a single-interface SPP propagating on a flat surface is considered, which constitutes a good approximation also for grating-based sensors, since the surface modulation affects the real part of K_{spp} in a negligible way [23; 99]:

$$\beta = \frac{\omega}{c} \sqrt{\frac{\varepsilon_{mr} n^2}{\varepsilon_{mr} + n^2}} \equiv \frac{\omega}{c} \cdot N$$

Being n the refractive index of the probed medium.

As far as grating-based sensors are concerned, the refractometric sensitivities Σ_n are given as follows, for angular or wavelength interrogation, respectively:

$$\Sigma_{n,\theta} = \frac{\partial\theta}{\partial n} = \frac{1}{\cos\theta}\left(\frac{\varepsilon_{mr}}{\varepsilon_{mr}+n^2}\right)^{\frac{3}{2}} = \frac{1}{\cos\theta}\left(\frac{\mathrm{N}}{n}\right)^3$$

$$\Sigma_{n,\lambda} = \frac{\partial\lambda}{\partial n} = \frac{\left(\frac{\varepsilon_{mr}}{\varepsilon_{mr}+n^2}\right)^{\frac{3}{2}}}{\frac{j}{\Lambda}+\frac{n^3}{2\sqrt{\varepsilon_{mr}}|\varepsilon_{mr}+n^2|^{3/2}}\cdot\frac{d\varepsilon_{mr}}{d\lambda}} = \frac{\left(\frac{\mathrm{N}}{n}\right)^3}{\frac{j}{\Lambda}-\frac{d\mathrm{N}}{d\lambda}}$$

Being j the diffraction order. These relations assume that the incident radiation comes from air or vacuum and enters the sensitive layer with a certain incidence angle θ; in these means they differ from the ones reported in some literature, which are immersed into the medium of n refractive index [77; 98] . The transformation between the two forms is reported in Appendix 8.2[c].

Two contributions can be recognized to the overall Σ_n, one due to the SPP mode intrinsic sensitivity and one related to the interrogation strategy:

$$\Sigma_n = \frac{\partial Y}{\partial N}\cdot\frac{\partial N}{\partial n}$$

with Y = θ or λ. The second factor is independent on the chosen interrogation strategy and provides the following contribution: $\frac{\partial N}{\partial n} = \left(\frac{\mathrm{N}}{n}\right)^3$. The trend of the N/n factor is reported in Fig. 24, showing a much higher contribution at lower wavelengths.

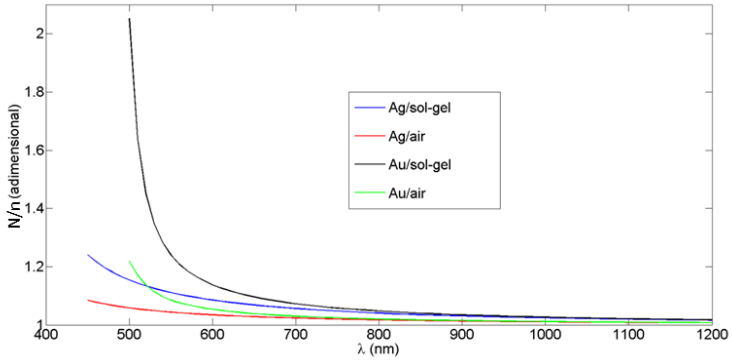

Fig. 24: Trend of the N/n factor for different interfaces, including gold or silver as the metal, and as the dielectric air or a sol-gel material with the refractive index of Fig. 30 of Chapter 4.1[b], that is of about 1.52.

Under the Lorentzian approximation, the widths of the resonances in the two cases are obtained by the imaginary part of the SPP momentum as follows: $FWHM_Y = 2\frac{c}{\omega}(\Gamma_i+\Gamma_r)\frac{\partial Y}{\partial N}$.

As a consequence, the Figure of Merit is the same for the two approaches and is given by:

$$FOM = \frac{\Sigma_{n,Y}}{FWHM_Y} = \frac{1}{2(\Gamma_i+\Gamma_r)}\cdot\frac{\omega}{c}\cdot\left(\frac{\mathrm{N}}{n}\right)^3$$

When considering the intensity interrogation case, the maximum sensitivity is achieved when the slope $\frac{dR}{dk_T}$ is maximum. It can be shown for prism-based sensors, under the lorentzian approximation for the reflectance introduced in Paragraph 1.3[d], that the slope is maximized

under the $\Gamma_r = \frac{\Gamma_i}{2}$ condition [31]. Interestingly enough, this does not correspond to the optimal coupling condition, given by $\Gamma_i = \Gamma_r$; in fact, the reflectance depends more strongly on the coupling when under a weak coupling regime. This has been shown to be a general result and a crucial parameter for the SPR sensor resolution [36].

b. Superior performances of the Long Range modes

Generally speaking, the sensitivity of the plasmon as a probe depends on the interaction volume of the SPP evanescent field with the analyte [97]. A long propagation, a deep penetration into the sensitive layer and a strong enhancement of the field intensity are advantageous properties for sensing applications.

In realistic configurations, with the incident light spot much greater than the SPP wavelength, during the propagation more and more energy leaks into the guided mode, increasing the field enhancement in the proximity of the surface with respect to the incident wave [31; 100]. A longer propagation implies a superior sensitivity and a sharper resonance curve: for this reason Long Range modes are broadly recognized as promising probes for sensing applications [101-106]. In fact, great enhancement in sensitivity [101; 103], resolution [106] and limit of detection [102; 104] have been demonstrated.

Theoretical evaluations of the LR SPP sensitivity are not found in literature.

c. Sensitivity enhancement in conical mounting

It has been established that the conical mounting provides an enhancement in sensitivity, especially when the second resonance is exploited as a probe [107-110]. The reason of this enhancement can be understood both geometrically and analytically.

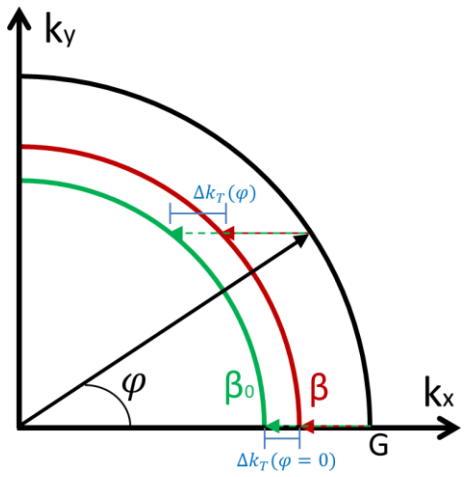

Fig. 25: Geometrical proof of the sensitivity enhancement associated with the azimuthal rotation, if the exposure to the analyte induces a variation of the SPP momentum from β_0 to β. The Δk_T segment, representing the corresponding variation in the transferred momentum, clearly increases with φ, for the same variation of β.

The geometrical proof is represented in Fig. 25, where β_0 is the momentum of the SPP resonance for the unperturbed structure and β the one after the exposure to the analyte. Obviously, the momentum variation, $\Delta\beta = \beta - \beta_0$, does not depend on the azimuth, but the read quantity, Δθ or

$\Delta\lambda$, does. In fact, the variation of the transferred momentum, Δk_T, increases with φ as it is apparent from the figure.

The analytical proof is given as follows. Having defined χ as the angle between $\vec{\beta}$ and $\hat{x}$, the coupling conditions becomes:

$$\begin{cases} \vec{\beta} \cdot \hat{x} = \beta \cos\chi = G\cos\varphi - k_T \\ \vec{\beta} \cdot \hat{y} = \beta \sin\chi = G \sin\varphi \end{cases}$$

From the second condition, an expression for $\cos\chi$ can be derived as follows:

$$\cos\chi = \sqrt{1 - \sin^2\chi} = \sqrt{1 - \left(\frac{G}{\beta}\sin\varphi\right)^2}$$

Together with the first condition, it leads to: $\beta\sqrt{1 - \left(\frac{G}{\beta}\sin\varphi\right)^2} = G\cos\varphi - k_T$ for a generic β.

The variation of transferred momentum due to the interaction with the analyte can then be evaluated as follows:

$$\Delta k_T = k_T - k_{T0} = -\sqrt{\beta^2 - (G\sin\varphi)^2} + \sqrt{\beta_0^2 - (G\sin\varphi)^2} \equiv -\sqrt{\beta^2 - (G\sin\varphi)^2} + B$$

It is reasonable to introduce the approximation: $\beta \equiv \beta_0 + \delta$ with $\delta << \beta$ => $\beta^2 \approx \beta_0^2 + 2\beta_0\delta$

Thus: $\sqrt{\beta^2 - (G\sin\varphi)^2} \approx \sqrt{\beta_0^2 + 2\beta_0\delta - (G\sin\varphi)^2} \approx B + \frac{\beta_0\delta}{B}$

That gives, in conclusion:

$$\Delta k_T \approx -\frac{\beta_0\delta}{B} = \frac{-\beta_0\delta}{\sqrt{\beta_0^2 - (G\sin\varphi)^2}}$$

This formula shows that Δk_T increases in modulus for increasing azimuthal angle φ.

In particular, $|\Delta k_T| = |\delta|$ for φ = 0, and it increases until the maximum allowed φ is reached, given by $\varphi^* = \sin^{-1}\left(\frac{\beta}{G}\right)$, when the square-root vanishes and $|\Delta k_T|$ formally diverges. This divergence arises from the fact that, according to the coupling conditions, around φ^* a slight variation in β could abruptly cancel the possibility to excite the SPP. Actually, this would be rigorously true only if the resonance had null width, thus the divergence is not seen in real cases.

It is observed that the width of the resonance also increases with φ, but the sensitivity increases faster, in such a way that an overall improvement of the Figure of Merit is achieved in conical mounting [107].

d. Factorization

To conclude, an analytical expression for the sensitivity which includes the contribution of conical mounting can be derived as [107]:

$$\Sigma_{n,\theta} = \frac{\partial\theta}{\partial n} = \frac{\partial\theta}{\partial k_T}\frac{\partial k_T}{\partial\beta}\frac{\partial\beta}{\partial n} = \frac{\partial\theta}{\partial(\sin\theta)}\frac{\partial(\sin\theta)}{\partial N}\frac{\partial N}{\partial n}$$

To give:

$$\Sigma_{n,\theta} = \frac{N^4}{n^3} \cdot \frac{\Lambda/\cos\theta}{\lambda\cos\varphi - \Lambda\sin\theta}$$

Introducing the solutions for θ of the resonance conditions, taken from Chapter 1.3[b] or Appendix 8.2[a], a plot of the modulus of the refractometric sensitivity as a function of the azimuth can be drawn, as in Fig. 26.

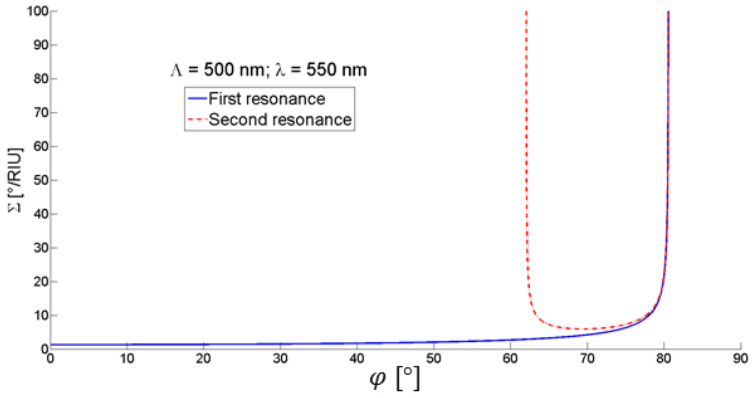

Fig. 26: Modulus of the refractometric sensitivity of the two resonances of an air/gold SPP at λ = 550 nm, under angular interrogation on a Λ = 500 nm grating. The blue curve is referred to the first resonance and its sensitivity formally diverges at the maximum azimuth φ*, the red one to the second, diverging both at φ* and at the minimum azimuth to be excited.

3. Computational Methods

In order to completely describe the coupling of light with plasmonic structures and the plasmon propagation and interactions, computational approaches are needed.

In this Section two useful tools will be introduced:

- Chandezon's method, which provides a rigorous solution to the problem of a monochromatic wave incident on a diffraction grating
- The modal analysis through Finite Element Method, which allows to calculate the plasmonic modes supported by a certain structure

This two methods provide different and complementary information, useful to model a plasmonic structure and investigate its response.

3.1. Chandezon's method

Among the algorithms developed to compute the optical response of periodically patterned multilayer structures, Chandezon's method (also called C-method) proved to be one of the most efficient and stable.

In its original form, introduced by Chandezon et al., it solved the problem of a monochromatic plane wave incident on a perfectly conducting grating [111; 112]. Working with a non-orthogonal coordinate system to map the sinusoidal interfaces into parallel planes, it expands the fields in Fourier series and reduce the problem to an eigenvalue problem to be solved in each medium. Many author contributed to extend and improve the method, allowing application to conical mounting configuration [113], to multilayer gratings of arbitrary profile [114-116] and to the digital grating case [117]. Numerical stability [118] and efficiency [119] have also been improved over the years.

The C-method has been implemented in MATLAB environment by G. Ruffato [27] in order to compute the optical response of sinusoidal multilayer plasmonic gratings and produce reflectance spectra directly comparable to experimental data [120].

The basic feature of the method is to map the sinusoidal interfaces into parallel planes, through the introduction of a non-orthogonal coordinate system. Maxwell's equations are solved in their covariant formulation in the new reference system [121]. To do this, the fields are expanded in pseudo-Fourier series, according to Bloch-Floquet's theorem applied to the periodicity along the x direction [122; 123]. With a truncation to the order N, a set of 8N+4 partial differential equations is derived for each medium. It can be demonstrated that the calculated solution tends to the exact solution for $N \rightarrow \infty$ for a broad class of configurations [124].

The multilayer structure is built in the code by setting the proper geometrical parameters (grating period and peak-to-valley height, layer thickness) and refractive index of each layer. The radiation wavelength, polarization, incidence angle and azimuth can be set. The obtained spectra show a very good agreement with experimental data [125].

3.2. Modal Analysis

It is known that Maxwell equations can be cast as an eigenvalue problem, in strong analogy with Schrödinger equation in Quantum Mechanics. This fact is widely applied in Photonics to calculate the optical Bloch modes supported by photonic crystals, characterized by translational symmetries [122]. In this framework, transparent non-dispersive materials only are typically involved, leading to a generalized linear eigenvalue equation. Frequency can be taken as eingenvalue and the dispersion relation is straightforwardly calculated as $\omega(\vec{k})$, for each chosen value of the momentum. This does not happen in the plasmonic crystal slabs analyses, where material dispersion plays a crucial role and dissipation is strong, so the resulting eigenvalue equation remains nonlinear.
In order to solve this eigenvalue problem, a finite-elements-based numerical method for the modal analysis of such structures is proposed, which allows to retrieve complex Bloch modes dispersions.

The foundation of the method consists in considering as eigenvalue the wave vector instead of the frequency, i.e. specifying the frequency and solve for the wave vector to obtain $\vec{k}(\omega)$. There are many reasons for this choice [126]. First, in plasmonic materials the dielectric function strongly depends upon frequency, thus only if the wavevector is calculated as a function of frequency the eigenvalue problem has to be solved only once, and not iteratively. Second, the wavevector is more useful as a complex eigenvalue because it contains all the information about propagation and losses of the mode. Third, the external exciting field has fixed real frequency, that is the same of the excited plasmonic mode, so to fix the frequency is a more suitable description for this kind of experiments.

To this aim, Helmoltz equation is reformulated in a weak form, leading to a quadratic eigenvalue equation in k [127]. This formulation finds a natural solution in the frame of the Finite Elements Method, which inherently handles weak forms of partial differential equations, and it allows dealing with a general class of materials: dispersive, lossy and possibly anisotropic [128].

A crucial point is that the analysis of plasmonic crystals requires to handle not only proper bound modes but also leaky modes, i.e. modes that can couple to propagating waves in the surrounding environment, leading to radiative losses. This gives rise to a complication in the models, because proper boundary conditions have to be imposed at the edge of the computational domain, in order to simulate an open space, avoiding back-effects of the emitted radiation that perturb the calculation of the eigenmode profile.

One approach uses a discretization of the wave vectors space, called Plane Wave Expansion method, with Perfectly Matched Layers (PMLs) which correctly absorb leakage radiation at the boundary [129]. PMLs are characterized by slowly space varying relative permittivity and permeability, properly designed in order to minimize reflection of plane waves impinging on them at arbitrary incidence. This method can well deal with arbitrary dispersive materials, but not with losses. Other methods based on discretization of real space (like Finite Elements and Finite Differences) can handle the lossy dispersive problem but are computationally very expensive.

Our chosen approach to calculate the Bloch band structure of dispersive lossy photonic crystal slabs adopts the weak formulation of the Helmholtz's equation, with FEM discretization of the system, and with the addition of PMLs to deal with leakage radiation at the boundary of the unit

cell domain [99]. The method was fully implemented by P. Zilio in the commercial software COMSOL Multiphysics, suitable to deal with an approach of this kind [130].

This analysis allows to extract information about the real and imaginary parts of the plasmonic mode propagation vector for the actual structures, including the presence of the grating. As an example, Fig. 27(a) reports the imaginary parts of the dispersion relations of the plasmonic modes propagating on a symmetrical dielectric-metal-dielectric structure. For both the LR and SR SPP, a comparison is made between the values calculated under flat structure approximation and the ones obtained by Modal Analysis for the real patterned structure, showing that the effect of the grating cannot be neglected. In addition, the plot of the eigenmode field profiles displays the symmetric or antisymmetric nature of the fields, thus allowing a clear identification of the LR SPPs and SR SPPs, and shows possible waveguide modes in the dielectric layers. Fig. 27(b) shows the distribution of the longitudinal electric field for the LR and SR SPPs into a symmetrical multilayer structure; leakage radiation is seen as plane waves into the two half-spaces.

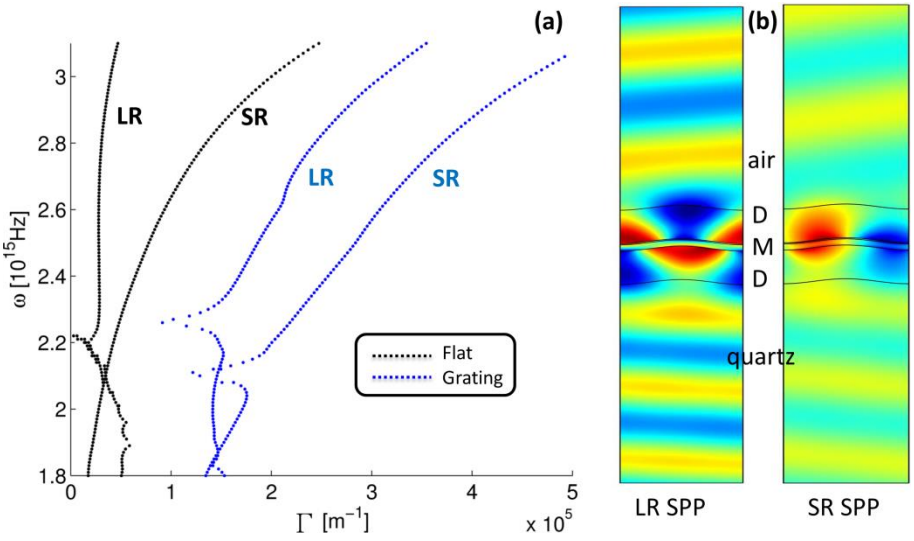

Fig. 27: Some illustrative results of Modal Analysis on a symmetrical multilayer structure with grating period = 570 nm and peak-to-valley amplitude 70 nm. (a) scatter plot of the imaginary part of the dispersion relation for LR and SR SPPs: a comparison between the full calculation (blue dots) and the outcomes of a flat-structure approximation. (b) longitudinal electric field profiles for the two coupled modes: antisymmetric for the LR and symmetric for the SR; color scale in arbitrary normalization.

A model was prepared in order to study the losses of an SPP mode propagating on a particular structure. The scheme of the simulation domain can be seen in Fig. 28(a), together with an actual simulation in Fig. 28(b).

The desired multilayer structure is built and meshed and the modes supported by the structure are identified by Modal Analysis. A specific mode can be selected and launched on a flat metal-air interface at the left boundary of the model. The SPP wave then reaches a sinusoidal profile, where it is partially reflected and partially couples to the grating Bloch-mode. Once the SPP Bloch mode is correctly excited, it propagates along the grating with its own complex propagation constant, being its energy partially dissipated into the metal and partially irradiated, since the grating provides coupling with free radiation. Leakage radiation is clearly visible in Fig. 28(b), as plane waves in the upper and lower half-spaces, then absorbed by PML at the boundaries. Radiative losses in each half-space are measured as fluxes through a certain set surface, represented by the

red line in Fig. 28(a), while intrinsic losses are directly calculated as dissipation into the metal layers; eventually, the relative weight of the various loss channels can be extracted. The reason why the red line is not closer to the surface is that this produces artefacts in the outcome, probably due to near-field effects.

This model provides valuable information, but it requires careful design of the boundaries of the simulation domain for each specific case. Many parameters need to be carefully controlled, in order to correctly gather the leakage radiation avoiding back-reflections, that would cause overestimation, or leakage from the integration domain, resulting in underestimation. In particular, PMLs provide absorption without reflection at the upper and lower boundaries, while lateral boundaries have to be dealt with by positioning perfect mirrors that reflect the radiation towards the integration surface. A different setup is required, depending on the direction of leakage radiations, that may be emitted onwards or backwards by the propagating SPP.

Moreover, the left side of the simulation domain cannot be closed, since a slit is needed to allow the mode to be launched into the system, and it has to be large enough to avoid undesired interactions of the SPP field with its borders. Finally, a sufficiently long waveguide has to be designed in order to almost completely dissipate the SPP and ensure a correct calculation of the losses.

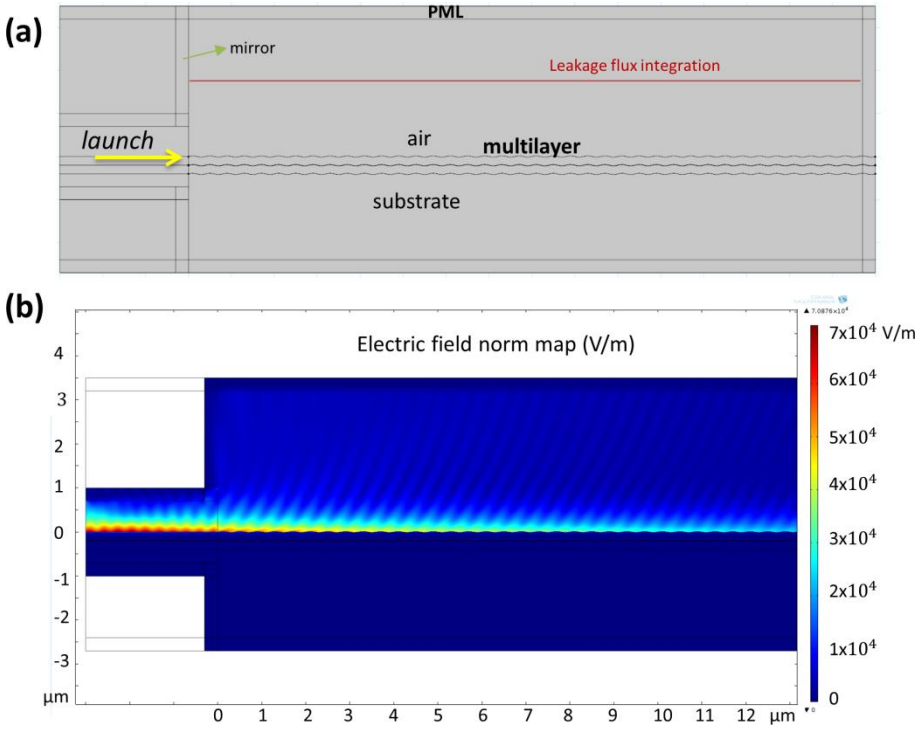

Fig. 28: (a) The simulation domain scheme with the multilayer structure and the appropriate boundaries. (b) Map of the electric field norm produced by a simulation of an air/gold single-interface SPP propagating on a grating with a 400 nm period and 30 nm amplitude, with a frequency corresponding to a free-radiation wavelength of 650 nm.

4. Experimental

In this Section, experimental procedures and instruments are introduced.

The first Chapter is devoted to materials; in particular the choice of suitable metals to support SPPs and the special materials exploited for specific fabrication steps and for sensing. The synthesis of some polymeric materials is briefly described.

In the second Chapter, nanofabrication techniques are addressed. This includes thin-film and monolayer deposition techniques, Laser Interference Lithography for the fabrication of periodically patterned surfaces and Nano-Imprint Lithography for a quick, high throughput, replication of the structures.

Finally, in the last two Chapters characterization techniques are described, related both to the morphological characterization of the samples, by Scanning Electron Microscopy and Atomic Force Microscopy, and to the optical characterization. This last task is performed with a Spectroscopic Ellipsometer, an instrument capable of many different kind of measurements, included the reconstruction of the refractive index profile of a multilayer structure.

4.1. Materials

a. Metals

The SPP dispersion relation only has a solution if one of the media has a negative real part of the permittivity. This condition occurs in a plasma for electromagnetic waves of frequency higher than the plasma frequency, a characteristic quantity defined as $\omega_P = \sqrt{N_e f_e}$ and related to the proper frequency of oscillation of the free electrons [7; 50]. This is also valid for metals or doped semiconductors since, according to the Drude-Lorentz model, their optical properties depend on the conduction electrons, that can be treated as a free electron gas [45; 46].

The choice of the metal is crucial, because it strongly affects both the real and the imaginary parts of K_{spp}: high dissipation implies a shorter propagation, a larger FWHM and eventually a lower FOM. Fig. 29 shows the propagation length calculated through the theoretical formula reported in Paragraph 1.1[b] for various interfaces. Gold is much more dissipative than silver, but silver presents poor chemical stability; in fact it quickly oxidates if exposed to air.

A good compromise is to fabricate a bimetallic structure, where silver guarantees a narrow resonance while a gold layer protects silver from oxidation [132-134]. Sometimes an adhesion layer is introduced between the resist and the gold or silver layer, typically a few nanometers of chromium [108]. The main role of the adhesion layer is to avoid detachment of the metals when the structure is exposed to liquids. The main drawback is that, since Cr is strongly dissipative, the possibility to excite the SPP with a light beam incident through the substrate is prevented.

It is important to note that the optical constants of films can considerably vary with the preparation conditions and techniques; moreover, different characterization techniques may provide different results [48]. All the materials used for the present work have been characterized by Spectroscopic Ellipsometry (see Paragraph 4.4[b]).

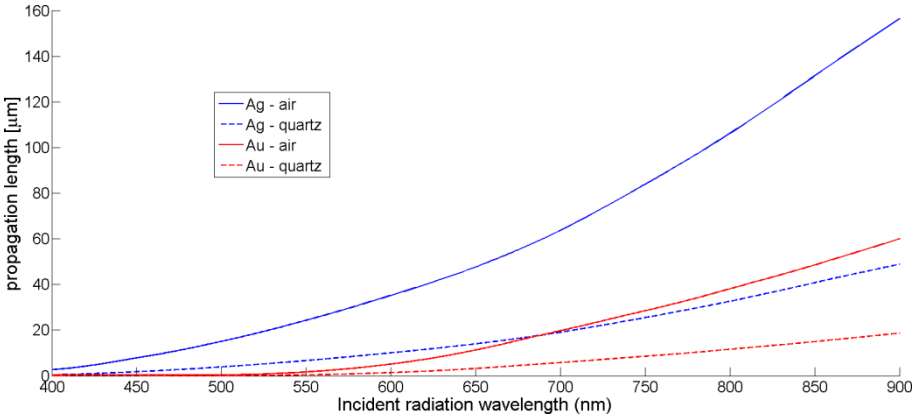

Fig. 29: Theoretical propagation length for SPP modes propagating on silver/air, silver/quartz, gold/air and gold/quartz interfaces, as a function of the corresponding free radiation wavelength ($\lambda = \frac{2\pi c}{\omega}$). The dispersion relation for single-interface SPPs on a flat surface has been used, thus radiative losses are not kept into account. The optical constants of the actual materials used in our laboratory have been measured.

b. Functional materials for fabrication

Different kinds of functional materials are needed for fabrication and applications.

As far as fabrication steps are concerned, a photoresist is needed to perform Laser Interferential Lithography, described in Paragraph 4.2[b], while an appropriate patternable material has to be employed for Nano-Imprinting Lithography (see Paragraph 4.2[c]).
A photoresist is a dielectric material that changes its solubility to a particular solvent (the developer) after exposure to radiation of specific energy, usually UV or X radiation [135]. There are two types of resist materials: the "positive tone resist" becomes more soluble when exposed to radiation, while the "negative tone" becomes less soluble. The commercial S1805 positive photoresist (Microposit, Shipley) has been used to fabricate samples for the present work.

A polydimethylsiloxane mold (PDMS) is typically used to produce negative replica of a master sample. PDMS preparation was done using the Sylgard 184 Silicone Elastomer Kit (Dow Corning), which comes in two parts: a prepolymer and a curing agent. A mixture of the two components was prepared in 1 to 10, curing agent to prepolymer, weight ratio and outgassed inside a desiccator connected to a vacuum pump for about 1 hour. Polymerization can be thermally induced.
Using the negative replica, the pattern can be transferred through Nano-Imprinting to films of different kinds of suitable materials, which will support the final structure.

Two different kind of materials were used to this aim. A thiolene resin film (NOA 61) was employed to support decoupled thin films, that effectively support single-interface surface plasmons on the interface with the environment [136]. NOA is a UV-curable polymer, meaning that it hardens by cross-linking of the polymer chains under UV exposition.

A more versatile material was developed and exploited for many applications, namely a functional and porous sol-gel film of phenyl-bridged polysilsesquioxane (ph-PSQ) [137]. Ph-PSQ is an organic-inorganic hybrid sol-gel material synthesized via a sol-gel process using the 1,4-bis(triethoxysilyl)benzene monomer (96% purity, Sigma-Aldrich) at room temperature [138].

Its most interesting characteristic is the possibility to be used both as a patternable layer for the sinusoidal nanostructure fabrication, for which it works as a thermoset resist (meaning that the curing process is triggered by heat), and as a sensitive layer, due to the possibility to incorporate active species into the hybrid network [139].

c. Functional materials for sensing

The sensitive layer is a crucial component of the sensing device, the functional film optimized to capture a specific analyte (see Section 2). In the present work, different kinds of sensitive materials, aimed to detect different analytes, have been prepared and tested; in particular, ph-PSQ have been exploited for xylene detection after suitable functionalization.

A solution of 1,4-bis(triethoxysilyl)benzene, ethanol (EtOH) and bi-distilled water was mixed in monomer/H2O=1/6 molar ratio, using hydrochloric acid (HCl) 1M as catalyst. The Si-C bonds linking two ethoxysilanes to the bridging benzene ring are hydrolytically stable. As hydrolysis and condensation progress, a three dimensional SiO_x network, incorporating benzene rings as network formers, grows and the solution becomes more viscous.

These rings constitute the recognition elements for the analyte, and the porosity of the matrix provides an high specific surface area for the interaction.

Fig. 30 reports the measured refractive index of a ph-PSQ film in the visible and near-infrared range. This material offers a combination of sensitivity, transparency and patternability, making it a valuable resource for many applications.

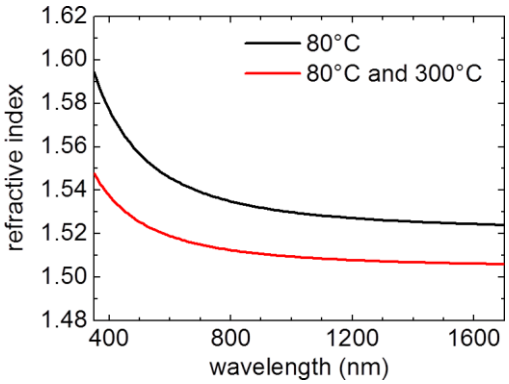

Fig. 30: Refractive index profiles of a 200 nm thick ph-PSQ layer, after a thermal treatment at 80°C for 30 min, and with an additional annealing step at 300°C for 30 min. Data were obtained by Spectroscopic Ellipsometry (see Chapter 4.4[b]).

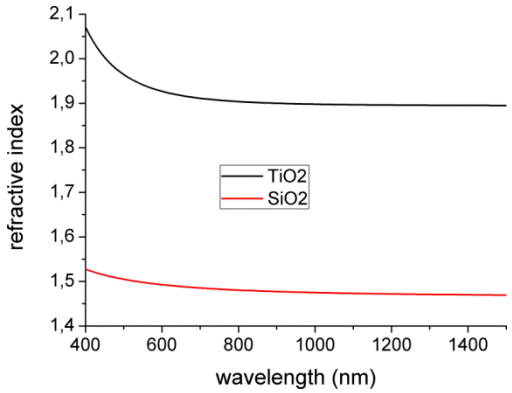

Fig. 31: Plot of the refractive index of the TiO_2 and SiO_2 sols, measured by Spectroscopic Ellipsometry.

Two kinds of sensitive layer have been produced and tested against hydrogen and Volatile Organic Compounds (see Chapter 6.2): a SiO_2 and a TiO_2 sol. The silica sol was prepared starting from tetraethyl orthosilicate ($Si(OC_2H_5)_4$, TEOS), ethanol, trimethoxy phenylsilane ($C_6H_5CH_2CH_2Si(OCH_3)_3$, PTMS), water and hydrochloric acid [140], with molar ratios: TEOS/PTMS=1, H_2O/(TEOS+PTMS))=4.5, EtOH/(TEOS+PTMS)=4, HCl/(TEOS+PTMS)=0.05. After 2 hours of reaction, a solution of Gold(III) chloride hydrate ($HAuCl_4$) in ethanol, 8%-molar with respect to the SiO_2, was added and the sol was further stirred for 1 hour.

TiO_2 nanoparticles were synthesized by adding 10.5 mmol of Titanium Tetraisopropoxide ($Ti(OPri)_4$) into a previously prepared solution containing water, hydrochloric acid and methanol [141] with molar ratios H_2O/TiOPr=12.25, HCl/ TiOPr=1.72. The solution was stirred for 60 minutes at room temperature and then heated in an oil bath at 70 °C and kept at this temperature for four hours under reflux. Particles were then precipitated and dispersed in methanol obtaining a clear TiO_2 anatase sol.

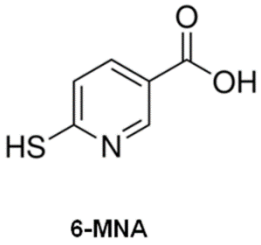

Fig. 32: Chemical formula of the 6-mercaptonicotinic acid (6-MNA) molecule, with its thiol group (HS).

Finally, 6-mercaptonicotinic acid (6-MNA), commercially available (Sigma-Aldrich), was exploited as sensitive layer for TNT traces detection. The formula of this organic molecule is represented in Fig. 32, showing the presence of a thiol group, H-S. Thanks to the thiol group, 6-MNA is capable of self-assemble into a monolayer over a gold surface (see Chapter 4.2[a]), and it is known to provide high sensitivity and specificity towards TNT detection [142].

4.2. Fabrication

Sinusoidal gratings were obtained by soft Nano-Imprint Lithography (NIL), using elastomeric stamps replicating sinusoidal masters. A set of masters were fabricated on silicon wafers by Laser Interferential Lithography (LIL) in Lloyd's mirror configuration [143] using the S1805 photoresist. Negative replicas were fabricated by using a polydimethylsiloxane(PDMS) mold, and the pattern was transferred to a ph-PSQ or a NOA film.

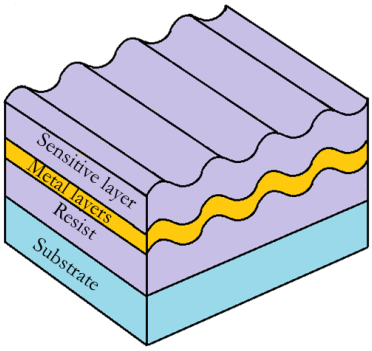

Fig. 33: Sketch of the final multilayer structure.

Metal layers were evaporated over the patterned resist with the following receipts: 5 nm of chromium and 40 nm of gold over the NOA structures, while 37 nm of silver and 7 nm of gold over ph-PSQ gratings. Finally, the desired sensitive layer was deposited over the metals. The final structures appear as in Fig. 33.

a. Thin film deposition techniques

The fabrication of plasmonic crystals requires the deposition of thin films both of metals (from few nanometers to tens) and dielectrics (few hundreds of nm), and also of molecular monolayers.

Electron-gun evaporation is a suitable technique to deposit thin metal films [48]. A source is forced to sublimate by electron bombardment and the vapor is transported to a substrate where it condense to a solid film. The process is performed in high vacuum to avoid contaminations of the film. The silver, gold and chromium layers for our structures were deposited by e-gun evaporation, with nm-level control of the film thickness [144].

All the other layers (photoresist, patternable materials and thick sensitive layers), except for the 6-MNA monolayers, were deposited by spin coating.
An excess amount of a resist solution is placed on the substrate, which is then rotated at high speed [145]. In this way the fluid is spread until the desired thickness is achieved, controlled by the initial solution concentration and the rotation speed.

Finally, the 6-MNA layer for TNT sensing is self-assembled, since this molecule spontaneously bonds to the gold surface by adsorption, being the anchoring promoted by the thiol group [146]. In fact, gold is preferred to silver for SAMs formation, as it binds thiols with a high affinity and it does not undergo any undesired reactions with them. The procedure simply consist in cleaning the grating surface (10 minutes in a 5:1:1 dd-H_2O:NH_4OH:H_2O_2 solution) and then immerse it in a 6 mM 6-MNA in ethanol solution for 24 hours.

b. Interferential Lithography

Highly regular large area gratings were fabricated by Laser Interference Lithography (LIL), since this technique is very suitable to achieve periodic patterns [143].
A photoresist film, the Microposit S1805, was applied to a flat substrate by spin coating and then exposed to an appropriate pattern of UV radiation. The fundamental concept of LIL is to obtain periodicity by interference between two LASER wavefronts.
A simple configuration to achieve this is Lloyd's-Mirror Interferometer, represented in Fig. 34, which exploit as the two interfering beams a direct beam and a reflected one [147].

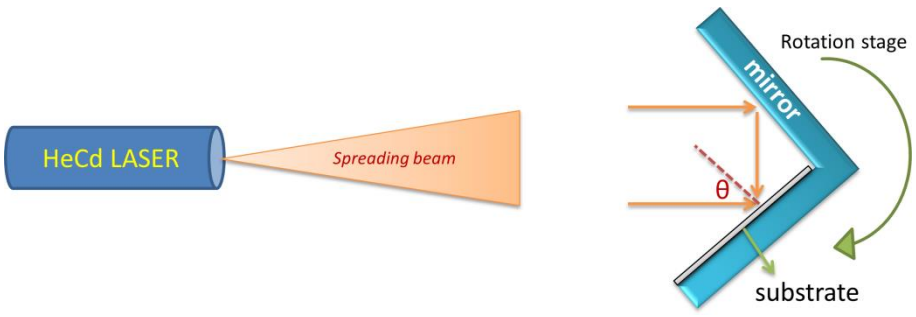

Fig. 34: Schematic representation of Lloyd's configuration for Interferential Lithography.

Pictures of the LIL setup in National Laboratory IOM-CNR at Basovizza (Trieste) can be seen in Fig. 35. It is based on Lloyd's mirror configuration and employs a continuous-wave 50mW Helium Cadmium (HeCd) LASER emitting a TEM_{00} single mode at 325 nm as light source, with a 30 cm coherence length [144].
The beam is spatially filtered to remove noise and, after a 2 m long free-space propagation, it illuminates both the sample and a mirror perpendicular to it. Thus, interference between the direct light and its mirror image forms a standing wave pattern on the photosensitive substrate. The setup need to be optimized for a specific value of the grating period, that is controlled by the θ angle according to:

$$\Lambda = \frac{\lambda_{laser}}{2 \sin \theta}$$

After the exposure, a developer solution removes the more soluble areas and the result is a modulated surface. The desired grating periodicity is obtained by adjusting the incident angle, while the grating amplitude depends on the light intensity: the higher the intensity, the higher the amplitude. Light intensity is controlled through the distance of the mirror from the beam source.

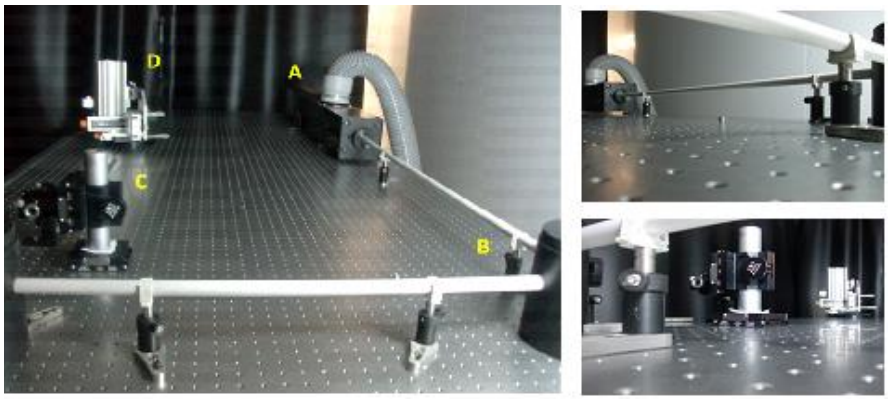

Fig. 35: Pictures of the LIL setup in use at IOM-CNR, with tagged optical elements. A – LASER source; B – mirrors; C - spatial filter; D – interferometer.

c. Nano-Imprinting

Soft lithographic techniques provide a low-cost and high throughput way to fabricate many replicas of a given master structure, with features from 30 nm to 100 μm [148; 149]. The fabrication process consists in the realization of negative replica made of polydimethylsiloxane (PDMS) of the nanostructured masters, in our case the gratings produced by LIL, and in the pattern transfer by soft Nano-Imprint Lithography (NIL) on another suitable material, like ph-PSQ or NOA.

Two different receipts were used.
Decoupled thin films for single-interface SPP propagation were based on NOA, that works as a UV-curable polymer [136]. The PDMS mold was fabricated curing the PDMS layer dropped onto the resist grating, provided by LIL, at 60°C for 4 hours. The nano-pattern was then imprinted onto a NOA film supported onto a microscope glass slide, illuminating the PDMS mold with Ultra-Violet (UV) light (λ=365 nm) for 30 s, using a standard metal halide 50 mW/cm2 lamp (DYMAX UV Light flood lamp curing system). A 12 hour thermal treatment at 50°C was then performed in order to increase the resin adhesion onto the glass substrate. A 5 nm chromium adhesion layer and a 40 nm gold film were evaporated to obtain the final metallic grating. This kind of structures have been applied to TNT sensing (see Chapter 6.1).

Thin films for symmetric structures were fabricated with ph-PSQ, that works as a thermoset resist for the NIL. The procedure consists on pouring the prepolymer and curing agent mixture for PDMS on the master, thermally curing it at 70° C in a convection oven for about 1 hour to promote polymerization, and successively peeling the replica off the master [150].
In order to transfer the pattern on ph-PSQ, the sol-gel films were deposited on fused silica slides, using a solution of 30 g/l SiO2 concentration, by spin coating at 5000 rpm for 60 s, resulting in a 200 nm thick layer. PDMS replica were gently pressed with a finger on fresh-deposited ph-PSQ films, and the assembly was cured with a 30 min thermal treatment at 80 °C in an oven, before delicately peeling the mould off the sample.

Some examples of the good results achievable by means of this relatively simple technique are shown in the figures of the next Chapter. Appendix 8.2[d] addresses a possible bad result to be avoided, related to an incomplete filling of the mold by the fluid resist.

4.3. Morphological Characterization

Two main instruments were used in order to provide morphological characterization of the plasmonic structures.

The Scanning Electron Microscope (SEM) can image the samples surface in a wide range of scales, allowing to evaluate the pattern uniformity over large area but also estimate the grating period and check the possible roughness. Examples of a wide-area image and a detailed one are reported in Fig. 36.

The Atomic Force Microscope provides a reconstruction of the grating profile, allowing to measure both the period and the amplitude of the grating, and the possible presence of higher harmonics. Examples of an AFM surface reconstruction and profile are shown in Fig. 37(a) and (b).

The two methods will be briefly described in the following paragraphs.

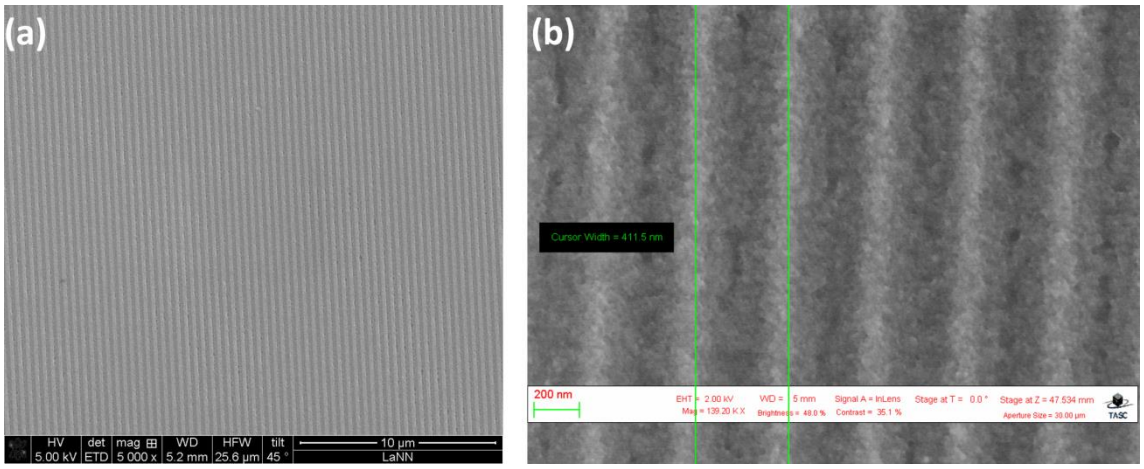

Fig. 36: Two examples of SEM images of plasmonic gratings fabricated by NIL: (a) a large area scan shows the remarkable homogeneity of the structure over a quite large scale; (b) a zoomed image allows to estimate the grating period using a measuring tool. (The images are relative to different samples and have an illustrative purpose).

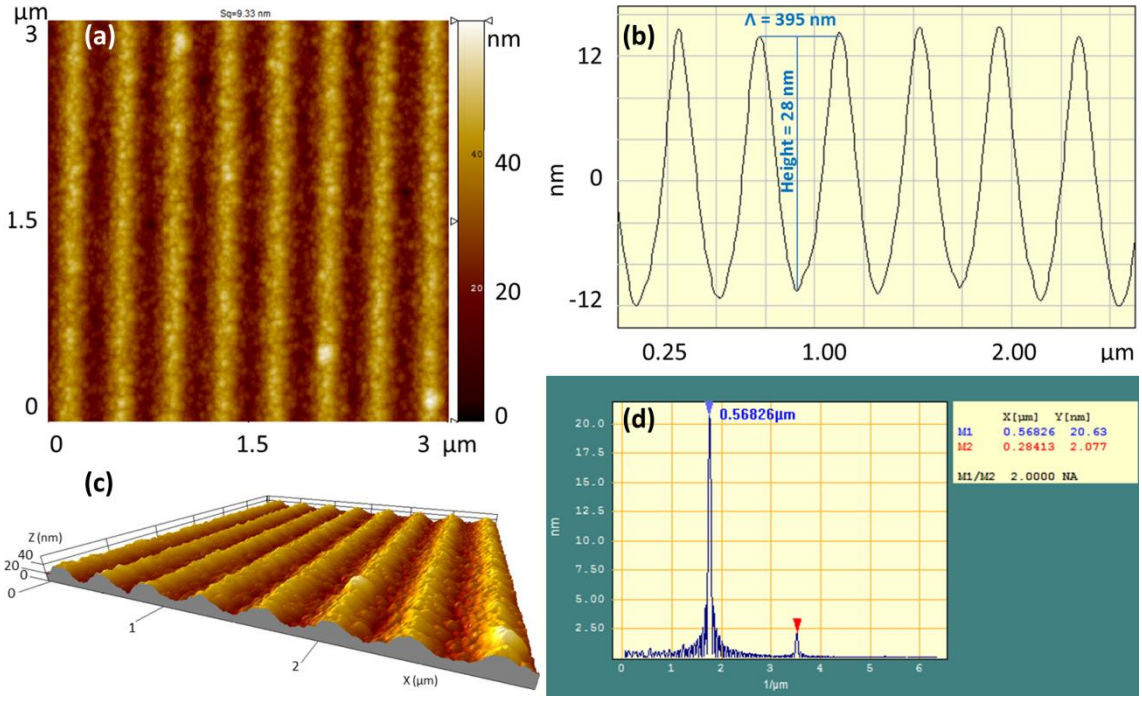

Fig. 37: Four kinds of graphs provided by AFM analysis of samples fabricated as described in the previous Chapter: (a) plane reconstruction of the patterned surface; (b) graph of the sinusoidal grating profile with estimation of its period and amplitude; (c) three-dimensional reconstruction of the grating profile; (d) Fourier coefficients of the Fourier transformed pattern, showing its almost pure sinusoidal nature, since superior order harmonics are suppressed. (The images are relative to different samples and have an illustrative purpose).

a. Scanning Electron Microscopy

The Scanning Electron Microscope scans the sample with a high energy electron beam and produces high resolution 2D images [151].

Electrons are produced by thermoionic emission from a metallic cathode and then accelerated towards an anode, with an energy ranging from hundreds of eV to 40 keV, while electromagnetic lenses focus the beam to a diameter of the order of nm. In order to avoid scattering of the beam by air molecules, the sample chamber and the beam itself are kept in high vacuum.
The interaction volume of the electrons into the material is teardrop-shaped and extends from about 100 nm to 5 µm into the sample, depending on electron beam energy, material atomic number and sample density. Into this volumes the primary beams electrons can undergo scattering and absorption processes.
Emitted signals are:
- high energy electron reflection by elastic scattering
- secondary electrons emission by inelastic scattering processes
- electromagnetic radiation emission

We typically set a beam current of 98 pA and a beam voltage of 5 keV for the surface scan and used the low energy secondary electrons as the signal for the image collection.
These electrons are detected through the use of a scintillator photomultiplier device and a distribution map of the signal intensity is reconstructed.

If the beam is perpendicular to the surface a symmetrical signal is expected. Varying the incidence angle, the signal will be brighter where the secondary electrons have a minor distance to cover to get out from the sample: in this way surface deformations are highlighted.
Typical SEM resolutions are from 1 to 20 nm: small features and nanoparticles are visible. In Fig. 38 two detailed images are reported.

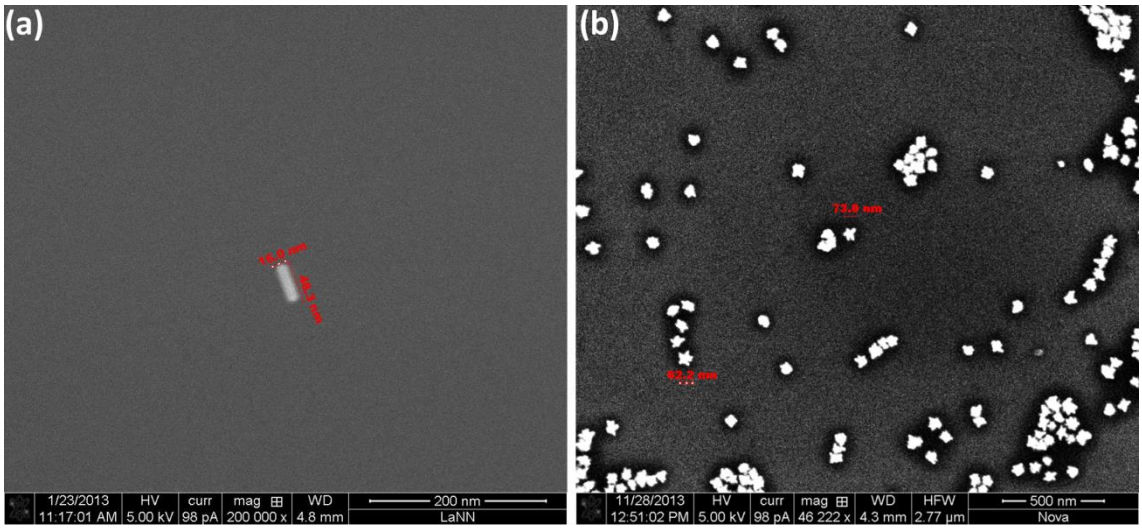

Fig. 38: Two examples of observation of very small features by SEM: (a) single gold nanorods scattered on a Si substrate; (b) gold "nanostars" nanoparticle, scattered on a Si substrate; the points are visible in some of them. Images taken on commission from M. Cittadini, who synthetized the nanoparticles [152].

A limitation of the instrument is that electrons incident on the sample need to flow away, otherwise the charge accumulates in the scanned region and tends to repel more incoming electrons. This means that a conductive surface is needed to obtain clear images. In the case of plasmonic gratings, this limits the application of this instrument to the observation of the structures after the evaporation of the metal layers and before the deposition of a thick sensitive layer.

b. Atomic Force Microscopy

The Atomic Force Microscope is a kind of microscope that perform a scan by a microscopic probe, a tip that is moved close to the sample surface and detect attractive or repulsive forces of the order of the nanoNewton [153].

The AFM tip, of nanometric dimension, is supported by an oscillating cantilever. Working in non-contact mode, the tip is brought close to the surface and the cantilever is put in oscillation using a piezoelectric. Weak Van der Waals forces at sample-tip interface cause a shift of the cantilever oscillation frequency, that is detected by optical means. In fact, a LASER beam illuminates the cantilever and the reflected beam is detected by a quad photodetector, consisting in two pairs of photodiodes: differential signals from the photodetector reveals variations in the oscillation frequency, traducing in an overall resolution of the instrument down to 0.1 nm. Moreover, a 3D reconstruction of the sample surface is possible, like the one reported in Fig. 37(c).

The peak-to-valley height of the grating profile can be estimated from the Abbot curve as the height variation between the values corresponding to the 3% and 97% of the bearing area. The

grating period is calculated from the position of the peak in the Fourier spectrum of the grating profile obtained averaging over the horizontal scanned lines in an AFM image; see Fig. 37(d).

4.4. Optical Characterization

All the optical measurements have been performed with a J.A. Woollam Co. Variable Angle Spectroscopic Ellipsometer (VASE), like the one in Fig. 39. This versatile instrument can provides many different working configurations and techniques [154]. The relevant ones for the present work are reflectance measurements, spectroscopic ellipsometry, and scatterometry.

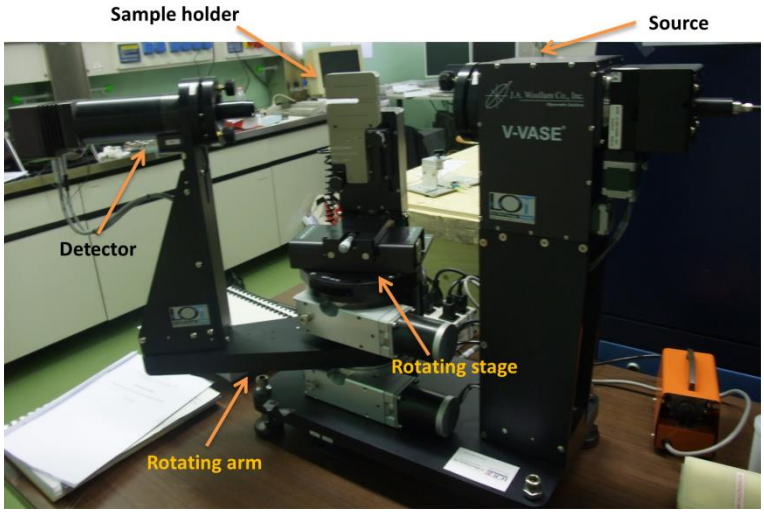

Fig. 39: A Variable Angle Spectroscopic Ellipsometer, with the main components tagged.

The light source is composed by a xenon lamp, a monochromator and a polarizer, allowing to obtain approximately monochromatic beams with arbitrary polarization in the visible and near-infrared range.

The sample-holder and the arm supporting the detector can be separately moved to perform different kind of scans, with angular and wavelength spectroscopic resolution of 0.05°÷0.5° and 0.2÷0.5 nm respectively. A minimum angular distance of 30° between the source and the detector is required, otherwise they would collide. The spot size is normally of some mm^2 but it can be reduced mounting focusing probes.
A manual goniometer can be mounted on the sample holder in order to control azimuthal rotation with an accuracy estimated in about 1°.

a. Reflectance measurements

This simple configuration is the main way to investigate the optical response of plasmonic gratings. The source and the detector are set in a $\theta/2\theta$ configuration, i.e. the detector always receives the reflected beam, or, more precisely since the sample surface is periodically patterned, the zero-order diffracted beam. Since the detector need to be at least 30° away from the source to avoid collision, the minimum incidence angle is 15°.

Wavelength, polarization and incidence angle of the incident light can be set, and an angular or spectral scan can be performed: in both cases, the excitation of a surface mode reveals itself as a dip in the reflectance spectrum. A goniometer can be mounted on the sample-holder, which allows to set the azimuthal angle, realizing the configuration known as conical mounting.

In order to perform gas sensing tests, the sample has to be placed into a sealed chamber in which a gas carrying the analyte flows. For most tests of this kind reported in the present work, the Woollam HTC-100 heat stage and chamber was adopted, shown in Fig. 40. In this setup, the light beam can only enter through the portholes, visible at the sides of the chamber, thus the only available incidence angle is fixed to 70°.

Fig. 40: Picture of a Woollam HTC-100 chamber, mounted on its stage.

b. Spectroscopic Ellipsometry

Spectroscopic Ellipsometry is a well-established and widely used method to determine the dielectric function of a material [48; 155]. Linearly polarized light, that is neither s- nor p-polarized, impinging at oblique angles becomes elliptically polarized after the reflection. From the orientation and ratio of the axes of the ellipse, the ratio of the reflectance coefficients for p- and s-polarized light can be calculated, $\mathcal{R} = \frac{r_p}{r_q}$. This operation is performed for a certain range of wavelenghts; then from $\mathcal{R}$, that is in general complex, and the incidence angle, the real and imaginary parts of the refractive index are derived.

When Ellipsometry is performed, effects due to diffraction by the grating are undesirable: for this reason, flat layers of the material to be characterized have to be prepared. Through fitting procedures, both the optical properties and the film thickness may be obtained.

In particular, normal dispersion regimes, for materials almost transparent over the measured wavelength range, can be described by the Cauchy dispersion function, while Urbach absorption tail far away from resonances is treated through an exponential model [46]. This approach fails for strongly absorbing materials; anomalous dispersion and resonant absorption are described implementing the Lorentz Oscillator model [45].

c. Scatterometry

Scatterometry, or Diffrattometry, basically consists in looking for the first-order diffraction peak, and it
allows to estimate the grating period by means of an optical measurement.
Due to the Bragg diffraction by the grating, the diffracted beam of n-th order comes out from the sample at an angle θ_n satisfying the following relation [21]:

$$\frac{2\pi}{\lambda}\sin\theta_n = \frac{2\pi}{\lambda}\sin\theta_i + n\frac{2\pi}{\Lambda}$$

The n = ± 1 peak can be searched by fixing the incidence angle and light wavelength and moving the detector in an angular scan. Once located the angular position of a first-order peak, θ±1, the grating period can be extracted according to:

$$\Lambda = \frac{\pm\lambda}{\sin\theta_{\pm1} - \sin\theta_i}$$

The dominant source of uncertainty comes from the determination of θ_1, while uncertainties on the values of λ and θ_i can be neglected. The error on Λ, given by the propagation formula, typically comes to be below 5 nm, making it a good estimation of the grating period:

$$\sigma_\Lambda = \left(\frac{\partial\Lambda}{\partial\theta_1}\right)^2 \sigma_{\theta_1}^2 = \frac{\lambda}{(\sin\theta_1 - \sin\theta_i)^2}|\cos\theta_1|\sigma_{\theta_1}$$

5. Advancements in Plasmonics

This Section represents the core of the present work. An extensive investigation on the propagation of Surface Plasmon Polaritons on the anisotropic surface defined by the 1D grating is performed, taking into consideration both the real part of the momentum, related to the coupling conditions and the propagation direction, and the imaginary part, related to its linewidth and losses.

In the first Chapter, the coupling scheme introduced in Chapter 1.3[b] is generalized to the other available experimental configurations; general geometrical and analytical treatments are provided to be able to predict the optical response of a generic plasmonic grating. This includes maps of the angular position of an SPR resonance, from the point of view of the coupling configuration.
Moreover, the possible propagation directions of the SPP with respect to the grating grooves, achievable through the grating coupling, are found.

The second Chapter is devoted to the study of the imaginary part of the SPP momentum, in relation to the SPP losses and the width of the SPR dip. In particular, effects related to the incident light polarization, the grating amplitude and the propagation direction are investigated, with a physical interpretation of the results.

Exploiting the predictive power of the developed tools, we were able to study the behaviour of the coupled modes in conical mounting. In particular, the second resonance dip of the LR mode and the SR mode have been observed for the first time. The observations are reported together with a study of their losses.

Finally, the problem of theoretically calculate the sensitivity of an SPR sensor is addressed. Different contribution factors are evaluated, both under angular and spectral interrogation, with particular attention to the effect of azimuthal rotation. The Section ends with some considerations on the Figure of Merit.

5.1. Two-dimensional SPP coupling and propagation

In this Chapter a general treatment of the coupling conditions will be introduced. The matching between the real part of the SPP momentum and the incident radiation will be unravelled by geometrical and analytical means. A handy way to generate predictive maps of the achievable resonances on a given structure is provided. This treatment have been recently published in the Plasmonics journal [156].

The propagation direction of a grating-excited SPP mode with respect to the grating grooves is also calculated and general remarks are made.

a. Generalized coupling scheme

The geometrical representation of the vector coupling conditions described in Chapter 1.3[b] does not include every available configuration, since it is limited to the case in which the Bragg grating vector, $G = {}^{2\pi}/_{\Lambda}$, is greater in modulus than the SPP momentum, β.

As seen before, in that case the resonance conditions are expressed by:

$$\begin{cases} \vec{\beta} \cdot \hat{x} = G\cos\varphi - k_T \\ \vec{\beta} \cdot \hat{y} = G \sin\varphi \end{cases}$$

The geometrical representation looks as in Fig. 41 (that is the same as Fig. 11). Recalling the results of Chapter 1.3[b], it can be seen that, for a range of φ and λ values, two solutions are allowed, corresponding to the excitation of two SPPs of momentum equal in modulus but different in direction. Correspondingly, two dips for each single wavelength are observed in the experimental reflectance spectra. For increasing wavelength a critical condition λ_c is reached, when the transferred momentum vector is tangential to the β circle and the two solutions become degenerate. For $\lambda > \lambda_c$ the coupling becomes impossible. The same happens when keeping the wavelength fixed and increasing φ; in this case the maximum azimuth that allows a plasmonic resonance to exist is given by the formula: $\varphi^* = \sin^{-1}\left(\frac{\beta}{G}\right)$.

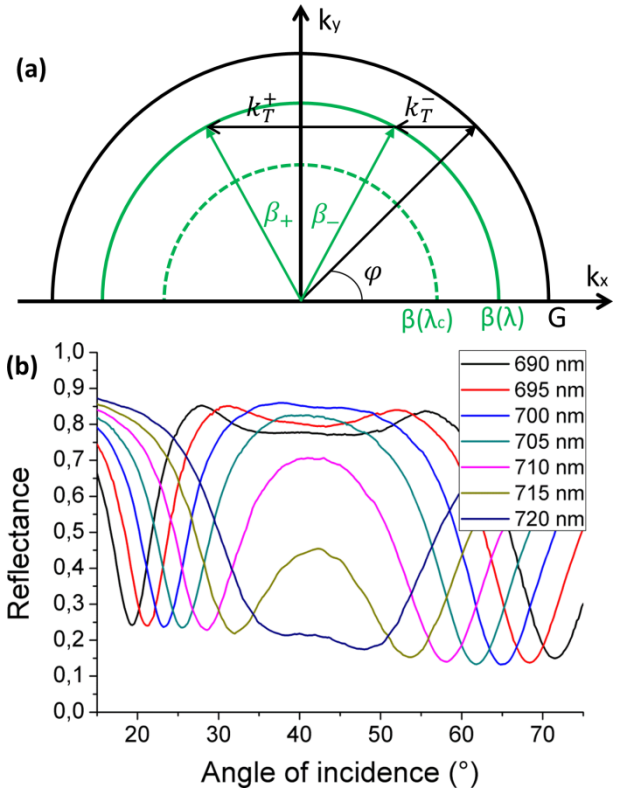

Fig. 41: In order to recall the results of Chapter 1.3.b, Fig. 11 is reproduced here. (a) Vector coupling scheme in the G > β regime for a generic azimuth φ. It shows the double resonance for a generic wavelength and the degenerate case for the critical wavelength λ_C, corresponding to the maximum wavelength that allows the excitation of the SPP. (b) Typical high-azimuth reflectance spectra associated to the coupling scheme shown in (a).

This model will now be extended to the G < β case.

The new vector scheme is represented in Fig. 42(a) and looks quite different from the previous. The G circle is now inside the β circle and again there are two ways to satisfy the resonance conditions, which in this case are:

$$\begin{cases} \vec{\beta} \cdot \hat{x} = \mp G\cos\varphi - k_T \\ \vec{\beta} \cdot \hat{y} = \mp G \sin\varphi \end{cases}$$

Unlike the previous case, the evolutions of the spectra in response of an increase in φ or in λ are different from each other. When two resonances exist, by increasing the azimuth a "merging condition" will be reached as in the G > β case, but only at $\varphi = \frac{\pi}{2}$ for any wavelength. On the contrary, at fixed azimuth and for increasing λ values, the dips are expected to move towards smaller incidence angles. This behaviour can be experimentally verified on long-period gratings, for example with Λ≈1 μm, as the ones used to collect the spectra reported in Fig. 42(b).

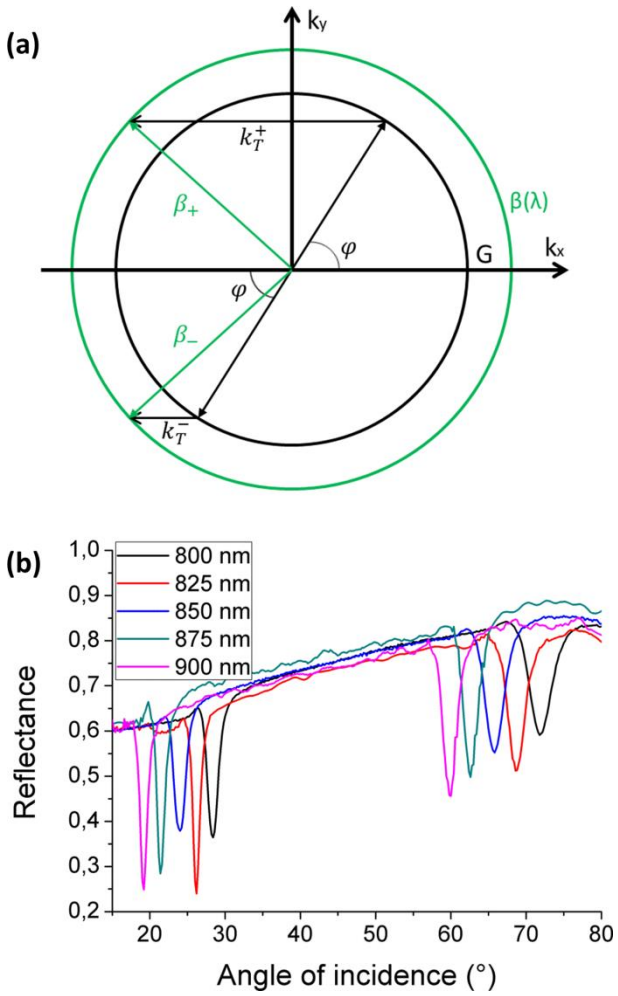

Fig. 42: Analogue to Fig. 41 for the G < β regime. (a) Sketch of the coupling scheme, and (b) corresponding reflectance spectra collected at high azimuthal angle for grating period Λ=1 μm and azimuth φ=70°.

b. General treatment of the resonance conditions

It is useful to classify all the possible conditions that allows one, two or no SPP to be resonantly excited.

In order to lighten the notation, we introduce the adimensional R and N parameters, where $R \equiv \frac{\lambda}{\Lambda}$ and $N \equiv \frac{\beta}{k_i}$. Recalling the conventions of Chapter 1.3, $k_i = \frac{2\pi}{\lambda}$ is the momentum of the incident light and N can be intended as an effective refractive index for the SPP. In the case of single-interface SPP, for instance, N is known to be $\sqrt{\frac{\varepsilon_{mr}\varepsilon_d}{\varepsilon_{mr}+\varepsilon_d}}$, being ε_{mr} and ε_d the relative permittivity of the metal and dielectric respectively.

The G > β case corresponds to the R>N condition. The expression that gives the angular positions of the two resonances, which is derived in Appendix 8.2(a), can then be rewritten as:

$$\sin\theta_{\pm} = R\cos\varphi \pm \sqrt{N^2 - R^2(\sin\varphi)^2}$$

For a certain fixed wavelength λ, the values of N and R are also determined. The requirement of reality for the square-root term, together with the $\sin\theta_{\pm} \in [0,1]$ condition, set the whole conditions for the existence of one, two or no solutions, as reported in the first three ranges of Table 1. In particular:

- From the requirement of reality of the square-root term, the value of the azimuth φ is limited by the condition: $\sin\varphi \leq \frac{N}{R}$, corresponding to: $\cos\varphi \geq \sqrt{1-\frac{N^2}{R^2}}$
- The $\sin\theta_{-} \leq 1$ condition is satisfied either for $\cos\varphi \leq \frac{1}{R}$ or for $\cos\varphi \geq \text{Max}\left(\frac{1}{R}, \frac{1+R^2-N^2}{2R}\right)$.
- The condition for the second resonance, $\sin\theta_{+} \leq 1$, can be satisfied only if $\cos\varphi \leq \frac{1}{R}$ and gives the further condition $\cos\varphi \leq \frac{1+R^2-N^2}{2R}$.

Putting together the conditions, and defining $\varphi^{+} \equiv \cos^{-1}\left(\frac{1+R^2-N^2}{2R}\right)$ and $\varphi^{*} \equiv \sin^{-1}\frac{N}{R}$, the first resonance can be excited for every φ that satisfies: $\cos^{-1}\frac{1}{R} \leq \varphi \leq \varphi^{*}$ or

$0 \leq \varphi \leq \text{Min}\left\{\cos^{-1}\frac{1}{R}, \varphi^{+}, \varphi^{*}\right\}$

And the second resonance for: $\text{Max}\left\{\cos^{-1}\frac{1}{R}, \varphi^{+}\right\} \leq \varphi \leq \varphi^{*}$

At this point the number of allowed solutions depends on the relation between, R and N:

- If $N \leq R \leq \sqrt{N^2+1}$ the hierarchy of the terms comes to be:

  $$\frac{1}{R} \geq \frac{1+R^2-N^2}{2R} \geq \sqrt{1-\frac{N^2}{R^2}}$$

  Thus the first resonance is excited for every φ between 0 and φ^{*} and the second when $\varphi^{+} \leq \varphi \leq \varphi^{*}$; this case is reported in the third line of Table 1.
- If $\sqrt{N^2+1} \leq R \leq N+1$ the hierarchy becomes

  $$\frac{1+R^2-N^2}{2R} \geq \sqrt{1-\frac{N^2}{R^2}} \geq \frac{1}{R}$$

  In this case the first resonance exists for each φ between 0 and φ^{+} while the second cannot be excited. This is the second line of the Table.
- If $N+1 \leq R$ also φ^{+} becomes negative and no solution of the resonance conditions is allowed.

In the G<β case, corresponding to R<N, the resonance conditions are given by:

$$\sin\theta_{\pm} = \sqrt{N^2 - R^2(\sin\varphi)^2} \pm R\cos\varphi$$

The main difference is that this time the square root is always real for $\varphi \in \left[0, \frac{\pi}{2}\right]$.

The request that $\sin\theta_- \leq 1$ gives $\cos\varphi \geq \frac{N^2-R^2-1}{2R}$ while $\sin\theta_+ \leq 1$ gives the same conditions as in the R>N case:

$$\cos\varphi \leq \text{Min}\left\{\frac{1}{R}, \left(\frac{1+R^2-N^2}{2R}\right)\right\} = \frac{1+R^2-N^2}{2R}$$

Again, three cases can be distinguished, as reported in the last three lines of Table 1.

- If $\sqrt{N^2-1} \leq R \leq N$ then $\frac{N^2-R^2-1}{2R} \leq 0$, implying that the first resonance is excited for $\varphi \in \left[0, \frac{\pi}{2}\right]$, while the second exists when $\varphi^+ \leq \varphi \leq \frac{\pi}{2}$.
- If instead $N-1 \leq R \leq \sqrt{N^2-1}$ it happens that $\frac{1+R^2-N^2}{2R} \leq 0$, implying that the second resonance cannot exist, while the first is allowed only in the azimuthal range between 0 and $\varphi^- \equiv \cos^{-1}\left(\frac{N^2-R^2-1}{2R}\right)$.
- If $R \leq N-1$ also φ^- becomes negative and no resonance is allowed.

Obviously, if G = β the conditions become degenerate. Since this treatment only generically involves the β value of the SPP momentum, and not its dispersion relation, it is valid for any kind of SPP mode under grating coupling.

Conditions	Dip 1	Dip 2
$R \geq N+1$	/	/
$N+1 \geq R \geq \sqrt{N^2+1}$	$[0, \varphi^+]$	/
$\sqrt{N^2+1} \geq R \geq N$	$[0, \varphi^*]$	$[\varphi^+, \varphi^*]$
$N \geq R \geq \sqrt{N^2-1}$	$\left[0, \frac{\pi}{2}\right]$	$\left[\varphi^+, \frac{\pi}{2}\right]$
$\sqrt{N^2-1} \geq R \geq N-1$	$[0, \varphi^-]$	/
$N-1 \geq R$	/	/

Table 1: Angular ranges allowing plasmonic resonance dips, for each R/N relation.

c. Existence maps

Mapping the conditions of existence of the resonances, for any azimuthal angle, provides a straightforward tool to predict the behaviour of the dips under operative conditions. This can be simply done at a fixed wavelength implementing the equations derived in the previous Paragraph and drawing a curve on the (φ, θ) plane, described by the points that fulfil the resonance conditions. Two examples are shown in Fig. 43, for two cases corresponding to the central lines of Table 1.

The lower branch of each curve is the locus of the points in which the first resonance dip is found, while the upper branch corresponds to the second dip. An angular interrogation spectrum corresponds to a vertical slice of such a map: the intersections between a vertical line at the set azimuthal angle and the curve give the angular positions of the SPP resonances.

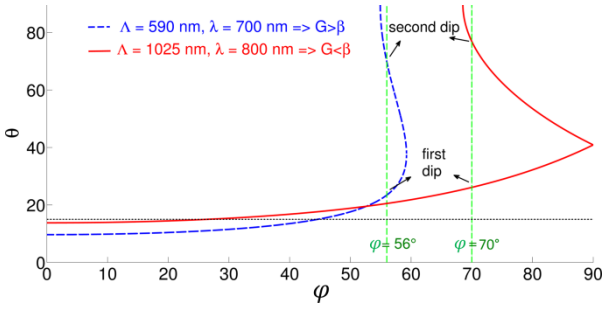

Fig. 43: Existence maps of the dip position in the (φ, θ) plane, for a plasmonic grating with 37 nm of silver and 7 nm of gold. The dashed curve that ends at a certain azimuth refers to a G > β case with incident wavelength λ = 700 nm and shows the known fact that over a certain maximum azimuth the SPP cannot be excited for any incidence angle. The intersection with the dashed line of a 56° azimuth corresponds to the spectrum at λ = 700 nm in Fig. 41(b). The solid curve is relative to a G < β case, with λ=800 nm. The intersection with the dashed line of a 70° azimuth shows the resonances of the corresponding spectrum in Fig. 42(b). The superior branch of the curves indicates the (φ, θ) values to visualize the second dip. The horizontal dotted line, set at θ = 15°, represents the lower limit of accessible angles for the ellipsometer optical bench (see Chapter 4.4).

Since the generation of the maps is not based on complicated calculations, they can be a quick way to scan different sets of parameters and predict the optical response of plasmonic gratings, provided that one also has a quick way to calculate the momentum of the expected SPP modes with little computational effort.

d. Analysis of the SPP propagation direction

Since the coupling schemes are represented in the (x,y) base, they do not allow to appreciate the propagation direction of an SPP mode with respect to the grating grooves.

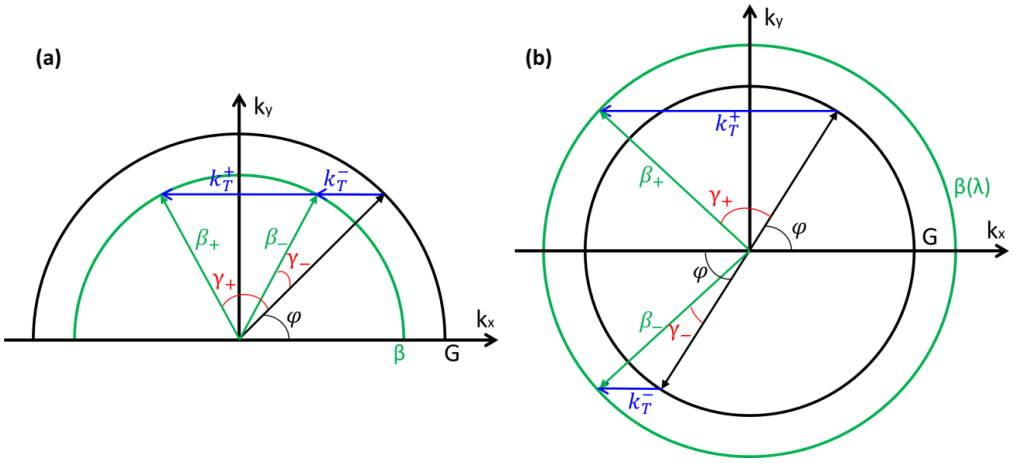

Fig. 44: Definition of γ in the four cases: (a) first and second resonances in the G>β case; (b) first and second resonances in the G<β case. Quantities related to the first and second resonances are identified with a minus and a plus sign, respectively. The γ angle defines the propagation direction on the plane, with respect to the grating Bragg vector.

The direction can be defined as in Fig. 44 as an angle between $\vec{\beta}$ and $\vec{G}$, hereafter called γ, and some general results can be given. A case-by-case analysis follows.

- G>β; first resonance

In this case the following formula for γ holds:

$$\gamma = -\varphi + \tan^{-1}\frac{\mathrm{G}\sin\varphi}{\sqrt{\beta^2 - \mathrm{G}^2\sin^2\varphi}}$$

and γ(φ) is a monotonically increasing function of φ.

Proof:

The resonance conditions, including the γ angle, are:

$$\beta\cos(\varphi+\gamma) = G\cos\varphi - k_T$$
$$\beta\sin(\varphi+\gamma) = G\sin\varphi$$

From which γ can be extracted as follows:

$$\gamma = -\varphi + \tan^{-1}\frac{\mathrm{G}\sin\varphi}{\mathrm{G}\cos\varphi - \mathrm{k_T}}$$

Considering fixed values for G and β, φ and k_T are not independent variables, since they are bound by the $\beta^2 = \left|\vec{\beta}\cdot\hat{x}\right|^2 + \left|\vec{\beta}\cdot\hat{y}\right|^2$ constraint, that, under these resonance conditions, gives:

$$k_T = G\cos\varphi \pm \sqrt{\beta^2 - \mathrm{G}^2\sin^2\varphi}$$

The right solution is the one with the minus sign, since the other is relative to the second resonance. Thus:

$$\gamma(\varphi) = -\varphi + \tan^{-1}\frac{\mathrm{G}\sin\varphi}{\sqrt{\beta^2 - \mathrm{G}^2\sin^2\varphi}}$$

By calculating its first derivative, we obtain:

$$\frac{d\gamma}{d\varphi} = -1 + \frac{G\cos\varphi}{\sqrt{\beta^2 - \mathrm{G}^2\sin^2\varphi}}$$

That is positive under the G>β condition, proving that γ(φ) is monotonically increasing.

■

As a consequence, γ reaches its maximum value under these conditions at the maximum available, φ*, derived in the previous Paragraph as the limiting condition for the reality of the square-root term. This maximum value is then $\gamma^* = -\varphi^* + \frac{\pi}{2} = \frac{\pi}{2} - \sin^{-1}\frac{\beta}{G}$, or equivalently:

$$\gamma^* = \cos^{-1}\left(\frac{\beta}{G}\right)$$

- G<β; first resonance

Here the γ angle obeys to the following formula:

$$\gamma = \varphi - \tan^{-1}\frac{\mathrm{G}\sin\varphi}{\sqrt{\beta^2 - \mathrm{G}^2\sin^2\varphi}}$$

that again is a monotonically increasing function of φ.

Proof:

Resonance conditions for this case are as follows:

$$\beta\cos(\varphi-\gamma)=G\cos\varphi+k_T$$
$$\beta\sin(\varphi-\gamma)=G\sin\varphi$$

From which γ can be extracted according to:

$$\gamma=\varphi-\tan^{-1}\frac{G\sin\varphi}{G\cos\varphi+k_T}$$

The $\beta^2=\left|\vec{\beta}\cdot\hat{x}\right|^2+\left|\vec{\beta}\cdot\hat{y}\right|^2$ constraint gives, under these conditions, only one physical solution:

$$k_T=-G\cos\varphi+\sqrt{\beta^2-G^2\sin^2\varphi}$$

And consequently:

$$\gamma=\varphi-\tan^{-1}\frac{G\sin\varphi}{\sqrt{\beta^2-G^2\sin^2\varphi}}$$

This time the derivative has the following form:

$$\frac{d\gamma}{d\varphi}=1-\frac{G\cos\varphi}{\sqrt{\beta^2-G^2\sin^2\varphi}}$$

Due to the sign inversion and the inverted relation between G and β, it is positive all the same, i.e γ(φ) is a monotonically increasing function.

■

The highest γ value achievable under these conditions is then: $\gamma_M=\gamma\left(\frac{\pi}{2}\right)=\gamma_M=\frac{\pi}{2}-\tan^{-1}\frac{G}{\sqrt{\beta^2-G^2}}$, or equivalently:

$$\gamma_M=\cot^{-1}\left(\frac{G}{\sqrt{\beta^2-G^2}}\right)$$

- Second resonances

There is no need to separate the two cases, since the resonance conditions are the same.
Unlike before, for the second resonances γ(φ) is a monotonically decreasing function of φ and it is given by:

$$\gamma=\pi-\varphi-\tan^{-1}\frac{G\sin\varphi}{\sqrt{\beta^2-G^2\sin^2\varphi}}$$

Proof:

The resonance conditions may be written as follows:

$$-\beta\cos(\pi-\varphi-\gamma)=G\cos\varphi-k_T$$
$$\beta\sin(\pi-\varphi-\gamma)=G\sin\varphi$$

From which γ is extracted as:

$$\gamma=\pi-\varphi+\tan^{-1}\frac{G\sin\varphi}{G\cos\varphi-k_T}$$

The β^2 constraint is in this case:

$$k_T = G\cos\varphi + \sqrt{\beta^2 - G^2\sin^2\varphi}$$

Thus:

$$\gamma = \pi - \varphi - \tan^{-1}\frac{G\sin\varphi}{\sqrt{\beta^2 - G^2\sin^2\varphi}}$$

Its first derivative has the following form:

$$\frac{d\gamma}{d\varphi} = -1 - \frac{G\cos\varphi}{\sqrt{\beta^2 - G^2\sin^2\varphi}}$$

And it is clearly negative, meaning that in this case γ decreases for increasing φ values.

■

These results imply that the γ^* and γ_M limiting values, previously derived as maximum angles achievable through the first coupling, represent minimum γ values achievable through the second resonance, in the G>β and G<β case respectively.

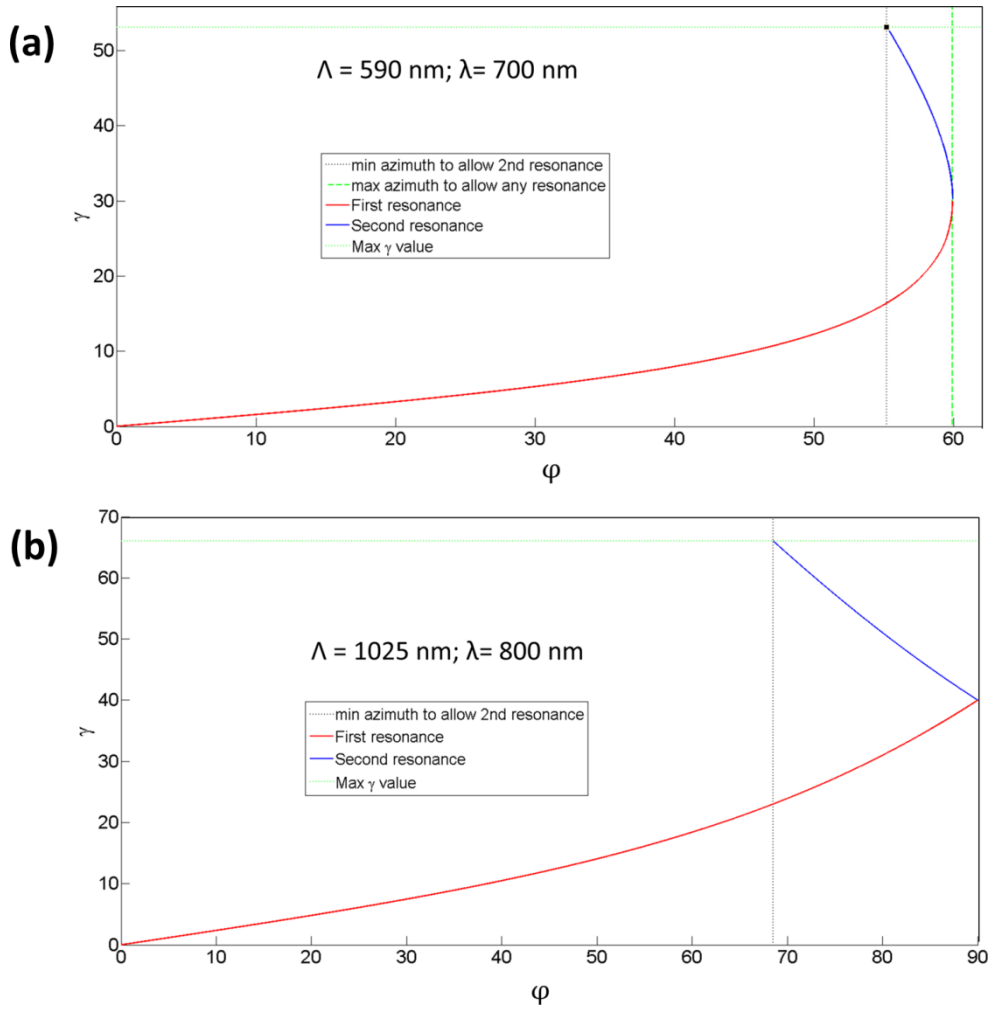

Fig. 45: γ-maps, describing the propagation direction of SPP modes as a function of φ, having G and β fixed; the modes are the same investigated in Fig. 43 and are supported by 37 nm Ag / 7 nm Au plasmonic gratings. (a) a choice of λ and Λ which implies G > β; (b) a G<β case.

However, a maximum γ achievable through the second resonance, and then generally achievable by grating coupling, exists for any G, β set and it is fixed by the minimum azimuthal angle at which the second resonance appears: φ^+.
As derived in the previous Paragraph, it is given by:

$$\varphi^+ = \cos^{-1}\frac{k_i^2 - \beta^2 + G^2}{2Gk_i}$$

These equations may be implemented to obtain maps similar to the ones produced in the previous Paragraph, but in the (φ, γ) plane. As an example, Fig. 45 shows the γ-maps corresponding to the two cases already studied in Fig. 43: one for G>β and one for G<β.

It is worthwhile to point out that φ and γ must not be confused, and in particular an SPP can never be excited along the direction perpendicular to the grating Bragg vector, i.e. at γ=90°. This is simply understood by noting that, in order to such a coupling to happen, $\vec{\beta}$, $\vec{G}$ and $\vec{k}_T$ should be the sides of a rigth triangle with $\vec{k}_T$ as the hypotenuse, implying the impossible condition that k_T should be greater than β.
From another point of view, the relation between λ and θ could be investigated for G and β fixed. By comparing the γ-maps to the (φ, θ) maps, it is clear that γ increases with θ, but θ increases faster, leaving γ at a value less than 90°.

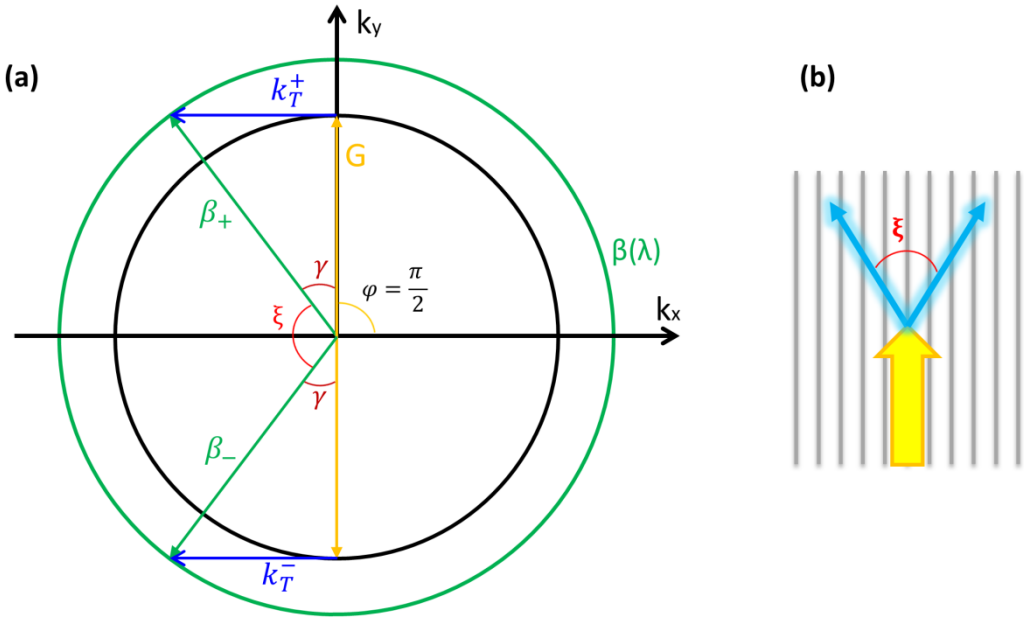

Fig. 46: The condition of simultaneous excitation of two different SPP modes by the same light beam. (a) the resonance scheme in the momentum space; (b) a sketch of phenomenon on the grating surface, with the yellow arrow representing the incident light and the blu arrows the excited plasmons.

As a final remark, we point out that an unique configuration exists in the G<β case, for φ = 90°, in which two SPP modes propagating towards different directions are simultaneously excited by the same light beam, as represented in Fig. 46.
The angular separation, ξ, between $\vec{\beta}_+$ and $\vec{\beta}_-$ is given by $\xi = \pi - 2\gamma_M = \pi - 2\cot^{-1}\left(\frac{G}{\sqrt{\beta^2 - G^2}}\right)$, that can be simplified into:

$$\xi = 2\tan\left(\frac{G}{\sqrt{\beta^2 - G^2}}\right)$$

These two modes are identical because, due to the symmetry of the grating, γ presents a γ = - γ symmetry, besides the π periodicity.

5.2. Resonance shape and SPP propagation

A deep investigation on the SPR dip shape in relation to losses will now be performed.

In order to provide "optimal coupling" between free radiation and an SPP mode, commonly intended as the condition in which the reflected intensity in a spectrum fall to 0, grating amplitude and incident light polarization can be set, as described in Chapter 1.3[c]. Anyway, the dependences of the dip shape on polarization and on amplitude have a deeply different physical meaning.

According with the interpretation given in Chapter 1.3[d], losses are responsible for the FWHM of the plasmonic resonances. A study of the relation between FWHM, losses and the experimental parameters is performed in this Chapter in three steps:

- Analysis of the independence of the FWHM on the incident light polarization
- Analysis of the dependence of radiative losses on the grating amplitude
- Analysis of the effect of the azimuthal rotation

The aim is to give a physical insight into the meaning of the "optimal coupling" in relation to the shape of the resonance peak and the mode losses and propagation length. The understanding of the mechanisms that determine the resonance width (and consequently the Figure of Merit) and the propagation length of the SPP could reasonably prove useful for various applications.

In this chapter the resonances will be studied in the momentum space, i.e. the usual dips in the spectra will be transformed, through the coupling conditions, into peaks described by functions [1-R](k), of approximate Lorentzian shape.

a. Effects of polarization

As it is apparent from the analysis in Chapter 1.3[c], wrongly polarized light (the TE component in the null azimuth case) is just reflected by the surface, since it does not interact with the grating. This implies that polarization does not affect at all the behavior of the SPP mode, in particular its losses, because it only determines the fraction of the incident intensity that will be involved in the coupling mechanism.

This explanation is consistent with the fact that plasmonic resonances relative to the same mode excited at different polarizations present the same FWHM, as in the example reported in Fig. 47. The only effect is a rescale of the Lorentzian curve area.

For this reason, effects related to polarization setting can be ignored in the following analyses. In particular, when working at an arbitrary azimuth, optimal polarization to achieve coupling can be freely set without consequences on the FWHM of the SPR.

From the viewpoint of losses, the procedure of setting the optimal polarization for a generic azimuth does not correspond to set the $\Gamma_i=\Gamma_r$ condition, which is related to the interaction between free radiation and SPP mode through the coupler.

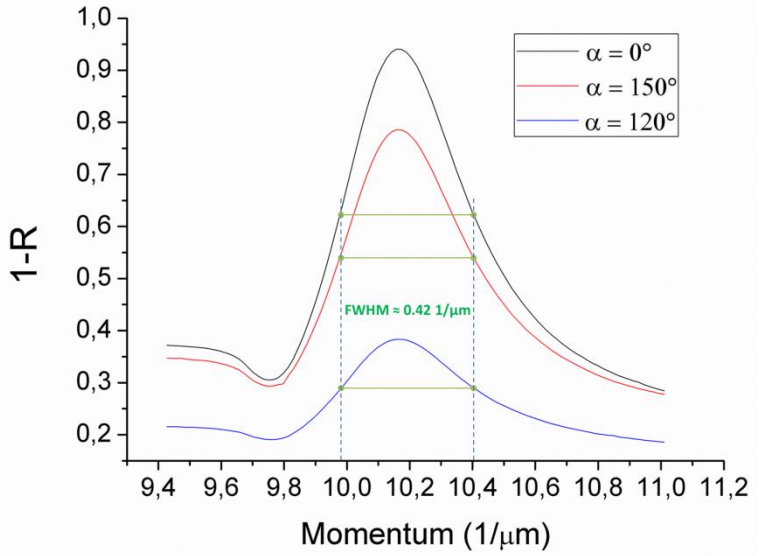

Fig. 47: Resonance peaks in the momentum space corresponding to the excitation of a single-interface gold/air SPP at λ=600 nm, for different values of the incident light polarization. These are experimental data from a NOA / 5 nm chromium / 40 nm gold structure (see Chapter 4.2) with a 500 nm grating period and a 20 nm amplitude. Lorentzian fit provides the FWHM, that comes to be equal within the error for all polarization values.

b. Dependence on the grating amplitude

As far as the effect of the grating amplitude on losses is concerned, we had the following expectations based on reasonable considerations:

- The loss term representing dissipation into the metal layer, Γ_i, should be independent on the grating amplitude, due to its intrinsic nature. In particular, it should have the same value it has in the flat case, that can be analytically predicted in simple configurations, as seen in Section 1.
- The radiative loss term, Γ_r, should strongly depend on the amplitude in a continuous way. In particular, it should tend to 0 with the amplitude, since in that case there would be no coupling between the SPP mode and a free radiation field.
- Optimal coupling should be achieved when the $\Gamma_i=\Gamma_r$ condition is satisfied, according to the analysis reported in Chapter 2.2[a].
- The same results should be achieved both by measuring the SPR Full Width at Half Maximum or the directly the losses of a launched plasmon.

Computational methods introduced in Section 3 provide a fast and cheap way to test these predictions; the two methods produce independent and complementary data to be compared for consistency. In particular, in Chandezon's simulations, spectra were produced setting different values for the grating amplitudes, then the plasmonic resonances were transformed into the momentum space and lorentzian fits were performed in order to extract the FWHM.

By Modal Analysis, the same modes were selected and launched along the same patterned surface until they were dissipated, as described in Chapter 3.2 with particular reference to Fig. 28. The model provided the power fractions dissipated by radiative and intrinsic losses; the total losses could be extrapolated by fitting the exponential decay of the intensity of the propagating SPP.

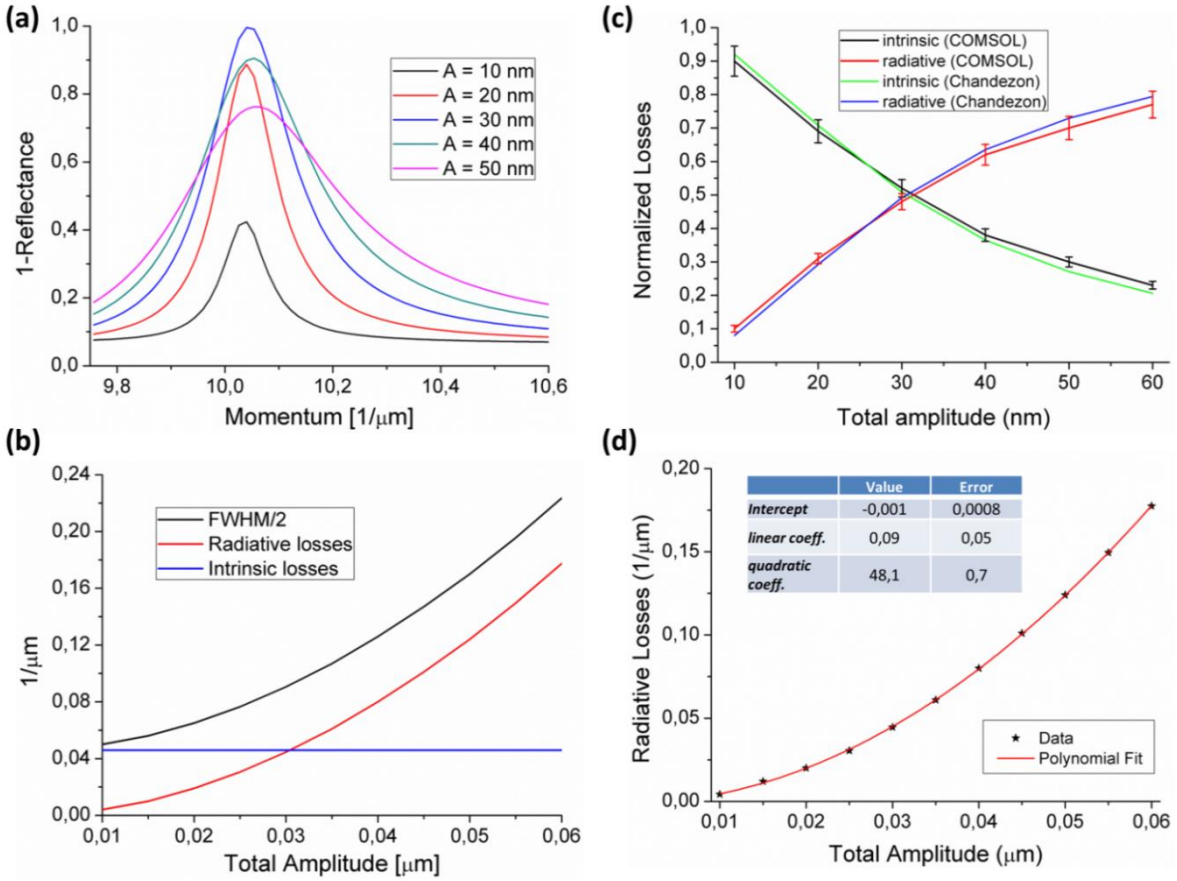

Fig. 48: Results of the simulations of a single-interface SPP excited with λ = 650 nm on an Au/air plasmonic grating with period Λ = 400 nm. (a) SPR peaks in the momentum space, for different values of the total amplitude A; the optimal amplitude is identified as 30 nm. (b) Trend as functions of the amplitude A of the SPR half width at half maximum (black line), approaching the fixed value of the intrinsic losses (blue line) as A→0, and of the radiative losses (red line), crossing Γ_i at the above-mentioned optimal amplitude. (c) Comparison between Chandezon's and COMSOL data, showing their consistency within errors. (d) A second-order polynomial fit of the radiative losses trend gives a proportionality to A^2 within the error.

The data provided by Chandezon's simulations are found to be consistent with the expectations. As an example, Fig. 48 reports the analysis of a set of data, related to a single-interface air/gold SPP excited with 650 nm incident light on a grating of period 400 nm. Box (a) shows the resonance peaks in the momentum space for various values of the total (peak-to-valley) amplitude; optimal coupling is achieved for A ≈ 30 nm, with the reflectance nearly going to zero.

Lorentzian fits provided the FWHM of each resonance, that is known to be equal to $2(\Gamma_i + \Gamma_r)$; we estimated Γ_i with the analytical formula for a flat surface and verified consistency. In fact, the black curve in Fig. 48(b) shows the trend of FWHM/2, i.e. the total losses, approaching the

theoretical value of Γ_i as the amplitude goes towards 0. Thus it is suitable to calculate Γ_r as $\Gamma_r(A) = \frac{\mathrm{FWHM}(A)}{2} - \Gamma_i$, that is represented by the red curve going to 0 with A in Fig. 48(b).

In Fig. 48(c) the consistency between the data generated by the Chandezon's method and the ones provided by COMSOL simulations is demonstrated. As explained in Chapter 3.2, the model implemented in COMSOL suffered a series of issues related to the correct evaluation of incoming and outgoing energy: this fact produces a significant uncertainty in the results.

The final and most interesting result of this Paragraph is found by fitting Γ_r as a function of A with a polynomial of second degree, as shown in Fig. 48(d). We observe that not only the intercept is zero within the errors, as it had to be, but also the linear term, meaning that Γ_r is proportional to A^2 with a very good agreement:

$$\Gamma_r \propto A^2$$

By varying the wavelength or the grating period, some fluctuations of the coefficient of proportionality have been observed, but without recognizing a regular pattern.

We suggest a possible interpretation of the quadratic relation, from the point of view of the quantum interference model for the surface plasmon resonance. The idea, introduced in Chapter 1.3[d], consists in interpreting the reflectance dip as the result of destructive interference between two indistinguishable paths for a photon that travels from the source to a detector [34]. Then we could draw the two corresponding Feynman diagrams as in Fig. 49, where the SPP mode is treated as a virtual intermediate state, and develop the model as follows [123; 157; 158].

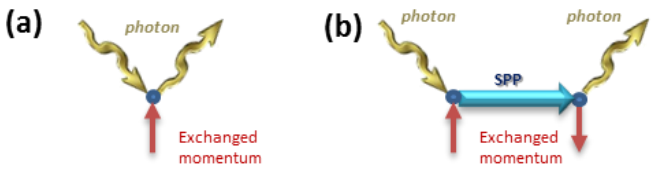

Fig. 49: Feynman diagrams for (a) the 0-th order diffraction of the photon by the surface and (b) virtual excitation of a surface mode and re-emission.

If r_a and r_b are the probability amplitudes of the two diagrams, respectively, the total probability of the process is given by their interference: $R = |r_a + r_b|^2$. We assume $r_a \approx 1$ and look for the phase difference between r_a and r_b.

According to Feynman Rules, r_b is given by the product of a $\sqrt{\sigma}$ factor for each vertex, representing a coupling parameter between the SPP and the photon, and a propagator G_{SPP} associated to the internal line:

$$r_b = \left(\sqrt{\sigma}\right)^2 \cdot G_{SPP}(k_T)$$

Since SPPs are electronic excitations, we assume the following form for its momentum space propagator, i.e. the one corresponding to a Dirac field: $G_{SPP}(\beta) = \frac{-i}{p-\beta+i\Gamma}$.

Here $\beta+i\Gamma$ is the complex eigenvalue of the SPP mode, and $\vec{p} \equiv \vec{k}_T + \vec{G}$ the momentum provided by the incident photon and the grating. We obtain a total probability amplitude:

$$R = 1 + \frac{\sigma^2 - 2\sigma\Gamma}{(p-\beta)^2 + \Gamma^2}$$

Remembering that $\Gamma=\Gamma_i+\Gamma_r$, this equation is to be compared to the Lorentzian form for the SPR resonance:

$$R = 1 - \frac{4\Gamma_i\Gamma_r}{(p-\beta)^2 + (\Gamma_i+\Gamma_r)^2}$$

In order to have consistency between the two, we get: $\sigma = 2\Gamma_r$ and thus $\sqrt{\sigma} \propto A$.

In conclusion, in this framework the proportionality of Γ_r to A^2 becomes natural, by associating the amplitude to the vertex constant, as the parameter that gives the coupling strength. A better formalization of the assumption is needed, and a further analysis is worthwhile in order to understand the origin and properties of the coefficient of proportionality.

c. Anisotropy

We now intend to address the effects of the surface anisotropy on the loss terms. In particular, we will demonstrate that the following relation holds for the total losses along an arbitrary direction, defined by the γ angle with respect to the grating Bragg vector as in Chapter 5.1[d]:

$$\Gamma(\gamma) = \Gamma_i + \Gamma_r(\gamma) = \Gamma_i + \Gamma_r(0)\cdot\cos^2\gamma$$

Where $\Gamma_r(\gamma)$ represents the radiative loss term as a function of γ, and in particular $\Gamma_r(0)$ gives losses along $\vec{G}$.

Proof:

We can keep into account the system anisotropy by building the two index ellipses for the real and imaginary parts of the complex effective dielectric functions, defined in relation to the SPP propagation along the two principal directions: parallel to $\vec{G}$ and perpendicular to it [18; 43; 44].

$$\frac{x_G^2}{Re(\varepsilon_G)} + \frac{x_\perp^2}{Re(\varepsilon_\perp)} = 1; \quad \frac{x_G^2}{Im(\varepsilon_G)} + \frac{x_\perp^2}{Im(\varepsilon_\perp)} = 1$$

We need to pass to the effective refractive indexes: $\frac{\beta}{k_i}$, describing the SPP propagation, and $\frac{\Gamma}{k_i}$, which contains the information about its dissipation. Due to the quadratic relation between dielectric functions and refractive indexes (see Chapter 1.5[a]), the four axes of the new two ellipses are:

$$\sqrt{Re(\varepsilon_G)} = \frac{\sqrt{\beta_G^2 - \Gamma_G^2}}{k_i}; \quad \sqrt{Im(\varepsilon_G)} = \frac{\sqrt{\beta_G\Gamma_G}}{k_i}$$

$$\sqrt{Re(\varepsilon_\perp)} = \frac{\sqrt{\beta_\perp^2 - \Gamma_\perp^2}}{k_i}; \quad \sqrt{Im(\varepsilon_\perp)} = \frac{\sqrt{\beta_\perp\Gamma_\perp}}{k_i}$$

Hereafter we will drop the k_i normalization and work directly with the complex SPP momenta.

With reference to Fig. 50, we recall that, according to the parametric equations for an ellipse of a_1, a_2 axes, the coordinates of a generic point along the curve are given by: $(a_1\cos\gamma\,, a_2\sin\gamma)$.

Thus we can write the following equations for β and Γ of an SPP propagating along an arbitrary direction:

$$\begin{cases} \beta^2 - \Gamma^2 = (\beta_G^2 - \Gamma_G^2)\cos^2\gamma + (\beta_\perp^2 - \Gamma_\perp^2)\sin^2\gamma \\ \beta\Gamma = \beta_G\Gamma_G\cos^2\gamma + \beta_\perp\Gamma_\perp\sin^2\gamma \end{cases}$$

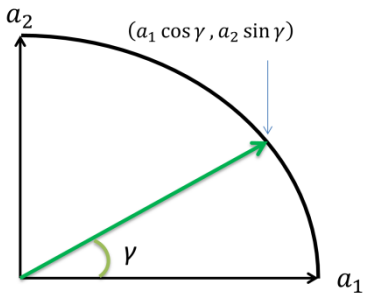

Fig. 50: Quadrant of an ellipse, with the coordinates of a generic point according to the parametric equations.

At this point we exploit the knowledge acquired in the previous Paragraph, to introduce the relations:

$$\beta_\perp = \beta_0; \quad \beta_G = \beta_0 + \delta$$
$$\Gamma_\perp = \Gamma_i \quad \Gamma_G = \Gamma_i + \Gamma_r(0)$$

Where β_0 is the momentum calculated for the SPP propagating on a flat surface, and the small perturbation $\delta << \beta_0$ keeps into account the slight difference between β_0 and β_G, the momentum for propagation along $\vec{G}$.
Inserting these relations into the previous equation, we get:

$$\begin{cases} \beta^2 - \Gamma^2 = (\beta_0 + \delta)^2\cos^2\gamma - [\Gamma_i + \Gamma_r(0)]^2\cos^2\gamma + (\beta_0^2 - \Gamma_i^2)\sin^2\gamma \\ \beta\Gamma = (\beta_0 + \delta)[\Gamma_i + \Gamma_r(0)]\cos^2\gamma + \beta_0\Gamma_i\sin^2\gamma \end{cases}$$

Since all the loss terms are much smaller than the real momenta, we can neglect into the first equation all the terms quadratic not only in δ but also in Γ, Γ_i, $\Gamma_r(0)$. Under this approximation, that equation gives the solution: $\beta(\gamma) \approx \beta_0 + \delta\cos^2\gamma$.

To obtain our final result, we will introduce this relation into the second equation, together with the substitution: $\Gamma(\gamma) = \Gamma_i + \Gamma_r(\gamma)$. This is based on the assumptions that an SPP mode propagating along any direction should have an intrinsic and a radiative loss term, physically distinguished, and that the intrinsic term should not depend on the propagation direction. The final equation becomes:

$$\Gamma_i(\beta_0 + \delta\cos^2\gamma) + \Gamma_r(\gamma)(\beta_0 + \delta\cos^2\gamma) = \Gamma_i(\beta_0 + \delta)\cos^2\gamma + \beta_0\Gamma_i\sin^2\gamma + \Gamma_r(0)\cdot(\beta_0 + \delta)\cos^2\gamma$$

That gives: $\Gamma_r(\gamma)\cdot(\beta_0 + \delta\cos^2\gamma) = \Gamma_r(0)\cdot(\beta_0 + \delta)\cos^2\gamma$. This can also be rewritten as follows:

$$\Gamma_r(\gamma) = \Gamma_r(0)\cdot\cos^2\gamma + \frac{\delta\cdot\Gamma_r(0)}{\beta_0}\sin^2\gamma\cos^2\gamma$$

Since δ is very small, tipically three order of magnitude with respect to β_0, it is safe to neglect the second term of $\Gamma_r(\gamma)$ to come to our conclusion.

■

According to the results of the previous Paragraph, we can also say that

$$\Gamma_r(\gamma) \propto A^2\cos^2\gamma$$

Meaning that the amplitude has to be "reduced" of a $\cos\gamma$ factor to keep into account the anisotropic propagation.

d. Azimuthal effect

In addition to the dependence of losses on γ, a geometrical distortion of the resonance shape is also created by the azimuthal rotation: a corrective factor to calculate the SPR FWHM need to be derived. To this aim, we report in Fig. 51 the usual resonance scheme including a finite width of the resonance.

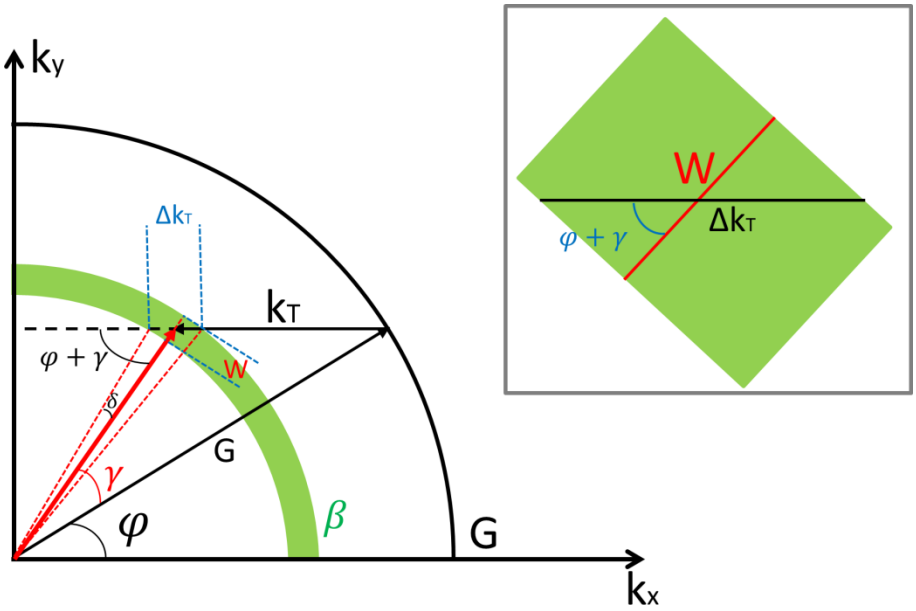

Fig. 51: The usual resonance scheme is drawn pointing out the width of the plasmonic resonance. The red arrow represents the momentum β of an SPP propagating along the direction defined by the γ angle with respect to the grating Bragg vector G. Its own linewidth is proportional to the imaginary part of its momentum. The inset shows a detail that clarifies the geometrical relation between W and the measured width.

The red arrow represents the momentum β of an SPP propagating along the direction defined by the γ angle with respect to $\vec{G}$. Its own width is given by: W ≡ FWHM = 2Γ(γ).
Experimentally we scan the transferred momentum $k_T = k_i \sin\theta$ to couple the SPP, observing a certain spread Δk_T. Correspondingly, a certain spread of the SPP propagation direction exists, represented by the small δ angle.

The relation between W and Δk_T can be derived from geometrical considerations under some approximations, all related to the fact that δ is small. The first is to neglect any possible variation of W in the angular range 2δ, that is $W(\gamma+\delta) \approx W(\gamma-\delta) \approx W(\gamma)$. The second is to approximate the annular sector as a rectangle. The result is the scheme in the inset of Fig. 51, from which it is apparent that:

$$W = \Delta k_T \cos(\varphi+\gamma)$$

and consequently:

$$\Gamma_r(\gamma) = \frac{\Delta k_T}{2}\cos(\varphi+\gamma) - \Gamma_i$$

With analogous geometrical considerations, a similar expression can be derived for the other coupling configurations, where the corrective factors for the width are:

$$\begin{array}{ll} \cos(\varphi-\gamma) & G<\beta \text{ case, } 1^{st} \text{ resonance} \\ \cos(\pi-\varphi-\gamma) & 2^{nd} \text{ resonance, both cases} \end{array}$$

Combining these equations to the ones, for the calculation of γ, of Chapter 5.1[d], an unified expression is immediately derived for the corrective factor in all the four cases, that is:
$\cos\left[\tan^{-1}\frac{G\sin\varphi}{\sqrt{\beta^2-G^2\sin^2\varphi}}\right]$.

Using the trigonometric relation $\cos(\tan^{-1}x)=\frac{1}{\sqrt{x^2+1}}$, it can be rewritten as follows:

$$\cos\left[\tan^{-1}\frac{G\sin\varphi}{\sqrt{\beta^2-G^2\sin^2\varphi}}\right]=\sqrt{1-\left(\frac{G}{\beta}\sin\varphi\right)^2}$$

Eventually, our result can be expressed by the following relation, valid for any configuration:

$$\Delta k_T(\gamma)=\frac{W(\gamma)}{\sqrt{1-\frac{G^2}{\beta^2}\sin^2\varphi}}=2\frac{\Gamma_i+\Gamma_r(0)\cdot\cos^2\gamma}{\sqrt{1-\frac{G^2}{\beta^2}\sin^2\varphi}}$$

We will discover in Chapter 5.4[e] how this result is of great importance for the sensing strategy based on the conical mounting configuration.

This approximation is expected to be good as long as the configuration is far from the top of the β circle, i.e. far from the merging point of the two resonances. This condition is represented in Fig. 52. Before a certain azimuth, the two resonances are still separated, but the approximation made could become rough, due to the increase of the spread angle δ. At a certain point the two resonances merge into one, with a very large width and then, increasing further the azimuth, its width decreases until the dip disappears.

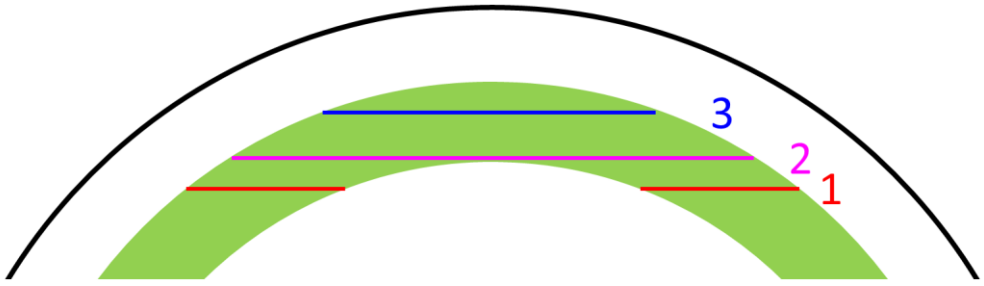

Fig. 52: At the top of the scheme of Fig. 51, the merging condition is approached. For lower φ values, the two resonances are separated (segment 1), then the merging produces a single large dip with the width represented by segment 2. Increasing further the azimuth, the width gradually decreases (segment 3) until the dip disappears.

With reference to Fig. 53, we suggest how to address the two situations.
With the help of Fig. 53(a), the length of segment 3 can be derived by elementary geometrical considerations as:

$$\Delta k_T=\sqrt{[\beta+\Gamma(\gamma_1)]^2-(G\sin\varphi)^2}+\sqrt{[\beta+\Gamma(\gamma_2)]^2-(G\sin\varphi)^2}$$

Where:

$$\gamma_1 = -\varphi + \tan^{-1}\frac{G\sin\varphi}{\sqrt{\beta^2 - G^2\sin^2\varphi}}$$
$$\gamma_2 = \pi - \varphi - \tan^{-1}\frac{G\sin\varphi}{\sqrt{\beta^2 - G^2\sin^2\varphi}}$$

The case relative to segment 1 is represented in Fig. 53(b), where we assume this time that δ is not negligible. Thus, we need to subtract an half-chord of the smaller ellipse from the one of the larger, keeping into account the different angular positions, as follows:

$$\Delta k_T = \sqrt{[\beta + \Gamma(\gamma - \delta)]^2 - (G\sin\varphi)^2} - \sqrt{[\beta - \Gamma(\gamma + \delta)]^2 - (G\sin\varphi)^2}$$

The value of δ is needed; it can be extracted by exploiting the previous approximation as a first-order step to give the length of the AB segment as: $\overline{AB} = \Gamma(\gamma)\tan(\varphi + \gamma)$.
This is the length of a chord which can also be written in terms of the distance between the two points, A and B, that have coordinates:

$$A = [(\beta - \Gamma(0))\cos\gamma\,;\ \ (\beta - \Gamma_i)\sin\gamma]$$
$$B = [(\beta - \Gamma(0))\cos(\gamma + \delta)\,;\ \ (\beta - \Gamma_i)\sin(\gamma + \delta)]$$

In conclusion, δ can be extracted by the following equation for the $\overline{AB}$ distance:

$$[\Gamma(\gamma)\tan(\varphi + \gamma)]^2 = [\beta - \Gamma(0)]^2 \cdot [\cos(\gamma + \delta) - \cos\gamma]^2 + [\beta - \Gamma_i]^2 \cdot [\sin(\gamma + \delta) - \sin\gamma]^2$$

And used to calculate a more accurate value for Δk_T.

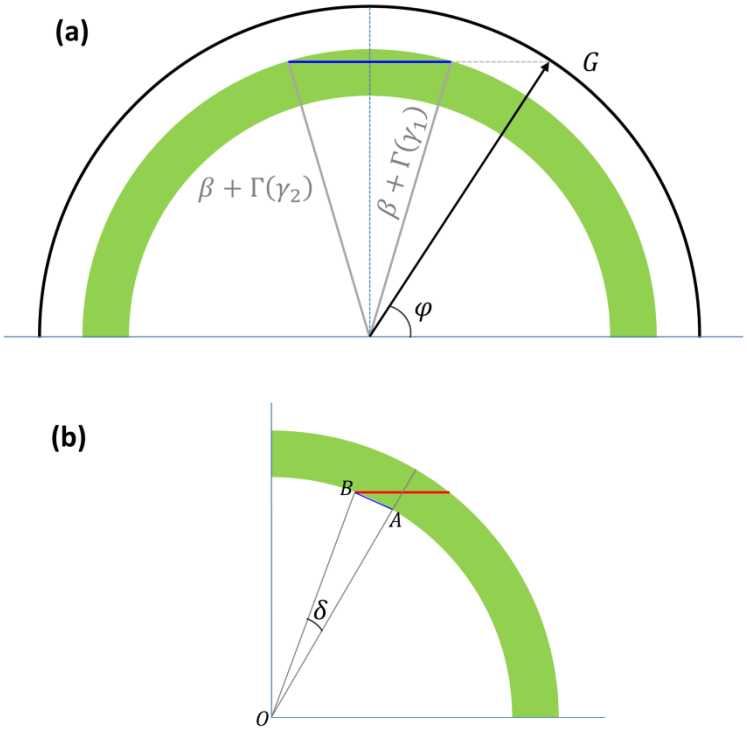

Fig. 53: (a) Scheme to illustrate how to calculate Δk_T after the merging of the resonances. (b) Scheme to illustrate how to calculate the δ angle.

e. Validation

We verified the validity of our model by collecting experimental spectra from a plasmonic grating of period 465 nm and amplitude 15 nm. The stack was made of a gold film, of thickness 40 nm, over a chromium adhesion layer of 5 nm, over a resist layer (see Section 4 for the experimental details). Angular spectra were collected under conical mounting at φ = 0, 10, 20, 30 and 40°, setting the optimal polarization according to the formula of Chapter 1.3[c], for three different wavelengths. With these parameters, the configuration falls into the G>β case, first resonance.

For each SPR dip, the angular spectrum was transformed into a transferred-momentum spectrum, and Δk_T was extracted as the FWHM of a Lorentzian fit around the resonance. For each wavelength, we theoretically calculated Γ_i and then we used Δk_T at null azimuth to calculate $\Gamma_r(0)$ as:

$$\Gamma_r(0) = \frac{\Delta k_T(\varphi = 0)}{2} - \Gamma_i$$

This was used as a reference point; for each wavelength, a theoretical curve defined by the function $\Gamma_r(0) \cdot \cos^2 \gamma$ was compared to the experimental points for $\Gamma_r(\gamma)$.

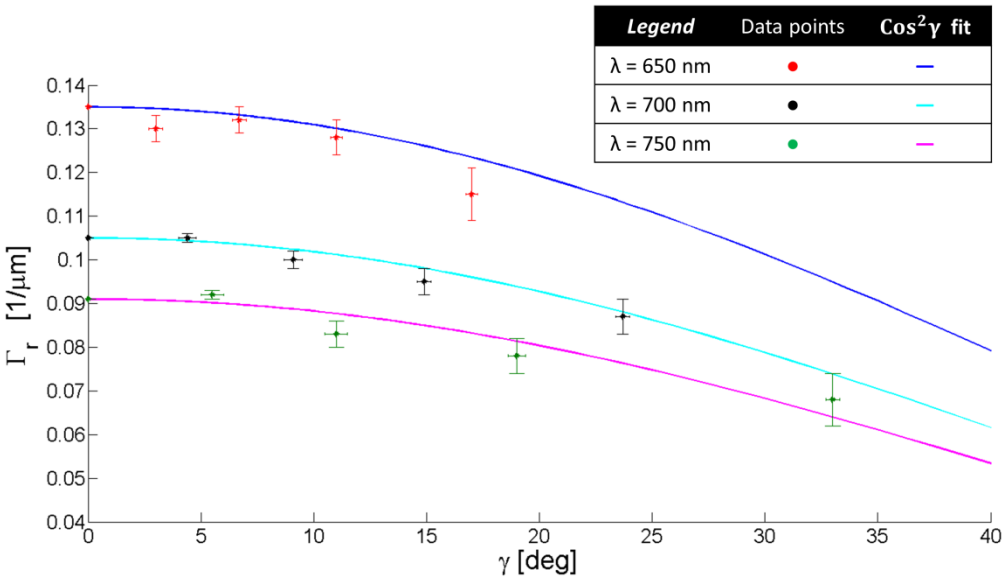

Fig. 54: Validation of the model by comparison to experimental data.

Such points were provided as follows. Among the formulas on disposal to calculate γ and Γ_r from the data, we chose to work with the following, from Chapter 5.1[d], because they do not require to calculate the SPP momentum, β:

$$\gamma = -\varphi + \tan^{-1}\frac{G \sin\varphi}{G\cos\varphi - k_T}$$

$$\Gamma_r = \frac{\Delta k_T}{2} \cdot \frac{G\cos\varphi - k_T}{\sqrt{G^2 + k_T^2 - 2k_T G\cos\varphi}}$$

Uncertainties on γ and Γ_r were obtained from the errors on the measured quantities or fit outputs, through the propagation formulas:

$$\sigma_\gamma^2 = \left(\frac{\partial\gamma}{\partial\Lambda}\right)^2 \sigma_\Lambda^2 + \left(\frac{\partial\gamma}{\partial\varphi}\right)^2 \sigma_\varphi^2 + \left(\frac{\partial\gamma}{\partial k_T}\right)^2 \sigma_{k_T}^2$$

$$\sigma_{\Gamma_r}^2 = \left(\frac{\partial\Gamma_r}{\partial\Lambda}\right)^2 \sigma_\Lambda^2 + \left(\frac{\partial\Gamma_r}{\partial\varphi}\right)^2 \sigma_\varphi^2 + \left(\frac{\partial\Gamma_r}{\partial k_T}\right)^2 \sigma_{k_T}^2 + \left(\frac{\partial\Gamma_r}{\partial\Delta k_T}\right)^2 \sigma_{\Delta k_T}^2$$

The error on Λ comes from the AFM, SEM and scatterometry measurements, errors on k_T and Δk_T are among the outputs of the resonance fits, and σ_φ is due to the experimental setup. From a comparison of the terms, the dominant source of error comes to be the determination of the azimuthal angle φ, that is estimated in about 1° due to the manual regulation of the goniometer.

The results of this procedure are reported in Fig. 54 and show a good agreement with the expectations.

5.3. Coupled modes in conical mounting

An extensive investigation of the behaviour of coupled modes on thin films in the conical mounting configuration were missing in the literature and will now be presented. The theoretical treatment introduced in Chapter 5.1 will now be exploited to predict the angular positions of the second resonant coupling of both SR and LR SPPs. The corresponding dips will be experimentally observed for the first time, fulfilling the predictions.

The propagation length of the modes will also be investigated, combining simulations by Modal Analysis with the results of the previous Chapter. In particular, it is suggested that the Long Range SPP propagation length can be sensibly enhanced in conical mounting with respect to the null-azimuth case.

All the results exposed in this Chapter have been recently published in the Plasmonics journal [156].

a. Theoretical and computational approaches

Generalized coupled conditions and maps introduced in Chapter 5.1 were applied to the coupled modes case, by exploiting the approximated formulas derived in Chapter 1.2[c] to calculate their momenta in a quick and computationally cheap way.

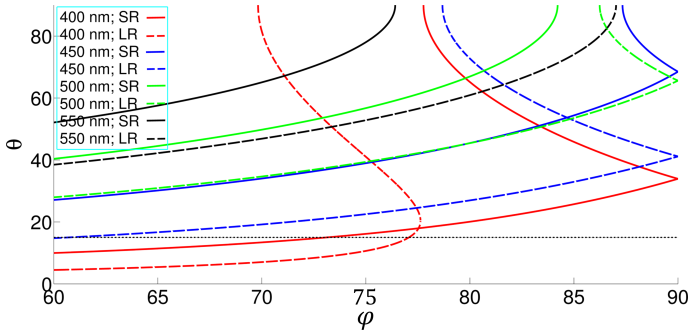

Fig. 55: Existence maps for different values of the grating period Λ, at fixed incident wavelength λ = 650 nm. The solid lines show the SR SPP resonances, while the dashed lines show the LR SPP modes. Lower values of Λ provide better conditions to experimentally see the second resonance dips.

We were interested in exploring a suitable configuration to observe the second resonant excitation of a LR and a SR SPP on a multilayer structure as the one represented in Fig. 33 of Chapter 4.2,

where the thin metal film consists in 37 nm of Ag and 7 nm of Au, and the symmetrical dielectric layer is achieved with two thick layers of ph-PSQ (see Paragraph 4.1[b]).

Fig. 55 shows the LR and SR existence maps for increasing values of the grating period, at a fixed typical wavelength widely used for most optical applications. A period around 400 nm turns out to allow favourable configurations where the second resonant coupling can be observed for both LR and SR SPP, while for higher values of the period the superior branch goes out of the angular range.

These models do not allow to address issues related to the imaginary part of the SPP momentum, because they are based on an implicit dispersion relation that would be strictly valid only in the case of flat surfaces. In presence of a sinusoidal modulation of the surface, however, it is known that the use of these formulas is a good approximation to calculate the real part, β, of the SPP momentum, but not the imaginary part, Γ [99]. In fact, the grating turns out to strongly enhance the radiative losses and consequently Γ.

For this reason, in order to get a deeper view of SPP propagation and field distribution, we performed numerical Finite Elements simulations by means of the commercial software COMSOL Multiphysics. The modal analysis method introduced in Chapter 3.2 has been applied, providing the real and imaginary parts of the SPP momentum, for a SPP propagating along a direction parallel to $\vec{G}$ or perpendicular to it: $\beta_G + i \cdot \Gamma_G$ and $\beta_\perp + i \cdot \Gamma_\perp$.

As demonstrated in Chapter 5.2[c], the total losses along a generic direction defined by the γ angle are given by:

$$\Gamma(\gamma) = \Gamma_\perp + (\Gamma_G - \Gamma_\perp)\cos^2\gamma$$

The γ angle is calculated from experimental data through the coupling conditions, with the formulas introduced in Chapter 5.1[d]: the $\gamma = \varphi - \tan^{-1}\frac{G\sin\varphi}{G\cos\varphi + k_T}$ relation works for the first resonance in the G < β case, while $\gamma = -\varphi + \tan^{-1}\frac{G\sin\varphi}{G\cos\varphi - k_T}$ can be used in all the other cases, provided that the π periodicity can be exploited to bring the obtained values into the [0°, 90°] interval.

For each calculated eigenmode of interest, its electric or magnetic field profiles into the multilayer structure have been plotted, visually displaying the symmetric or antisymmetric nature of the mode, its properties of confinement and irradiation.

b. Results and discussion

Exploiting the predictive power of the existence maps, we were able to identify the suitable conditions to observe the second resonant coupling of SR and LR SPPs, hereafter called S2 and L2 respectively. The first SR and LR dips will be instead identified as S1 and L1 respectively.

Some limitations to the experimental observations need to be taken into account. The minimum angle of incidence available on the ellipsometer optical bench is 15°, represented by the horizontal dotted line in the maps: resonances at lower angles will not be accessible. Moreover, due to dip broadening at high azimuthal and incidence angles, resonances should have a sufficiently large angular separation to be resolved, otherwise they superpose. These restrictions do not allow to clearly observe the four resonances in a single reflectance spectrum, and we are forced to choose different configurations in which the selected modes can be clearly and separately recorded.

We chose to work with wavelengths in the visible range, since this is the typical working condition for most optical applications in plasmonics. Fig. 55 shows the LR and SR existence maps for increasing values of the grating period. Since short periods allow more favourable conditions for the second resonant coupling to be observed, we fabricated plasmonic structures with periods around 400 nm, characterized by the metal layer immersed into a symmetric dielectric environment. This was obtained through the procedures described in Chapter 4.2, using as a functional material for the final symmetric structure the porous hybrid sol-gel ph-PSQ introduced in Chapter 4.1[b].

Considering a plasmonic grating of 400 nm period, we built the map of resonance for an incident wavelength of 633 nm, which is suitable for practical applications employing widespread used He-Ne lasers. The map is shown in Fig. 56(a). For $\varphi = 75°$ the L2 dip is visible together with the S1 one, while the L1 dip cannot be measured with the ellipsometer and the S2 mode cannot be excited at this azimuth.

The experimental reflectance spectrum of Fig. 56(b) reveals the two expected dips, whose angular position well agrees with theoretical predictions. The incident polarization α was set to its optimal value (see Chapter 1.3[c]) in order to minimize the reflectance at the second resonant angle θ of the LR mode.

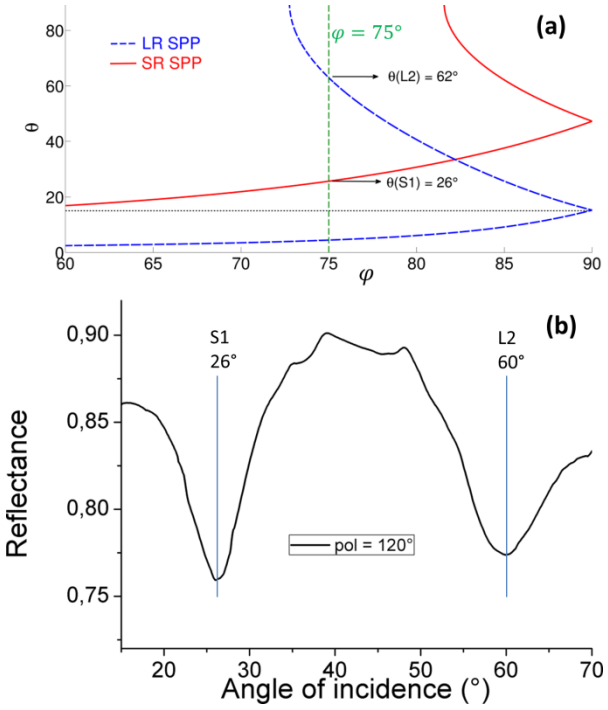

Fig. 56: Prediction and observation of the second LR resonant coupling (L2) on a sample of period Λ=400 nm. (a) The map predicts that for incident wavelength λ=633 nm the L2 dip can be observed at azimuth φ= 75° together with the S1 dip, while the L1 falls below the ellipsometer angular range and the S2 cannot be excited at this azimuth. (b) Experimental reflectance spectrum for Λ=400 nm, λ=633 nm and φ= 75°. Well defined dips are observed where expected, confirming the theoretical prediction. The polarization was chosen to minimize the reflectance at the L2 resonant polar angle θ.

As an additional analysis, we calculated the propagation angle of each SPP and considered it as a parameter in the COMSOL software simulations, in order to obtain the real and imaginary parts of the SPP momentum propagating along that specific direction. From the imaginary part Γ achieved

in this way, the propagation length L is extrapolated as the distance after which the field intensity decays of a factor 1/e, according to the general definition given in Paragraph 1.1[b]. Its values are reported in Table 2, compared to the case of a flat surface, showing the increase of the propagation length as the direction of propagation deviates from the $\vec{G}$ direction. It is worthwhile to note that the SPP propagation distance on a flat surface is much longer than the one over the grating; by increasing the γ angle this value can be approached.

Incident λ = 633 nm	γ (deg)	L (μm)
Flat, or $\vec{\beta} \perp \vec{G}$ on a grating	90	13.2
$\vec{\beta} \parallel \pm\vec{G}$ on a grating	0	4.3
L1 at φ= 75°	6	4.3
L2 at φ= 75°	32	5.3

Table 2: Propagation length of the LR SPP excited with light of wavelength λ=633 nm for different propagation directions, defined as the γ angle between the grating vector $\vec{G}$ and the SPP momentum $\vec{\beta}$. The propagation lengths are numerically calculated for our experimental structure.

Through COMSOL simulations we also produced the plots of the profile of the transverse magnetic field intensity into the multilayer structure, depicted in the $(\hat{G}, \hat{z})$ plane. Results are reported in Fig. 57 for both a mode propagating along $\vec{G}$ and along the direction perpendicular to $\vec{G}$. It is apparent how the radiation field is very strong in the γ=0° case, while it is absent in the γ=90°, when the mode is almost identical to a SPP propagating on a flat surface.

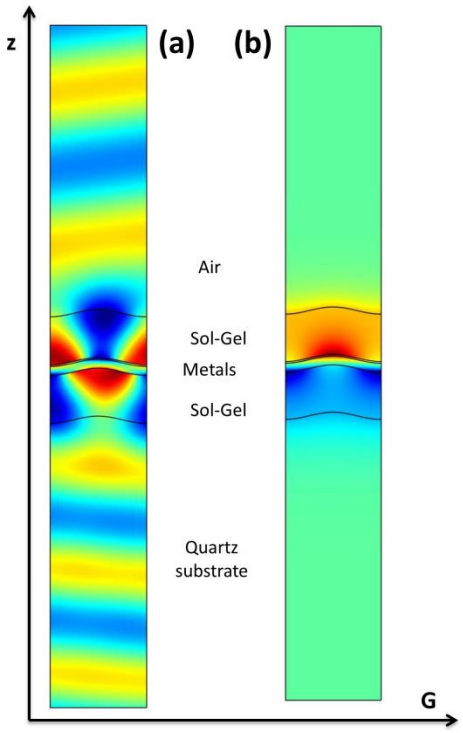

Fig. 57: Longitudinal electric field profile in the $(\hat{G}, \hat{z})$ plane, for a LR SPP excited with incident wavelength λ = 633 nm over a 400 nm grating with 30 nm amplitude, along the directions (a) parallel to the $\vec{G}$ vector and (b) perpendicular to it. The colours represent arbitrary units for the field intensity.

On the same sample, by increasing the wavelength, it is possible to excite the LR mode in the G > β regime, as shown in the map of Fig. 58(a). Choosing a sufficiently high azimuth only the SR modes can be excited: we show the map for λ = 660 nm and intersect the curves for the azimuth $\varphi = 84°$. The experimental reflectance spectrum shown in Fig. 58(b) fully confirms the theoretical prediction.

The incident polarization was set to its optimal value in order to maximize the depth of the S2 dip, which is around 100°, therefore it was tuned at different values in order to show its effect on the dip depth. It is verified that the depth is maximum for the optimal polarization while the dips disappear when the polarization is rotated of 90°, as expected. This constitutes a further validation of the plasmonic nature of the observed dips.

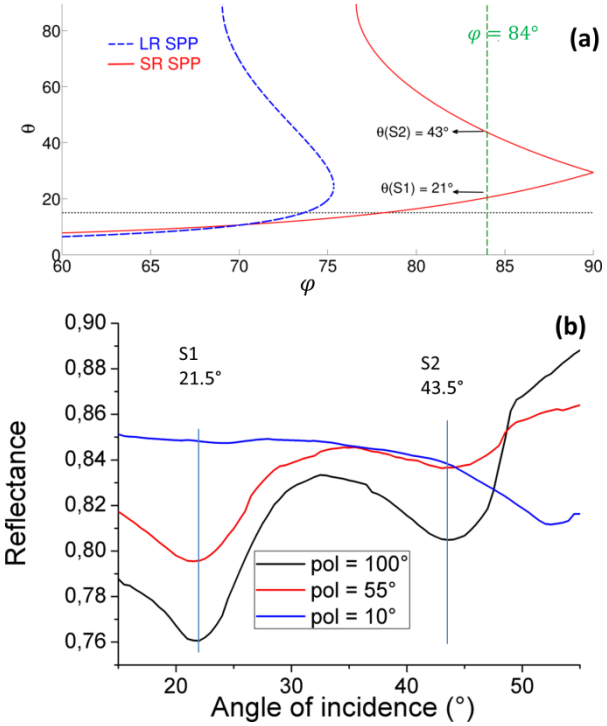

Fig. 58: Prediction and observation of the S2 dip on the same sample. (a) The existence map shows that the LR-SPP can be put in the G > β regime by setting an higher wavelength (660 nm, in this case) for the incident light. For a sufficiently high azimuth only the SR mode can be excited. (b) The experimental spectra at azimuth φ = 84° show the dips S1 and S2 where predicted. A further check of the plasmonic nature of the dips is their dependence on the polarization. In fact the coupling with the radiation is optimized for the theoretical optimal polarization, while the dips disappear for orthogonal polarization.

Incident λ = 660 nm	γ (deg)	L (μm)
Flat, or $\vec{\beta} \perp \vec{G}$ on a grating	90	3.4
$\vec{\beta} \parallel \pm\vec{G}$ on a grating	0	2.1
S1 at φ = 84°	12	2.1
S2 at φ = 84°	24	2.2

Table 3: propagation length of the SR SPP excited with light of wavelength λ=660 nm for different propagation directions, defined by the angle γ between the grating vector $\vec{G}$ and the SPP momentum $\vec{\beta}$. The propagation lengths are numerically calculated for our experimental structure.

Following the same procedure as for the Long Range modes, we report in Table 3 the propagation lengths for the different observed Short Range modes, also compared with the flat surface case. We also report the magnetic field intensity profile in Fig. 59 for the SR modes, verifying the presence of a radiation field produced by the presence of the grating also in this case.

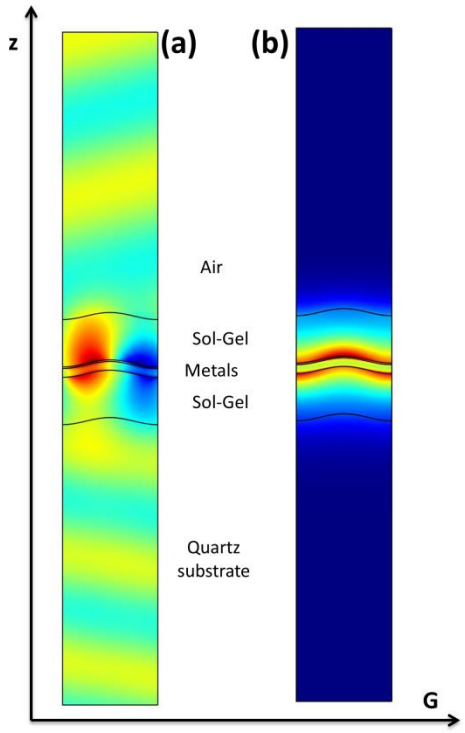

Fig. 59: Longitudinal electric field profile in the $(\hat{G}, \hat{z})$ plane, for a SR SPP excited with incident wavelength λ=660 nm over a 400 nm grating with 30 nm amplitude, along the directions (a) parallel to the $\vec{G}$ vector and (b) perpendicular to it. The colours represent arbitrary units for the field intensity.

Mode	LR, λ= 633 nm	SR, λ= 633 nm	LR, λ= 660 nm	SR, λ= 660 nm
Dissipation inside the metal slab	0.42	0.73	0.33	0.70
Radiative losses in air	0.27	0.13	0.37	0.13
Radiative losses in quartz	0.31	0.14	0.30	0.17
Total radiative losses	0.58	0.27	0.67	0.30

Table 4: Radiative losses versus dissipation for SPP modes propagating along the direction of the G vector on a 400 nm pitch grating of 30 nm amplitude. The values are calculated by COMSOL simulations and represent the dissipated power fractions.

By comparing the data reported in Table 2 with Table 3, it clearly emerges that the propagation direction on the grating affects the value of the propagation length in a more effective way for the LR SPP modes with respect to the SR SPP ones; in particular, the propagation length along a flat surface with respect to a grating is much higher for the LR. The reason can be comprehended by examining the data shown in Table 4: the grating-induced radiative losses contribute to the total

dissipation of the SPP power for more than the 50% in the case of LR modes, while in the SR case such a contribution represents less than the 30%. It is reasonable to suppose that the SR modes are proportionally less affected by the radiative losses, due to their strong dissipation into the metal and their shorter propagation distance.

c. Conclusions and perspectives

In conclusion, we performed an optimization of the plasmonic structure for the excitation of double Long Range and Short Range SPPs with the same frequency and for different propagation directions. We fabricated the plasmonic gratings and observed for the first time the second resonant coupling of LR and SR SPP modes at high azimuthal angles, fulfilling our predictions. We also performed, with the aid of COMSOL simulations, a deep investigation of the propagation distance of the modes on the surface showing the strong connection of this property to the propagation direction with respect to the grating grooves. In particular, the LR propagation length is strongly affected by the grating-induced radiative losses.

This result opens the way for innovative configurations of plasmonic architectures, suitable for instance for the realization of miniaturized portable gas sensing or biosensing devices. We introduce the possibility to take advantage of the combination of two contributions to the sensitivity enhancement: the choice of the suitable SPP mode for a specific sensing configuration and the achievement of sensitivity-enhanced resonant coupling through azimuthal rotation. In Chapter 6.3 a first experimental validation of this purpose will be provided, concerning the application to a gas sensing device, in particular exploiting the sensitivity of the L2 resonance for xylene detection.

5.4. SPR sensitivity calculations

This Chapter is devoted to theoretical calculations of the sensitivity of an SPP mode in a multilayer structure. This is a somewhat subtle problem; a general solution cannot be given, since the calculation strongly depends on the structure details and the specific sensing mechanism.

A decomposition into relevant factors, in the way introduced in Section 1.5, may be useful to better understand the contributions of different mechanisms to the overall sensitivity. In this Chapter, contributions related to the choice of the sensitive layer, the particular SPP mode and the conical mounting will be analyzed in angular scan; after this, the extension to the spectral scan case will be addressed.

a. Role of the sensitive layer

The first step is to separate the contribution related to the sensitive layer only from the *refractometric sensitivity* related to the SPR response, as follows:

$$\Sigma \equiv \frac{\partial Y}{\partial n}\frac{\partial n}{\partial c}$$

Where Y represents the final read quantity, that is θ or λ in the cases of our interest, and $\frac{\partial n}{\partial c}$ is the sensitive layer response to a certain concentrations of analyte in the environment. This factor cannot be expressed in a general form, valid for any kind of sensitive layer, due to the very different mechanisms that may be involved [41].

For example, in some cases the sensitive layer is constituted by a monolayer of molecules immobilized close to the surface, designed to bind to the analyte molecules; in this case an analysis of the response needs to keep into account the evolution in time of the fraction of surface coverage towards some equilibrium condition or the saturation of the sensitive layer [159].
A treatment based on an effective refractive index approach, as introduced in Chapter 1.4[a], is simpler but it only makes sense in the case of sufficiently uniform films.

Attention should be paid also in the case of a thick porous sensitive layer. Methods exist to approximately calculate the optical constants change due to the filling of the pores with a substance of different refractive index [160], but such an approximation is unlikely to be good. In fact, interaction mechanisms between the analyte and the porous matrix are generally involved, otherwise the sensitive layer would not be selective; mechanisms of this kind, which have the effect to inject or subtract electrons, are addressed in Chapter 6.2.

b. Generalized modal factor

A second step is to extract a term describing the contribution of the particular plasmonic mode:

$$\frac{\partial Y}{\partial n} \equiv \frac{\partial Y}{\partial N} \cdot \frac{\partial N}{\partial n}$$

Assuming n to be an effective refractive index felt by the propagating SPP mode, we know that for a single-interface SPP the modal factor is: $\frac{\partial N}{\partial n} = \left(\frac{\mathrm{N}}{n}\right)^3$.
Incidentally, we note that, thanks to the symmetry of N with respect to ε_d and $|\varepsilon_m|$, this factor would have the same form if n was effectively interpreted as $n \equiv \sqrt{|\varepsilon_m|}$.

For the coupled modes, the sensing mechanism consists in the change of the effective refractive index only on one side of the thin film, leading to a symmetry breaking. For this reason, in order to estimate the sensitivity of a LR or SR SPP, it is necessary to evaluate its response to a small deviation from the symmetry of the structure. Approximate analytical expressions for $\frac{\partial \beta_L}{\partial n}$ and $\frac{\partial \beta_S}{\partial n}$ may be given as follows:

$$\begin{cases} \dfrac{\partial \beta_L}{\partial n} \approx -\dfrac{k_i^2}{\beta_L} \cdot \dfrac{\varepsilon_d}{\varepsilon_m} (\varepsilon_d - \varepsilon_m) \left(\dfrac{\sqrt{\varepsilon_d}}{2} + \dfrac{1}{\sqrt{\varepsilon_d}} \right) \cdot \dfrac{\sqrt{\beta_L^2 - k_i^2 \varepsilon_d}}{\sqrt{\beta_L^2 - k_i^2 \varepsilon_m}} \tanh\left(k_i a \sqrt{\varepsilon_d - \varepsilon_m}\right) \\ \dfrac{\partial \beta_S}{\partial n} \approx -\dfrac{k_i^2}{\beta_S} \cdot \left(\dfrac{\varepsilon_d}{\varepsilon_m}\right)^3 \cdot \left(\dfrac{\sqrt{\varepsilon_d}}{2} + \dfrac{1}{\sqrt{\varepsilon_d}} \right) \dfrac{(\varepsilon_d - \varepsilon_m)}{\tanh^3\left(k_i a \sqrt{\varepsilon_d - \varepsilon_m}\right)} \cdot \dfrac{\sqrt{\beta_S^2 - k_i^2 \varepsilon_m}}{\sqrt{\beta_S^2 - k_i^2 \varepsilon_d}} \end{cases}$$

Proof:

We have to start from the general implicit dispersion relation for thin-film modes, as derived in Chapter 1.2:

$$\tanh(k_m a) = \frac{\sqrt{\rho_m - \rho_{d1}}\sqrt{\rho_m - \rho_{d2}} \mp \sqrt{\rho_m + \rho_{d1}}\sqrt{\rho_m + \rho_{d2}}}{\sqrt{\rho_m - \rho_{d1}}\sqrt{\rho_m - \rho_{d2}} \pm \sqrt{\rho_m + \rho_{d1}}\sqrt{\rho_m + \rho_{d2}}}$$

A slight asymmetry can be introduced assuming $\rho_{d2} = \rho_{d1} + \Delta \equiv \rho_d + \Delta$; by neglecting terms of the second order in Δ we obtain:

$$\sqrt{\rho_m - \rho_{d1}}\sqrt{\rho_m - \rho_{d2}} \approx \rho_m - \rho_d - \frac{\Delta}{2}$$
$$\sqrt{\rho_m + \rho_{d1}}\sqrt{\rho_m + \rho_{d2}} \approx \rho_m + \rho_d + \frac{\Delta}{2}$$

The almost-symmetric dispersion relations for the LR and SR SPPs then become:

$$\tanh(k_m a) \approx -\frac{\rho_d}{\rho_m} - \frac{\Delta}{2\rho_m} \quad (\text{quasi} - \text{LR mode})$$
$$\tanh(k_m a) \approx -\frac{\rho_m}{\rho_d} + \frac{\Delta}{2}\frac{\rho_m}{\rho_d^2} \quad (\text{quasi} - \text{SR mode})$$

At this point, we want to derive the new approximated dispersion relations for the real part of the SPP momenta, β_L' and β_S', as perturbations to the ones derived in Chapter 1.2[c], hereafter labelled $\beta_{L,0}$ and $\beta_{S,0}$. In order to do this, we proceed exploiting the usual approximations for the unperturbed terms of the equations and introducing the unperturbed solutions into the perturbation terms, as follows:

$$\tanh\left(k_i a\sqrt{\varepsilon_d - \varepsilon_m}\right) \approx -\frac{\varepsilon_m}{\varepsilon_d}\frac{\sqrt{\beta_L'^2 - k_i^2\varepsilon_d}}{k_i\sqrt{\varepsilon_d - \varepsilon_m}} - \frac{\Delta}{2}\frac{\varepsilon_m}{\sqrt{\beta_{L,0}^2 - k_i^2\varepsilon_m}}$$
$$\tanh\left(k_i a\sqrt{\varepsilon_d - \varepsilon_m}\right) \approx -\frac{\varepsilon_d}{\varepsilon_m}\frac{k_i\sqrt{\varepsilon_d - \varepsilon_m}}{\sqrt{\beta_S'^2 - k_i^2\varepsilon_d}} + \frac{\Delta}{2}\frac{\varepsilon_d^2}{\varepsilon_m}\frac{\sqrt{\beta_{S,0}^2 - k_i^2\varepsilon_m}}{\beta_{S,0}^2 - k_i^2\varepsilon_d}$$

Carrying the calculations, we obtain for the LR SPP:

$$\beta_L' \approx k_i\sqrt{\varepsilon_d + (\varepsilon_d - \varepsilon_m)\left(\frac{\varepsilon_d}{\varepsilon_m}\right)^2\left[\tanh^2\left(k_i a\sqrt{\varepsilon_d - \varepsilon_m}\right) + \Delta\cdot\frac{\varepsilon_m}{\sqrt{\beta_{L,0}^2 - k_i^2\varepsilon_m}}\tanh\left(k_i a\sqrt{\varepsilon_d - \varepsilon_m}\right)\right]} \approx$$
$$\approx \beta_{L,0} + \frac{\Delta}{2}\cdot\frac{k_i^2}{\beta_{L,0}}\cdot\frac{\varepsilon_d^2}{\varepsilon_m}(\varepsilon_d - \varepsilon_m)\cdot\frac{\tanh\left(k_i a\sqrt{\varepsilon_d - \varepsilon_m}\right)}{\sqrt{\beta_{L,0}^2 - k_i^2\varepsilon_m}}$$

And in a similar way, for the SR SPP:

$$\beta_S' \approx \beta_{S,0} + \frac{\Delta}{2}\cdot\frac{k_i^2}{\beta_{S,0}}\cdot\frac{\varepsilon_d^4}{\varepsilon_m^3}\cdot\frac{(\varepsilon_d - \varepsilon_m)}{\tanh^3\left(k_i a\sqrt{\varepsilon_d - \varepsilon_m}\right)}\cdot\frac{\sqrt{\beta_{S,0}^2 - k_i^2\varepsilon_m}}{\beta_{S,0}^2 - k_i^2\varepsilon_d}$$

Now we have the responses of the LR and SR modes to a change in the ρ_d parameter, which are:

$$\frac{\beta_L' - \beta_{L,0}}{\Delta} = \frac{k_i^2}{\beta_{L,0}}\cdot\frac{\varepsilon_d^2}{2\varepsilon_m}(\varepsilon_d - \varepsilon_m)\cdot\frac{\tanh\left(k_i a\sqrt{\varepsilon_d - \varepsilon_m}\right)}{\sqrt{\beta_{L,0}^2 - k_i^2\varepsilon_m}}$$
$$\frac{\beta_S' - \beta_{S,0}}{\Delta} = \frac{k_i^2}{\beta_{S,0}}\cdot\frac{\varepsilon_d^4}{2\varepsilon_m^3}\cdot\frac{(\varepsilon_d - \varepsilon_m)}{\tanh^3\left(k_i a\sqrt{\varepsilon_d - \varepsilon_m}\right)}\cdot\frac{\sqrt{\beta_{S,0}^2 - k_i^2\varepsilon_m}}{\beta_{S,0}^2 - k_i^2\varepsilon_d}$$

In order to transform this into a response to a refractive index change, we have to explicate the origin of Δ. If a slight change in the refractive index of one half-space is introduced, as $n_2 = n_1 + \delta$, what happens to the momenta is as follows (with $n_1 \equiv n = \varepsilon_d^2$ and $k_{d1} \equiv k_d$):

$$k_{d2}^2 = \beta^2 - k_i^2 n_2^2 \approx k_d^2(1 - 2n\delta)$$

Thus $k_{d2} \approx k_d - n\delta k_d$ and finally: $\rho_{d2} = \rho_{d1} - \delta \cdot \rho_{d1}\left(n + \frac{2}{n}\right) \equiv \rho_{d1} + \Delta$. This means that we just need to multiply the found relations for the factor:

$$\frac{\Delta}{\delta} = -\rho_{d1}\left(n + \frac{2}{n}\right) = -\frac{k_d}{\varepsilon_d}\left(\sqrt{\varepsilon_d} + \frac{2}{\sqrt{\varepsilon_d}}\right)$$

And introduce the corresponding expressions for k_d, to obtain our result.

■

These formulas constitute a first attempt to evaluate a priori the intrinsic sensitivity of the coupled modes, but they prove to be too rough an approximation, especially in the SR SPP case. Anyway, they point out the notable information, supported by simulations with Chandezon's method, that $\frac{\partial \beta_S}{\partial n}$ is greater than $\frac{\partial \beta_L}{\partial n}$, meaning that the superior performances of the LR modes in sensing applications is likely to be ascribed to the deeper penetration of their fields into the dielectric, that implies a different response of the effective refractive index to the presence of an analyte.

c. Generalized coupling factor

As shown in Chapter 2.2[c], it is known that the azimuthal rotation provides an enhancement in sensitivity. This information is enclosed in a $\frac{dk_T}{dN}$ factor that transforms a variation of the SPP momentum into a variation of the transferred momentum from the incident light to the mode, and is included into the further decomposition of $\frac{\partial Y}{\partial N} \equiv \frac{dY}{dk_T}\frac{dk_T}{dN}$.
It can be easily demonstrated that this enhancement factor is independent on the particular coupling configuration between the four examined.

In fact, it is sufficient to take the four possible resonance conditions for the grating coupling at a generic azimuth φ:

$$k_T = G\cos\varphi \pm \sqrt{\beta^2 - G^2(\sin\varphi)^2} \quad \text{for } G > \beta$$
$$k_T = \sqrt{\beta^2 - G^2(\sin\varphi)^2} \pm G\cos\varphi \quad \text{for } G < \beta$$

And observe that the modulus of the derivative comes to be the same for all four cases:

$$\left|\frac{ds_T}{dN}\right| = \frac{\frac{N}{R}}{\sqrt{\left(\frac{N}{R}\right)^2 - (\sin\varphi)^2}}$$

Where the $R \equiv \frac{\lambda}{\Lambda}$ and $N \equiv \frac{\beta}{k_i}$ notation of Chapter 5.1[b] have been recalled, and the transferred momentum have been renormalized according to $s_T \equiv \frac{k_T}{k_i}$.

This formula predicts a sensitivity enhancement associated to the azimuthal rotation, for a fixed value of the $\frac{N}{R}$ ratio; in fact $\left|\frac{ds_T}{dN}\right| = 1$ for $\varphi = 0$ and it increases with φ.

In the G > β case, $\left|\frac{ds_T}{dN}\right|$ diverges when the well-known limiting azimuth, $\varphi^* = \sin^{-1}\left(\frac{N}{R}\right)$, is reached, while in the G < β case it tends to the finite maximum value $\frac{N}{\sqrt{N^2-R^2}}$ for $\varphi = \frac{\pi}{2}$. This difference between the two cases is apparent in the plots of Fig. 60.

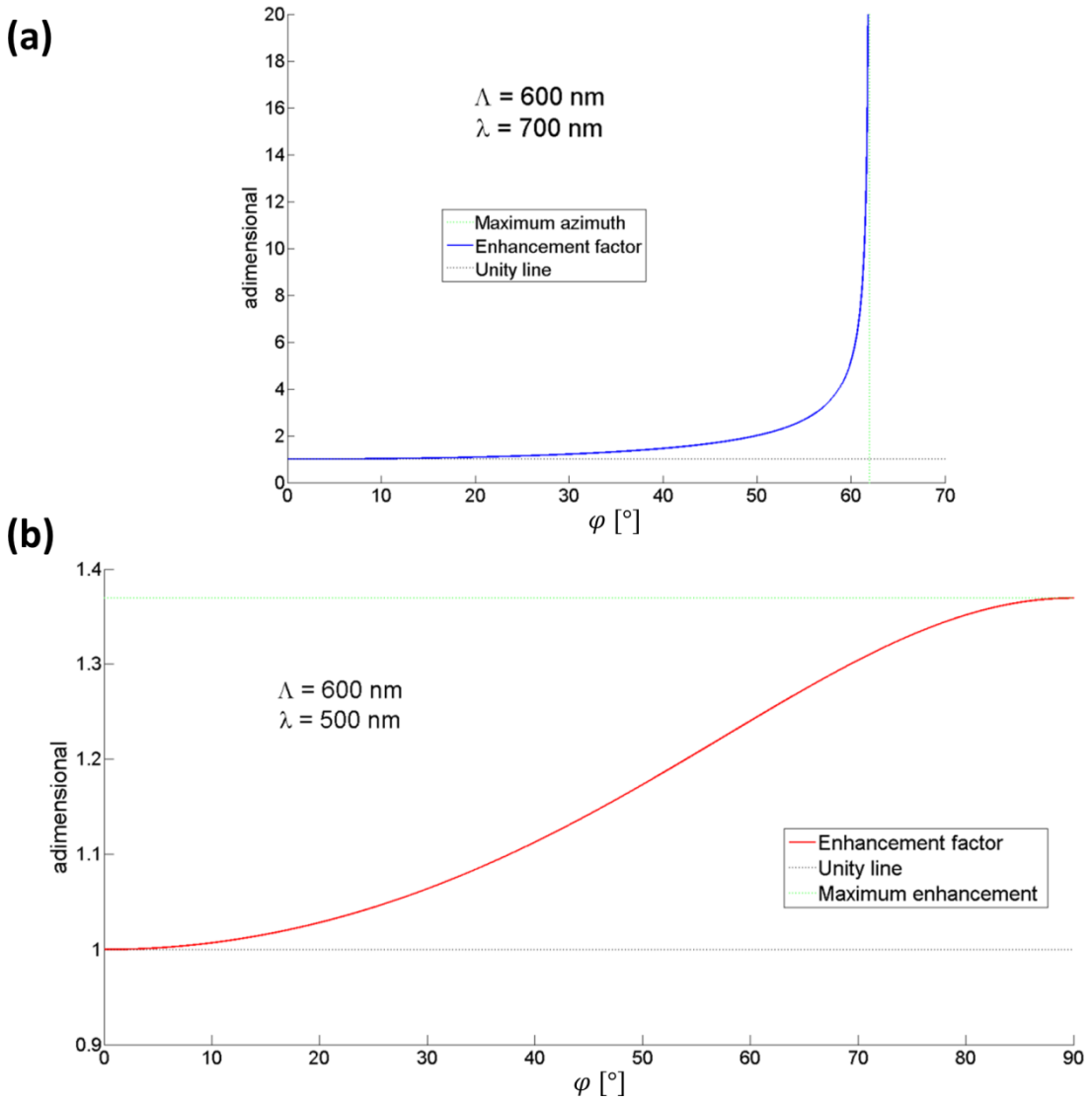

Fig. 60: Trends of the azimuthal factor for an air/gold SPP on a Λ = 600 nm grating. (a) At λ = 600 nm it falls into the G>β case, thus it shows a divergence at φ=φ*; (b) At λ = 500 nm it falls into the G<β case, it shows no divergence and it reaches a maximum value for the enhancement at φ=90°. In both cases there is no enhancement for φ=0°.

Keeping the sign into account, a minus sign appears for the first G > β resonance, because it is the only one in which an increase in β requires a decrease in k_T to be compensated, as it can be noticed by observing the resonance schemes.

In the θ-scan case, the complete factorized form for any coupling condition can then be written as follows:

$$|\Sigma_{n,\theta}| = \left(\frac{N}{n}\right)^3 \cdot \frac{1}{\cos\theta} \cdot \frac{N}{\sqrt{N^2 - \left(\frac{\lambda}{\Lambda}\sin\varphi\right)^2}}$$

Having introduced the *scan factor* $k_i \frac{d\theta}{dk_T} = \frac{1}{\cos\theta}$ that provides a divergence for theta = 90°.

The existence of divergences in the expressions for the sensitivity are due to the fact that, ideally, the resonance would suddenly disappear when certain conditions are reached. However, this would really happen only for infinitely sharp resonances; in reality, due to the finite width of any resonance, its disappearance is seen as a progressive flattening.
For example, Fig. 61 analyzes the evolution of the SPR around the maximum azimuth for a G>β case. Increasing φ, the two resonant dips get closer to each other and merge into one; increasing further, the single dip gradually disappears. The corresponding evolution of the dips width is clarified by the scheme in Fig. 52.

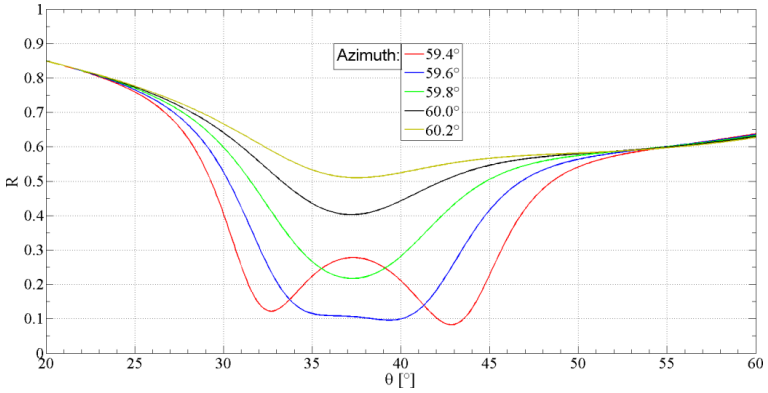

Fig. 61: Simulated angular spectra for a gold/air interface at λ=600 nm, Λ=500 nm, collected around the limiting azimuth φ* ≈ 59.6°.

The factorization approach is good to clarify the contributions of different physical aspects and the meaning of divergences. However, fixed Λ and λ, the θ and φ angles are not independent variables, because they are bound by the coupling conditions; an expression for the total refractometric sensitivity should keep this into account in order to be useful to characterize real sensors.
In Fig. 62 we chose to plot $\Sigma_{n,\theta}$ as a function of θ, since from this viewpoint the whole angular range is always continuously scanned from 0° to 90°, with a transition from the first to the second resonance at a critical angle $\theta^* = \sin^{-1}\sqrt{\left|\frac{\lambda^2}{\Lambda^2} - N^2\right|}$, and with only one resonance for each angle. To generate this plot, $\Sigma_{n,\theta}$ have been rewritten using the fact that, from the coupling conditions, the following relation holds:

$$\cos^2\varphi = \left[\frac{\lambda^2 - \Lambda^2 M^2 + (\Lambda\sin\theta)^2}{2\lambda\Lambda\sin\theta}\right]^2$$

Leading to:

$$\Sigma n,\theta = \mp\frac{N^4}{n^3}\cdot\frac{2\tan\theta}{\left|\sin^2\theta + N^2 - \frac{\lambda^2}{\Lambda^2}\right|}$$

Where, again, the minus sign only holds for the first G>β resonance (in this case the expression into the modulus would in fact be negative; we preferred to keep the formula in this more informative format).

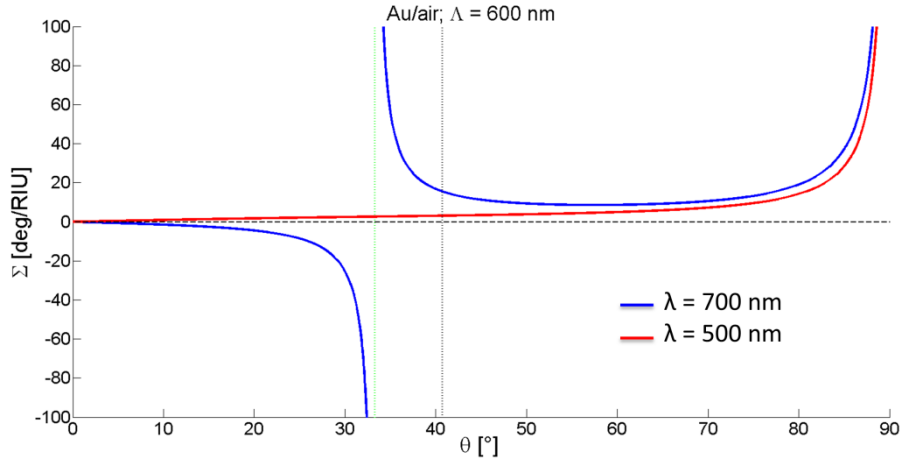

Fig. 62: Total refractometric sensitivity for air/gold SPPs excited through a Λ = 600 nm grating. The blue curve, at λ = 600 nm, is in the G>β regime and it shows a divergence at θ=θ*, indicated by the green line, where it transit from the first to the second resonance. The red curve is at λ = 500 nm and falls into the G<β regime; the vertical black dotted line marks where it transit from the first to the second resonance (this happens at φ=90°). Both curves diverges at θ=90°, due to the tan(θ) factor.

d. The spectral-scan case

In the case of spectral scan, we need to consider the variation of n(λ) at least over an interval around the resonance; this makes problematic a factor-by-factor approach. An overall refractometric sensitivity can be derived by total differentiation on the coupling conditions. Exploiting the $\beta^2 = \left|\vec{\beta}\cdot\hat{x}\right|^2 + \left|\vec{\beta}\cdot\hat{y}\right|^2$ constraint, they can be stated in the following general form, where the plus sign holds for the first resonance in the G < β case only:

$$N^2 = \frac{\lambda^2}{\Lambda^2} + (\sin\theta)^2 \mp 2\frac{\lambda}{\Lambda}\cos\varphi\sin\theta$$

If this expression is differentiated in n and λ, one obtains:

$$2N\frac{dN}{dn}dn + 2N\frac{dN}{d\lambda}d\lambda = \frac{2\lambda}{\Lambda^2}d\lambda \mp \frac{2}{\Lambda}\cos\varphi\sin\theta\, d\lambda$$

And so:

$$\frac{d\lambda}{dn} = \frac{dN}{dn}\frac{N}{\frac{\lambda}{\Lambda^2} \mp \frac{1}{\Lambda}\cos\varphi\sin\theta - N\frac{dN}{d\lambda}}$$

It can be easily proved that, for φ=0, this expression for $\Sigma_{n,\lambda}$ is equal to the one reported in Chapter 2.2[a].

As in the θ-scan case, we can still use the resonance conditions to eliminate a variable from the equations; the sign ambiguity will also disappear. We eventually come to:

$$\Sigma_{n,\lambda} = \frac{dN}{dn}\cdot\frac{2\lambda N}{\frac{\lambda^2}{\Lambda^2} + N^2 - (\sin\theta)^2 - \lambda N\frac{dN}{d\lambda}}$$

It is interesting to observe that the modal contribution $\frac{dN}{dn}$ remained as a separate factor, allowing us to identity the rest of the expression as $\frac{\partial\lambda}{\partial N}$.

Anyway, the $\frac{dN}{d\lambda}$ factor also depends on the chosen mode and its role is crucial. Since the rest of the denominator is always globally positive, the existence of divergences depends in fact on this last term.

We also note that the explicit presence of the θ angle is due to the fact that, fixed λ and Λ (thus all the other explicit parameters in the formula), it always exists a value of the azimuth φ for which the resonance is at a certain θ. Usually, for our applications θ is fixed to 70°, due to the characteristics of the setup, as presented in Chapter 4.4[a].
Without loss of generality, $\frac{dN}{d\lambda}$ can be decomposed into $\frac{dN}{d\varepsilon_d}\frac{d\varepsilon_d}{d\lambda} + \frac{dN}{d\varepsilon_m}\frac{d\varepsilon_m}{d\lambda}$, where ε_m is the real part of the metal permittivity and $\varepsilon_d=n^2$, redefined to uniform the notation. It is immediately clear that, for an evaluation of this factor, the knowledge of the dielectric functions of both materials are needed, at least.

If we limit our analysis to the single-interface SPP case, we know that $\frac{dN}{d\varepsilon_d} = \frac{N^3}{2\varepsilon_d^2}$, and the same for the ε_m term. Thus $\frac{dN}{d\lambda}$ can be rewritten as:

$$\frac{N^3}{2}\left[\frac{1}{\varepsilon_d^2}\frac{d\varepsilon_d}{d\lambda} + \frac{1}{\varepsilon_m^2}\frac{d\varepsilon_m}{d\lambda}\right]$$

Where the two terms in brackets could in general have the same order of magnitude.

These formulas will prove to be useful to evaluate the sensor response in Chapter 6.2.

e. Figure of Merit in conical mounting

As introduced in Chapter 2.1, sensitivity alone does not keep into account the accuracy with which the dip position can be determined; for this reason, the Figure Of Merit represents a more significant parameter to characterize the performance of an SPR sensor.

Thanks to the analysis of the resonance width exposed in Chapter 5.2, we can now examine the evolution of the FOM under conical configuration. What we will find is that the improved performances of SPR sensors under conical mounting are in fact due to the reduction of the FWHM of a mode propagating along a direction different than $\vec{G}$.

Recalling from Chapter 2.2[a] that $FWHM_Y = \frac{W}{k_i}\cdot\frac{\partial Y}{\partial N}$, where Y can correspond to either λ or θ, we obtain:

$$\mathrm{FOM}_Y = \frac{|\Sigma_{n,Y}|}{FWHM_Y} = \frac{\frac{\partial Y}{\partial N}\cdot\frac{\partial N}{\partial n}k_i}{2[\Gamma_i + \Gamma_r(\gamma)]\cdot\frac{\partial Y}{\partial N}} = \frac{\partial N}{\partial n}\cdot\frac{k_i}{2[\Gamma_i + \Gamma_r(\gamma)]}$$

Introducing the trend of Γ_r as a function of the propagation direction, we come to our final result:

$$\mathrm{FOM}_{\lambda,\theta} = \frac{\partial N}{\partial n}\cdot\frac{k_i}{2[\Gamma_i + \Gamma_r(0)\cdot\cos^2\gamma]}$$

As an example, in Fig. 63(a) we plot this function for the same two cases as in Fig. 62, and in Fig. 63(b) the cases relative to a structure with the same parameters but silver instead of gold; radiative losses were assumed to be equal to intrinsic losses at γ = 0°. Since these maps neglect the behavior of the resonance width in the proximity of the merging conditions, as described in Chapter 5.2[d], the blue curves are expected to strongly deviate from the real case around the pink line.

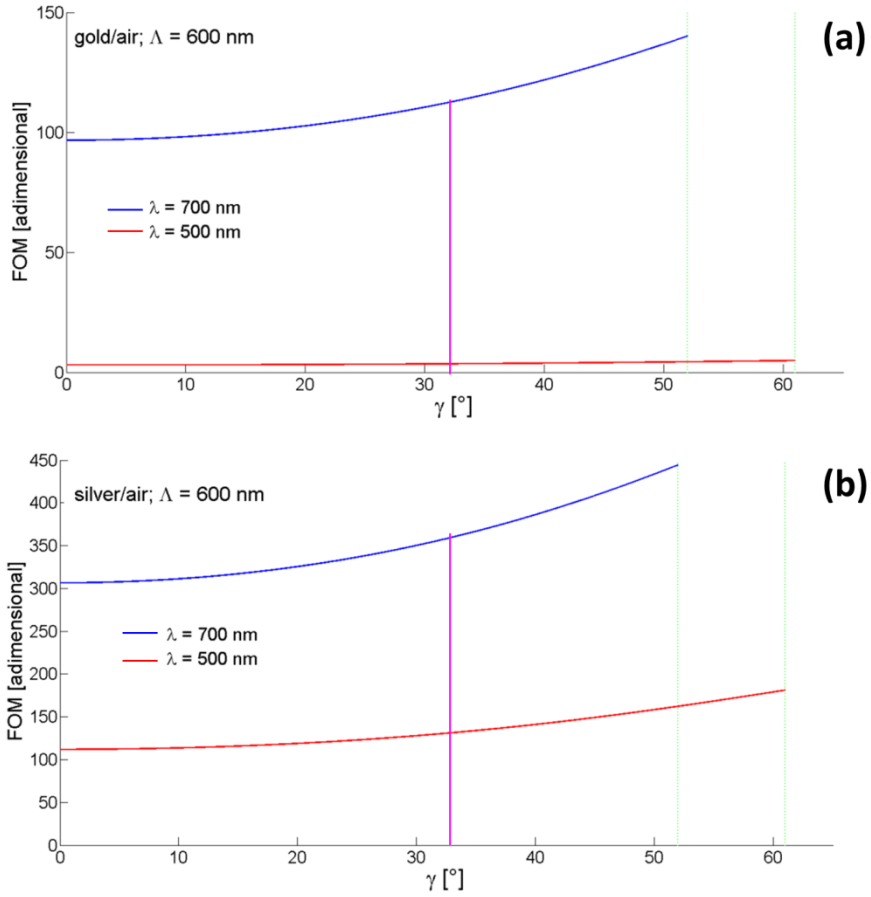

Fig. 63: Trend of the Figure of Merit versus the γ angle for SPP single-interface modes excited through a grating of Λ = 600 nm. Blue curves are for λ = 700 nm and red curves for λ = 500 nm, the green lines marks the maximum γ achievable in each case. It has been assumed $\Gamma_r(0) = \Gamma_i$. (a) Gold/air interface: the mode at λ = 500 nm is strongly suppressed by the resonant absorption of gold around this wavelength. (b) For comparison, the silver/gold case is reported. Higher wavelengths are favoured due to the k_i factor. The pink line marks the merging conditions for the G>β case (blue curve).

6. Sensing applications

The concepts introduced in Section 5 have been applied to the realization of actual sensing devices, in particular for Xylene and other Volatile Organic Compounds, hydrogen and explosives.

The availability of sensing devices capable to detect explosive traces is of great importance to the environmental monitoring of pollution from unexploded land mines, industrial leakage at manufacturing facilities and improper disposal, but most of all to terrorism related safety issues [161; 162]. In order to satisfy the growing demand, currently adopted explosive detection systems require an improvement in term of sensitivity, costs and handiness.
Commonly used explosives are organic compounds and can be classified into six broad classes based on their chemical properties, most of them having extremely low vapor pressures at room temperature, indicating that these molecules are extremely sticky and easily adsorbed by surfaces [163]. Among all the types of explosives, its stability and explosive power make the Trinitrotoluene (TNT) a favorite choice for terrorist activities; for this reason the ability of TNT trace detection on clothes or baggage is crucial to ensure safety of airports and other potential targets.

Rapid and accurate hydrogen detection in air is an essential safety issue related to present and future technology, in order to prevent the possibility of explosions due to mixtures with air [164]. Hydrogen may be produced by many industrial chemical or metallurgical processes, and by undesirable reactions in nuclear plants. Moreover, hydrogen represents a clean, sustainable and abundant energy carrier and chemical reactant, thus the demand for safe production, storage, transportation and application is growing.
At standard temperature and pressure, it is colorless, odorless, tasteless, non-toxic, but on the other hand is volatile and extremely flammable, making it complex to be handled and stored. A leakage of hydrogen more than 4% in volume concentration (the lower explosive limit, LEL) in air would lead to an explosive atmosphere. Many kinds of hydrogen detection techniques are available, with no one showing optimum performance overall, including sensitivity, selectivity, resolution, detection range, cost-effectiveness, stability; the most suitable technology for a certain specific application depends on the operating requirements.

Volatile Organic Compounds (VOCs) are organic chemicals with high vapor pressure at room temperature, resulting in a large evaporation or sublimation from the liquid or solid form into the surrounding air. The need of devices for the detection of some Volatile Organic Compounds is dictated by their dangerousness to human health or to the environment [165].

Aromatic hydrocarbons are a kind of VOCs which constitute a common and serious threat to groundwater reservoirs deriving from contaminated sites, including areas used for fuel operations, refineries, gasoline stations, and gasification sites. Moreover, they are indoor air pollutants emitted by daily life objects and construction materials, such as adhesives, paint, manufactured wood products, cleaning agents, etc. They are strongly related to sick syndrome, such as headache, sickness, skin allergy. In particular, benzene is known to be a strong carcinogen, which is highly mobile in the environment [166].

6.1. TNT sensing

The main pressure towards the development of more sophisticate devices for the detection of explosive traces is due to the growing of terrorist activity.

At the present time, the most common techniques for the explosive detection include ion mobility spectrometry (IMS), mass spectrometry (MS), and gas chromatography (GC). Most of these devices are, however, rather bulky, expensive, and require time-consuming procedures. Thus, the research in explosive trace detection has been moved to nanosensors, thanks to their potentially high sensitivity, miniaturization and scalability [163].

In general explosive nanosensors can be divided into two categories: *receptor-free* and *receptor-based* nanosensors. *Receptor-free nanosensors* are based on detecting physical properties of explosives (e.g. thermodynamic, chemical, or optical properties), while *receptor-based nanosensors* achieve selectivity through the specific interaction between the receptor molecule and the explosive analyte, and they currently are the most explored type of explosive sensors.

Chemical selectivity in explosive detection based on receptors originates from the chemical interaction between the explosive molecules and the receptor molecules. For reversible detection, explosive molecules must bind to the receptors with weak chemical bonds that can be broken at room temperature, like van der Waals interactions or hydrogen bonding.

In this Chapter we present some preliminary results aimed to the realization of a new TNT sensor prototype, in which the high sensitivity achieved by SPR in conical mounting is combined with the use a suitable sensitive layer for TNT detection, well known in literature. A 6-MNA SAM was deposited onto a gold sinusoidal grating and the whole system was then characterized under azimuthal control. The adsorption kinetics of TNT onto the SAM sensing layer was monitored as a function of sensor exposition time to TNT gaseous flow.

a. Estimate of TNT saturation concentration

In order to perform experimental tests of TNT detection, an environment with known TNT concentration has to be provided. The simplest way is to work in the saturation condition, when an equilibrium is established between a TNT source that sublimates and the environment of a small recipient.

When the equilibrium is reached, the concentration can be given with good approximation by the Ideal Gas Law, since low pressures are involved [167]:

$$c = \frac{P}{k_B T}$$

Where P is the pressure, T the temperature and k_B the Boltzmann constant. For a generic substance, the pressure under saturation condition, called "saturated vapour pressure", depends itself on the temperature, according to the Antoine equation [168]:

$$P_{sat} = 10^{\left(A - \frac{B}{C+T}\right)}$$

The A, B and C parameters are called "Antoine constants" and depends on the material. Literature is not unanimous in the determination of the Antoine constants for TNT [168; 169]. Different slopes for the dependence of P_{sat} on the temperature are found, and the reason for this discrepancy is unclear, the only common information being that C = 0 in the temperature range of interest, the

temperature being expressed in the absolute scale, which implies that P_{sat} only vanishes at the absolute zero [170]. Two sets of the Antoine constants at room-temperature are reported in Table 5.

Ref.	Temperature range	A	B [K]
Handbook [168]	293 to 353 K	16.596	5874.238
Pella [169]	287 to 330 K	14.435	5175

Table 5: Two different sets of Antoine constants for TNT, taken from the literature.

Taking the Antoine equation for TNT with C=0, together with the Ideal Gas Law, the saturated vapour concentration can be given by the following formula:

$$c_{\text{sat}} = \frac{10^{\left(\text{A}-\frac{\text{B}}{\text{T}}\right)}}{k_B T}$$

Which quickly increases with the temperature. If A and B are given in SI units, this formula gives the concentration in m^{-3}. The conversion into mass fraction expressed in ppb is obtained introducing the TNT molecular mass, m_{TNT} = 227 amu = 3.769x10^{-25} kg, and the air density, ρ = 1.3 kg/m^3, into the equation:

$$c_{\text{ppb}} = \frac{m_{TNT}}{\rho} \cdot c_{\text{sat}} = \frac{m_{TNT}}{\rho\, k_B} \cdot \frac{10^{\left(9+\text{A}-\frac{\text{B}}{\text{T}}\right)}}{T}$$

With the Antoine constants reported in Table 5, the concentration is calculated and reported in Fig. 64. Due to the exponential growth, a wide range of concentration values can be provided heating the chamber with a common hot-plate, ranging from some tens to some thousands of ppb.

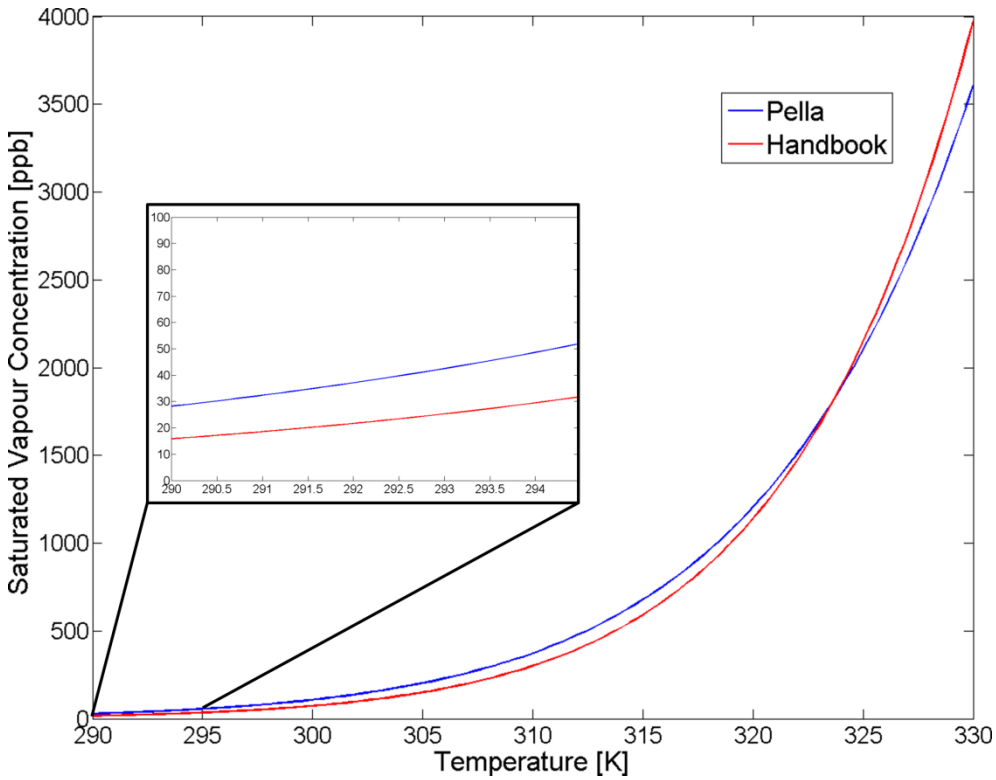

Fig. 64: Saturated vapor concentration as a function of the temperature in the chamber. The two different trends are obtained using the two sets of Antoine constants reported in Table 5. The inset focus the detail of the curves at low temperatures.

In conclusion, the equation allow to estimate the TNT concentration in a saturated environment, with the limitation that, since the correct Antoine constants for our specific TNT sample are unknown, the concentration under our experimental conditions will fall into a certain range of variability.

b. Transient to saturation

An estimation of the time required to the chamber to reach saturation is given, in order to know for how long the sensor will find itself in transient conditions. In order to saturate the chamber, enough mass has to sublimate from a TNT sample and diffuse.

The sublimation rate from a disk of r radius is given by [170]:

$$\frac{dm}{dt} = 4D \cdot r \cdot c_{\text{sat}}$$

where D is the diffusion coefficient. On the other hand, the total mass needed to saturate the V volume of the chamber is $M = c_{sat}V$. Thus the total time τ can be extracted by the integrated expression:

$$\frac{M}{\tau} = \frac{c_{\text{sat}}V}{\tau} = 4D \cdot r \cdot c_{\text{sat}}$$

And it comes to be $\tau = \frac{V}{4Dr}$, that is temperature-independent, because both the sublimation rate and the saturated vapour concentration depend in the same way on the temperature, compensating each other. For an hypothetical volume of 10 cm^3 and r = 1 cm, the time is estimated in about 1 minute.

Diffusion obeys the Fick's law, which states that the flux of particles is proportional to the gradient of concentration, through the diffusion coefficient [167]: $\text{flux} = -D\frac{\partial c}{\partial x}$ .The diffusion time can be estimated as $t \approx \frac{d^2}{D}$ where d is the dimension of the system. The values of the TNT diffusion coefficient found in literature present discrepancies up to the 30%, while its dependence on the temperature is negligible; the mean value is $D = 5.59 \times 10^{-6}\ m^2/s$ [170]. For this estimation a prudent value of $D = 5 \times 10^{-6}\ m^2/s$ could be taken: if d≈10 cm, the formula gives a time of 2000 s, i.e. about 30 minutes.

According to these calculations, the sublimation is relatively fast and the dominant factor is the diffusion. Moreover, the process is approximately temperature-independent. For a chamber of major dimension of less than 10 cm, half an hour is a reasonably overestimated time scale to ensure the saturation of the chamber.

On the opposite, an optimistic estimate may be given by taking the distance of the sensor from the source as the relevant dimension scale, instead of the chamber dimension. For a distance of 5 cm, the transient time goes down to less than 10 minutes, likely underestimated.

c. Adsorption Kinetics

Antoine equation links the concentration into the chamber to the temperature, but experimental data give the plasmonic resonance shift as a function of the temperature. In order to fit the data, a theoretical relation between the shift, Δ_θ, and the concentration has to be provided. This means that the adsorption kinetics of the analyte by the sensitive layer has to be investigated.

The problem can be approached through the model introduced by Langmuir for the adsorption of gas molecules into adsorption centers on a solid surface [171; 172]. Generally speaking, the number N_a of adsorbed molecules evolves according to the following equation, based on a balance between the adsorption and desorption rates [159]:

$$\frac{dN_a}{dt} = k_a N_g (N_{sat} - N_a) - k_d N_a$$

Where N_g is the number of free gas molecules, N_{sat} the maximum possible number of adsorbed molecules (i.e. the total number of adsorption sites, and thus a saturation condition for the layer) and the k_a, k_d parameters determine the rates of adsorption and desorption, respectively. The equation expresses the fact that the absorption rate depends on the number of free molecules and the number of free adsorption centers, while desorption only depends on the number of adsorbed molecules.

Some approximations could be made for our experimental conditions. Since the environment is kept saturated by a TNT source, the molecules reservoir N_g will be kept constant in spite of the adsorption. The desorption rate parameter k_d, that can be rewritten as $1/\tau_r$ for a certain mean residential time of an adsorbed molecule before being released, is expected to be much smaller than k_a, because the sensitive layer is optimized in order to bond to the TNT molecules and hold them for a relatively long τ_r.

Thus the desorption rate may be neglected, meaning that molecules will be go on being adsorbed until the filling of all the sites on disposal, i.e. until saturation of the sensitive layer. A further, reasonable, assumption will be the resonance shift to be proportional to the number of adsorbed molecules, $\Delta_\theta \equiv \sigma N_a$, and in particular $s \equiv \sigma N_{sat}$ will represent the maximum shift at saturation [40].

Eventually, rewriting the equation in term of the TNT concentration into the saturated chamber instead of the total number of free molecules, $k_a N_g \equiv K_a c_{sat}$, we obtain:

$$\frac{d\Delta_\theta}{dt} \approx K_a c_{sat} (s - \Delta_\theta)$$

That can be integrated until a generic τ time to give:

$$\Delta_\theta = s \cdot (1 - e^{-\tau \cdot c_{sat} \cdot K_a})$$

This result is useful to fit the data from a so-called *kinetic measurement*, where a sensor is exposed to an atmosphere saturated of TNT at constant temperature, and the shift of the SPP resonance position over time is measured.

d. Experimental

6-Mercaptonicotinic acid (6-MNA) is well-known in literature as an high performance sensitive element towards TNT detection [142]. As introduced in Chapter 4.1[c], 6-MNA molecules have the tendency to bind to a gold surface forming a self–assembled monolayer.

In order to exploit it as a sensitive layer on an SPR sensor, a sinusoidal master of period 500 nm were fabricated through LIL and replicas were made following the first receipt of Chapter 4.2[c]. The pattern was finally transferred onto a NOA film; a 5-nm thick chromium adhesion layer and a 40-nm thick gold layer were evaporated on the patterned surface.

The presence of the adhesion layer was essential to guarantee the stability of the structure during the cleaning of the surface and the deposition of the 6-MNA layer, because these steps required to expose the samples to liquids.

Success of the sensitive layer self-assembly was checked through the SPR response of the structure.
Fig. 65 shows a plasmonic resonance dip in a spectral scan, for λ = 625 nm at φ = 52° and polarization set to its optimal value α = 140°, taken before and after the exposure to the 6-MNA solution. A shift of 1.2 ± 0.1 is observed.

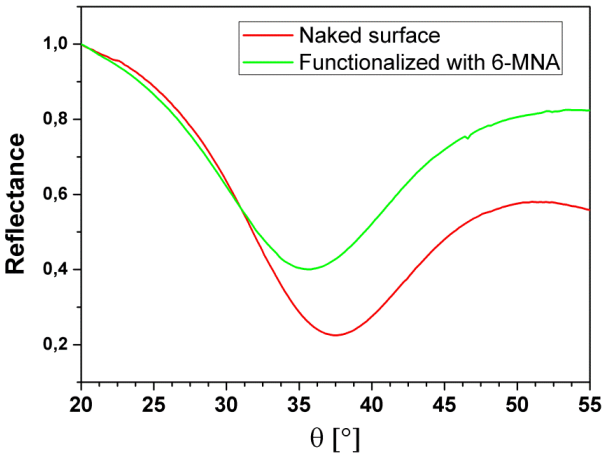

Fig. 65: Spectral scans with parameters: λ = 625 nm, φ = 52° and α = 140°, before (red curve) and after (green curve) the deposition of 6-MNA over the gold surface; it shows the SPR response to the functionalization.

The TNT detection test was performed by mounting onto the ellipsometer the usual incubation chamber (see Chapter 4.4[a]), of main dimension of about 10 cm. Inside the chamber, an aluminium box containing the TNT powders was placed at about 5 cm from the sample holder, where the sensor was fixed. After sealing the chamber, the sysem was left at room temperature for the time needed to reach the environment saturation and then sensing measurements were performed.

The chamber windows allowed a single entering angle for the incident light, corresponding to an incidence angle of 70°; spectra were then collected in spectral scan. A kinetic measurement was performed at room temperature, collecting data points at scheduled times after the beginning of the exposition: 30, 45, 60, 90, 120 min and overnight.

e. Results

The collected spectra of the TNT kinetic measurement are reported in Fig. 66.
The first spectrum was collected as a reference before the exposition to TNT; the second was taken after 30 minutes to ensure that chamber saturation had been reached. The SPR response after 30 minutes suggests that this time was reasonably overestimated as a transient.

The errors on the dips positions were provided by Lorentzian fits of the SPRs and then propagated to the shifts; the shift of the resonance dip as a function of the incubation time was fitted with the Langmuir formula for the adsorption kinetics, as reported in Fig. 67.
The output gave a shift at saturation s = 17.91 nm, and a characteristic time scale of the exponential of $c_{\mathrm{sat}} \cdot \mathrm{K_a} = 0.003\ \mathrm{min}^{-1}$.

The concentration was estimated, by applying the Antoine equation, to be in the range 45 ± 15 ppb, depending on the chosen set of Antoine constants, at a temperature of 22 ± 1 °C.

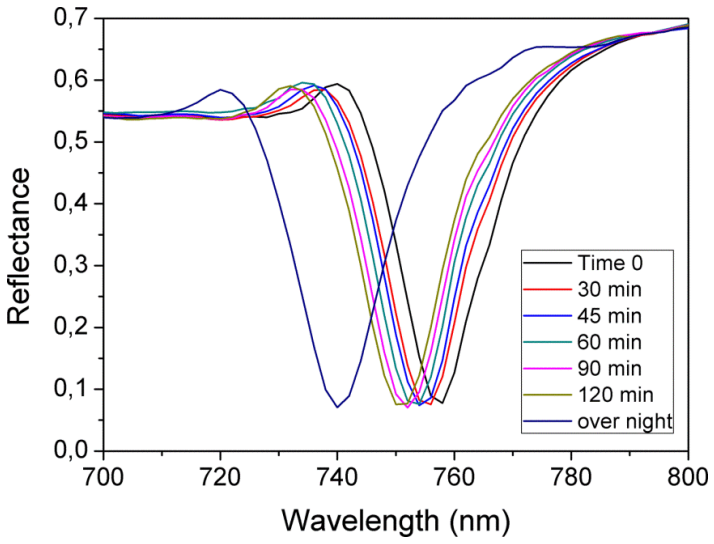

Fig. 66: Experimental spectra collected at scheduled times, being time = 0 the moment in which the sample was put into the incubation chamber together with the TNT source. The last measure was taken after one night, for a total of about 17 hours.

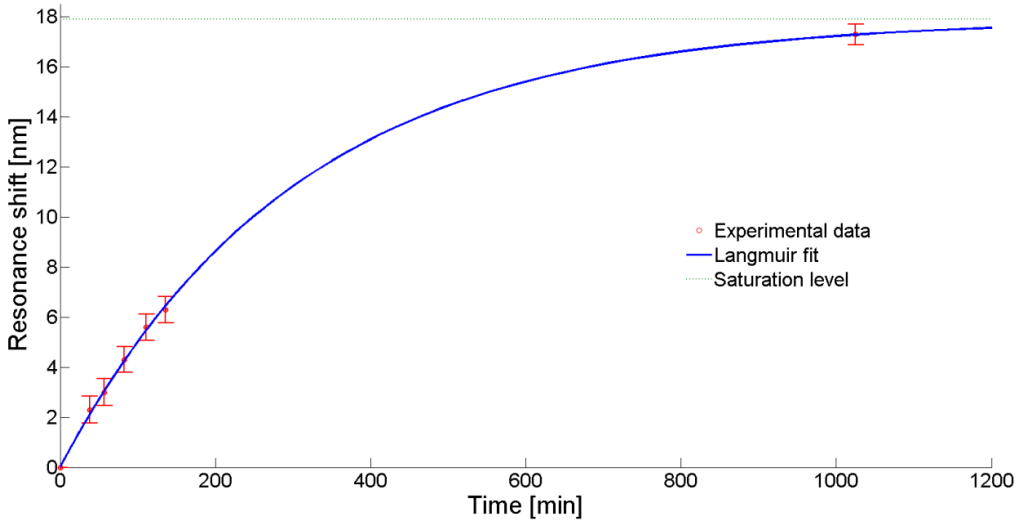

Fig. 67: Fit of the experimental data points with the Langmuir formula; errors on the dips positions were provided by Lorentzian fits and propagated to the shifts. The saturation level indicated by the green dotted line is an output of the Langmuir fit and corresponds to a shift of 17.91 nm.

In conclusion, we performed an experiment that demonstrates the possibility to detect TNT traces down to concentrations of a few tens of ppb, combining the azimuthally rotated SPR approach with a standard SAM-based sensitive layer. The response of the sensor in time has been investigated by studying the adsorption kinetics at room temperature. A perceivable shift is observable after less than 30 minutes and saturation is reached within 20 hours.
These results are to be intended as preliminary, and they open the way to a number of improvements, including optimization of the sensor structure and the sensing configuration, and tests against other explosives.

6.2. H_2 and VOCs sensing with a nanocomposite matrix

In this Chapter, the SiO_2 and TiO_2 based functional materials described in Chapter 4.1[c] will be exploited as sensitive layers for both hydrogen and aromatic hydrocarbons; the main difference between the two materials is that the SiO_2 is an insulator while the TiO_2 is a semiconductor.

Good performances are obtained with both the sensitive layers, including the possibility to distinguish the interaction with hydrogen from the one with VOCs looking at the direction of the SPR dips shift.

Although in this case all measures were taken at null azimuth, theoretical approaches and methods introduced in Section 5 came into aid in the identification of the resonances and interpretation of the results.

a. Experimental

Two kinds of plasmonic crystals were fabricated by Nano-Imprinting Lithography on a 200-nm patternable ph-PSQ film treated at 500°C, as described in Chapter 4.2. The period of these gratings was of 570 nm, as confirmed by AFM characterization.
Over some of them the SiO_2 solution was spin-coated as a sensitive layer, and the TiO_2 solution over the others. All the thin films were deposited by spin coating at 3000 rpm for 30 s over the metallic gratings, dried at 100°C for 5min and finally annealed in a muffle furnace at 300°C for 1 h in air. With the same procedure, the same films were also deposited over flat SiO_2 substrates to perform spectroscopic ellipsometry (see 4.4[b]).

Thickness and refractive index of the functional layers have been measured by spectroscopic ellipsometry on the flat samples, in the 400-1500 nm wavelength range. The results gives a thickness of 180 nm for the SiO_2 film and of 130 nm for the TiO_2 film; their refractive index is reported in Fig. 68, compared to that of the ps-PSQ underlying film.

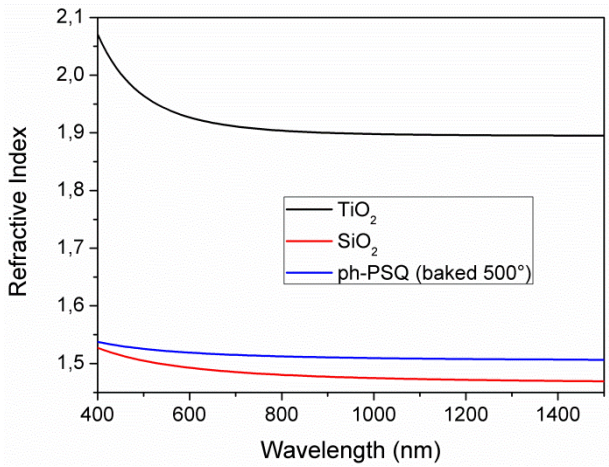

Fig. 68: Refractive indices of the three functional materials involved in the structures in exam.

In order to evaluate the effective symmetry of these structures, we calculated the effective refractive index approximately perceived by an SPP propagating along the film, according to EMA (as introduced in Chapter 1.4[a]). EMA was applied considering a single-interface SPP mode on a silver surface, with the boundary conditions of an infinite semi-space filled of air over the sensitive layer and an infinite quartz substrate under the ph-PSQ layer. The resulting dielectric functions

are plotted in Fig. 69, showing that SiO_2-based structures are symmetrical at low wavelengths and TiO_2-based at wavelengths around 930 nm.
When the structures are effectively symmetrical, they can support the thin-film coupled modes as described in Chapter 1.2.

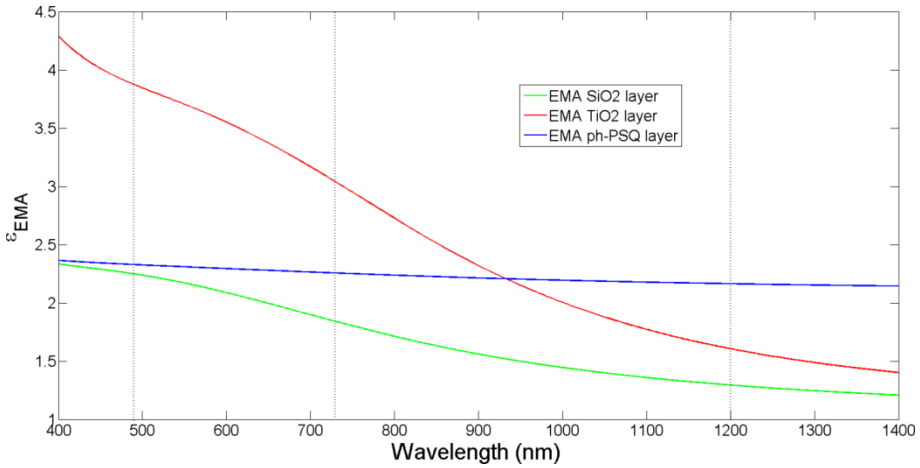

Fig. 69: Effective dielectric functions evaluated by EMA for the actual structures in exam. The green and red curves represents the ε_{EMA} for the upper half-space for SiO_2 and TiO_2 structures, respectively, while the blue curve represents the ε_{EMA} for the lower half-space. Thus where the green or red curve is close to the blue one, the corresponding structure is effectively symmetric. The vertical dotted lines locate the wavelengths at which the observed resonances fall.

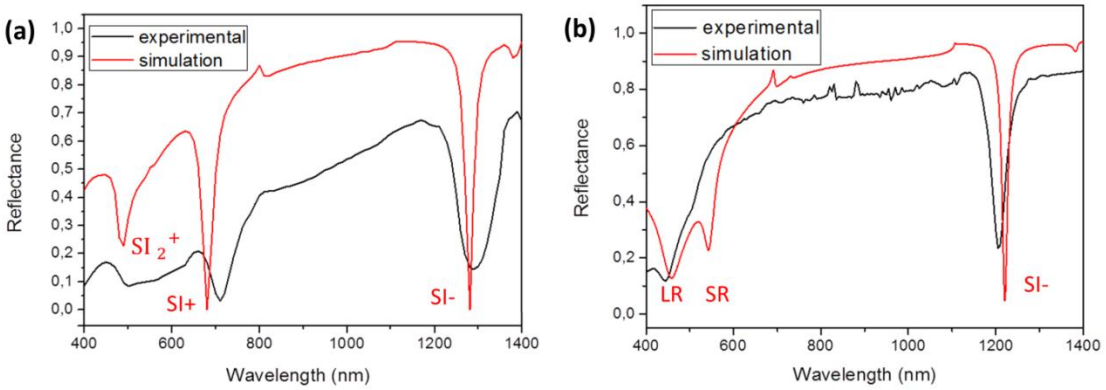

Fig. 70: Experimental reflectance spectra (black lines) compared to simulations (red lines) for the plasmonic crystals with: (a) TiO_2 sensitive layer and (b) SiO_2 sensitive layer. The illumination is front-side at a fixed incidence angle of 70° and null azimuth. The nature of the modes is identified through comparison to their theoretical momenta, as follows: the dips labelled SI corresponds to single-interface modes, with a sign indicating if the coupling is additive or subtractive and a number "2" for a mode coupled through the second diffraction order, while LR is a Long Range and SR a Short Range.

In Fig. 70 typical experimental reflectance spectra are shown, compared to the simulated one, at an incident angle of 70° and null azimuth, for both the fabricated plasmonic crystals. A set of dips can be seen, associated to the resonant coupling of the incident radiation with SPP modes supported by the thin-film structure. The simulations are in good agreement and the nature of the modes can be identified through a comparison with theoretical expectations, provided by the EMA analysis and the methods of Chapter 5.1.

All the modes labelled SI are recognized as Single-Interface modes on the upper surface of the metal layer. In particular, the SI- modes are excited via subtractive coupling, i.e. $\beta = G - k_T$, since they falls into the G>β case; on the opposite, the mode labelled SI+ is excited via additive coupling, $\beta = G + k_T$, being into the G<β case. At, lower wavelengths the spectrum of the TiO_2-based structure presents an SPR dip corresponding to a second order additive excitation, $\beta = 2G + k_T$, thus it is labelled as SI_2^+. Finally, the SiO_2-based structure is effectively symmetrical at low wavelengths, according to the EMA analysis reported in Fig. 69; in fact, coupled modes (Long Range, LR, and Short Range, SR) are visible in the simulated spectrum, even if only partially in the experimental one, where the SR SPP seems to be suppressed.

The quite well defined dips, SI- and SI+, will be exploited for the sensing tests. We can give an estimation of their refractometric sensitivity, using the formulas derived in Chapter 5.4[d]; for single-interface modes and with θ=70°, the refractometric sensitivity is given by:

$$\Sigma_{n,\lambda} = \left(\frac{N}{n}\right)^3 \cdot \frac{2\lambda N}{\frac{\lambda^2}{\Lambda^2} + N^2 - 0.883 - \lambda \frac{N^4}{2}\left[\frac{1}{\varepsilon_d^2}\frac{d\varepsilon_d}{d\lambda} + \frac{1}{\varepsilon_m^2}\frac{d\varepsilon_m}{d\lambda}\right]}$$

For the cases of interest, it gives the values reported in Table 6. The sensitivities are comparable, with a slight enhancement at lower wavelengths.

Resonance region		$\boldsymbol{\Sigma_{n,\lambda}}$ ***(estimated)***
TiO_2	700 nm	650 nm/RIU
	1200 nm	600 nm/RIU
SiO_2	1200 nm	580 nm/RIU

Table 6: Estimation of the refractometric sensitivity in spectral scan for the resonances of interest.

b. Hydrogen sensing

Although great number of hydrogen sensors is found in literature, based on many different operation principles, each one presents specific advantages and disadvantages that make it suitable for some applications and unsuitable for others [164].
Optical sensors are safe, since they do not provide a potential source of ignition in explosive atmospheres, and they are almost unaffected by electromagnetic noise. Grating-based SPR sensors have the further advantage of great miniaturization and integration possibility.

Usually, this kind of devices exploit a thin palladium layer as a sensitive layer [173; 174] because palladium acts like a catalyst to split the H_2 molecules into atomic hydrogen. As a drawback, palladium makes the structures susceptible to mechanical damage on exposure to hydrogen.

We propose a grating-coupled SPR sensing device for hydrogen detection, fabricated with low-cost techniques and materials, avoiding the use of palladium, or other expensive materials like platinum. The possibility to detect little volumetric concentrations down to 1% is demonstrated.

Gas sensing tests have been performed at 300 °C, with H_2 10000 ppm, in N_2 flux with a flow rate of 0.4 L/min. Reflectance spectra have been acquired, scanning the wavelength in the 300-1500 nm range. The results are reported in Fig. 71 and in Table 7 for the two main dips of the TiO_2 sample and the only well-defined dip of the SiO_2 phenyl functionalized sample. The exposure of the

sensor to the gas produces a blue shift of all the resonances. Both layers demonstrated to be sensitive to low concentrations of hydrogen, down to 10000 ppm.

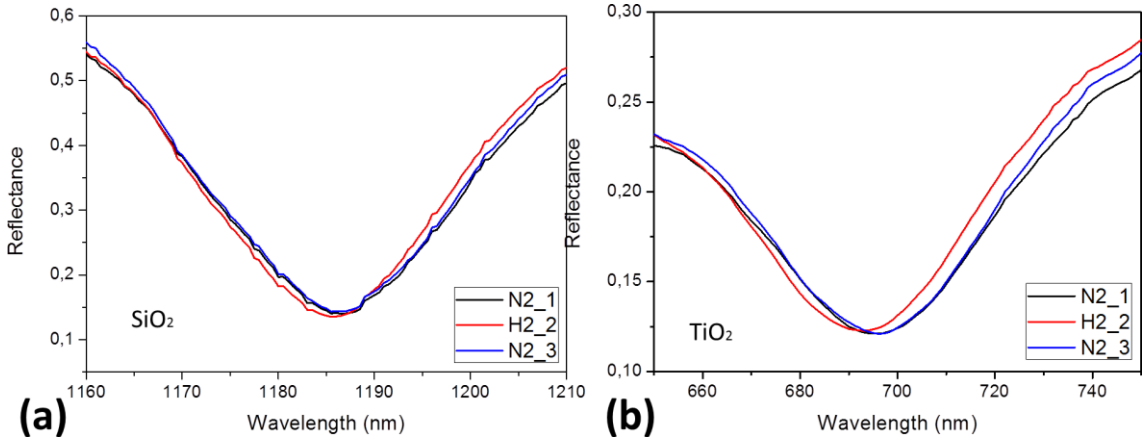

Fig. 71: Sensing tests towards hydrogen at 300°C with sensitive layer of (a) SiO_2 and (b) TiO_2.

Resonance dip		*Shift*
TiO_2	700 nm	3 nm
	1200 nm	1 nm
SiO_2	1185 nm	1 nm

Table 7: Shift of the SPR dips under H_2 flux.

Comparing the performances of the two different sensitive layers with the expectances, we observe that the much greater response of the dip of the TiO_2 at 700 nm is hardly justified by the refractometric sensitivity alone. Moreover, neither of the two layers prove to be sensitive at room temperature.

Further investigations are in progress to understand the reason for this discrepancy, that we believe to be due to the different nature of the sensitive layers, since SiO_2 is an insulator and TiO_2 is a semiconductor. A hint comes from the nature of the interaction mechanism with the analyte, that is presumed to be related to the injection of electrons, provided by the reducing reaction of H_2, into the conduction band of the sensitive material [175]. In both materials, at high temperature the oxygen vacancies in the oxide matrix result in the formation of intragap states in the band gap. At room temperature they are absent, but at 300°C they constitute the crucial element that allows the injected electrons to jump to the conduction band, increasing the free electron density and thus affecting the optical properties. In addition, since the TiO_2 has a band gap of 3.2 eV, an energy that falls in the near UV, it is reasonable that lower wavelengths can promote the electronic transition, resulting in an enhanced response.

c. Aromatic VOCs detection

As introduced at the beginning of this Section, aromatic hydrocarbons are a threat for health and environment, resulting in a growing the demands for simple, cost-effective, selective and highly-sensitive methods of detection is growing. The sol materials introduced in the previous Paragraphs are promising candidate to monitor A-VOCs because of the strong interaction between

the benzene rings of the target gas with the phenyl group of the SiO_2 matrix [176], or with the Ti^{4+} group in the case of the TiO_2 matrix [177].

The tests have been performed at room temperature, with three different Aromatic Volatile Organic Compound (A-VOC), namely benzene 30 ppm, toluene 30 ppm and xylene 10 ppm, in air flux with a flow rate of 0.4 L/min.

Fig. 72 shows some reflection spectra of the samples TiO_2 and SiO_2 phenyl functionalized when exposed to multiple air-A VOC cycles, producing a red-shift of the dips. The results of the sensing tests are summarized in Table 8.

Again, the dip at lower wavelength proves to be the most sensitive. The comparison between the performances of the two sensitive layers at high wavelength suggests a superior efficiency of the sensing mechanism of the SiO_2 phenyl functionalized. However, a deeper investigation should be performed in order to understand the reasons of this discrepancy.

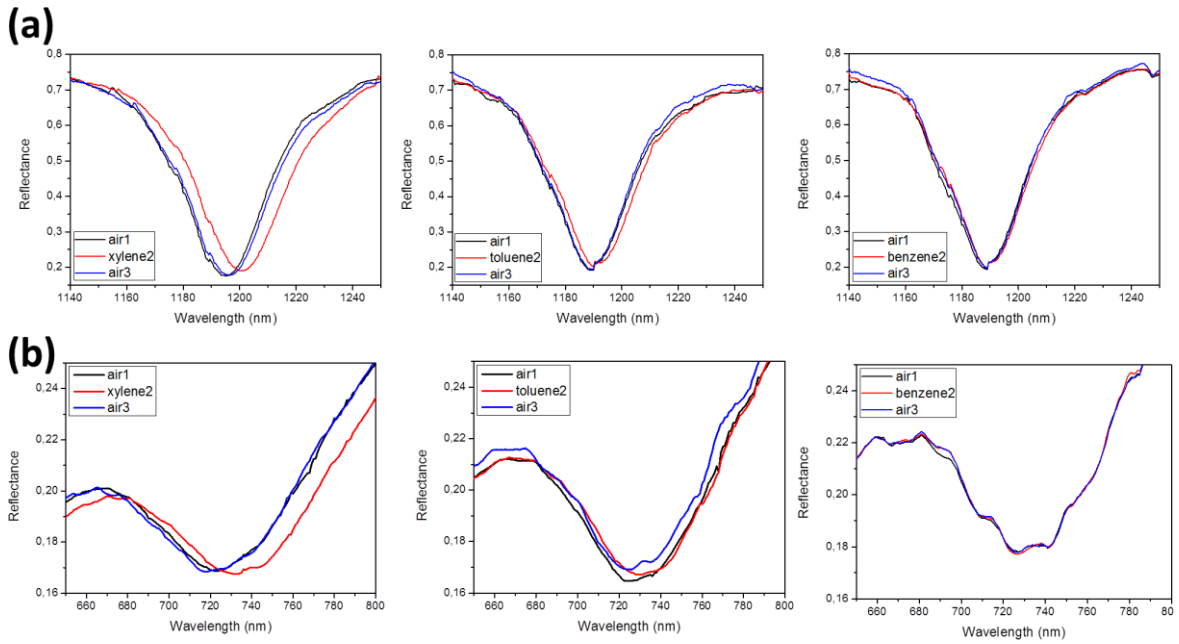

Fig. 72: (a) Sensing test with xylene, toluene and benzene on the plasmonic crystal with sensitive layer of SiO_2 phenyl functionalized; (b) Sensing test with xylene, toluene and benzene on the plasmonic crystal with sensitive layer of TiO_2 (dip at 730nm).

Analyte	Shift of the SPR at 1250 nm (TiO_2)	Shift of the SPR at 730 nm (TiO_2)	Shift of the SPR at 1190 nm (SiO_2)
Xylene	2nm	11nm	6 nm
Toluene	1nm	5nm	2,5 nm
Benzene	/	/	0,5 nm

Table 8: Measured shifts in the sensing tests of the two sensitive layers towards A-VOCs.

A clear information that emerges from the data is that the shift increases with the number of CH_3 groups in the A-VOC molecules: no one for benzene, one for toluene and two for xylene. This is in accordance with the literature, since the binding of the VOCs to the sensitive layer is expected to be promoted by this group [178]. In addition, since this mechanism is based on the subtraction of

electrons from the sensing material, the opposite response, in term of direction of the shift, with respect to the hydrogen case is reasonable.

d. Conclusions

Both sensitive materials, one insulating and functionalized with phenyl groups and the other semiconductor, showed good optical response, with reversible dynamics, towards different kinds of analytes.

Hydrogen detection, characterized by a blue shift of the SPR dips, have been demonstrated down to 10000 ppm at 300 °C; detection of 30 ppm of benzene, toluene and xylene has also been achieved at room temperature.

Further investigations are suggested in order to well understand the mechanisms of interaction between the analytes and the sensitive layers, but such analysis is beyond the purposes of the present work.

6.3. Xylene sensing with coupled modes in conical mounting

Sinusoidal surface plasmon metallic gratings (SPGs) were fabricated, embedded in a functional material, phenyl-bridged polysilsesquioxane (ph-PSQ). The metal layer is in contact with the environment through the sol-gel film, that works as sensitive element, changing its dielectric properties upon interaction with aromatic hydrocarbons. The combination of sensitivity, transparency and patternability offered by ph-PSQs gives the exceptional possibility to fabricate innovative optical sensors with straightforward processes. An embedded SPG is a thin metal slab waveguide, in which coupled modes introduced in Chapter 1.2 can be excited. An extended experimental and theoretical characterization of the optical properties of the plasmonic device was performed. The sensor performance was tested against the detection of 30 ppm xylene, monitoring the influence of the target gas on the SPPs modes. A reversible red-shift of the reflectance dips of both LR and SR SPP resonances in the 1.9-2.9 nm range was observed and correlated to the interaction with the analyte. An enhancement in sensitivity associated with the rotation of the grating grooves with respect to the scattering plane (azimuthal rotation) was verified within the experimental errors. Collected data are compatible with theoretical predictions assuming a variation of the film refractive index of 0.011 ± 0.005.

a. Experimental

Nanostructured plasmonic sensors were fabricated as sinusoidal SPGs embedded in a porous sol-gel film of ph-PSQ, following the procedure described in Chapter 4.2. Ph-PSQ is an organic-inorganic hybrid sol-gel material synthesized by acid catalyzed sol–gel process from phenyl-bridged silsesquioxane (ph-SQ) precursors (see Paragraph 4.1[b]). It has the crucial property of being suitable both as a patternable material for soft lithography at the nanoscale and as a sensitive layer. In fact, recognition elements for the analyte are incorporated in the hybrid network, that presents a large specific surface area due to his porosity.

The ph-PSQ films were deposited by spin coating on the substrates, tuning solution concentration in EtOH and/or spin coating speed in order to obtain, after a thermal treatment at 80 °C for 30 min, a thickness of about 200 nm. The post deposition bake is necessary to promote solvent evaporation and to reach a stable cross-linking degree.

Before metal deposition, the ph-PSQ film coating the fused silica slab was patterned through Nano Imprint Lithography using soft stamps, which are elastomeric replica of masters. The employed masters had been fabricated through Laser Interference Lithography on commercial resist films

and exhibited a sinusoidal pattern, of 570 nm pitch and 70 nm peak-to-valley height. The substrate size was approximately 2×2 cm^2. The fabrication process consists in the realization of negative replica made of polydimethylsiloxane (PDMS) of the nanostructured masters, and in the pattern transfer by soft NIL on ph-PSQ films coating fused silica slabs, obtaining a uniformly patterned area of about 1.5×1.5 cm^2. The fabricated sinusoidal patterns, positive replica of the master structures, were imaged through an AFM in non-contact mode for a morphological characterization.
Then, a metallic bilayer made of 7 nm of gold (Au) on top of 37 nm of silver (Ag) was deposited in vacuum onto the sinusoidal ph-PSQ gratings; AFM images of the metalized sinusoidal structures were again recorded to characterize the structure morphology. Finally, the sensitive layer deposition was performed: a ph-PSQ film was spin-coated on top of the metallic grating, setting the same deposition parameters as for the first resist film. The sample was thermally treated at 80 °C for 30 min to promote solvent evaporation.
The functionality of ph-PSQs is conveyed by the presence of an organic group incorporated into the hybrid network, the benzene ring, which interacts through an affinity binding, reasonably a π - π stacking, with aromatic hydrocarbons [176; 179]. In particular, in the present work the study is concentrated on the detection of xylene molecules. An annealing treatment at 300 °C for 30 min was made on the samples before gas sensing tests, in order to stabilize the structure in terms of cross-linking degree, and to promote outgassing of adsorbed species.

Ph-PSQ films are optically transparent and they were deposited on transparent fused silica substrates, thus allowing the two illumination configurations: the standard 'direct' illumination condition, with the light beam incident on the sensitive layer first, and the 'reverse' side mode illumination, with the light beam incident on the substrate first [180].
Optical characterization of the structures was performed by collecting reflectance spectra using a variable-angle spectroscopic ellipsometer and comparing them to simulated spectra, produced through Chandezon's method (see Chapter 3.1). The SPP modes can be identified by the values of their momentum.

In order to test the gas sensing performance, samples were mounted in gas chambers optically coupled to the ellipsometer and reflectance spectra were recorded.
The sensor was probed in a direct illumination condition, when using the customized commercial cell shown in Chapter 4.4[a], equipped with fixed input and output windows perpendicular to the incoming and reflected beams. In this case, measurements could be carried out at a single, fixed angle of incidence of 70°. Alternatively, the sensor was mounted in reverse side mode inside a home-made gas [180].
The sample was probed on the back side, and reflectance data could be collected at different values of the angle of incidence.

Spectra were recorded during successive cycles of exposures to nitrogen (N2, the carrier) and to xylene at a concentration of 30 ppm xylene (10 ppm orto-xylene, 10 ppm meta-xylene, and 10 ppm para-xylene concentration in N2), being the exposure to N2 atmosphere aimed to regenerate the sensor. Plasmonic dips were monitored, and their angular shift for a fixed wavelength of the incident light beam, or their red-shift for a fixed angle of incidence, were correlated to the interaction with the analyte.
Such measurements were repeated for a number detection/regeneration cycles, each exposure step lasting few tens of minutes. The sensor was mounted in the null azimuth and in the azimuthally rotated configuration, choosing the wavelengths and incidence angles giving the best

SPR response for each configuration. A comparison between the reflectance signals in the two controlled atmospheres was performed to estimate sensor sensitivity.

b. Characterization of the plasmonic structures

An analysis of the surface morphology of the imprinted ph-PSQ layer, before metal deposition, and of the SPGs has been performed using AFM in non-contact mode. Fig. 73 shows the 2D image of the sinusoidal profile transferred onto ph-PSQ films. The grating periodicity is 570 nm while the peak-to-valley height is 70 nm, with a few percent precision due to AFM calibration issues. In Fig. 74 the 2D image of the sinusoidal structure obtained after metal evaporation are shown. The grating periodicity and the peak-to-valley height are basically unchanged within the experimental errors, and the estimated roughness of the metal coating is of 2.7 nm RMS. The sensitive layer was also deposited on the SPG by spin coating.

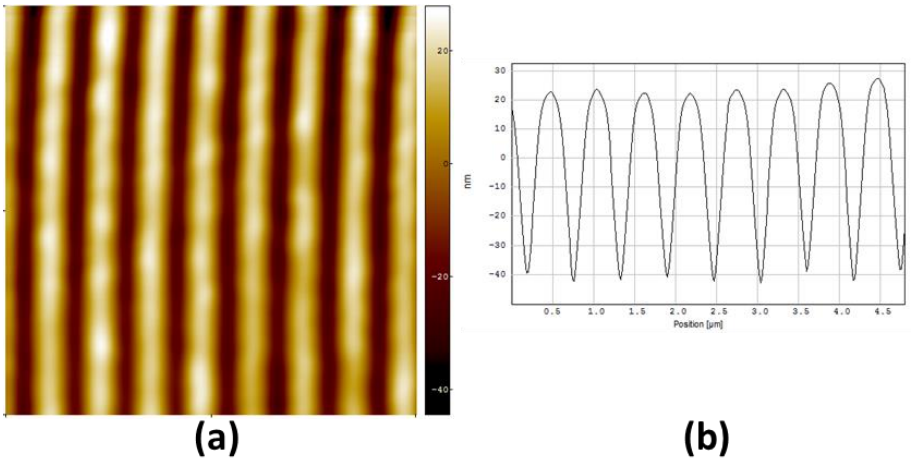

Fig. 73: (a) 2D AFM recording of a ph-PSQ film, imprinted using a PDMS replica of a sinusoidal master. The scanning area is of 5x5 µm². (b) Cross-sectional profile of the pattern obtained averaging about one hundred scanned lines.

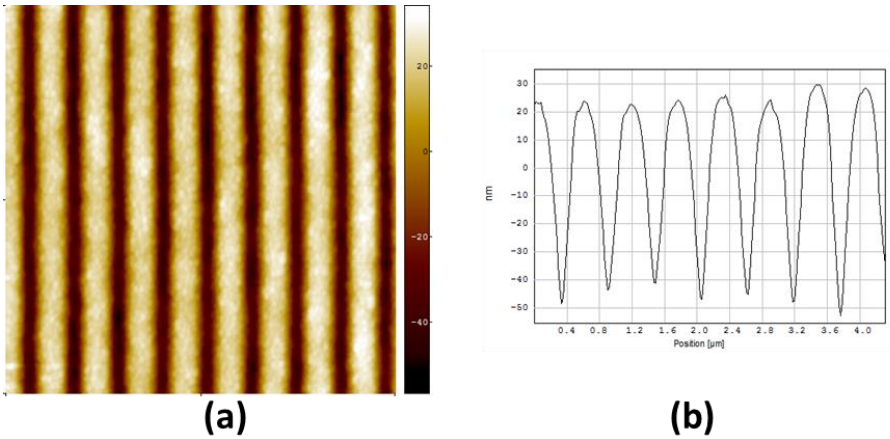

Fig. 74: (a) 2D AFM recording of a SPG, before deposition of the sensitive layer on top. The scanning area is of 5x5 µm². The roughness of the metal coating is 2.7 nm RMS. (b) Cross-sectional profile of the pattern obtained averaging about one hundred scanned lines.

Figures from Fig. 75 to Fig. 77 show the reflectance spectra of a fabricated sample, both experimentally measured and simulated. Well defined dips corresponding to single-interface SPPs are observed for SPGs, before the deposition of the sensitive layer, in standard illumination configuration of the surface (Fig. 75).

The spectra are perfectly reproduced by simulations with the Chandezon's method.
Attention has to be paid when reverse illumination is simulated: since the program deals with layers much thinner than 1 mm, the sample substrate is treated as an infinite half-space. This means that the program works as the light source was into the glass; in order to compare simulated spectra with experimental ones, they have to be transformed using the Snell's Law into the realistic case of light entering the glass substrate from air.
After deposition of the sensitive layer, the sensor structure is symmetric, and two coupled plasmonic modes are observed in both configurations for sensor illumination. The two dips in the reflectance curves, for a fixed wavelength of the incident light, have been identified by the values of their momenta as LRSPP and SRSPP. Also in this case, simulated curves show a good agreement with experimental data (Fig. 76 and Fig. 77).

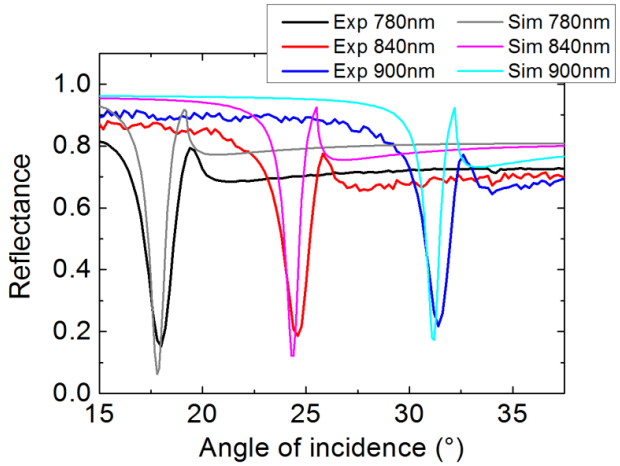

Fig. 75: Experimental and simulated reflectance spectra of a SPG, before sensitive layer deposition, for p polarized incident light in standard illumination mode, and null azimuth. The spectra are reported as a function of the angle of incidence for a set of wavelengths in the 780-960 nm range. They show a single dip for each wavelength, which is a single-interface SPP.

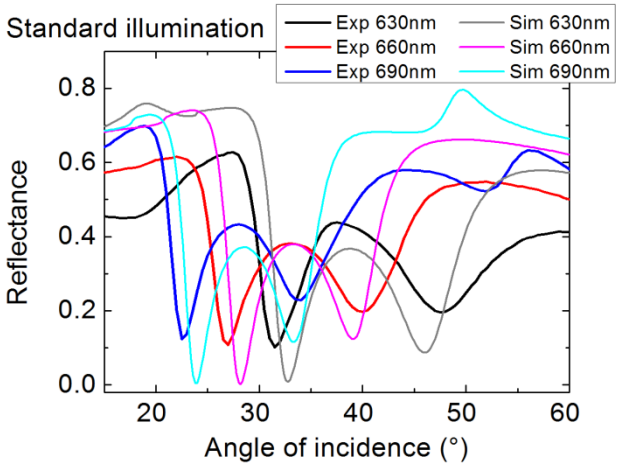

Fig. 76: Experimental and simulated reflectance spectra of a SPG embedded in ph-PSQ films, for p polarized incident light in standard illumination mode, and null azimuth. The spectra are reported as a function of the angle of incidence for a set of wavelengths in the 630-690 nm range. They show two dips for each wavelength: the LRSPP at smaller angles, the SRSPP at higher angles of incidence.

The resonance depth is probably altered by the surface roughness, which was not taken into account in the numerical simulations. Moreover, the experimentally observed dip widening

provides an indication of the degree of disuniformity of the grating within the illumination spot of the ellipsometer. The spectrum in Fig. 77 is taken under reverse side illumination. Thanks to the symmetry of the structure, the angular position of the dips is the same they have in the standard illumination mode.

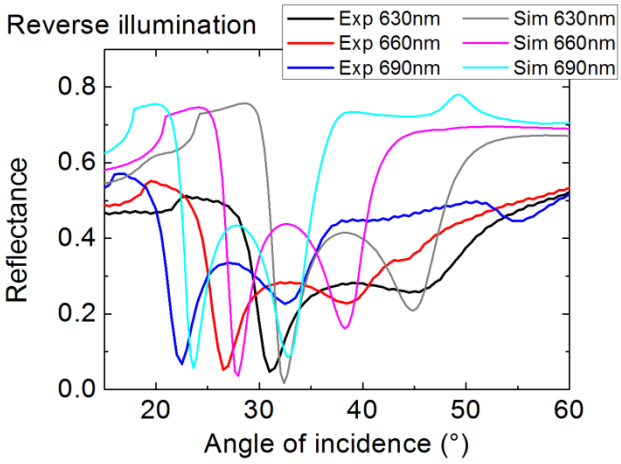

Fig. 77: Experimental and simulated reflectance spectra of a SPG embedded in ph-PSQ films, for p polarized incident light in reverse side illumination mode, and null azimuth. The spectra are reported as a function of the angle of incidence for the same set of wavelengths as in figure 6. They show the LRSPP at smaller angles, the SRSPP at higher angles of incidence.

The results of the modal analysis carried out with COMSOL for the complete plasmonic architecture are shown in Fig. 78, Fig. 79 and Fig. 80. In Fig. 78(a) the real part of the Transverse Magnetic (TM) plasmonic mode dispersions is superimposed to reflectance maps obtained with the Chandezon's method, illuminating the structure from the air side with p polarized light. Two modes appear from the modal analysis, which are clearly correlated to reflectance dips. An inspection of the eigenmode magnetic field profiles, in the direction orthogonal to the incidence plane, into the multilayer structure (Fig. 79) allows to identify the modes as one LR SPP (symmetric magnetic field profile) and one SR SPP (antisymmetric magnetic field profile). Propagation length and penetration depth of the plasmonic modes are calculated from the imaginary part of the propagation constant. This is readily obtained with the present analysis by taking the imaginary parts of the calculated complex eigenvalues. In Fig. 78(b) we report the imaginary part of the LR SPP and SR SPP propagation constants in flat structure approximation (black dots) and for a sinusoidally corrugated structure of 570 nm period and 70 nm peak-to-valley height (blue dots). A relevant increase, almost an order of magnitude for the LR SPP mode, in the imaginary parts is found in presence of a sinusoidal modulation of the surface. Such behavior is mainly ascribed to strongly increased radiative losses, as explained in Chapter 1.3[d]. The values of the propagation constants and penetration depth obtained at 633 nm wavelength of the incident light are reported in Table 9.

In Fig. 80 the same analysis is performed for the Transverse Electric (TE) polarization case. One single mode is found which corresponds to a narrow dip in reflectance. The mode is a waveguide mode of the upper dielectric layer (exposed to the environment), of the kind introduced in Chapter 1.4[c], as can be verified looking at the electric fields calculated with a modal analysis (Fig. 80(b)).

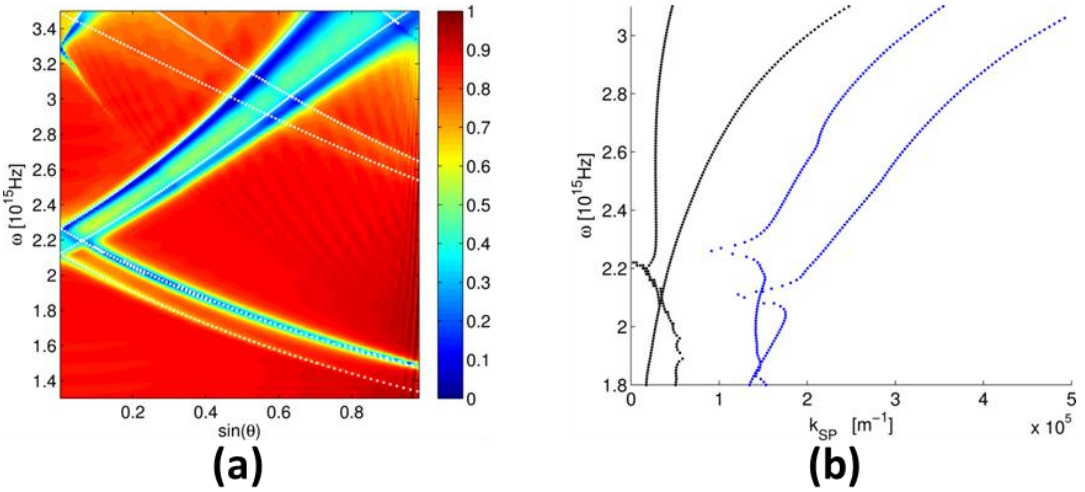

Fig. 78: (a) Scatter plot of the TM eigenmodes of the structure calculated by COMSOL (white dots) superimposed to the TM reflectance calculated through the Chandezon's method. (b) Dispersion relation of the imaginary part of the propagation constant for the plasmonic modes in flat structure approximation (black dots) and for a sinusoidally corrugated structure of 570 nm period and 70 nm peak-to-valley height (blue dots).

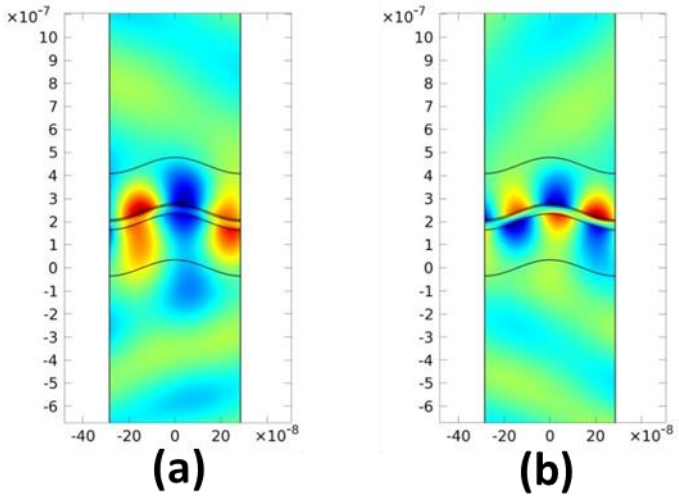

Fig. 79: Profiles of the magnetic field component orthogonal to the incidence plane into the multilayer structure calculated with the modal analysis at λ = 633 nm: (a) shows the symmetric Bloch mode, or LRSPP and (b) the antisymmetric Bloch mode, or SRSPP. In the plot, the orthogonal and vertical axis scales are in units of meter.

λ = 633 nm	**LRSPP**	**SRSPP**
Propagation length	3 μm	2 μm
Penetration depth	115 nm	85 nm

Table 9: Estimates of propagation length and penetration depth of the excited LRSSP and SRSSP, for incident wavelength λ = 633 nm.

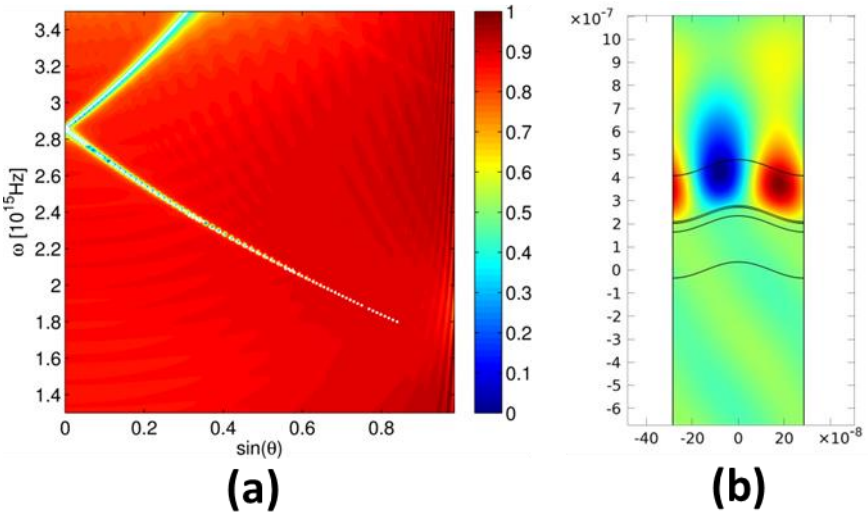

Fig. 80: (a) Scatter plot of the TE eigenmodes of the structure calculated by COMSOL (white dots) superimposed to the TE reflectance calculated by means of the Chandezon's method. (b) Distribution of the electric field component orthogonal to the incidence plane, calculated with the modal analysis at λ = 710 nm. This is identified as a waveguide mode guided into the sensitive layer. In (b), the orthogonal and vertical axis scales are in units of meter.

c. Xylene sensing with LR and SR SPPs

For gas sensing tests, reflectance spectra were acquired in N2 atmosphere and in the presence of xylene at a concentration of 30 ppm, after exposing the sensor alternatively to the two different environments for tens of minutes. In this way, gas molecules were reasonably given the time to diffuse through the sensitive layer until a dynamic equilibrium with the environment was achieved. The data acquisition time for a single spectrum varied, according to the investigated wavelength range, from a few minutes to a few tens of minutes. Thus, the amount of detected analyte molecules interacting with the sensitive porous film underwent a negligible variation during spectra acquisition.

Exploring the output of gas sensing preliminary tests (not shown) revealed the importance of a pre-annealing step at 300 °C for 30 min on the plasmonic sensors, to achieve a long-term stability for the cross-linking degree of the sol-gel film, and to promote the elimination of adsorbed species. Fig. 81 shows the reflectance spectra of the sensor after the thermal treatment at 300 °C in standard illumination mode at a fixed incidence angle of 70° at null azimuth (a), and at 60° azimuth (b). Since coupling strength and plasmonic resonance depth strictly depend on the polarization angle of the incident light (see Paragraph 1.3[c]), such angle was set to 0° (p polarization) in the first case, and to 150° in the rotated grating case, respectively, to optimize reflectance dips. The spectra are characterized by a number of plasmonic dips identified through simulations. For increasing wavelengths, in plot (a), LRSPP at 455 nm, SRSPP at 560 nm and a second LRSPP resonance at 1255 nm. In plot (b), LRSPP at 550 nm, SRSPPs at 610-625 nm, TE mode at 710 nm, the second LRSPP at 940 nm and the second SRSPP at 1030 nm. The spatial extension of the LRSPPs determines a lower spread of the momenta in the reciprocal space with respect to the SR modes, generally resulting in a higher figure of merit for the resonance.

The results from xylene sensing are reported in Fig. 82 and Fig. 83. The plots of Fig. 82 show in detail the three plasmonic dips characterizing the reflectance spectra of the sensor at 70° incidence angle, in standard illumination mode, for p polarized incident light at null azimuth. When the sensor was immersed in xylene atmosphere at a concentration of 30 ppm, the plasmonic dips

corresponding to the excitation of LRSPPs underwent red-shifts of 2.5±1.3 nm and of 2.9±0.9 nm, for the first and the second resonance respectively, and the dip corresponding to the excitation of the SRSPP of 1.9±0.8 nm. During regeneration, the minimum position moved back towards the starting point.

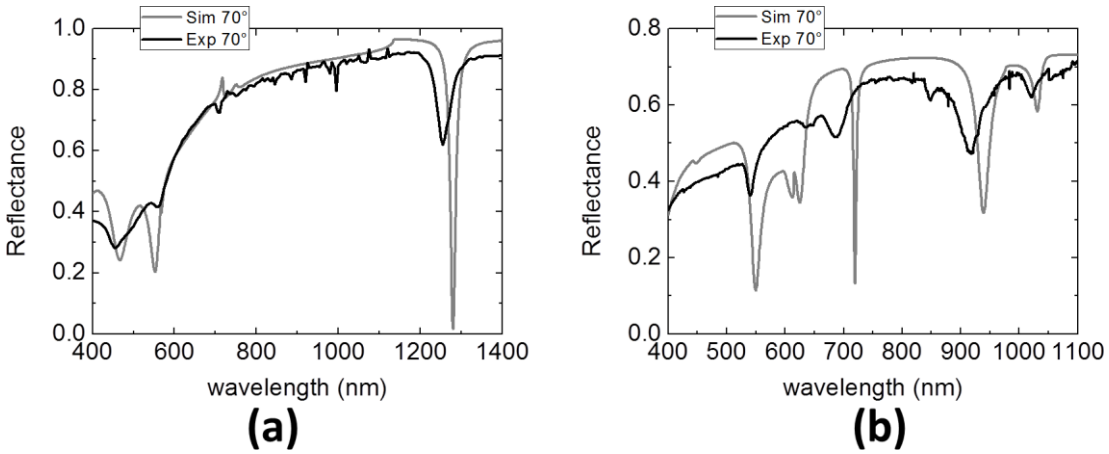

Fig. 81: Experimental and simulated reflectance spectra, at 70° incidence angle, of a SPG embedded in ph-PSQ films, after a 30 min annealing at 300 °C. (a) Spectrum acquired in standard illumination mode at null azimuth with p polarized incident light: the set of plasmonic dips, for increasing wavelength, were identified as LRSPP, SRSPP and a second LRSPP resonance. (b) Spectrum at 60° azimuth with a 150° polarization angle for the incident light: the dips are identified as LRSPP, SRSPPs, TE mode, and the second LRSPP and SRSPP resonances.

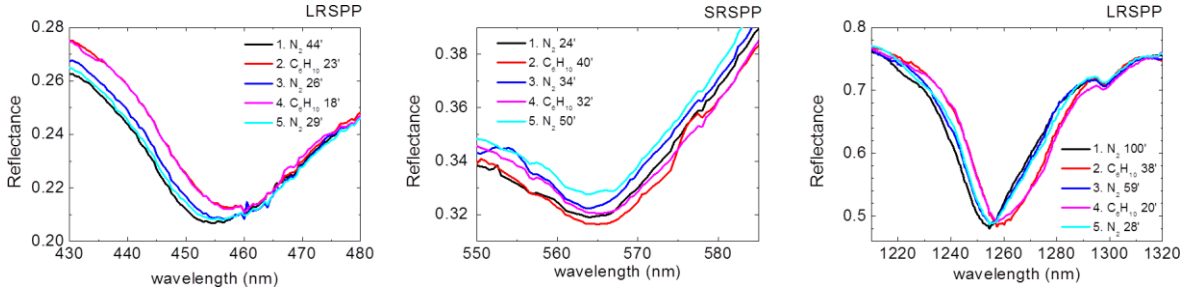

Fig. 82: Reflectance spectra measured in N2 atmosphere and in xylene at a concentration of 30 ppm, at 70° incidence angle, in standard illumination mode at null azimuth with p polarized incident light. The shift in wavelength is of 2.5±1.3 nm, 1.9±0.8 nm and 2.9±0.9 nm for the three plasmonic dips ordered by increasing wavelength, respectively.

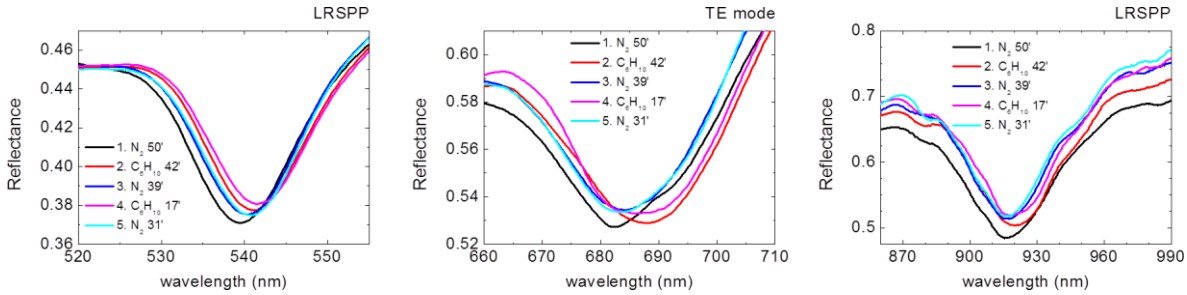

Fig. 83: Reflectance spectra measured in N2 atmosphere and in xylene at a concentration of 30 ppm, at 70° incidence angle, in standard illumination mode at 60° azimuth with a 150° polarization angle for the incident light. The measured shift in wavelength is of 1.2±0.9 nm, 3.8±0.9 nm, and 4.4±1.1 nm for the three resonances ordered by increasing wavelength, respectively.

The estimated error associated to the wavelength shifts is a standard deviation over multiple repeated cycles: the major contribution is given by the initial variation in sensor response before a regime behaviour is reached (after about a ten of exposure/regeneration cycles) and by statistical fluctuations. Such an error is really significant and substantially contributes to the final sensor response, for to the very small wavelength shifts to be measured.

Analogue data in terms of response and regeneration behavior were collected rotating the sensor at 60° azimuth for 150° polarization angle of the incident light (Fig. 83). Only the three deeper and sharper modes of the spectrum in Fig. 81(b) were examined: the two LR resonances and the TE mode propagating in the dielectric layer. The recorded red-shifts taking place during exposure to 30 ppm xylene were of 3.8±0.9 nm for the TE mode, 1.2±0.9 nm and 4.4±1.1 nm for the first and second LRSPP resonances respectively. All collected data are summarized in the plot of Fig. 84.

An attempt to experimentally measure the variation Δn in the refractive index of the active sol-gel film, corresponding to analyte interaction, was performed via spectroscopic ellipsometry on flat films. Such a variation resulted to be very small (≤ 0.01), and limited by the resolution of the technique. Thus, we cannot define the experimental sensitivity in terms of $\Delta\lambda$/RIU.

From simulations at 0° azimuth, we calculated a theoretical sensitivity, $\Delta\lambda/\Delta n$, of 150 nm for the first LR SPP, 350 nm for the second LR resonance, and of 100 nm for the SR SPP. Rotating the plasmonic sensor at 60° azimuth, the sensitivity at fixed angle of incidence became 200 nm and 500 nm for the first and second LRSPPs respectively, 350 nm for the SRSPP, and 450 nm for the TE mode.

Combining the theoretical sensitivity with measured values of $\Delta\lambda$ returned by a set of different LR and SR modes, we estimate the film Δn after interaction with 30 ppm xylene as 0.011±0.005. It was obtained by averaging over the variations in refractive index calculated for a set of sensing data.

From such numbers, we clearly comprehend that the plasmonic gas sensor was exploited in conditions close to the limits of its performance, but still a measurable shift of the plasmonic resonance could be appreciated. At high azimuth an increase in sensitivity is theoretically expected. The experimentally measured wavelength shifts for the different plasmonic modes at 60° azimuth are compatible with predicted values within the experimental errors.

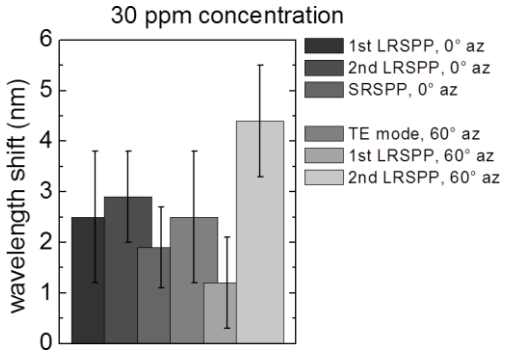

Fig. 84: Summary of the measured wavelength shifts for exposure to xylene at a concentration of 30 ppm, in standard illumination mode at null azimuth with p polarized incident light and at 60° azimuth with a 150° polarization angle for the incident light.

7. Conclusions

The propagation of Surface Plasmon Polaritons on anisotropic surfaces represented by sinusoidal gratings have been extensively investigated.
The outcomes of the present work include results in basic Plasmonics, the development of concepts and methods useful for the prediction of the optical response of a generic plasmonic grating, and also some promising applications to actual sensing devices.

A general analytical treatment of the conditions for grating coupling between free radiation and SPP modes have been derived and validated, producing maps capable to predict the angular position of the resonance dips in the reflectance spectra with minimum computational effort. While the exploitation of powerful and expensive computational methods is growing, this approach represents a handy and quick tool to design or characterize a plasmonic structure.

The analysis have been extended to the mapping of the propagation direction of the excited SPP mode on the grating surface, defined by its angle with respect to the grating Bragg vector. The relation between the propagation angle and the azimuthal angle is thus unravelled.
A unique configuration have been identified, in which two identical SPP modes are simultaneously excited by the same light beam and propagate along different directions.

A deep investigation of how the propagation on the patterned surface affects radiative losses have been performed, providing interesting results.
The expected relations between losses and resonance width have been verified, and it has been shown and explained that they are unaffected by the incident light polarization.

The dependence of radiative losses on the grating amplitude have been found to be a quadratic law, and a physical interpretation of this result have been suggested, through a quantum mechanical model of the resonant coupling.

The dependence of radiative losses on the propagation direction has also been derived, from a model of anisotropic effective refractive index.
These results have been transformed, through the coupling relations, to the reference system of the coupling setup, in order to directly compare the predictions to experimental data. The model is in fact validated by this comparison.

The second resonant coupling of Long Range and Short Range SPPs in conical mounting have been predicted and the corresponding dips observed for the first time. It has been shown that a relevant enhancement of the propagation length of a Long Range mode can be achieved in conical mounting, with respect to the null-azimuth case.

Theoretical formulas to evaluate the sensitivity of SPP modes for sensing applications have been derived, including configurations that had not be considered before. In particular, the factor related to conical mounting have been generalized and applied to the spectral interrogation case.
A general expression for the Figure of Merit have been derived, showing that the sensitivity enhancement in conical mounting is primarily due to the reduction of radiative losses.

Some structures have been tested as gas sensing devices for analytes of interest for health and food safety, environmental monitoring and counter-terrorism.
The possibility to detect traces of TNT, hydrogen and aromatic Volatile Organic Compounds, by means of SPR grating-based sensors, have been demonstrated.
In particular, the superior sensitivity achievable by combining the exploitation of Long Range SPPs with the conical mounting configuration have been demonstrated, in a test against xylene.

8. APPENDICES

8.1. Fundamentals of plasmonics

Mainly calculations and proofs, apart for some basic remarks on the view of a SPP as a quasi-particle in a Solid State Physics framework.

a. SPPs as quantum quasi-particles

In a Quantum Field Theory framework, SPPs may be seen as a kind of *quasi-particles* [46].

Electric field in matter always produces a polarization wave, according to $\vec{P} = \varepsilon_0[\varepsilon(\omega) - 1]\vec{E}$. As a consequence, light travelling in a solid is a superposition of an electromagnetic wave and the polarization wave, and this mixed state is quantized, i.e. it can exchange energy only by integer multiples of ħω.

The polarization wave includes several kind of excitations, that are considered "quasi-particles" for two reasons: because they exist only in matter and not in vacuum, and because their momentum is a "quasi-momentum", defined within an arbitrary additive constant vector [181]. These quasi-particles are:

- Phonons, representing relative motion of different ions in the material
- Excitons, associated to electron-hole pair excitations
- Plasmons, describing collective motions of the electron cloud with respect to the nuclei and inner shells

The general case will be a quantized mixed state of an electromagnetic wave and a polarization wave, i.e. of photons and quasi-particles: due to their nature, these are themselves quasi-particles called "polaritons", a name composed of the terms "polarization" and "photon". They can be depicted as a continuous energy exchange between an electromagnetic wave exciting the oscillators, which in turn re-radiate an electromagnetic wave, and so on.
In a second quantization picture, the interaction Hamiltonian between photons and a generic quasi-particle is written as follows:

$$H = \sum_k \hbar\omega_k a_k^\dagger a_k + \sum_{k'} E(k') B_{k'}^\dagger B_{k'} + i\hbar \sum_k g_k \left(B_k^\dagger a_k + a_k^\dagger B_k\right)$$

The first two terms contain the number operators of the photons ($a_k^\dagger a_k$) and the quasi-particles ($B_{k'}^\dagger B_{k'}$), and correspond to the hamiltonian of the non-interacting system [123]. The third term describes the interaction and contains the creation/annihilation operators (for example, $B_k^\dagger a_k$ destroys a photon and creates a quasi-particle); g_k contains the information about the transition probability.

Introducing a linear combination of creation and annihilation operators of photons and quasi-particles, $p_k \equiv u_k B_k + v_k a_k$, with a proper choice of the u_k and v_k coefficients the Hamiltonian could be diagonalized into the interaction-free form:

$$H = \sum_k E_k p_k^\dagger p_k$$

Where p_k and $p_k^\dagger$ are the annihilation and creation operators for the mixed state corresponding to a free quasi-particle: the polariton [182].

b. Real and imaginary parts of the SPP momentum

The SPP momentum $K_{spp} = \frac{\omega}{c}\sqrt{\frac{\varepsilon_d \varepsilon_m}{\varepsilon_d+\varepsilon_m}}$ is in general complex, because the metal dielectric function $\varepsilon_m = \varepsilon_{mr} + i\varepsilon_{mi}$ is usually complex.

In an explicit form, the effective refractive index: $N = \sqrt{\frac{\varepsilon_d \varepsilon_m}{\varepsilon_d+\varepsilon_m}} = \sqrt{\frac{(\varepsilon_d \varepsilon_{mr}+i\varepsilon_d \varepsilon_{mi})\cdot(\varepsilon_d+\varepsilon_{mr}-i\varepsilon_{mi})}{(\varepsilon_d+\varepsilon_{mr}+i\varepsilon_{mi})(\varepsilon_d+\varepsilon_{mr}-i\varepsilon_{mi})}}$

Under the reasonable approximation $|\varepsilon_{mr}| \gg |\varepsilon_{mi}|$, the second order terms in $\frac{\varepsilon_{mi}}{\varepsilon_{mr}}$ can be neglected, obtaining:

$$N \approx \sqrt{\frac{\varepsilon_d \varepsilon_{mr}\cdot(\varepsilon_d+\varepsilon_{mr}) + i\varepsilon_d^2 \varepsilon_{mi}}{(\varepsilon_d+\varepsilon_{mr})^2}} = \sqrt{\frac{\varepsilon_d \varepsilon_{mr}}{\varepsilon_d+\varepsilon_{mr}}}\cdot\sqrt{1+i\frac{\varepsilon_{mi}}{\varepsilon_{mr}}\frac{\varepsilon_d}{\varepsilon_d+\varepsilon_{mr}}}$$

In order to calculate the square root of a complex number it is convenient to pass to the exponential notation:

$z = \rho e^{it} = \rho(\cos t + i\sin t)$ with $\rho = |z|$, $\cos t = \frac{Re(z)}{|z|}$ and $\sin t = \frac{Im(z)}{|z|}$; then

$$\sqrt{z} = \sqrt{\rho}e^{\frac{it}{2}} = \sqrt{\rho}\left(\cos\frac{t}{2} + i\sin\frac{t}{2}\right) = \sqrt{\rho}\left(\sqrt{\frac{1+\cos t}{2}} + i\sqrt{\frac{1-\cos t}{2}}\right) = \sqrt{\frac{\rho+Re(z)}{2}} + i\sqrt{\frac{\rho-Re(z)}{2}}$$

In our case $z = 1 + i\frac{\varepsilon_{mi}}{\varepsilon_{mr}}\frac{\varepsilon_d}{\varepsilon_d+\varepsilon_{mr}}$ then $Re(z) = 1$ and $\rho = \sqrt{1+\left(\frac{\varepsilon_{mi}}{\varepsilon_{mr}}\frac{\varepsilon_d}{\varepsilon_d+\varepsilon_{mr}}\right)^2} \approx 1 + \frac{1}{2}\left(\frac{\varepsilon_{mi}}{\varepsilon_{mr}}\frac{\varepsilon_d}{\varepsilon_d+\varepsilon_{mr}}\right)^2$, thus:

$$\begin{cases} \sqrt{\frac{\rho+Re(z)}{2}} = \sqrt{1+\frac{1}{4}\left(\frac{\varepsilon_{mi}}{\varepsilon_{mr}}\frac{\varepsilon_d}{\varepsilon_d+\varepsilon_{mr}}\right)^2} \approx 1 \\ \sqrt{\frac{\rho-Re(z)}{2}} = \sqrt{\frac{1}{4}\left(\frac{\varepsilon_{mi}}{\varepsilon_{mr}}\frac{\varepsilon_d}{\varepsilon_d+\varepsilon_{mr}}\right)^2} = \frac{1}{2}\frac{\varepsilon_{mi}}{\varepsilon_{mr}}\frac{\varepsilon_d}{\varepsilon_d+\varepsilon_{mr}} \end{cases}$$

In conclusion, the approximated explicit forms for the real and imaginary parts of the momentum are:

$$\begin{cases} Re(K_{spp}) \equiv \beta = \frac{\omega}{c}\sqrt{\frac{\varepsilon_d \varepsilon_{mr}}{\varepsilon_d+\varepsilon_{mr}}} \\ Im(K_{spp}) \equiv \Gamma = \frac{\omega}{c}\left(\frac{\varepsilon_d \varepsilon_{mr}}{\varepsilon_d+\varepsilon_{mr}}\right)^{\frac{3}{2}}\frac{\varepsilon_{mi}}{2\varepsilon_{mr}^2} \end{cases}$$

In particular, it is demonstrated that β has the same expression than K_{SPP}, substituting ε_m with ε_{mr}. This result will be extended to the coupled modes in the next section.

Relaxing the approximation, the real part would be:

$$\beta = \frac{\omega}{c}\sqrt{\frac{\varepsilon_d}{2}}\sqrt{\frac{(\varepsilon_d+\varepsilon_{mr})\varepsilon_{mr} + \varepsilon_{mi}^2 + \sqrt{[(\varepsilon_d+\varepsilon_{mr})\varepsilon_{mr}]^2 + \varepsilon_d^2\varepsilon_{mi}^2}}{(\varepsilon_d+\varepsilon_{mr})^2 + \varepsilon_{mi}^2}}$$

c. Long Range propagation

Some information about the propagation length of a LR SPP may be extracted by an approximated expression for Γ_L. Under the quite strong assumption that the film is thin enough to approximate the hyperbolic tangent to its argument, i.e. $\tanh(k_m a) \approx k_m a$, the real and imaginary parts of the LR SPP dispersion relation take the following form [13]:

$$\beta_L \approx \frac{\omega}{c}\sqrt{\varepsilon_d}\left[1+\frac{\varepsilon_d}{2}\left(\frac{\omega}{c}a\right)^2\cdot\frac{(\varepsilon_{\mathrm{mr}}^2+\varepsilon_{\mathrm{mi}}^2-\varepsilon_{\mathrm{d}}\varepsilon_{\mathrm{mr}})^2-\varepsilon_{\mathrm{d}}^2\varepsilon_{\mathrm{mi}}^2}{(\varepsilon_{\mathrm{mr}}^2+\varepsilon_{\mathrm{mi}}^2)^2}\right]$$

$$\Gamma_L \approx \frac{\omega}{c}\sqrt{\varepsilon_d}\left(a\frac{\omega}{c}\varepsilon_d\right)^2\cdot\frac{\varepsilon_{\mathrm{mi}}(\varepsilon_{\mathrm{mr}}^2+\varepsilon_{\mathrm{mi}}^2-\varepsilon_{\mathrm{d}}\varepsilon_{\mathrm{mr}})}{(\varepsilon_{\mathrm{mr}}^2+\varepsilon_{\mathrm{mi}}^2)^2}$$

Using also the fact that $\varepsilon_{mr} \gg \varepsilon_{mi}$, they become:

$$\beta_L \approx \frac{\omega}{c}\sqrt{\varepsilon_d}\left[1+\frac{\varepsilon_d}{2}\left(\frac{\omega}{c}a\right)^2\cdot\left(1-\frac{\varepsilon_{\mathrm{d}}}{\varepsilon_{\mathrm{mr}}}\right)^2\right]$$

$$\Gamma_L \approx a^2\left(\frac{\omega}{c}\right)^3\left(\sqrt{\varepsilon_d}\right)^5\cdot\varepsilon_{\mathrm{mi}}\left(\frac{1}{\varepsilon_{\mathrm{mr}}^2}-\frac{\varepsilon_{\mathrm{d}}}{\varepsilon_{\mathrm{mr}}^3}\right)$$

The propagation length is given by:

$$L \equiv \frac{1}{2\Gamma_L} = \frac{\varepsilon_{\mathrm{mr}}^3}{\left(\sqrt{\varepsilon_{\mathrm{d}}}\right)^5}\cdot\frac{1}{\varepsilon_{\mathrm{mi}}(\varepsilon_{\mathrm{mr}}-\varepsilon_{\mathrm{d}})}\cdot\frac{1}{2a^2}\left(\frac{\omega}{c}\right)^{-3}$$

Interesting enough, ε_{mr} and, inversely, ε_d affect L in a more effective way than ε_{mi}; a low refractive index of the dielectric and a high real part of the metal permittivity ensure a long propagation distance. The reason is that under these conditions the field spends less time into the metal layer, thus reducing dissipation [7; 8].

d. Real part of the coupled modes momentum

Starting with the approximated expression for the LR SPP,
$K_{\mathrm{Long}} \approx \frac{\omega}{c}\sqrt{\varepsilon_{\mathrm{d}}+(\varepsilon_{\mathrm{d}}-\varepsilon_{\mathrm{m}})\left(\frac{\varepsilon_{\mathrm{d}}}{\varepsilon_{\mathrm{m}}}\right)^2\left[\tanh\left(\frac{\omega}{c}a\sqrt{\varepsilon_{\mathrm{d}}-\varepsilon_{\mathrm{m}}}\right)\right]^2}$, it will now be proved that

$$\beta_{\mathrm{L}} \approx \frac{\omega}{c}\sqrt{\varepsilon_{\mathrm{d}}+(\varepsilon_{\mathrm{d}}-\varepsilon_{\mathrm{mr}})\left(\frac{\varepsilon_{\mathrm{d}}}{\varepsilon_{\mathrm{mr}}}\right)^2\left[\tanh\left(\frac{\omega}{c}a\sqrt{\varepsilon_{\mathrm{d}}-\varepsilon_{\mathrm{mr}}}\right)\right]^2}$$

The first step is to decompose the square root term inside the hyperbolic tangent in its real and imaginary parts, using the known generic formulas:

$$\sqrt{a+ib} = p+iq$$

$$p = \frac{1}{\sqrt{2}}\sqrt{\sqrt{a^2+b^2}+a}$$

$$q = \frac{\mathrm{sgn}(b)}{\sqrt{2}}\sqrt{\sqrt{a^2+b^2}-a}$$

Thus:

$$\frac{a\omega}{c}\sqrt{(\varepsilon_{\mathrm{d}}-\varepsilon_{\mathrm{mr}})-i\varepsilon_{mi}} = \frac{\omega a}{c\sqrt{2}}\left[\sqrt{\sqrt{(\varepsilon_{\mathrm{d}}-\varepsilon_{\mathrm{mr}})^2+\varepsilon_{mi}^2}+(\varepsilon_{\mathrm{d}}-\varepsilon_{\mathrm{mr}})}-i\sqrt{\sqrt{(\varepsilon_{\mathrm{d}}-\varepsilon_{\mathrm{mr}})^2+\varepsilon_{mi}^2}-(\varepsilon_{\mathrm{d}}-\varepsilon_{\mathrm{mr}})}\right]$$

For the hyperbolic tangent, the procedure is as follows:

$$\tanh(p+iq)=\frac{\sinh(p+iq)}{\cosh(p+iq)}=\frac{\sinh p\cos q+i\cosh p\sin q}{\cosh p\cos q+i\sinh p\sin q}=\frac{\sinh p\cosh p+i\sin q\cos q}{(\cosh p\cos q)^2+(\sinh p\sin q)^2}=$$
$$=\frac{1}{2}\frac{\sinh 2p}{(\cosh p\cos q)^2+(\sinh p\sin q)^2}+\frac{i}{2}\frac{\sin 2q}{(\cosh p\cos q)^2+(\sinh p\sin q)^2}\equiv x+iy$$

The next step is to expand in series the following polynomial:

$$\left(\frac{\varepsilon_d^3}{\varepsilon_{mi}^2}-\frac{\varepsilon_d^2}{\varepsilon_{mi}}\right)(x+iy)^2=$$
$$=(x^2-y^2+2ixy)\left[\left(\frac{\varepsilon_d^3(\varepsilon_{mr}^2-\varepsilon_{mi}^2)}{\varepsilon_{mr}^4+\varepsilon_{mi}^4+2\varepsilon_{mr}^2\varepsilon_{mi}^2}-\frac{\varepsilon_d^2\varepsilon_{\mathrm{mr}}}{m_r^2+\varepsilon_{mi}^2}\right)+i\left(\frac{-2\varepsilon_{\mathrm{mr}}\varepsilon_{mi}\varepsilon_d^3}{\varepsilon_{mr}^4+\varepsilon_{mi}^4+2\varepsilon_{mr}^2\varepsilon_{mi}^2}+\frac{\varepsilon_d^2\varepsilon_{mi}}{\varepsilon_{mr}^2+\varepsilon_{mi}^2}\right)\right]=$$
$$=(x^2-y^2)\left(\frac{\varepsilon_d^3(\varepsilon_{mr}^2-\varepsilon_{mi}^2)}{\varepsilon_{mr}^4+\varepsilon_{mi}^4+2\varepsilon_{mr}^2\varepsilon_{mi}^2}-\frac{\varepsilon_d^2\varepsilon_{\mathrm{mr}}}{\varepsilon_{mr}^2+\varepsilon_{mi}^2}\right)-2xy\left(\frac{-2\varepsilon_{\mathrm{mr}}\varepsilon_{mi}\varepsilon_d^3}{\varepsilon_{mr}^4+\varepsilon_{mi}^4+2\varepsilon_{mr}^2\varepsilon_{mi}^2}+\frac{\varepsilon_d^2\varepsilon_{mi}}{\varepsilon_{mr}^2+\varepsilon_{mi}^2}\right)+$$
$$+i\left[(x^2-y^2)\left(\frac{-2\varepsilon_{\mathrm{mr}}\varepsilon_{mi}\varepsilon_d^3}{\varepsilon_{mr}^4+\varepsilon_{mi}^4+2\varepsilon_{mr}^2\varepsilon_{mi}^2}+\frac{\varepsilon_d^2\varepsilon_{mi}}{\varepsilon_{mr}^2+\varepsilon_{mi}^2}\right)+2xy\left(\frac{\varepsilon_d^3(\varepsilon_{mr}^2-\varepsilon_{mi}^2)}{\varepsilon_{mr}^4+\varepsilon_{mi}^4+2\varepsilon_{mr}^2\varepsilon_{mi}^2}-\frac{\varepsilon_d^2\varepsilon_{\mathrm{mr}}}{\varepsilon_{mr}^2+\varepsilon_{mi}^2}\right)\right]$$

Calling this block A+iB, what we need is to take the real part of the square root of $\varepsilon_{\mathrm{d}}+A+iB$.

Using the formulas for the square root: $\beta_{\mathrm{L}}=\frac{\omega}{\mathrm{c}\sqrt{2}}\sqrt{\sqrt{(\varepsilon_{\mathrm{d}}+A)^2+B^2}+(\varepsilon_{\mathrm{d}}+A)}$

This is a complicated expression, but it is reasonable to neglect the quadratic terms in $\varepsilon_{\mathrm{mi}}$ with respect to the ones in $\varepsilon_{\mathrm{mr}}$.

With this approximation, $\frac{\omega}{\mathrm{c}}a\sqrt{(\varepsilon_{\mathrm{d}}-\varepsilon_{\mathrm{mr}})-i\varepsilon_{\mathrm{mi}}}\approx\frac{\omega}{\mathrm{c}}a\sqrt{(\varepsilon_{\mathrm{d}}-\varepsilon_{\mathrm{mr}})}$, meaning that $q\approx 0$.

As a consequence, $x+iy=x=\tanh p$ and then:

$$A+iB=x^2\left(\frac{\varepsilon_d^3(\varepsilon_{mr}^2-\varepsilon_{mi}^2)}{\varepsilon_{mr}^4+\varepsilon_{mi}^4+2\varepsilon_{mr}^2\varepsilon_{mi}^2}-\frac{\varepsilon_d^2\varepsilon_{\mathrm{mr}}}{\varepsilon_{mr}^2+\varepsilon_{mi}^2}\right)+ix^2\left(\frac{-2\varepsilon_{\mathrm{mr}}\varepsilon_{mi}\varepsilon_d^3}{\varepsilon_{mr}^4+\varepsilon_{mi}^4+2\varepsilon_{mr}^2\varepsilon_{mi}^2}+\frac{\varepsilon_d^2\varepsilon_{mi}}{\varepsilon_{mr}^2+\varepsilon_{mi}^2}\right)$$

That can be approximated as follows:

$$A+iB\approx x^2\left(\frac{\varepsilon_d^3}{\varepsilon_{mr}^2}-\frac{\varepsilon_d^2}{\varepsilon_{mr}}\right)+ix^2\left(\frac{-2\varepsilon_{mi}\varepsilon_d^3}{\varepsilon_{mr}^3}+\frac{\varepsilon_d^2\varepsilon_{mi}}{\varepsilon_{mr}^2}\right)=\left(\frac{x\varepsilon_{\mathrm{d}}}{\varepsilon_{mr}}\right)^2(\varepsilon_{\mathrm{d}}-\varepsilon_{\mathrm{mr}})+i\left(\frac{x\varepsilon_{\mathrm{d}}}{\varepsilon_{mr}}\right)^2\frac{\varepsilon_{\mathrm{mi}}}{\varepsilon_{\mathrm{mr}}}(\varepsilon_{\mathrm{mr}}-2\varepsilon_{\mathrm{d}})$$

It can be observed that B<<A, due to the $\frac{\varepsilon_{\mathrm{mi}}}{\varepsilon_{\mathrm{mr}}}$ factor. For this reason, B^2 can be neglected in $(d+A)^2+B^2$.

In conclusion:

$$\beta_{\mathrm{L}}\approx\frac{\omega}{\mathrm{c}}\sqrt{(\varepsilon_{\mathrm{d}}+A)}=\frac{\omega}{\mathrm{c}}\sqrt{\varepsilon_{\mathrm{d}}+\left(\frac{x\varepsilon_{\mathrm{d}}}{\varepsilon_{mr}}\right)^2(\varepsilon_{\mathrm{d}}-\varepsilon_{\mathrm{mr}})}=\frac{\omega}{\mathrm{c}}\sqrt{\varepsilon_{\mathrm{d}}+(\varepsilon_{\mathrm{d}}-\varepsilon_{\mathrm{mr}})\left(\frac{\varepsilon_{\mathrm{d}}}{\varepsilon_{\mathrm{mr}}}\right)^2\left[\tanh\left(\frac{\omega}{\mathrm{c}}\mathrm{a}\sqrt{\varepsilon_{\mathrm{d}}-\varepsilon_{\mathrm{mr}}}\right)\right]^2}$$

As previously claimed.

In the same way, it could be proved that:

$$\beta_{\mathrm{S}}\approx\frac{\omega}{\mathrm{c}}\sqrt{\varepsilon_d+\frac{(\varepsilon_d-\varepsilon_{\mathrm{mr}})\left(\frac{\varepsilon_d}{\varepsilon_{\mathrm{mr}}}\right)^2}{\left[\tanh\left(\frac{\omega}{c}a\sqrt{\varepsilon_d-\varepsilon_{\mathrm{mr}}}\right)\right]^2}}$$

8.2. SPP/radiation coupling

This appendix includes the explicit derivation of some formulas related to the SPP coupling and sensitivity, and some remarks about Nano-Imprinting.

a. Explicit solutions of the coupling conditions

Defining the χ angle as the angle between $\vec{\beta}$ and $\hat{x}$, the coupling conditions can be rewritten as follows:

$$\begin{cases} \pm\beta\cos\chi = \dfrac{2\pi}{\Lambda}\cos\varphi - \dfrac{2\pi}{\lambda}\sin\theta \\ \beta\sin\chi = \dfrac{2\pi}{\Lambda}\sin\varphi \end{cases}$$

Introducing the effective refractive index $N \equiv \beta\frac{\lambda}{2\pi}$, the second equation gives $\sin\chi = \frac{\lambda}{\Lambda}\frac{\sin\varphi}{N}$, from which:

$\cos\chi = \sqrt{1-\sin^2\chi} = \sqrt{1-\left(\frac{\lambda}{\Lambda}\frac{\sin\varphi}{N}\right)^2}$ to be used into the first as follows:

$$\sin\theta = \frac{\lambda}{\Lambda}\cos\varphi \mp N\cos\chi = \frac{\lambda}{\Lambda}\cos\varphi \mp N\sqrt{1-\left(\frac{\lambda}{\Lambda}\frac{\sin\varphi}{N}\right)^2}$$

This is the general solution for the angular positions of the two resonances.

b. Dependence of the reflectance on the polarization

As discussed in Chapter 1.3, the reflectance at a plasmonic resonance is expected to depend on the polarization angle α, the incidence angle θ and the azimuthal angle φ according to:

$$R \propto |\cos\alpha\cos\theta\sin\varphi + \sin\alpha\cos\varphi|^2$$

This formula can be developed as follows:

$$\begin{aligned} R &\propto (\cos\alpha\cos\theta\sin\varphi + \sin\alpha\cos\varphi)^2 \\ &= \cos^2\alpha\cos^2\theta\sin^2\varphi + \sin^2\alpha\cos^2\varphi + 2\cos\alpha\cos\theta\sin\varphi\sin\alpha\cos\varphi = \\ &= \frac{\cos^2\alpha\cos^2\theta\sin^2\varphi}{2} + \frac{(\sin^2\alpha+\cos 2\alpha)\cos^2\theta\sin^2\varphi}{2} + \frac{\sin^2\alpha\cos^2\varphi}{2} + \frac{(\cos^2\alpha-\cos 2\alpha)\cos^2\varphi}{2} + \frac{\sin 2\alpha\sin 2\varphi\cos\theta}{2} = \\ &= \frac{\cos 2\alpha}{2}(\cos^2\theta\sin^2\varphi - \cos^2\varphi) + \frac{\cos^2\theta\sin^2\varphi}{2} + \frac{\cos^2\varphi}{2} + \frac{\sin 2\alpha\sin 2\varphi\cos\theta}{2} = \\ &= \frac{\cos^2\theta\sin^2\varphi+\cos^2\varphi}{2}\left[1 + \cos 2\alpha\frac{\cos^2\theta\sin^2\varphi-\cos^2\varphi}{\cos^2\theta\sin^2\varphi+\cos^2\varphi} + \sin 2\alpha\frac{\sin 2\varphi\cos\theta}{\cos^2\theta\sin^2\varphi+\cos^2\varphi}\right] \end{aligned}$$

The terms containing the polarization angle can be rewritten using the relation:

$$\cos(a+b) = \cos a\cos b - \sin a\sin b$$

In this specific case, this means:

$$\begin{cases} \cos(2\alpha+\alpha_0) = \cos\alpha_0\cos 2\alpha - \sin\alpha_0\sin 2\alpha \equiv \sqrt{1-X^2}\cos 2\alpha - X\sin 2\alpha \\ \cos\alpha_0 = \dfrac{\cos^2\theta\sin^2\varphi - \cos^2\varphi}{\cos^2\theta\sin^2\varphi + \cos^2\varphi} \\ \sin\alpha_0 = -\dfrac{\sin 2\varphi\cos\theta}{\cos^2\theta\sin^2\varphi + \cos^2\varphi} \end{cases}$$

In conclusion, the reflectance has the form:

$$R \propto \frac{\cos^2\theta \sin^2\varphi + \cos^2\varphi}{2}[1 + \cos(2\alpha + \alpha_0)]$$

With $\alpha_0 = \sin^{-1}\left[\frac{-\sin 2\varphi \cos\theta}{\cos^2\theta \sin^2\varphi + \cos^2\varphi}\right]$

c. Sensitivity calculations

Two different forms are found in the literature for the spectral sensitivity of grating-based SPR sensors, for both the angular and spectral interrogation cases. In fact, they are derived under somewhat different assumptions.

The formula for the sensitivity under angular interrogation, $\Sigma_{n,\theta} = \frac{\partial\theta}{\partial n}$, is found in the two following forms:

$$\Sigma_{n,\theta}^{(\text{out})} = \frac{1}{\cos\theta}\left(\frac{N}{n}\right)^3$$

$$\Sigma_{n,\theta}^{(\text{in})} = \frac{1}{n\cos\theta}\left[\left(\frac{N}{n}\right)^3 + \sin\theta\right]$$

The second one [77; 98] is valid if the whole apparatus, included the light source, is immersed into a dielectric half-space of refractive index n, or, in other words, it is valid inside the sensitive layer. In fact in this case the coupling condition assumes the form:

$$N = -n\sin\theta_n + \frac{\lambda}{\Lambda}$$

Where θ_n is the incidence angle of the impinging light measured inside the mentioned layer. Differentiating this formula in n and θ_n, one obtains $\frac{dN}{dn}dn = -\sin\theta_n\, dn - n\cos\theta_n\, d\theta_n$ and then:

$$\frac{d\theta_n}{dn} = -\left(\frac{dN}{dn} + \sin\theta_n\right)\frac{1}{n\cos\theta_n}$$

That corresponds in modulus to $\Sigma_{n,\theta}^{(\text{in})}$.

In realistic situations, light comes from air with a θ_0 incidence angle and enters the sensitive layer, being deflected according to Snell's Law: $\sin\theta_0 = n\sin\theta_n$. Since the measurand is the variation of θ_0, the sensitivity to be calculated should be $\frac{d\theta_0}{dn}$. Differentiating the Snell's Law one obtains the following equation:

$$\cos\theta_0\, d\theta_0 = \sin\theta_n\, dn + n\cos\theta_n \frac{d\theta_n}{dn} dn$$

That, using the previously derived expression for $\frac{d\theta_n}{dn}$, becomes:

$$\cos\theta_0\, d\theta_0 = dn\left[\sin\theta_n - \left(\frac{N}{n}\right)^3 - \sin\theta_n\right] = -\left(\frac{N}{n}\right)^3 dn$$

This corresponds in modulus to $\Sigma_{n,\theta}^{(\text{out})}$, which could also have been directly derived through differentiation of the coupling condition in air: $N = -\sin\theta_0 + \frac{\lambda}{\Lambda}$.

The same happens in the spectral interrogation case, with the two definitions:

$$\Sigma_{n,\lambda}^{(\mathrm{in})} = \left(\frac{\lambda}{n\Lambda} - \frac{N^3}{n\varepsilon_{mr}}\right) \cdot \left(\frac{1}{\Lambda} - \frac{dN}{d\lambda}\right)^{-1}$$

$$\Sigma_{n,\lambda}^{(\mathrm{out})} = \left(\frac{N}{n}\right)^3 \cdot \left(\frac{1}{\Lambda} - \frac{dN}{d\lambda}\right)^{-1}$$

The differentiation inside the sensitive layer gives in fact:

$$\frac{dN}{dn}dn + \frac{dN}{d\lambda}d\lambda = \frac{d\lambda}{\Lambda} - \sin\theta_n\, dn - n\frac{d(\sin\theta_n)}{dn}dn$$

The crucial difference between this case and the angular interrogation one is that, while in that case the fixed parameter λ was the same for $\Sigma_{n,\theta}^{(\mathrm{in})}$ and $\Sigma_{n,\theta}^{(\mathrm{out})}$, here the fixed parameter is θ_0 for $\Sigma_{n,\lambda}^{(\mathrm{out})}$ and θ_n for $\Sigma_{n,\lambda}^{(\mathrm{in})}$.

From Snell's Law: $\frac{d(\sin\theta_n)}{dn} = -\frac{\sin\theta_0}{n^2} = -\frac{\sin\theta_n}{n}$ that permits to transform $\Sigma_{n,\lambda}^{(\mathrm{in})}$ into $\Sigma_{n,\lambda}^{(\mathrm{out})}$.

d. Second harmonic in imprinting

During the fabrication of replicas via NIL as described in Chapter 4.2[c], when the mould is pressed on the patternable film, the polymer should fill for capillarity the sinusoidal profile. If this filling is not complete, thus the reproduction of the mould not faithful, the final structures may present a particular defect, consisting in a splitting of the peaks of the sinusoid, due to their flattening combined to the effect of capillary action at the sides.

This is clearly visible in the AFM analyses of such samples, as the ones reported in Fig. 85: the split peaks can be seen in the profile reconstruction, while Fourier analysis shows a secondary peak corresponding to a $\Lambda/2$ periodicity. These also have consequences on the reflectance spectra, since this second harmonic works in fact as a secondary periodicity $G' = \frac{4\pi}{\Lambda}$ which provides momentum for the coupling. A second series of dips appears in the spectra when such a defect is present.

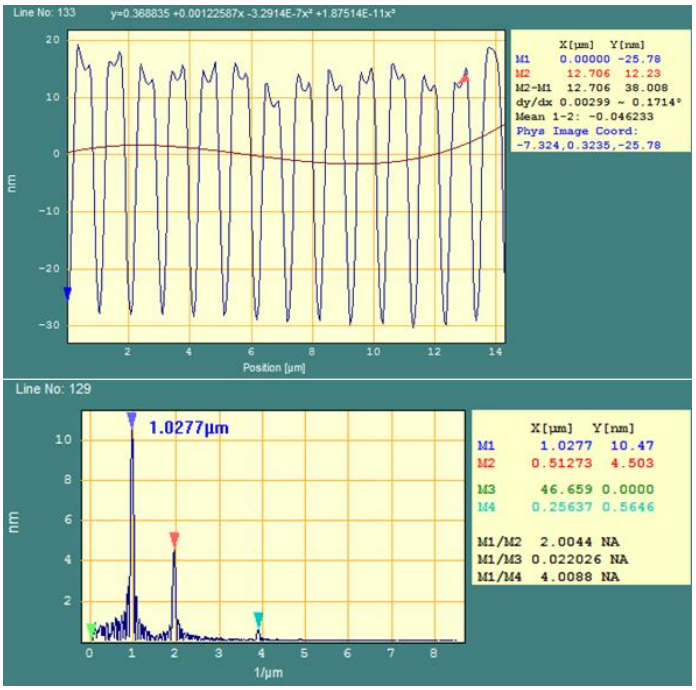

Fig. 85: AFM analysis of a defected sample; the presence of a second harmonic is visible in the grating profile and confirmed by the Fourier spectrum.

Ringraziamenti

Desidero ringraziare tutte le persone che hanno contribuito alla realizzazione di questa tesi.

I colleghi del LaNN con cui ho collaborato, in particolare Pierfrancesco e Gianluca per le proficue discussioni,

il "team esplosivi" (Agnese, Gioia) per l'esperimento sul TNT,

Gabriele per l'impegno profuso nel fabbricare campioni che mi soddisfacessero,

tutti coloro che mi hanno aiutato ad imparare a maneggiare programmi di simulazione e strumenti di caratterizzazione,

Denis e tutti gli altri per pranzi, feste e pause caffè che hanno reso unica l'esperienza in questo Gruppo,

e naturalmente il mio relatore Filippo per esserne stato l'artefice.

Inoltre:

Laura, Michela e Silvia per gli esperimenti svolti presso il Dipartimento di Ingegneria Industriale nell'ambito del Progetto PLATFORMS.

References

1. J. Zenneck (1907), *Über die Fortpflanzung ebener elektromagnetischer Wellen längs einer ebenen Leiterfläche und ihre Beziehung zur drahtlosen Telegraphie*. (Tr: *About the propagation of electromagnetic plane waves along a conductor plane and their relationship to wireless telegraphy*) Ann. der Physik **328** (10): 846–866
2. A. Sommerfeld (1949), *Partial Differential Equations in Physics*. Academic Press
3. U. Fano (1941), *The theory of anomalous diffraction gratings and of quasi-stationary waves on metallic surfaces (Sommerfeld's Waves)*. J. Opt. Soc. Am. **31**: 213-222
4. H. Raether (1980), *Surface plasmons on smooth and rough surfaces and on gratings*. Springer-Verlag
5. E.A. Stern and R.A. Ferrel (1960), *Surface Plasma Oscillations of a Degenerate Electron Gas*. Phys. Rev. **120**: 130-136
6. S.A. Maier (2007), *Plasmonics: Fundamentals and Applications*. Springer
7. J.D. Jackson (1998), *Classical Electrodynamics*, 3rd edition. Hamilton Printing Company.
8. A. Sommerfeld (1952), *Electrodynamics* (Lectures on Theoretical Physics, Vol. III). Academic Press
9. W.L. Barnes (2006), *Surface plasmon–polariton length scales: a route to sub-wavelength optics*. J. Opt. A **8**: S87–S93
10. E.N. Economou (1969), *Surface Plasmons in Thin Films*. Phys. Rev. **182** (2): 539-554
11. D. Sarid (1981), *Long-Range Surface-Plasma Waves on Very Thin Metal Films*. Phys. Rev. Lett. **47** (26): 1927-1930
12. J.J. Burke, G.I. Stegeman and T. Tamir (1986), *Surface-polariton-like waves guided by thin, lossy metal films*. Phys. Rev. B **33** (8): 5186-55201
13. F. Yang, J.R. Sambles and G.W. Bradberry (1991), *Long-range surface modes supported by thin films*. Phys. Rev. B **44** (11): 5855-5872
14. E. Prodan, C. Radloff, N.J. Halas and P. Nordlander (2003), *A hybridization model for the plasmon response of complex nanostructures*. Science **302**: 419–22
15. S.I. Bozhevolnyi and T. Søndergaard (2007), *General properties of slow-plasmon resonant nanostructures: nano-antennas and resonators*. Opt. Express **15**: 10869
16. A. Otto (1968), *Excitation of nonradiative Surface Plasma Waves in Silver by the Method of Frustrated Total Reflection*. Z. Phys. **216**: 398-410
17. E. Kretschmann and H.Z. Raether (1968), R*adiative decay of non-radiative surface plasmons excited by light*. Naturforsch **23**: 2135-2136
18. A. Sommerfeld (1954), *Optics* (Lectures on Theoretical Physics, Vol. IV). Academic Press
19. R.W. Wood (1902), *On a remarkable case of uneven distribution of light in a diffraction grating spectrum*. Proc. Phys. Soc. London **18**: 269
20. J.J. Cowan and E.T. Arakawa (1970), *Dispersion of surface plasmons in dielectric-metal coatings on concave diffraction gratings*. Z. Phys. **235** (2), 97
21. H. Ibach and H. Lüth (2009) *Solid-State Physics*. Springer
22. B.E. Warren (1990), *X-ray diffraction*. Dover Publications

23. Y.Y. Teng and E.A. Stern (1967), *Plasma radiation from metal grating surfaces*. Phys. Rev. Lett. **19**(9): 511-514
24. G.P. Bryan-Brown, J.R. Sambles and M.C. Hutley (1990), *Polarisation Conversion through the Excitation of Surface Plasmons on a Metallic Grating*. J. Mod. Opt. **37**: 1227-1232
25. M. Veith, K.G. Muller, S. Mittler-Neher and W. Knoll (1995), *Propagation and deflection of guided modes in planar waveguides via grating rotation*. Appl. Phys. B **60**: 1-4
26. F. Romanato, L.K. Hong, H.K. Kang, C.C. Wong, Z. Yun and W. Knoll (2008) *Azimuthal dispersion and energy mode condensation of grating-coupled surface plasmon polaritons*. Phys. Rev. B 77: 245435
27. G. Ruffato and F. Romanato (2013), *Near-field numerical analysis of surface plasmon polariton propagation on metallic gratings*. COMPEL: The International Journal for Computation and Mathematics in Electrical and Electronic Engineering **32** (6): 1779-1792
28. Y.K. Sirenko and S. Ström (2010), *Modern theory of gratings*, Springer
29. F. Romanato, K.H. Lee, G. Ruffato and C.C. Wong (2010) *The role of polarization on surface plasmon polariton excitation on metallic gratings in the conical mounting*. App. Phys. Lett. **96** (11): 111103
30. M.J. Adams (1981), *An introduction to optical waveguides*. John Wiley & Sons
31. E.M. Yeatman (1996), *Resolution and sensitivity in surface plasmon microscopy and sensing*. Biosens. Bioelectron. **11**: 635–649
32. K. Johansen, H. Arwin, I. Lundstrom and B. Liedberg (2000), *Imaging surface plasmon resonance sensor based on multiple wavelengths: sensitivity considerations*. Rev. Sci. Instrum. **71** (9): 3530–3538
33. M. Neviere, P. Vincent, R. Petit and M. Cadilhac (1973), *Systematic study of resonances of holographic thin film couplers*. Opt. Comm. **9**(1): 48–53
34. S. Herminghaus, M. Klopfleisch and H.J. Schmidt (1994), *Attenuated total reflectance as a quantum interference phenomenon*. Opt. Lett. **19** (4): 293-295
35. B. Gallinet, T. Siegfried, H. Sigg, P. Nordlander and O.J.F. Martin (2013), *Plasmonic Radiance: Probing Structure at the Ångström Scale with Visible Light*. Nano Lett. **13**: 497−503
36. M. Piliarik and J. Homola (2009), *Surface plasmon resonance (SPR) sensors: approaching their limits?* Opt. Express **17**: 16505–16517
37. A. Raman, W. Shin and S. Fan (2013), *Upper bound on the modal material loss rate in plasmonic and metamaterial systems*. Phys. Rev. Lett. **110**: 183901
38. J.C. Quail, J.G. Rako and H.J. Simon (1983), *Long-range surface-plasmon modes in silver and aluminum films*. Opt. Lett. **8**: 377–9
39. A.E. Craig, G.A. Olson and D. Sarid (1983), *Experimental observation of the long-range surface-plasmon polariton*. Optics letters **8**: 380–2
40. L.S. Jung, C.T. Campbell, T.M. Chinowsky, M.N. Mar and S.S. Yee (1998), *Quantitative Interpretation of the Response of Surface Plasmon Resonance Sensors to Adsorbed Films*, Langmuir **14**: 5636-5648
41. H.E. de Bruijn, B.S.F. Altenburg, R.P.H. Kooyman and J. Greve (1991), *Determination of thickness and dielectric constant of thin transparent dielectric layers using surface plasmon resonance*. Opt. Comm. **82**: 425-432

42. I.R. Hooper and J.R. Sambles (2003), *Surface plasmon polaritons on thin-slab metal gratings*, Phys. Rev. B **67**: 235404
43. W. Pauli (1973), *Optics and the Theory of Electrons*. The MIT Press
44. G.R. Fowles (1989), *Introduction to Modern Optics*, 2nd edition. Dover Publications
45. M. Fox (2010), *Optical Properties of Solids*, 2nd edition. Oxford University Press
46. C. Klingshirn (2005), *Semiconductor Optics*, 2nd edition. Springer
47. L.D. Landau, E.M Lifshitz and L.P. Pitaevskii (1984), *Electrodynamics of Continuous Media*, 2nd edition. Pergamon Press
48. O.S. Heavens (1991), *Optical properties of thin solid films*. Dover Publications
49. R.P. Feynman, R.B. Leighton and M. Sands (1964), *The Feynman Lectures of Physics*, Vol. 2. Addison-Wesley
50. P.M. Bellan (2008), *Fundamentals of Plasma Physics*. Cambridge University Press
51. E. Comini, G. Faglia and G. Sberveglieri (2008), *Solid State Gas Sensing*. Springer
52. C. Elosua, I.R. Matias, C. Bariain and F.J. Arregui (2006), *Volatile Organic Compound Optical Fiber Sensors: A Review*. Sensors **6**, 1440
53. J. Homola, S.S. Yee and G. Gauglitz (1999), *Surface Plasmon resonance sensors: review*. Sens. Actuators B **54**: 3-15
54. D.R. Shankaran, K.V. Gobi and N. Miura (2007), *Recent advancements in surface plasmon resonance immunosensors for detection of small molecules of biomedical, food and environmental interest*. Sens. Actuators B **121** (1): 158-177
55. D. Habauzit, J. Chopineau and B. Roig (2007), *SPR-based biosensors: A tool for biodetection of hormonal compounds*. Anal. Bioanal. Chem. **387** (4): 1215-1223
56. F.S. Ligler (2009), *Perspective on optical biosensors and integrated sensor systems*. Anal. Chem. **81**: 519-526
57. I. Abdulhalim, M. Zourob and A. Lakhtakia (2008), *Surface Plasmon Resonance for Biosensing: A Mini-Review*. Electromagnetics **28**: 214–242
58. L.M. Zhang and D. Uttamchandani (1988), *Optical chemical sensing employing surface plasmon resonance*. Electron. Lett. **23**: 1469–1470
59. J. van Gent, P.V. Lambeck, H.J. Kreuwel, G.J. Gerritsma, E.J. Sudhölter, D.N. Reinhoudt and T.J. Popma (1990), *Optimization of a chemooptical surface plasmon resonance based sensor*. Appl. Opt. **29** (19): 2843-2849
60. R.P.H. Kooyman, H. Kolkman, J. van Gent and J. Greve (1988), *Surface plasmon resonance immunosensors: sensitivity considerations*. Anal. Chim. Acta **213**: 35–45
61. B. Liedberg, I. Lundstörm and E. Stenberg (1993), *Principles of biosensing with an extended coupling matrix and surface plasmon resonance*. Sens. Actuat. B **11**: 63–72
62. J.S. Tung, J. Gimenez, C.T. Przysiecki and G. Mark (1998), *Characterization of recombinant hepatitis B surface antigen using surface plasmon resonance*. J. Pharm. Sci. **87**: 76–80
63. S. Miwa and T. Arakawa (1996), *Selective gas detection by means of surface plasmon resonance sensors*. Thin Solid Films **281–282**: 466–468

64. A. Abdelghani, J. M. Chovelon, N. Jaffrezic-Renault, C. Ronot-Trioli, C. Veillas and H. Gagnaire (1997), *Surface plasmon resonance fiber-optic sensor for gas detection*. Sens. Actuators B **39**: 407–410
65. A. Nooke, U. Beck, A. Hertwig, A. Krause, H. Krüger, V. Lohse, D. Negendank and J. Steinbach (2010), *On the application of gold based SPR sensors for the detection of hazardous gases*. Sens. and Actuators B **149**: 194–198
66. B. Liedberg, C. Nylander and I. Lundström (1983), *Surface plasmons resonance for gas detection and biosensing*. Sens. Actuators **4**: 299-304
67. D.C. Cullen, R.G. Brown and C.R. Lowe (1987), *Detection of immuno-complex formation via surface plasmon resonance on gold-coated diffraction gratings*. Biosensors **3**: 211–225
68. M. Minunni and M. Mascini (1993), *Detection of pesticide in drinking water using real-time biospecific interaction analysis (BIA).* Anal. Lett. **26**: 1441–1460
69. D.C. Cullen and C.R. Lowe (1990), *A direct surface plasmon-polariton immunosensor: preliminary investigation of the non-specific adsorption of serum components to the sensor interface*. Sens. Actuators B **1**, 576–579
70. A.H. Severs, R.B.M. Schasfoort and M.H.L. Salden (1993), *An immunosensor for syphilis screening based on surface plasmon resonance*. Biosensors Bioelectron. **8**, 185–189
71. J. Homola, J. Dostálek, S. Chen, A. Rasooly, S. Jiang and S.S. Yee (2002), *Spectral surface plasmon resonance biosensor for detection of staphylococcal enterotoxin B in milk*. Int. J.Food Microbiol. **75**: 61–69
72. D.R. Mernagh, P. Janscak, K. Firman and G.G. Kneale (1998), *Protein–protein and protein–DNA interactions in the Type I restriction endonuclease R.EcoR124I*. Biol. Chem. **379**, 497–503
73. W. Jin, X. Lin, S. Lv, Y. Zhang, Q. Jin Q and Y. Mu (2009), *A DNA sensor based on surface plasmon resonance for apoptosis-associated genes detection*. Biosens Bioelectron. **24** (5), 1266-9
74. C. Nylander, B. Liedberg and T. Lind (1982), *Gas detection by means of surface plasmons resonance*. Sens. Actuators **3**: 79–88
75. K. Matsubara, S. Kawata and S. Minami (1988), *Optical chemical sensor based on surface plasmon measurement*. Appl. Opt. **27**: 1160–1163
76. S. Löfås, M. Malmqvist, I Rönnberg, E. Stenberg, B. Liedberg and I. Lundström (1991), *Bioanalysis with surface plasmon resonance*. Sens. Actuators B **5**: 79–84
77. J. Homola, I. Koudela and S. Yee (1999), *Surface plasmon resonance sensor based on diffraction gratings and prism couplers: sensitivity comparison*. Sens. Actuators B **54**: 16-24
78. X.D. Hoa, A.G. Kirk and M. Tabrizian (2007), *Towards integrated and sensitive surface plasmon resonance biosensors: a review of recent progress*. Biosens. Bioelectron. **23**: 151-160
79. J. Dostálek, J. Homola and M. Miler (2005), *Rich information format surface plasmon resonance biosensor based on array of diffraction gratings*. Sens. Actuators B **107**: 154–161
80. K. Matsubara, S. Kawata and S. Minami (1988), *A compact Surface Plasmon Resonance Sensor for Measurement of Water in Process*, Appl. Spectrosc. **42**: 1375-1379
81. P. Adam, J. Dostálek and J. Homola (2006), *Multiple surface plasmon spectroscopy for study of biomolecular systems*. Sens. Actuat. B **113**: 774–781

82. J. Dostálek, H. Vaisocherova and J. Homola (2005), *Multichannel surface plasmon resonance biosensor with wavelength division multiplexing*. Sens. Actuat. B **108**: 758–764
83. J.M. Brockman, B.P. Nelson and R.M. Corn (2000), *Surface plasmon resonance imaging measurements of ultrathin organic films*. Annu. Rev. Phys. Chem. **51**: 41-63
84. J. Homola (2008), *Surface Plamon Resonance Sensors for Detection of Chemical and Biological Species*. Chem. Rev. **108**: 462-493
85. J. Homola (2006), *Surface Plasmon Resonance based sensors*. Springer
86. K.M. Byun, S.J. Kim and D. Kim (2007), *Grating-coupled transmission-type surface plasmon resonance sensors based on dielectric and metallic gratings*. Appl. Opt. **46**: 5703-5708
87. A.W. Drake (1967), *Fundamentals of applied probability theory*. McGraw-Hill, New York
88. K. Kukanskis, J. Elkind, J. Melendez, T. Murphy, G. Miller and H. Garner (1999), *Detection of DNA hybridization using the TISPR-1 surface plasmon resonance biosensor*. Anal. Biochem. **274**: 7-17
89. S. Sjolander and C. Urbanitzky (1991), *Integrated fluid handling system for biomolecular interaction analysis*. Anal. Chem. **63**: 2338-2345
90. T.M. Chinowsky, L.S. Jung and S.S. Yee (1999), *Optimal linear data analysis for surface plasmon resonance biosensors*. Sens. Actuators B **54**: 89-97
91. P. Tobiška and J. Homola (2005), *Advanced data processing for SPR biosensors*. Sens. Actuators B **107** (1): 162–169
92. K. Johansen, R. Stalberg, I. Lundström and B. Liedberg (2000), *Surface Plasmon Resonance: Instrumental Resolution using Photo Diode Arrays*. Meas. Sci. Tech. **11**: 1630-1638
93. G.G. Nenninger, M. Piliarik, J. Homola (2002), *Data analysis for optical sensors based on spectroscopy of surface plasmons*. Meas Sci Technol **13**: 2038
94. V. Thomsen, D. Schatzlein and D. Mercuro (2003), *Limits of detection in spectroscopy*. Spectroscopy **18**: 112-114
95. J. Homola (1997), *On the sensitivity of surface plasmon resonance sensors with spectral interrogation*. Sens. Actuators B **41**: 207-211
96. F.C. Chien and S.J. Chen (2004), *A sensitivity comparison of optical biosensors based on four different surface plasmon resonance modes*. Biosens. Bioelectron. **20**: 633–642
97. I. Abdulhalim (2007), *Biosensing configurations using guided wave resonant structures*. Optical waveguide sensing and imaging, NATO Science for Peace and Security Series B: 211–228; Springer-Verlag
98. A. Shalabney and I. Abdulhalim (2011), *Sensitivity-enhancement methods for surface plasmon sensors*. Laser Photonics Rev. **5**: 571–606
99. G. Parisi, P. Zilio and F. Romanato (2012), *Complex Bloch-modes calculation of plasmonic crystal slabs by means of finite elements method*. Opt. Express **20**: 16690
100. D. Sarid, R.T. Deck, A.E. Craig, R.K. Hickernell, R.S. Jameson and J.J. Fasano (1982), *Optical field enhancement by long-range surface-plasma waves*. Appl. Opt. **21**: 3933–3995
101. G.G. Nenninger, P. Tobika, J. Homola and S.S. Yee (2001), *Long-range surface plasmons for high-resolution surface plasmon resonance sensors*. Sens. Actuat. B **74**:145–151

102. R. Slavík and J. Homola (2007), *Ultrahigh resolution long range surface plasmon-based sensor*. Sens. Actuators B **123** (1): 10–12

103. M. Vala, S. Etheridge, J.A. Roach and J. Homola (2009), *Long-range surface plasmons for sensitive detection of bacterial analytes*. Sens. Actuators B **139** (1): 59–63

104. O. Krupin, H. Asiri, C. Wang, R.N. Tait and P. Berini (2013), *Biosensing using straight long-range surface plasmon waveguides*. Opt. Express **21** (1): 698-709

105. M. Vala, R. Robelek, M. Bocková, J. Wegener and J. Homola (2013), *Real-time label-free monitoring of the cellular response to osmotic stress using conventional and long-range surface plasmons*. Biosens. Bioelectron. **240** (1): 417-421

106. H. Shi, Z. Liu, X. Wang, J. Guo, L. Liu, L. Luo, J. Guo, H. Ma, S. Sun and Y. He (2013), *A symmetrical optical waveguide based surface plasmon resonance biosensing system*. Sens. Actuators B **185**: 91– 96

107. F. Romanato, K.H. Lee, H.K. Kang, G. Ruffato and C.C. Wong (2009), *Sensitivity Enhancement in grating coupled surface plasmon resonance by azimuthal control*. Opt. Express **17**: 12145-12154

108. A. Sonato, G. Ruffato, G. Zacco, D. Silvestri, M. Natali, M. Carli, G. Giallongo, G. Granozzi, M. Morpurgo and F. Romanato (2013), *Enhanced sensitivity azimuthally controlled grating-coupled surface plasmon resonance applied to the calibration of thiol-poly(ethylene oxide) grafting.* Sens. Actuators B **181**: 559-566

109. G. Ruffato and F. Romanato (2012), *Grating-Coupled Surface Plasmon Resonance in the conical mounting with polarization modulation*. Opt. Lett. **37**: 2718-2720

110. G. Ruffato, E. Pasqualotto, A. Sonato, G. Zacco, D. SIlvestri, M. Morpurgo, A. De Toni, F. Romanato (2013), *Implementation and testing of a compact and high-resolution sensing device based on grating-coupled surface plasmon resonance with polarization modulation*. Sensors and Actuators B **185**: 179-187

111. J. Chandezon, D. Maystre and G. Raoult (1980), *A new theoretical method for diffraction gratings and its numerical application*. J. Optics (Paris) **11** (4): 235-241

112. J. Chandezon, M.T. Dupuis and G. Cornet (1982), *Multicoated gratings: a differential formalism applicable in the entire optical region*. J. Opt. Soc. Am. **72** (7): 839-846

113. S.J. Elston, G.P. Bryan-Brown and J.R. Sambles (1991), *Polarization conversion from diffraction gratings*. Phys. Rev. B **44** (12): 6393-6400

114. G. Granet, J.P. Plumey and J. Chandezon (1995), *Scattering by a periodically corrugated dielectric layer with non identical faces*. Pure Appl. Opt. **4** (1): 1-5

115. T.W. Preist, N.P.K. Cotter and J.R. Sambles (1995), *Periodic multilayer gratings of arbitrary shape*. J. Opt. Soc. Am. A **12** (8): 1740-1749

116. L. Li, G. Granet, J.P. Plumey and J. Chandezon (1996), *Some topics in extending the C-method to multilayer-coated gratings of different profiles*. Pure Appl. Opt. **5** (2): 141-156

117. J.P. Plumey, B. Guizal and J. Candezon (1997), *Coordinate transformation method as applied to asymmetric gratings with vertical facets*. J. Opt. Soc. Am. A **14** (3): 610-617

118. L. Li (1994), *Multilayer-coated diffraction gratings: differential method of Chandezon et al. revisited*. J. Opt. Soc. Am. A **11**: 2816-2828

119. L. Li (2007), *Using symmetries of grating groove profiles to reduce computation cost of the C-method*. J. Opt. Soc. Am. A **24**: 1085-1096
120. G. Ruffato, G. Zacco and F. Romanato (2011), *Surface Plasmon Polaritons Excitation and Propagation on Metallic Gratings: far-field and near-field numerical simulations*. J. Mater. Sci. Eng. A **1**: 768-777
121. E.J. Post (1962), *Formal Structure of Electromagnetics*. North-Holland, Amsterdam
122. J.D. Joannopoulos , S.G. Johnson, J.N. Winn and R.D. Meade (2008), *Photonic Crystals*. Princeton University Press
123. W. Jones and N.H. March (1985), *Theoretical Solid State Physics*, Vol. 1. Dover Publications
124. L. Li (1999), *Justification of matrix truncation in the modal methods of diffraction gratings*. J. Opt. A **1**: 531-536
125. G. Ruffato (2012), *Plasmonic gratings for sensing devices*. Ph.D. thesis, Università degli Studi di Padova, Italy
126. M. Davanço, Y. Urzhumov and G. Shvets (2007), *The complex Bloch bands of a 2D plasmonic crystal displaying isotropic negative refraction*. Opt. Express **15**: 9681
127. C. Fietz, Y. Urzhumov and G. Shvets (2011), *Complex k band diagrams of 3D metamaterial/photonic crystals*. Opt. Express **19**: 19027
128. B.P. Hiett, J.M. Generowicz, S.J. Cox, M. Molinari, D.H. Beckett and K.S. Thomas (2002), *Application of finite element methods to photonic crystal modeling*. IEEE Proc. - Sci. Meas. Technol. **149**: 293
129. S. Shi, C. Chen and D. W. Prather (2005), *Revised plane wave method for dispersive material and its application to band structure calculations of photonic crystal slabs*. Appl. Phys. Lett. **86**: 043104
130. P. Zilio (2013), *Mechanisms of surface plasmon polariton propagation for nano-optics applications*. Ph.D. thesis, Università degli Studi di Padova, Italy
131. S. Ekgasit, C. Thammacharoen and W. Knoll (2004), *Surface Plasmon Resonance Spectroscopy Based on Evanescent Field Treatment*. Anal. Chem. **76**: 561-568
132. X.C. Yuan, B.H. Ong, Y.G. Tan, D.W. Zhang, R. Irawan and S.C. Tjin (2006), *Sensitivity–stability-optimized surface plasmon resonance sensing with double metal layers*. J. Opt. A, Pure Appl. Opt. **8**: 959–963
133. B.H. Ong, X. Yuan and S.C. Tjin (2007), *Bimetallic Silver–Gold Film Waveguide Surface Plasmon Resonance Sensor*. Fiber and Integrated Optics **26**(4): 229-240
134. P. Lecaruyer, M. Canva and J. Rolland (2007), *Metallic film optimization in a surface plasmon resonance biosensor by the extended Rouard method*. Appl. Opt. **46**: 2361– 2369
135. M. Madou (2002), *Fundamentals of Microfabrication*. CRC Press
136. A. Sonato (2014), *Nanofabrication and development of surface plasmon resonance platforms for sensing applications*. Ph.D. thesis, Università degli Studi di Padova, Italy
137. L. Brigo, G. Grenci, A. Carpentiero, A. Pistore, M. Tormen, M. Guglielmi and G. Brusatin (2011), *Positive resist for UV and X-ray lithography synthesized through sol–gel chemistry*. J. Sol-Gel Sci. Technol. **60** (3): 400–407

138. D.A. Loy and K.J. Shea (1995), *Bridged Polysilsesquioxanes. Highly Porous Hybrid Organic-Inorganic Materials*. Chem. Rev. **95** (5): 1431–1442

139. L. Brigo, G. Grenci, L. Baù, A. Carpentiero, F. Mancin, F. Romanato, M. Tormen, M. Guglielmi and G. Brusatin (2011), *Hybrid porous resist with sensing functionality*. Microelectron. Eng **88** (8): 1913-1916

140. C.J. Brinker, G.C. Frye, A.J. Hurd and C.S. Ashley (1991), *Fundamentals of sol-gel dip coating*. Thin Solid Films **201**: 97-108

141. A. Antonello, G. Brusatin, M. Guglielmi, V. Bello, G. Mattei, G. Zacco and A. Martucci (2011), *Nanocomposites of titania and hybrid matrix with high refractive index*. J. Nanopart. Res. **13** (4): 1697-1708

142. G. Zuo, X. Li, Z. Zhang, T. Yang, Y. Wang, Z. Cheng and S. Feng (2007), *Dual-SAM functionalization on integrated cantilevers for specific trace-explosive sensing and non-specific adsorption suppression*. Nanotechnology **18** (25): 255501

143. G. Zacco, F. Romanato, A. Sonato, D. Sammito, G. Ruffato, M. Morpurgo, D. Silvestri, M. Carli, P. Schiavuta and G. Brusatin (2011), *Sinusoidal plasmonic crystals for bio-detection sensors*. Microelectron. Eng. **88**: 1898-1901

144. G. Zacco (2012), *Plasmonic Nanostructures for Enhanced Photovoltaics*. Ph.D. thesis, Università degli Studi di Padova, Italy

145. D.B. Hall, P. Underhill and J.M. Torkelson (1998), *Spin coating of thin and ultrathin polymer films*. Polym. Eng. Sci. **38** (12): 2039-2045

146. J.C. Love, L.A. Estroff, J.K. Kriebel, R.G. Nuzzo and G.M. Whitesides (2005), *Self-assembled monolayers of thiolates on metals as a form of nanotechnology*. Chem. Rev. **105**: 1103–69

147. H. Lloyd (1831), *On a New Case of Interference of the Rays of Light*. The Transactions of the Royal Irish Academy **17**: 171-177

148. Y. Xia and G.M. Whitesides (1998), *Soft Lithography*. Angew. Chem. Int. Ed. **37**: 550-575

149. J.A. Rogers and R.G. Nuzzo (2005), *Recent progress in soft lithography*. Materials today **8** (2): 50–56

150. A. Antonello, B. Jia, Z. He, D. Buso, G. Perotto, L. Brigo, G. Brusatin, M. Guglielmi, M. Gu and A. Martucci (2012), *Optimized Electroless Silver Coating for Optical and Plasmonic Applications*. Plasmonics **7** (4): 633-639

151. N. Yao and Z. L. Wang (2005), *Microscopy for Nanotechnology*. Kluwer Academic Publishers

152. M. Cittadini (2014), *Nanostructured materials for plasmonic based gas sensors*. Ph.D. thesis, Università degli Studi di Padova, Italy

153. S. N. Magonov and M. Whangbo (1996), *Surface Analysis with STM and AFM*. VCH

154. H. Fujiwara (2007), *Spectroscopic Ellipsometry: Principles and applications*. Wiley

155. P.Y. Yu and M. Cadorna (2005), *Fundamentals of Semiconductors*, 3rd edition. Springer

156. E. Gazzola, L. Brigo, G. Zacco, P. Zilio, G. Ruffato, G. Brusatin and F. Romanato (2013), *Coupled SPP Modes on 1D Plasmonic Gratings in Conical Mounting*. Plasmonics, **DOI**: 10.1007/s11468-013-9624-9

157. R.H. Ritchie, E.T. Arakawa, J.J. Cowan and R.N. Hamm (1968), *Surface-plasmon resonance effect in grating diffraction*. Phys. Rev. Lett. **21** (22): 1530-1533

158. C. Itzykson and J Zuber (2005), *Quantum Field Theory*. Dover
159. O.M. Jakšić, Ž.D. Čupic, Z.S. Jakšić, D.V. Randjelović and L.Z. Kolar-Anić (2013), *Monolayer gas adsorption in plasmonic sensors: comparative analysis of kinetic models*. Russ. Jour. Of Phys. Chem. A, **87** (13): 2134-2139
160. M. Scheller, S. Wietzke, C. Jansen and M. Koch (2009), *Modelling heterogeneous dielectric mixtures in the terahertz regime: a quasi-static effective medium theory*. J. Phys. D **42**: 065415
161. J. Yinon (2002), *Field detection and monitoring of explosives*. Trends Anal. Chem. **21**: 292
162. J.S. Caygill, F. Davis and S.P.J. Higson (2012), *Current trends in explosive detection techniques*. Talanta **88** (15): 14–29
163. L. Senesac and T.G. Thundat (2008), *Nanosensors for trace explosive detection*. Materials Today **11** (3): 28–36
164. T. Hübert, L. Boon-Brett, G. Black and U. Banach (2011), *Hydrogen sensors – A review*. Sens. Actuators B **157** (2): 329–352
165. The European Parliament and The Council Of The European Union (2004), *On the limitation of emissions of volatile organic compounds due to the use of organic solvents in certain paints and varnishes and vehicle refinishing products and amending Directive 1999/13/EC*. Official Journal of the European Union, Directive 2004/42/CE
166. US Department of Health and Human Services, Public Health Service, Agency for Toxic Substances and Disease Registry (2004): *Interaction Profile for Benzene, Toluene, Ethylbenzene and Xylenes*
167. D. Kondepudi and I. Prigogine (1998), *Modern Thermodynamics*. John Wiley & Sons
168. R. Stephenson and S. Malanowski (1987), *Handbook of the thermodynamics of organic compounds*. Elsevier New York
169. P.A. Pella (1977), *Measurement of the vapor pressures of tnt, 2,4-dnt, 2,6-dnt, and egdn*. The Journal of Chemical Thermodynamics **9** (4): 301-305
170. A. Gershanik and Y. Zeiri (2010), *Sublimation rate of TNT microcrystals in air*. J. Phys Chem A **114**: 12403-12410
171. I. Langmuir (1918), *The Adsorption of Gases on Plane Surface of Glass, Mica and Platinum*. The Research Laboratory of The General Electric Company: 1361–1402
172. D. Do (1998), *Adsorption analysis: equilibria and kinetics*. Imperial College Press
173. K. Lin, Y. Lu, J. Chen, R. Zheng, P. Wang and H. Ming (2008), *Surface plasmon resonance hydrogen sensor based on metallic grating with high sensitivity*. Opt. Express **16** (23): 18599-18604
174. P. Tobiska, O. Hugon, A. Trouillet, and H. Gagnaire (2001), *An integrated optic hydrogen sensor based on SPR on palladium.* Sens. Actuators B **74**: 168-172
175. A. Kolmakov and M. Moskovits (2004), *Chemical sensing and catalysis by one-dimensional metal-oxide nanostructures*. Annual Review of Materials Research **34**: 151-180
176. C.A. Hunter and J.K.M. Sanders (1990), *The nature of π – π interactions*. J. Am. Chem. Soc. **112**: 5525
177. M. Nagao and Y. Suda (1989), *Adsorption of benzene, toluene, and chlorobenzene on titanium dioxide*. Langmuir **5** (1): 42–47
178. M.O. Sinnokrot and C.D. Sherrill (2004), *Substituent Effects in π−π Interactions: Sandwich and T-Shaped Configurations*. J. Am. Chem. Soc. **126** (24): 7690–7697

179. M.C. Burleigh, M.A. Markowitz, M.S. Spector and B.P. Gaber (2002), *Porous Polysilsesquioxanes for the Adsorption of Phenols*. Environ. Sci. Technol. **36**: 2515-2518

180. E. Della Gaspera, S. Schutzmann, M. Guglielmi and A. Martucci (2011), *Spectroscopic ellipsometry analyses of thin films in different environments: an innovative "reverse side" approach allowing multi angle measurements*. Opt. Mater. **34**: 79-84

181. L.D. Landau, E.M Lifshitz and L.P. Pitaevskii (1980), *Statistical Physics – part 1*, 3rd edition. Pergamon Press

182. H. Haug and S. Koch (2004), *Quantum Theory of the optical and electronic properties of semiconductors*, 4rd edition. World Scientific